

# Modeling, Optimization and Design of High Power Medium Frequency Transformers

Présentée le 29 septembre 2023

Faculté des sciences et techniques de l'ingénieur  
Laboratoire d'électronique de puissance  
Programme doctoral en génie électrique

pour l'obtention du grade de Docteur ès Sciences

par

**Nikolina DJEKANOVIC**

Acceptée sur proposition du jury

Prof. A. P. Burg, président du jury  
Prof. D. Dujic, directeur de thèse  
Prof. E. Lomonova, rapporteuse  
Dr T. Gradinger, rapporteur  
Dr J. Smajic, rapporteur





*Dedicated to my dearest ones.*

*Action is the fundamental key to success.*

Pablo Picasso

# Abstract

The rising deployment of renewable energy sources and storage systems in today's power systems inevitably results in greater presence of DC-based technologies. To ensure efficient and safe power collection and distribution by means of medium voltage direct current (DC) grids, reliable and compact conversion devices are required to perform DC power transformation. Thereby, the isolated medium voltage converter technology provided by solid state transformers, and more specifically DC transformers, is regarded as the essential enabling technology. The medium frequency transformer (MFT), in addition to the power stages with semiconductor modules, is a crucial element in any such converter. Besides providing voltage adaption and galvanic isolation between the converter's input and output, it has a considerable impact on the converter's efficiency, power density, and proper operation.

In contrast to designing of line frequency transformers, which has been perfected for many years, the design of MFTs has still to be standardized and reach maturity. From the physical aspect, the rise in operating frequency benefits the reduction of magnetic component size and volume, which is a significant research motivator because it denotes weight and possibly cost savings. However, there is a number of new issues that must be accurately anticipated during the design process. Being operated within a power electronics converter, the MFT voltage excitation changes to a square wave with generally non-sinusoidal current waveforms. In turn, this affects the overall transformer losses and causes increased insulation stress. Moreover, the reduction of available surfaces for heat extraction puts emphasis on importance of thermal coordination. As can be seen, designing an MFT entails resolving a multiphysical optimization problem which considers all the essential domains and factors, including electric, magnetic, dielectric and thermal. Eventually, all the mentioned effects need to be carefully considered during the design process through adequate models.

The thesis focuses on filling the gap of modeling, optimization and design of a 1 MW core-type MFT, operated at 5 kHz as a part of a DC transformer which employs the resonant conversion principle. For this purpose, a design framework is established providing the electrical requirements and constraints for the MFT. Initially, a thorough state-of-the-art analysis of existing materials and technologies suitable for the task is presented, along with an overview of the models of the design-relevant MFT aspects. From there, a set of technologies is chosen, such as actively cooled pipe windings which are additionally submerged in oil for insulation and air-cooled, air-insulated core. It is not a common combination of technologies, which, thus, required additional consideration and modeling. The necessary models are either developed from scratch or adjusted from the literature and integrated within a design optimization algorithm. Finally, the design process revealed that out of the considered core materials, nanocrystalline material is the most suitable for 5 kHz operation. Moreover, from the pool of generated designs, a smaller set was delimited by applying design filters and fulfilling all the imposed constraints. From there, an optimal design is selected following the highest efficiency criterion, but having in mind the benefit of increased power density. Finally, the 1 MW 5 kHz MFT prototype was realized and thoroughly tested to validate and confirm the accuracy of the models employed in the design optimization tool.

**Keywords:** *Medium Voltage Direct Current Power Distribution Network, Direct Current Transformer, Solid State Transformer, Medium Frequency Transformer, Modeling, Optimization, Design*



# Zusammenfassung

Die zunehmende Verwendung erneuerbarer Energiequellen und Speichersysteme in heutigen Stromnetzen führt zwangsläufig zu einer stärkeren Nutzung von Gleichstromtechnik. Um eine effiziente und sichere Energiesammlung und -verteilung über Mittelspannungs-Gleichstromnetze zu gewährleisten, bedarf es zuverlässiger und kompakter Anlagen für die Gleichstrom-Leistungsumwandlung. Dabei wird die isolierte Mittelspannungswandlertechnologie, die von *Solid-State Transformers* und insbesondere von Gleichstromtransformatoren bereitgestellt wird, als wesentliche Grundlagentechnologie betrachtet. Der Mittelfrequenztransformator (MFT) ist neben den Leistungsstufen mit Halbleitermodulen ein entscheidendes Element in einem solchen Konverter. Er sorgt nicht nur für die Spannungsanpassung und die galvanische Trennung zwischen dem Eingang und dem Ausgang des Wandlers, sondern hat auch einen erheblichen Einfluss auf den Wirkungsgrad, die Leistungsdichte und den stabilen Betrieb des Converters.

Im Gegensatz zum Design von Netzfrequenztransformatoren, welches seit vielen Jahren optimiert wurde, muss das Design von MFTs noch technisch ausgereifter und standardisiert werden. Aus physikalischer Sicht führt die Steigerung der Betriebsfrequenz zu einer Verringerung der Größe und des Volumens der magnetischen Komponenten, was eine weitere wichtige Motivation für die Forschung auf diesem Gebiet ist, da die Verkleinerung der Komponenten zu Gewichts- und Kosteneinsparungen führen kann. Es gibt jedoch eine Reihe neuer Probleme, die in der konzeptionellen Planung berücksichtigt werden müssen. Beim Betrieb innerhalb eines leistungselektronischen Wandlers wird die MFT-Spannungserregung zu einem rechteckigen Signal mit einem im Allgemeinen nicht-sinusförmigen Stromverlauf. Dies wiederum wirkt sich auf die Gesamtverluste des Transformators aus und führt zu einer erhöhten Belastung der Isolierung. Darüber hinaus wird durch die Verringerung der für die Wärmeabfuhr zur Verfügung stehenden Flächen die Bedeutung der korrekten thermischen Koordination der Komponente betont. Wie man sieht, ist der konzeptionelle Aufbau eines MFT mit der Lösung eines multiphysikalischen Optimierungsproblems verbunden, bei dem alle wesentlichen elektrische, magnetische, dielektrische und thermische Aspekte berücksichtigt werden müssen. Letztendlich müssen alle genannten Effekte während des Entwurfsprozesses durch geeignete Modelle sorgfältig einbezogen werden.

Diese Dissertation befasst sich damit, die technischen Lücken bei der Modellierung, der Optimierung und dem Entwurf eines 1 MW-MFT zu schließen, der mit 5 kHz als Teil eines Gleichstromtransformators betrieben wird, welcher die Resonanzumwandlung nützt. Zu diesem Zweck ist ein Entwurfsrahmen erstellt worden, der die elektrischen Anforderungen und Einschränkungen für den MFT beinhaltet. Zunächst wird eine detaillierte Analyse des Stands der Technik in Bezug auf bestehende Materialien und Technologien, die für diese Aufgabe geeignet sind, sowie ein Überblick über die Modelle der konstruktionsrelevanten MFT-Aspekte vorgestellt. Basierend auf diesen Grundlagen, wird eine Reihe von Technologien ausgewählt, wie aktiv gekühlte Rohrwicklungen, die zur Isolierung zusätzlich in Öl getaucht sind, und ein luftgekühlter, luftisolierter Kern. Es handelt sich dabei um eine nicht alltägliche Kombination von Technologien, die daher zusätzliche Überlegungen und Modellierungen erforderte. Die notwendigen Modelle wurden entweder von Grund auf neu entwickelt oder aus der Literatur übernommen und in einen Design-Optimierungsalgorithmus integriert. Schließlich ergab der Designprozess, dass das Nanokristallin unter den in Betracht gezogenen Materialien am besten für den 5 kHz-Betrieb des Transformators geeignet ist. Auf Basis von Designfiltern und weiterer Kriterien ist aus den zahlreichen Designs eine Erstauswahl getroffen worden. Aus dieser verbliebenen Menge ist schliesslich das optimale Design ausgewählt worden, welches dem Kriterium der höchsten Effizienz folgt, aber auch eine höhere Leistungsdichte bietet. Schließlich wurde der 1 MW 5 kHz

MFT-Prototyp aufgebaut und gründlich getestet, um die Genauigkeit der im Design-Optimierungstool verwendeten Modelle zu überprüfen und zu validieren.

**Stichwörter:** *Mittelspannungs-Gleichstrom-Verteilungsnetz, Gleichstromtransformator, Solid-State Transformer, Mittelfrequenztransformator, Modellierung, Optimierung, Design*

# Résumé

Le déploiement croissant de sources d'énergie renouvelables et de systèmes de stockage dans les réseaux électriques actuels entraîne inévitablement une plus grande présence des technologies fondées sur le courant continu. Pour garantir l'efficacité et la sécurité de la collecte et de la distribution de l'électricité au moyen de réseaux de moyenne tension à courant continu (CC), des dispositifs de conversion fiables et compacts sont nécessaires pour effectuer la transformation de l'énergie en courant continu. C'est pourquoi la technologie des convertisseurs isolés de moyenne tension fournie par les solid state transformers, et plus particulièrement les transformateurs CC, est considérée comme une technologie essentielle. Le transformateur de moyenne fréquence (MFT), en plus des étages de puissance avec modules de semi-conducteurs, est un élément crucial de tout convertisseur de ce type. Outre l'adaptation de la tension et l'isolation galvanique entre l'entrée et la sortie du convertisseur, il a un impact considérable sur l'efficacité, la densité de puissance et le bon fonctionnement du convertisseur.

Contrairement à la conception des transformateurs de fréquence de ligne, qui a été perfectionnée pendant de nombreuses années, la conception des MFTs doit encore être normalisée et arriver à maturité. D'un point de vue physique, l'augmentation de la fréquence de fonctionnement permet de réduire la taille et le volume des composants magnétiques, ce qui constitue une motivation importante pour la recherche, car cela permet de réduire le poids et éventuellement les coûts. Cependant, un certain nombre de nouveaux problèmes doivent être anticipés avec précision au cours du processus de conception. Fonctionnant dans un convertisseur électronique de puissance, la tension d'excitation du MFT se transforme en onde carrée avec des ondes de courant généralement non sinusoïdales. Cela affecte les pertes globales du transformateur et augmente les contraintes d'isolation. En outre, la réduction des surfaces disponibles pour l'extraction de la chaleur met l'accent sur l'importance de la coordination thermique. Comme vu dans la thèse, la conception d'un MFT implique de résoudre un problème d'optimisation multiphysique qui prend en compte tous les domaines et facteurs essentiels : électriques, magnétiques, diélectriques et thermiques. En somme, tous les effets mentionnés doivent être soigneusement pris en compte au cours du processus de conception au moyen de modèles adéquats.

Cette thèse vise à combler les lacunes en matière de modélisation, d'optimisation et de conception d'un MFT de 1 MW à noyau, fonctionnant à 5 kHz en tant que partie d'un transformateur CC qui utilise le principe de conversion résonante. Pour ce faire, un cadre de conception est établi fournissant les exigences et les contraintes électriques pour la MFT. Dans un premier temps, une analyse approfondie de l'état de l'art des matériaux et technologies existants adaptés à cette tâche est présentée, ainsi qu'un aperçu des modèles d'aspects MFT pertinents pour la conception. De là, les technologies choisies sont les suivantes : enroulements de tubes refroidis activement et immergés dans de l'huile pour l'isolation, noyau refroidi à l'air et isolé à l'air, etc. Il ne s'agit pas d'une combinaison courante de technologies, ce qui a donc nécessité une réflexion et une modélisation supplémentaires.

Les modèles nécessaires sont soit développés à partir de zéro, soit adaptés à partir de la littérature et intégrés dans un algorithme d'optimisation de la conception. Finalement, le processus de conception a révélé que, parmi les matériaux de noyau considérés, le nanocristallin est le plus approprié pour un fonctionnement à 5 kHz. En outre, à partir de l'ensemble des conceptions générées, un ensemble plus restreint de matériaux a été retenu en appliquant des filtres de conception et en répondant à toutes les contraintes imposées. À partir de là, une conception optimale est sélectionnée selon le critère de l'efficacité la plus élevée, tout en gardant à l'esprit l'avantage d'une densité de puissance accrue. Enfin, le prototype 1 MW 5 kHz MFT a été réalisé et testé de manière approfondie pour valider et

confirmer la précision des modèles utilisés dans l'outil d'optimisation de la conception.

**Keywords:** *Réseaux de distribution d'énergie à courant continu à moyenne tension, Transformateur à courant continu, Solid State Transformer, Transformateur de moyenne fréquence, Modélisation, Optimisation de la conception*



# Acknowledgments

*Precisely one of the most gratifying results of intellectual evolution  
is the continuous opening up of new and greater prospects.*

Nikola Tesla

Once you start writing the acknowledgments, it means the PhD has really come to an end. What a journey it has been! I am very happy and grateful to have had such an experience, which was challenging and full of ups and downs (as life itself). Nevertheless, looking back, I enjoyed the amazing and enriching past four years. At this point, I would like to express my sincere gratitude to my thesis supervisor, Prof. Dražen Dujić, for giving me the opportunity to pursue this dream of mine and for always being available to advise and criticize. I believe he supported and guided me in my best interest, and I am thankful for all the engaging discussions we shared.

I would like to thank the members of the jury: Prof. Elena Lomonova from TU/e Eindhoven University of Technology, Dr. Jasmin Smajić from ETH Zurich, and Dr. Thomas Gradinger from Hitachi Energy Switzerland, for taking the time to evaluate my work and for a very interesting discussion during the defense, which provided me with valuable feedback. I would also like to thank Prof. Andreas Burg from EPFL for accepting the role of the jury president twice, for my PhD and candidacy exams.

Thinking about the path that led me to this point, I would like to thank my dear friend Dr. Anant Narula, who connected me to the right people during my time in Stockholm, which changed my course to power electronics oriented topics. Secondly, I would like to thank Dr. Diane Sadik for making the introduction to Power Electronic Laboratory (PEL) and Prof. Dujić. These two connections significantly determined my education direction and I am very grateful to them.

I would like to thank the members of the mechanical engineering workshop, and particularly to Maxime Raton, Laurent Chevalley, Nicolas Jaunin and Christophe Zurmühle for their help in manufacturing various mechanical parts of the transformer, for their patience, and valuable and constructive advice that significantly contributed to successful prototyping of the MFT.

Many thanks to Andrea for diligently proofreading the thesis. On the same note, I wish to thank all the colleague from PEL for the support, great atmosphere in the laboratory, numerous technical and non-technical discussions, lunches, drinks at Satellite and Taphouse and all the dear moments we shared together. I am grateful in particular to: my office colleagues, Xiaotong, Jules, Chengmin, and Stefan, then to Gabriele, Philippe, Ignacio, Pierre, ChangHwan, Max, and Emilien. Special thanks I owe to Anja, Stefan, Milan, Miodrag, Marko and Dragan, which were a part of PEL once I started my PhD and who made sure that I feel at home very fast. They also made a large part of the Serbian community in Lausanne with who I shared uncountable and priceless moments. I hope the friendships I made during my stay there will continue to grow in the future as well.

Throughout my life I was lucky to live in different cities around Europe and meet amazing people who I am happy to call my friends. I would like to thank in particular Jana, Ljiljana, Vesna, Jovana, Irena, Nemanja and Mladen, for their support, love and believing in me during this journey.

Finally, my deepest gratitude goes to my dear parents, Vida and Predrag, and my one and only amazing sister, Nataša. They have always provided unlimited support and love, had faith in me and I am very happy and grateful to have them in my life. It is needless to say that without their help this achievement would not be possible. *Hvala vam, volim vas!*

Lausanne, July 2023

Nikolina Đekanović



# List of Abbreviations

AC	Alternating Current
AF	Air Forced
Al	Aluminum
AN	Air Natural
BC	Boundary Condition
BIL	Basic Lightning Impulse
CFD	Computational Fluid Dynamics
CTC	Continuously Transposed Conductor
CTI	Comparative Tracking Index
Cu	Copper
DAB	Dual Active Bridge
DC	Direct Current
DCT	DC Transformer
DI	Deionized
EMC	Electromagnetic Compatibility
FEM	Finite Element Modeling
GOES	Grain Oriented Electrical Steel
HTC	Heat Transfer Coefficient
HV	High Voltage
HVDC	High Voltage DC
ID	Inner Diameter
IEA	International Energy Agency
IGBT	Insulated-Gate Bipolar Transistor
IGCT	Integrated Gate-Commutated Thyristor
IGSE	Improved Generalized Steinmetz Equation
ISOP	Input-Series Output-Parallel

LF	Low Frequency		
LFT	Line Frequency Transformer		
LLC-SRC	LLC Series Resonant Converter		
LV	Low Voltage		
LVDC	Low Voltage DC		
MF	Medium Frequency		
MFT	Medium Frequency Transformer		
MLT	Mean Length Turn		
MMF	Magnetomotive Force		
MPL	Magnetic Path Length		
MSE	Modified Steinmetz Equation		
MV	Medium Voltage		
MVDC	Medium Voltage DC		
NPC	Neutral Point Clamped		
OD	Outer Diameter		
ODAF	Oil Directed Air Forced		
OFAF	Oil Forced Air Forced		
OFAN	Oil Forced Air Natural		
OFWF	Oil Forced Water Forced		
ONAF	Oil Natural Air Forced		
ONAN	Oil Natural Air Natural		
ONWF	Oil Natural Water Forced		
OVC	Over-Voltage Protection Category		
PD	Partial Discharge		
PDN	Power Distribution Network		
PoD	Pollution Degree		
PV	Photovoltaic		
PW	Primary Winding		
PWM	Pulse-Width Modulation		
RC-IGCT	Reverse-Conducting Commutated Thyristor	Integrated	Gate-

RMS	Root Mean Square
SRC	Series Resonant Converter
SST	Solid-State Transformer
SW	Secondary Winding
TC	Thermocouple
THM	Thermal-Hydraulic Model
VPI	Vacuum-Pressure Impregnation
WCSE	Waveform Coefficient Steinmetz Equation
WCU	Water Cooling Unit
ZCS	Zero-Current Switching
ZVS	Zero-Voltage Switching



# Contents

<b>Abstract</b>	<b>i</b>
<b>Zusammenfassung</b>	<b>iii</b>
<b>Résumé</b>	<b>v</b>
<b>Acknowledgments</b>	<b>vii</b>
<b>List of Abbreviations</b>	<b>ix</b>
<b>1 Introduction</b>	<b>1</b>
1.1 Solid-State Transformer	4
1.2 Medium Frequency Transformer	6
1.3 Objectives and Contributions	8
1.4 Thesis Outline	9
1.5 List of Publications	10
<b>2 MFT Design Optimization Problem</b>	<b>13</b>
2.1 Introduction	13
2.1.1 Magnetic Circuit Modeling	14
2.1.2 Electric Circuit Modeling	15
2.1.3 Scaling Law	16
2.2 MFT Design Optimization Problem	18
2.2.1 Design Challenges	19
2.3 Available Technologies	23
2.3.1 Core Material	23
2.3.2 Winding Technology	27
2.3.3 Cooling Technology	29
2.3.4 Insulation Technology	30
2.4 MFT Construction Types	33
2.5 Modeling	34
2.5.1 Electrical Parameters	34
2.5.2 Core Losses	36
2.5.3 Winding Losses	37
2.5.4 Thermal Modeling	39
2.5.5 Mechanical Withstand Considerations	42
2.5.6 Design Methods	42
2.6 Summary	43
<b>3 MFT Design Space</b>	<b>45</b>
3.1 Introduction	45
3.2 Selected Technologies	47
3.3 Winding Arrangements	48
3.3.1 1-layer MFT Structure	49

3.3.2	3-winding MFT Structure	50
3.3.3	2-vessel MFT Structure	50
3.4	Design Optimization Algorithm	51
3.5	Summary	54
<b>4</b>	<b>MFT Leakage Inductance Modeling</b>	<b>55</b>
4.1	Introduction	55
4.2	1D Dowell's Model	56
4.3	2D Margueron's Model	58
4.3.1	Model Validation	61
4.4	Sensitivity Analysis	62
4.5	Summary	64
<b>5</b>	<b>Thermal-Hydraulic Model for Oil-Immersed Water-Cooled MFT Windings</b>	<b>67</b>
5.1	Introduction	67
5.2	Model Development	68
5.2.1	Thermal Part of THM	70
5.2.2	Hydraulic Part of THM	72
5.2.3	THM Implementation	74
5.3	THM Characterization and Validation	76
5.3.1	Experimental Setup	76
5.3.2	Measurements	78
5.4	Summary	82
<b>6</b>	<b>MFT Losses and Static Thermal Modeling</b>	<b>83</b>
6.1	Introduction	83
6.2	Core Loss Model	83
6.2.1	Analytical Core Loss Model	83
6.3	Winding Loss Model	85
6.3.1	1D Dowell's Model	85
6.3.2	Model Extension for Hollow Conductors	87
6.4	Static Thermal MFT Model	89
6.4.1	Thermal Core Model	90
6.4.2	Thermal Winding Model	93
6.4.3	Ambient Interface Model	99
6.5	Summary	101
<b>7</b>	<b>1 MW MFT Design Optimization</b>	<b>103</b>
7.1	Introduction	103
7.2	1 MW 2-vessel MFT Optimal Design	104
7.3	1 MW 2-vessel MFT Prototype Design	109
7.4	Summary	113
<b>8</b>	<b>1 MW MFT Prototype</b>	<b>115</b>
8.1	Introduction	115
8.2	Mechanical Construction	116
8.2.1	Core	116



8.2.2	Windings	117
8.2.3	Insulation Coordination	120
8.2.4	Full Prototype	121
8.3	Experimental Testing	122
8.3.1	Electrical Parameters	122
8.3.2	Partial Discharge Test	123
8.3.3	MFT Operation in DCT Test Setup	125
8.3.4	Thermal Measurements	128
8.4	Summary	129
<b>9</b>	<b>Conclusion and Future Work</b>	<b>131</b>
9.1	Summary and Contributions	131
9.2	Final Conclusions	134
9.3	Future Work	135
	<b>Appendices</b>	<b>137</b>
<b>A</b>	<b>Dimensionless Numbers</b>	<b>139</b>
A.1	Prandtl Number	139
A.2	Rayleigh Number	139
A.3	Reynolds Number	139
A.4	Nusselt Number	140
<b>B</b>	<b>Thermal Properties of Fluids</b>	<b>141</b>
<b>C</b>	<b>Multi-Winding MFT Configurations</b>	<b>143</b>



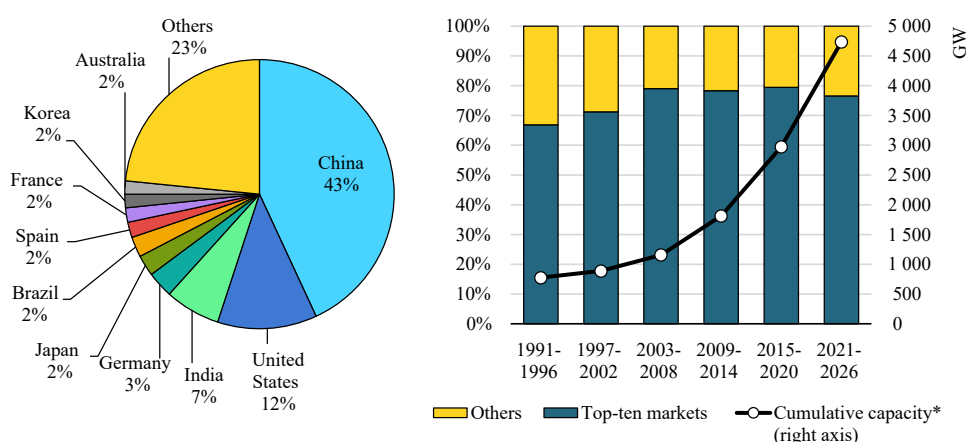
# 1

## Introduction

In contrast to the traditional Alternating Current (AC) power system, which typically does not include AC microgrids and features the radial structure, one can say that the concept of a modern power system relies on distributed energy generation and storage, i.e. generally speaking decentralization. Thereby, distributed generation is motivated by the fact that countries worldwide are encouraging the use of renewable energy resources with the goal to fight climate change, and optimally reach net zero emissions by 2050 [1]. Similarly, distributed storage makes local collections of electrical energy for use during critical periods to flatten the peaks and valleys of demand.

Among the leading renewable energy sources are Photovoltaics (PVs), wind, which are marked as variable renewables, and hydropower, which dominates in terms of the installed base. Some other less exploited resources include biomass and geothermal energy. A recent study conducted by the International Energy Agency (IEA) discusses past and future trends regarding renewable energy, as well as the main factors affecting its growth [2]. Among some of them are the employed technologies and the pace of innovation, together with implementation and grid integration challenges, but also social acceptance, financing, policies, and regulations in general.

**Fig. 1.1** shows the historical development of renewable capacities installed until today and a future forecast (2021 – 2026) based on the available public information about subsidies and agreements



IEA. All rights reserved.

**Fig. 1.1** Share of total installed renewable capacity for the top-ten countries, recorded from 1991 until today, including a forecast to 2026. Cumulative capacity relates to the capacity actually installed at the end of each five-year period [2].

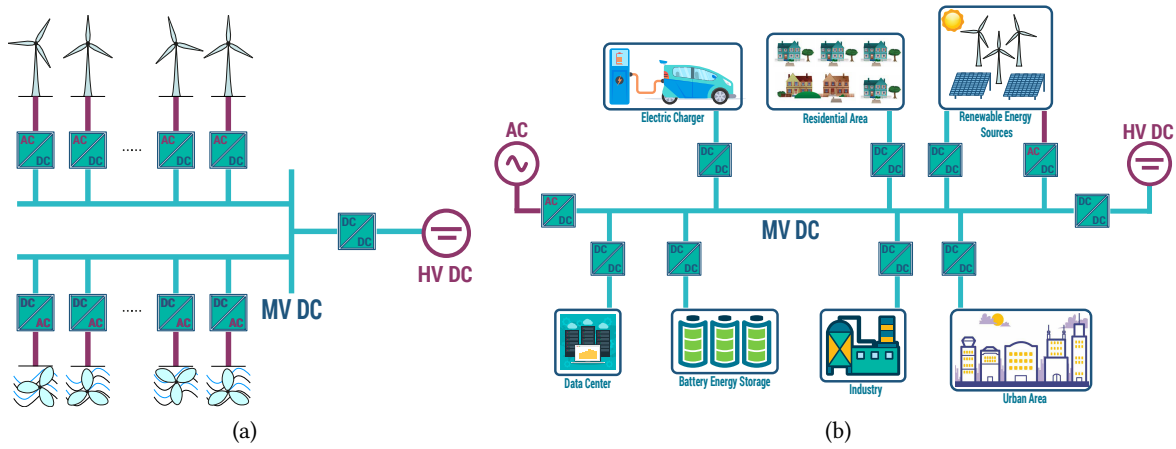


**Fig. 1.2** (a) MVDC collection grid in a radial configuration, with an offshore platform (MVDC-HVDC converter) and HVDC transmission, collecting tidal and wind power; (b) MVDC PDNs integrate various types of DC loads, such as data centers, electric chargers, industrial applications, residential and urban areas, support energy generation by renewable sources and storage facilities (through battery energy systems).

concerning future installations. The pie chart given on the left shows the distribution among the top-ten countries of the renewable capacity growth in the period 2021 – 2026. The People’s Republic of China stands out as the leader, with a 43% share in global growth, followed by the United States, Europe, and India. The chart on the right indicates that the overall market share between the top ten leading countries and the rest of the world remains approximately the same throughout the considered time period. One can conclude that there is tremendous resource potential in the rest of the countries outside of the top ten. Furthermore, according to IEA renewable electricity capacity is expected to reach more than 4800 GW by 2026, which astonishingly also corresponds to the current global power capacity of fossil fuels and nuclear energy combined. Note that PVs account for almost 60% of the overall forecasted renewable capacity over the considered period.

The technologies required to exploit the power of the sun through photovoltaics rely on Direct Current (DC). This is, however, not the case with wind turbines/generators, which inherently provide AC output. Nevertheless, the trend of decentralization, i.e. the increased deployment of renewable energy generation, which started several decades ago, allowed the DC technology to gradually increase its presence in otherwise AC-dominated systems. Based on the concept of DC collection grids, which is shown in **Fig. 1.2a** on the example of wind and tidal power, the produced energy can be gathered to a local Power Distribution Network (PDN), illustrated in **Fig. 1.2b**, before it is transferred to a utility power system. Today, more than ever, this signifies that the existing (AC) power systems need to adjust to the change and this is made possible thanks to energy conversion based on power electronics. With this in mind and the ever-growing trend of installed renewable capacity from **Fig. 1.1**, one can conclude that the future of power systems will be heavily power-electronics dominated.

DC technology pioneered in the High Voltage DC (HVDC) area with bulk power transmission systems. The world’s first commercial HVDC transmission system in Gotland, Sweden was installed in 1954 [5]. It proved to be particularly beneficial for undersea transmission over long distances (more than 100 km) when cables are used, due to the reduction of transmission losses [6]. Nowadays, numerous HVDC installations have been realized, predominantly on the Asian continent (approximately 130 GW),

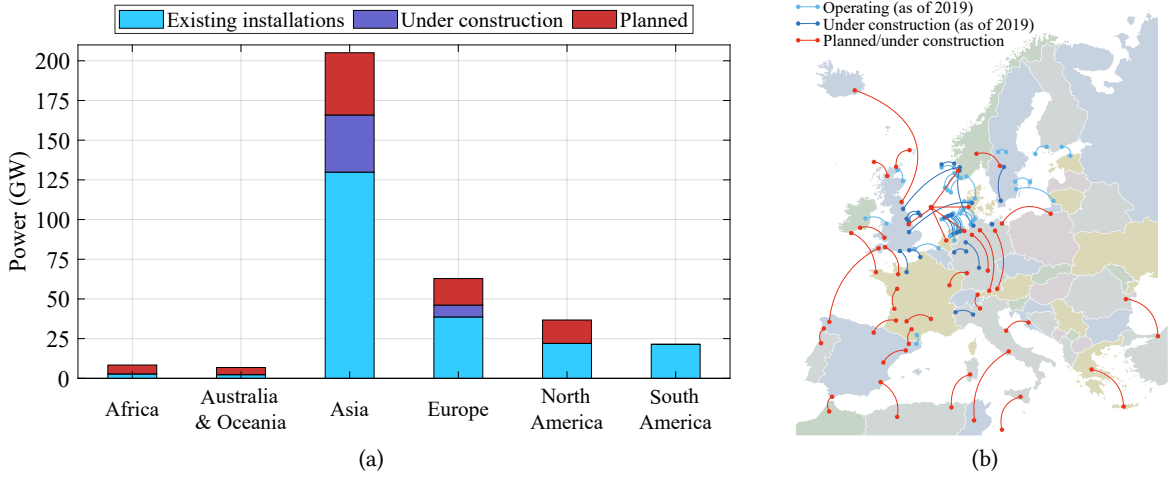


**Fig. 1.3** (a) Overview of the existing, under construction, and planned HVDC projects around the world [3]. (b) HVDC power transmission systems in Europe [4].

with 36 GW capacity currently under construction, and roughly the same amount planned [3]. The runner-up is Europe with a three times lower total capacity of 63 GW, followed by North and South America. A list of past, future, and ongoing HVDC projects is given in [3], whereas **Fig. 1.3a** provides an overview of HVDC power capacities across continents. **Fig. 1.3b** illustrates the locations of the existing and planned HVDC transmission lines covering Europe.

On the other hand, in the Low Voltage DC (LVDC) domain, the presence of DC technology in the distribution has been increased with the use of solar modules which produce Low Voltages (LVs). In a broader sense, DC experienced general expansion through portable electronic devices and data centers (server CPUs). The main reason behind it is that DC distribution promises an overall higher system efficiency, due to the reduced number of conversion stages and reduced complexity [7]–[10]. Nevertheless, increased efficiency is not the only consideration to keep in mind when AC vs. DC comparison is made. Namely, safety, stability, costs, aging, and Electromagnetic Compatibility (EMC) are some of the essentials that need to be closely looked at.

The DC voltage range from 1.5 kV up to 50 kV, which is henceforth referred to as the Medium Voltage (MV) domain, has not yet been fully explored and capitalized. This is partly due to a number of challenges (economical and partly technical), such as protection, missing standardized DC voltage levels, and the general lack of a strong business case in many applications. Nevertheless, there is unexploited potential to e.g. connect widely distributed sources of renewable energy, as already mentioned above, to energy storages (such as batteries), or to use DC to transfer off-shore power to the shore [11]. To be precise, this includes offshore wind parks connected to land by DC links, as well as solutions to exploit tidal power [12]–[14]. In general, Medium Voltage DC (MVDC) technology could improve the grid's overall efficiency and flexibility or even provide a full replacement of the existing AC systems. Therefore, it is possible to imagine MVDC collection systems and PDNs in future energy systems, as illustrated in **Fig. 1.2**.

On the other hand, MVDC distribution is already considered for marine on-board applications [15], [16]. Some of the reasons for this trend include the improved efficiency of the prime movers (engines

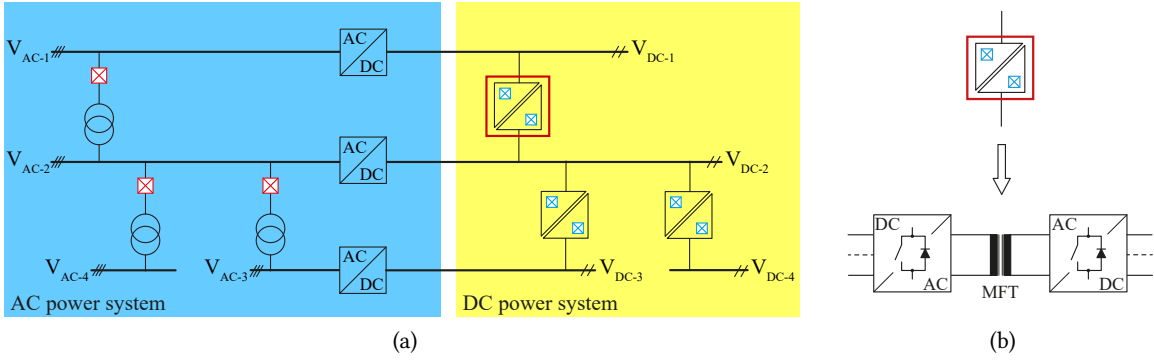


**Fig. 1.4** (a) Hybrid combination of state-of-the-art AC power system with future MVDC power distribution network; (b) The concept of DCT, which includes a MV converter galvanically isolated with an MFT. The converter stages are not shown explicitly since there is a variety of possible topologies and switching devices.

and gas turbines) since the generators do not need to be synchronized to the same AC network, reduction in the number of conversion stages, and easier integration of battery energy storages. Such PDNs are regarded as isolated microgrids, which are disconnected from the regular utility power systems and do not need to follow strict requirements, standards, or grid codes, which explains the accelerated progress [17].

## 1.1 Solid-State Transformer

Regarding the necessary enabling technology, Solid-State Transformers (SSTs) provide energy conversion and interconnection of any kind of AC or DC electric system, and they are considered to be the key emerging technology for future distribution grids. Today, the name SST is a collective synonym for various galvanically isolated converters, which can be implemented as single or modular. More precisely, an SST consists of at least two converter stages, which enable control of both input and output currents and voltages, and single or multiple Medium Frequency Transformers (MFTs) that facilitate galvanic isolation and voltage adaptation. The term SST has been first mentioned in [18]. The concept has been gaining popularity in last years and was successfully demonstrated through various prototypes, realized both in academia and industry [19], [20]. Additionally, this trend was supported by semiconductor companies that offer high-voltage devices with improved properties based on wide-band gap materials, such as silicon carbide. As a result, prototype systems have been realized for MVDC conversion using a wide range of possible converter topologies. Most of the relevant literature deals with either single-phase SSTs for traction on-board applications [21], [22] or with three-phase SSTs for smart-grids [23]–[25]. Furthermore, two large European projects UNIFLEX [26] and HEART [27] have also investigated similar applications using this concept. Recently, a European project HYPERRIDE [28] started looking into LV and MV of DC and hybrid AC-DC grids and the challenges tied to enabling technologies, field implementation, protection, and finally, commercialization.

This thesis work is a part of the EMPOWER project [29], sponsored by the European Research Council, which aims to develop a high-power isolated DC-DC converter operating in the MV range for future MVDC PDNs, named as DC Transformer (DCT). Such a device is classified as a type of SST, and it is considered to be the missing key component and the necessary building block of MVDC PDNs to enable a highly efficient, reliable and compact DC power transformation. In **Fig. 1.4a**, the DCT

is enclosed within a red rectangle and it is used to enable the interface between two DC grids at different voltage levels. The entire figure shows a hybrid combination of AC and DC PDNs. The AC side represents a state-of-the-art power system with several voltage levels that are interfaced with standard AC transformers and circuit breakers for protection. This side is further interconnected with the DC side through corresponding AC-DC converters. **Fig. 1.4b** provides more details about the DCT concept and bulk power processing, i.e. an isolated MV converter based on a single MFT and rated for the full power of the system.

In general, depending on the number of converter stages and MFTs used, the SSTs process power fractionally or in a bulk manner. For fractional power processing, multiple MFTs interconnect series- or parallel-connected converter stages. The Input-Series Output-Parallel (ISOP) concept, which is shown in **Fig. 1.5** on the example of DCT, is the one typically used to interconnect an MVDC grid with an LVDC grid. Until now, most of the designed and realized SST configurations were based on this concept [30]–[33]. However, depending on the applications' current and voltage requirements, different combinations, e.g. input-parallel output-parallel and input-series output-series are also possible. Regardless of the fact that power is processed fractionally, each of the MFTs in the ISOP configuration needs to be isolated for the full input and output voltage of the system. Moreover, the reliability of such SSTs is jeopardized, which is further supported by the fact that only demo units of SSTs are built, as mentioned earlier, and there are still no commercially available products on the market. This provides motivation to turn to single-stage conversion. Bulk power processing offers simpler overall integration of a power electronic system, primarily due to the lower number of components which aids system design and optimization. Nevertheless, the issue with severe insulation coordination requirements pertains, due to the MVDC application. This leads to the conclusion that insulation coordination represents a serious technical challenge irrespective of the SST type.

Some of the challenges the DCTs are still experiencing are related to protection. The already existing electromechanical circuit breakers implemented for AC grids cannot be directly used for DC needs, due to their low-impedance nature which prompts a shorter rise-time of the fault current (in the range of several microseconds or less). Therefore, DC circuit breakers are considered to be the key enabling technology for grid protection, where a fair amount of research is directed [34], [35]. Solutions based on solid state circuits, which rely on fast semiconductor devices to achieve current interruption and are predominantly proposed and implemented for LVDC breakers, prove to be promising [36]. However, to be able to clear faults sufficiently fast in MVDC grids requires and implies even higher breakdown voltages and losses compared to solid state LVDC breakers. The losses need to be dissipated, which

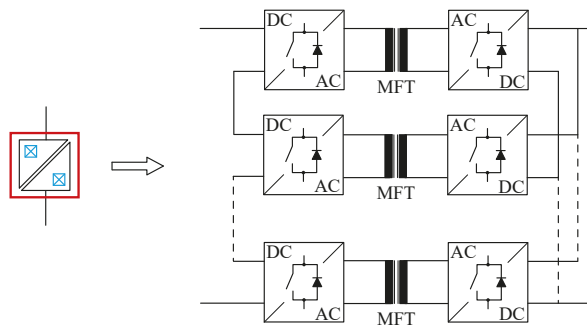


**Fig. 1.5** SST ISOP concept - an example of a possible implementation, based on the modular approach with multiple MFTs being sized for a fraction of the total converter power.

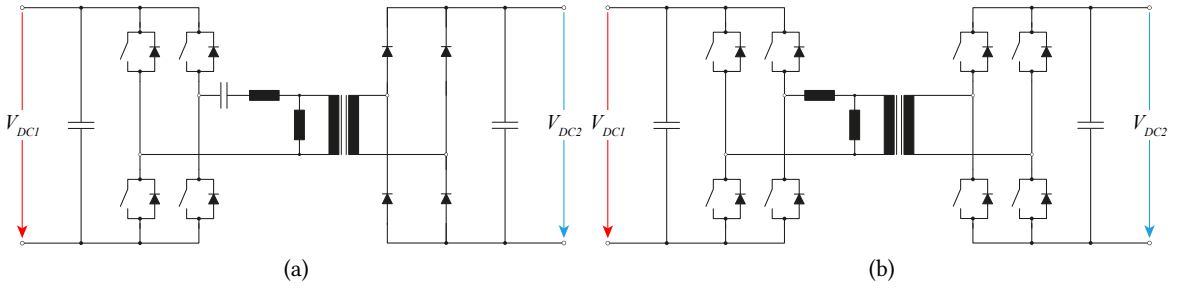


**Fig. 1.6** Commonly used topologies for high-power isolated DC-DC converters: (a) SRC and (b) DAB. The MFT is an essential part of both topologies. It is presented by its equivalent electric circuit with an ideal transformer, the magnetizing inductance connected in parallel, and the leakage inductance in series. Note that power stages are implemented as full-bridges only for illustration purposes and generally, many other topologies can be used.

further calls for a more effective cooling system, thus resulting in increased size and complexity. Even though DCTs enable not only MVDC distribution and collection grids but implicitly encourage increased use of renewable energy sources, these advantages and compounding benefits come at the expense of high cost and slightly reduced efficiency (compared to the traditional AC transformer). At the present moment, the technology and its implementation are expensive, which together with impaired efficiency make the DCT business case harder to put forward.

Regarding the commonly used converter topologies for high-power DCTs, there are two predominantly considered, namely, Series Resonant Converter (SRC) [37] and Dual Active Bridge (DAB) [38], shown in **Fig. 1.6**. Both topologies are galvanically isolated. The SRC is composed of an MFT and a resonant capacitor (which can be distributed on both transformer sides), placed between an active inverter and a passive diode rectifier. For bidirectional power flow, both power stages can be implemented as active. For high-power processing, the SRC is usually operated in open loop and slightly below the resonant frequency, characterized by a stiff transfer voltage ratio. Additionally, soft-switching (Zero-Current Switching (ZCS), Zero-Voltage Switching (ZVS)) and almost sinusoidal resonant currents can be achieved. From the various existing SRC topologies, the LLC Series Resonant Converter (LLC-SRC) is the most widely used one and it will be further considered and discussed in the thesis [39]–[41].

Similarly, the DAB consists of two active power stages and an MFT in between. The power flow is bidirectional and it is controlled by the phase shift between the primary and secondary square-wave voltages. In this way soft-switching can be reached, however, the converter requires closed-loop control of the power flow. The resulting transformer currents are piece-wise linear, thus, with higher harmonic content compared to SRC. Regarding the power stages of both converter types, they can be realized in several ways, such as full-bridge, half-bridge or Neutral Point Clamped (NPC) with split capacitors, and so on.

## 1.2 Medium Frequency Transformer

The topic of the thesis at hand deals with the optimal design and modeling of high-power core-type MFTs. As mentioned previously, the MFTs establish galvanic isolation between the power stages, which makes them an essential part of the DCT. When it comes to designing of MFTs, there is a



plethora of well-studied design methods, viable combinations of technologies and materials, as well as thermal and insulation coordination possibilities. Therefore, reaching an optimal MFT design for a certain set of electrical requirements implies without exception solving a complex non-linear multi-objective problem. The designers are interested in knowing the performance limits, i.e. the highest feasible efficiency, yet with the lowest attainable gravimetric and volumetric power densities. The final selection of the optimal design is eventually a compromise between multiple, often opposing, design characteristics.

Lastly, the fast pace of semiconductor development and their improved performance facilitates the exploitation of the medium frequency and medium voltage range. However, the MFT design and practical realization appear to be the bottleneck, considering the multi-objective nature of the problem, which also requires multiphysics considerations. On the one hand, the increase in the operating frequency has a positive effect on the volume reduction of magnetic components, which is a strong research driver, since it implies weight and potentially cost decrease. Naturally, the cost depends on the used materials, which tend to be more expensive since an improved performance at elevated frequencies is expected and desired. On the other hand, a smaller surface area due to volume reduction impairs loss dissipation, i.e. cooling capabilities, and requires the use of different insulating materials, which can cope with decreased distances. Additionally, the insulation is impacted by the medium voltage and high  $dv/dt$  values.

Before fully addressing the topic, the Medium Frequency (MF) range for transformer design needs to be arranged. From an antenna design perspective, the MF refers to the range of [300 kHz – 3 MHz]. By studying the so far realized MFT prototypes in the literature, one can easily see that the operating frequencies are significantly lower and that the definition of the MF range is generally ambiguous when it comes to MFT design for power electronics applications. To avoid confusion, for the work presented in this thesis, the frequency span is set to [1 kHz – 50 kHz].

The system-level properties of the DCT which provides the framework for the main topic of this thesis are summarized in the following:

- Resonant power conversion at the medium switching frequency, which utilizes soft-switching topologies such as the LLC converter;
- Bulk power processing with the open-loop operation, which does not require externally provided operating power point;
- Bidirectional operation with Reverse-Conducting Integrated Gate-Commutated Thyristors (RC-IGCTs) as the switching devices, due to their high current conducting capabilities, lower conduction losses, and improved reliability compared to standard semiconductor devices such as Insulated-Gate Bipolar Transistors (IGBTs). This type of device incorporates an IGCT and an antiparallel free-wheeling diode on the same wafer in one common package;
- RC-IGCT power stages are realized with heatsinks which are actively cooled with deionized water, and this cooling solution is adopted for the MFT windings as well;
- The operating converter frequency has an upper limit of 5 kHz due to particular selection of semiconductor devices.

Partly motivated by the defined framework, i.e. by the converter properties, the following set of technologies is selected, from the beginning of the thesis, for modeling and design of an optimal MFT:

- Copper round pipes as transformer windings with deionized water for internal cooling of the windings;
- Oil for insulation of the windings;
- Due to constrained operating frequency, the selection of the magnetic core material is narrowed down to grain oriented electrical steel, iron-based amorphous, and nanocrystalline tape alloys;
- Natural convection for cooling of the core.

### 1.3 Objectives and Contributions

The thesis focuses on technical challenges related to the design optimization and modeling, considering the selected technologies, of high-power MFTs intended for MVDC PDN applications and bulk power processing. The following points are analyzed in more detail:

- Combination of natural-convection oil-based insulation and active cooling with deionized water for transformer windings from different aspects;
- Identification of various challenges, their solutions, and benefits related to the employment of round copper pipes as MFT windings;
- Derivation of new models and extension of the existing ones to accurately model the combination of selected technologies;
- Effect of different winding arrangements on the efficiency and power density of core-type MFTs, along with their mutual comparison;
- Verification of the created design optimization methodology, which is behind the implemented 1 MW, 5 kHz MFT prototype.

From the conducted analyses, the main contributions of the thesis are extracted and summarized in the following:

- Analytical development, characterization, and experimental verification of the thermal-hydraulic model for insulating liquids, which includes consideration of the winding geometry;
- Construction and thorough testing of a 1 MW MFT regarding the electrical, thermal, and dielectric domain, with deep insights into both practical implementation and conducted testing;
- Proposed adjustments of the existing models for core-type MFTs with copper pipe windings;
- An overall static thermal model of the MFT, which provides estimations of the core and windings hot-spot temperatures;
- Demonstration of the feasibility of copper pipe windings with active cooling for high-power MV MFTs;
- Demonstration of the complete MFT prototype, with the selected materials and technologies, and a detailed description of the prototyping process.

## 1.4 Thesis Outline

The thesis manuscript is organized into 9 chapters, which are closer defined in the following.

**Chapter 2** provides an overview and a critical analysis of the current state-of-the-art regarding high-power MFT technologies. This includes an elaborate and systematic comparison between the employed technologies (concerning insulation and thermal coordination, winding type, and others) and the achieved power densities.

**Chapter 3** describes the framework within which the 1 MW MFT is to be designed with appropriately defined requirements. The framework applies to a DCT, which imposes various conditions on the MFT. Additionally, this chapter introduces technologies and material selections considered for an efficient MFT design, as well as three different winding arrangements that were studied in order to come to the optimal design. Lastly, the structure of the employed design optimization algorithm, based on the exhaustive search concept, is explained. Thereby, the missing models are identified and highlighted.

**Chapter 4** deals with the modeling of the leakage inductance for the three different winding arrangements, introduced in Chapter 3. The employed model is based on the method of magnetic images and it is verified with the help of numerical simulations, as well as experimentally. Additionally, a sensitivity analysis is performed on the effect of the relative position of the primary to secondary winding on the respective leakage inductance value.

**Chapter 5** presents a semi-analytical model, which is able to determine characteristic temperatures of the oil insulation, depending on the operating point of the MFT and the water-cooling unit. Moreover, the model is successfully validated with the help of an experimental setup (a single oil vessel and a pair of windings), which is equipped with thermocouples.

**Chapter 6** presents the employed models for the estimation of the core and winding losses, which are the main contributors to the overall transformer losses. Moreover, the chapter provides information about the complete thermal model of the MFT, which is of analytical nature and easy to integrate into the design optimization algorithm. The model is verified with the help of experimentally gathered measurements and Finite Element Modeling (FEM) simulations.

**Chapter 7** provides results from the design optimization tool regarding the design of the 2-vessel MFT structure in combination with the nanocrystalline core material. Based on the generated efficiency plots, a thorough analysis of several selected designs is conducted, which fulfill the set requirements and constraints and one of them is marked as optimal. Lastly, another MFT design is selected for prototyping, its characteristics are compared against the optimal design and are presented.

**Chapter 8** provides a detailed description of the realized 1 MW MFT prototype with highlighted manufacturing challenges, and showcases the results of the conducted electrical and power testing at the operating frequency of 5 kHz. The collected experimental data is used to verify the employed models in the design optimization tool and to validate the tool itself.

**Chapter 9** outlines the main contributions of the work presented in the thesis and draws the key conclusions. Lastly, some ideas and directions about future work are summarized and listed as well.

Finally, **Fig. 1.7** provides a graphical overview of the chapters' contents without the introduction and the concluding chapter. In this way, the reader is able to get a clear image of what each chapter is addressing.

## 1.5 List of Publications

In this section, the disseminated results published in different forms are listed.

### Journal papers:

- J1. N. Djekanovic and D. Dujic, "Copper Pipes as Medium Frequency Transformer Windings," *IEEE Access*, vol. 10, pp. 109 431–109 445, 2022
- J2. N. Djekanovic, M. Luo, and D. Dujic, "Thermally-Compensated Magnetic Core Loss Model for Time-Domain Simulations of Electrical Circuits," *IEEE Transactions on Power Electronics*, vol. 36, no. 7, pp. 8193–8205, 2021

### Conference papers:

- C1. N. Djekanovic and D. Dujic, "Winding geometry impact on high power medium frequency transformer design," in *2022 XIV International Symposium on Industrial Electronics and Applications (INDEL)*, 2022, pp. 1–8
- C2. N. Djekanovic and D. Dujic, "Design Optimization of a MW-level Medium Frequency Transformer," in *PCIM Europe 2022; International Exhibition and Conference for Power Electronics, Intelligent Motion, Renewable Energy and Energy Management*, 2022, pp. 1–10, (Best Paper Award)
- C3. N. Djekanovic and D. Dujic, "Modeling and Characterization of Natural-Convection Oil-Based Insulation for Medium Frequency Transformers," in *2022 IEEE Applied Power Electronics Conference and Exposition (APEC)*, 2022, pp. 604–610
- C4. N. Djekanovic, M. Luo, and D. Dujic, "Integrated Simulation Approach to Loss Calculations of Power Converter Systems," in *PCIM Europe digital days 2020; International Exhibition and Conference for Power Electronics, Intelligent Motion, Renewable Energy and Energy Management*, VDE, 2020, pp. 1–8
- C5. N. Djekanovic, M. Luo, and D. Dujic, "Modeling and Integrating Losses of Magnetic Components Into Time-Domain Electric Circuit Simulations," in *2020 IEEE 9th International Power Electronics and Motion Control Conference (IPEMC2020-ECCE Asia)*, IEEE, 2020, pp. 1055–1062

### Technical tutorials:

- T1. D. Dujic, J. Kucka, N. Djekanovic, G. Ulissi, and R. Barcelos, "Bulk DC-DC Conversion for MVDC Applications," in *2022 24th European Conference on Power Electronics and Applications (EPE '22 ECCE Europe)*, 2022

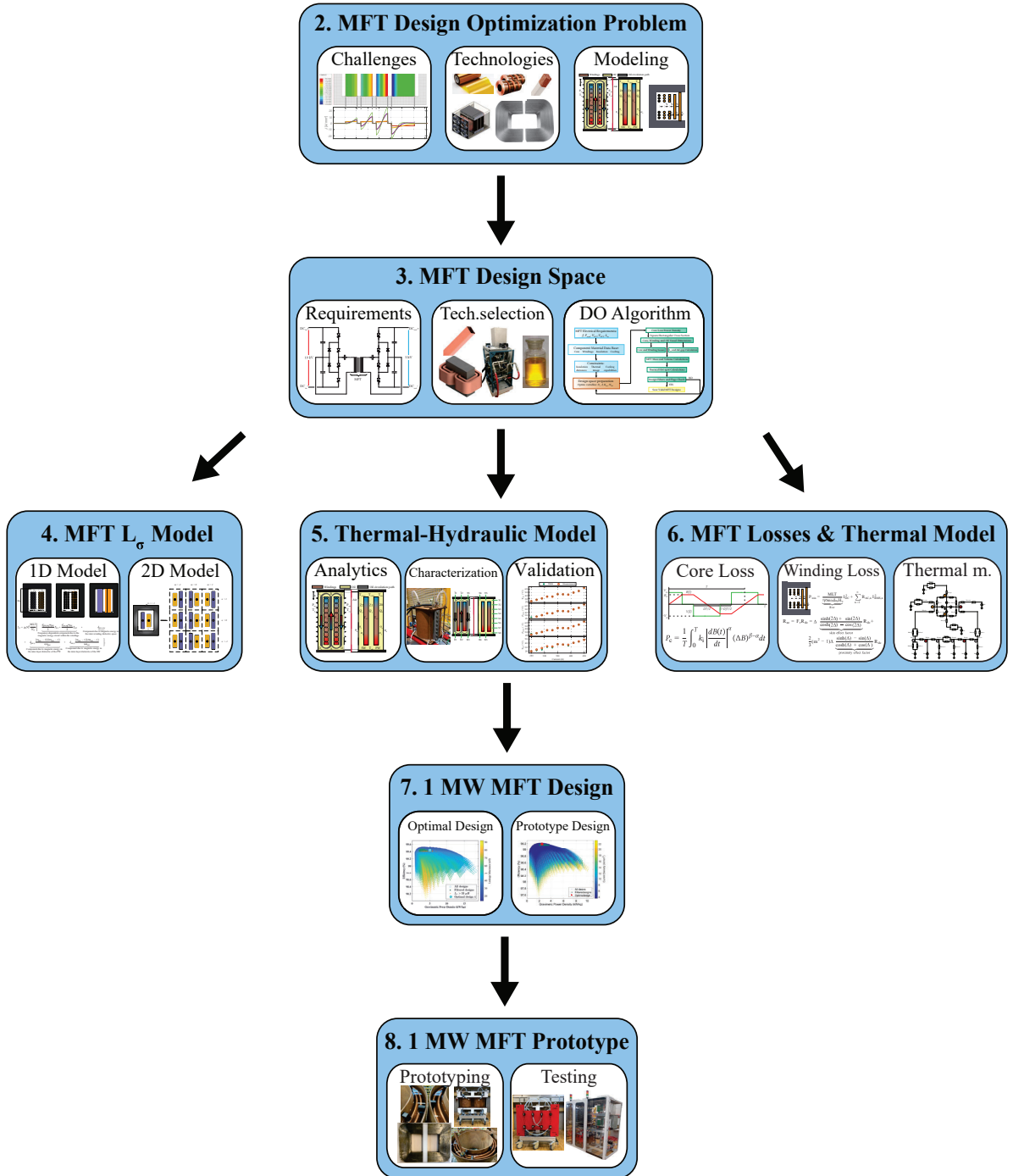


**Fig. 1.7** Illustrative overview of the thesis' chapters 2 – 8, not including the first and the last chapter.





Electrical domain	Magnetic domain	Electrical domain	Magnetic domain
Voltage $v$ [V]	MMF $\mathcal{F}$ [A]	Ohm's law: $\frac{v}{i} = R = \rho \frac{l}{A}$	$\frac{Ni}{\Phi} = \mathcal{R} = \frac{l}{\mu A}$
Current $i$ [A]	Flux $\Phi$ [Wb]	Kirchhoff's voltage law: $\sum_k R_k i = \sum_m v_m$	$\Phi \sum_k \mathcal{R}_k = \sum_m N_m i_m$
Resistance $R$ [ $\Omega$ ]	Reluctance $\mathcal{R}$ [ $1/H$ ]	Kirchhoff's current law: $\sum_k i_k = 0$	$\sum_k \Phi_k = 0$
Resistivity $\rho$ [ $\Omega m$ ]	Permeability $\mu$ [ $H/m$ ]		

(a)
(b)

**Tab. 2.1** Analogy between electrical and magnetic circuits: (a) Relevant quantities and (b) laws.

winding terminal with positive voltage polarity. The Mean Length Turn (MLT) designates what is considered to be the average length of a winding turn. The core geometry is described by the core cross section,  $A_{\text{core}}$  [ $m^2$ ], and the core window area,  $A_w$ . Thereby, the mutual flux shared between, i.e. linking the two windings is marked with  $\Phi_M$  [Wb], and the corresponding leakage fluxes are marked with  $\Phi_{\sigma 1}$  and  $\Phi_{\sigma 2}$  [42], [43]. While the mutual flux path is concentrated inside the core, the paths of leakage fluxes are mostly in the air. Note that every newly introduced variable is given with the corresponding unit in square brackets.

From the presented transformer example, two equivalent circuits are derived, the electrical and the magnetic one. Moreover, it is possible to draw an analogy between the two domains, regarding the relevant quantities and the main laws, as shown in **Tab. 2.1** [44].

Lastly, with the help of equivalent circuits, it is possible to simplify the derivation of models and analyze various effects, as well as the overall component performance. The governing equations for the two equivalent circuits are derived in the following subsections.

### 2.1.1 Magnetic Circuit Modeling

An equivalent circuit of the transformer example from **Fig. 2.1** in the magnetic domain is shown in **Fig. 2.2a**. It is expressed with the Magnetomotive Forces (MMFs) driving fluxes, which are restricted by magnetic reluctances. According to **Tab. 2.1b**, the reluctance value depends on the magnetic material properties and the geometry. Thereby, each core limb can be modeled and represented by single or multiple reluctances.

According to **Fig. 2.2a**, the total fluxes from PW and SW are given by

$$\Phi_1 = \Phi_M + \Phi_{\sigma 1}, \quad \Phi_2 = -\Phi_M + \Phi_{\sigma 2}. \quad (2.1)$$

From the magnetic circuit, shown in **Fig. 2.2a**, and after applying the equivalent of Kirchhoff's current law, the mutual flux linking the two coils can be expressed by the following

$$\Phi_M (\mathcal{R}_c + \mathcal{R}_g) = N_1 i_1 - N_2 i_2 \quad \Rightarrow \quad \Phi_M = \frac{N_1 i_1 - N_2 i_2}{\mathcal{R}_c + \mathcal{R}_g} = \frac{N_1 i_m}{\mathcal{R}_c + \mathcal{R}_g}, \quad \text{with} \quad i_m = i_1 - \frac{N_2}{N_1} i_2. \quad (2.2)$$

Thereby,  $i_m$  [A] represents the magnetizing current,  $\mathcal{R}_c$  [ $1/H$ ] and  $\mathcal{R}_g$  are the core and air gap reluctances, respectively. From the same magnetic circuit, the expressions for the leakage fluxes can be



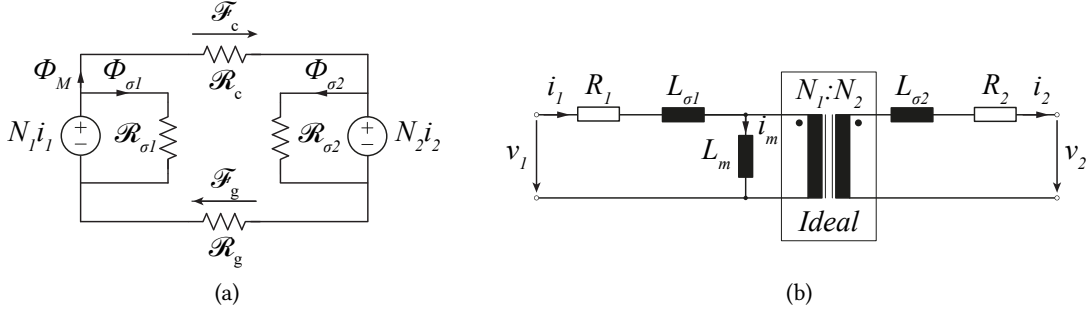


**Fig. 2.2** (a) Magnetic reluctance circuit and (b) equivalent electric circuit, derived based on the two-winding transformer illustrated in Fig. 2.1.

derived as follows

$$\Phi_{\sigma 1} = \frac{N_1 i_1}{\mathcal{R}_{\sigma 1}}, \quad \Phi_{\sigma 2} = \frac{N_2 i_2}{\mathcal{R}_{\sigma 2}}, \quad (2.3)$$

with  $\mathcal{R}_{\sigma 1}$  and  $\mathcal{R}_{\sigma 2}$  as reluctances of the leakage flux path. Replacing the derived expressions from (2.2) and (2.3) in (2.1) results in

$$\Phi_1 = \frac{N_1 i_m}{\mathcal{R}_c + \mathcal{R}_g} + \frac{N_1 i_1}{\mathcal{R}_{\sigma 1}}, \quad \Phi_2 = -\frac{N_1 i_m}{\mathcal{R}_c + \mathcal{R}_g} + \frac{N_2 i_2}{\mathcal{R}_{\sigma 2}}. \quad (2.4)$$

### 2.1.2 Electric Circuit Modeling

As for the equivalent electrical circuit of the two-winding transformer, the voltages at the primary and secondary terminals are given by the following

$$v_1 = R_1 i_1 + N_1 \frac{d\Phi_1}{dt}, \quad v_2 = -R_2 i_2 - N_2 \frac{d\Phi_2}{dt}. \quad (2.5)$$

The two resistances,  $R_1$  [ $\Omega$ ] and  $R_2$  are there to model winding resistances, present due to the limited electrical conductivity of the conductor. Negative signs in the second equation are due to the selected secondary current direction, indicated in Fig. 2.2b.

In the next step, the derived relations from (2.4) are inserted in (2.5), after calculating the corresponding derivatives. This results in

$$v_1 = R_1 i_1 + \frac{N_1^2}{\mathcal{R}_{\sigma 1}} \frac{di_1}{dt} + \frac{N_1^2}{\mathcal{R}_c + \mathcal{R}_g} \frac{di_m}{dt}, \quad v_2 = -R_2 i_2 - \frac{N_2^2}{\mathcal{R}_{\sigma 2}} \frac{di_2}{dt} + \frac{N_1 N_2}{\mathcal{R}_c + \mathcal{R}_g} \frac{di_m}{dt}. \quad (2.6)$$

Both voltage expressions can be simplified by identifying terms for magnetizing and leakage inductances, in accordance with the equivalent electrical circuit.

$$L_m = \frac{N_1^2}{\mathcal{R}_c + \mathcal{R}_g}, \quad L_{\sigma 1} = \frac{N_1^2}{\mathcal{R}_{\sigma 1}}, \quad L_{\sigma 2} = \frac{N_2^2}{\mathcal{R}_{\sigma 2}}. \quad (2.7)$$

This yields the following two equations

$$v_1 = R_1 i_1 + L_{\sigma 1} \frac{di_1}{dt} + L_m \frac{di_m}{dt}, \quad v_2 = -R_2 i_2 - L_{\sigma 2} \frac{di_2}{dt} + \frac{N_2}{N_1} L_m \frac{di_m}{dt}. \quad (2.8)$$

### 2.1.3 Scaling Law

The scaling law based on area product,  $A_p$  [m<sup>4</sup>], is commonly used for Line Frequency Transformer (LFT) design [45], [46]. It describes the dependency of the product of the winding (core window) area  $A_w$  and the core cross-section area  $A_{core}$  on the apparent power, the current density in the windings  $J_m$  [A/m<sup>2</sup>], the operating frequency  $f_{sw}$  [Hz] and the maximum flux density  $B_m$  [T]. The necessary core window area is given by the following

$$A_w = \frac{N_1 A_{cond1} + N_2 A_{cond2}}{K_u} = \frac{N_1 I_1 + N_2 I_2}{K_u J_m}, \quad (2.9)$$

with the help of the core window utilization coefficient  $K_u$  [1], which quantifies the maximum space occupied by Copper (Cu) in the core window, relative to its available area. Thereby, the primary and secondary conductor's cross-sectional areas,  $A_{cond1}$  [m<sup>2</sup>],  $A_{cond2}$ , are determined based on the selected current density  $J_m$ .

The primary and secondary number of turns are derived from Faraday's induction law, under the assumption of no flux bias and no core lamination (the effective cross-section area corresponds to the actual area). The following expressions are acquired:

$$N_1 = \frac{V_1}{K_f A_c f_{sw} B_m}, \quad N_2 = \frac{V_2}{K_f A_c f_{sw} B_m}, \quad K_f = \begin{cases} 4.0 & \text{square wave} \\ 4.4 = \frac{2\pi}{\sqrt{2}} & \text{sinusoidal wave} \end{cases} \quad (2.10)$$

In case the core material is laminated, the utilization factor needs to be introduced in order to obtain the effective cross-section area. The parameter  $K_f$  [1] is the waveform coefficient, defined by the excitation waveform. By inserting these expressions into (2.9), the following is obtained

$$A_w = \frac{V_1 I_1 + V_2 I_2}{K_u K_f A_{core} f_{sw} J_m B_m}. \quad (2.11)$$

After rearranging and acknowledging the input ( $P_i = V_1 I_1$ ) and output power equations ( $P_o = V_2 I_2$ ), the scaling law equation is derived as

$$A_p = A_w A_{core} = \frac{P_i + P_o}{K_u K_f f_{sw} J_m B_m} = \frac{P_t}{K_u K_f f_{sw} J_m B_m}, \quad (2.12)$$

with  $P_t$  [W] as the apparent power. Note that the area product scaling law from (2.12) is based on the apparent power, i.e. power-handling capability, of a transformer design, which can be approximately up to 2 times larger than the output power  $P_o$ , which is of interest to the user of the component [45]. The logic behind this considers that the primary side needs to handle the input power  $P_i$ , whereas the secondary processes the output power  $P_o$ , therefore, the transformer per design needs to accommodate the sum of the two powers.

Moreover, the core area product  $A_p$  is proportional to the transformer volume  $V_T$  [m<sup>3</sup>] and it offers a link between the power-handling capability of the core and its size. For cores of standard shapes and sizes, in low-power applications, the  $A_p$  value is assigned to the standard core sizes by the

manufacturer and it summarizes the dimensional and electrical properties of cores. The equation will be further used to identify the main factors influencing the transformer volume.

$$\Rightarrow V_T \propto \frac{1}{f_{sw}} \quad (2.13)$$

$$V_T \propto A_w A_{core} = \frac{1}{K_f K_u} \frac{P_t}{f_{sw} J_m B_m} \Rightarrow V_T \propto \frac{1}{J_m} \quad (2.14)$$

$$\Rightarrow V_T \propto \frac{1}{B_m} \quad (2.15)$$

The peak flux density  $B_m$  and the current density  $J_m$  are mostly limited by the core and conductor material properties and their thermal constraints, whereas the switching frequency  $f_{sw}$  is affected only by the switching devices used to provide excitation for the transformer. In that respect, considering today's power semiconductor devices and in contrast to all other aforementioned parameters, the frequency is the only parameter that can be significantly changed (within several orders of magnitude), thus having the most significant influence on the transformer size.

The first observation from (2.13) is that with the increasing operating frequency, the volume decreases, which directly implies an increase in the volumetric power density. This can be demonstrated both analytically and experimentally [46]. Even though it is not explicitly shown in the equations, volume reduction can entail weight reduction as well, which results in improved gravimetric power density. Nevertheless, counterexamples exist, such as the use of oil insulation, which reduces the volume, but increases the overall weight compared to a design with air insulation. However, the same equation does not indicate the critical frequency for which the relationship is no longer accurate, i.e. the frequency where high-frequency losses start to show a significant impact on the transformer design. Furthermore, a volume reduction has a significant impact on transformer insulation coordination. Due to decreasing distances between the main transformer components, such as windings and the core, more advanced and complex insulation materials (with higher dielectric strengths) need to be used. In other words, for a selected insulation system of a design, after a certain frequency, the distance reduction is no longer feasible. Moreover, it is possible to find an optimal frequency where the lowest weight and smallest volume can be achieved.

Furthermore, based on the parameter  $J_m$  which directly influences the cooling system effort, one can conclude that by improving the thermal coordination the transformer volume can be decreased, as given in (2.14). In a similar fashion, the increase of the flux density can be used to reduce the transformer volume (2.15). However, materials with high saturation values of magnetic induction are used for lower operating frequencies and vice versa, indicating a necessary trade-off [47]. This can be traced back to the fact that both flux density magnitude and frequency directly impact the core losses, i.e. high  $B_m$  values imply higher core losses, which can be managed only at certain frequencies. Vice versa, low-power transformer designs at very high frequencies (MHz range) operate at very low flux density values, in order to control the core losses. Furthermore, it should be noted that the thermal conductivity of the core material also has a strong impact on the thermal aspect of the transformer design and that this has not been considered in the core area product expression given above. Therefore, this relation provides only a simplified estimation of the transformer size and it does not show effects on the internal characteristics of the transformer (e.g. temperature rise), nor effects such as skin, proximity, fringing, and many more.

In the case of LFTs, the  $B_m$  value can be selected very close to the saturation flux density (considering a certain safety margin), and the winding current density  $J_m$  as the peak current density. Like this, the scaling law from (2.12) gives a good first estimation of the LFT dimensions. As for the MFT, the optimal design often exhibits lower flux and current density values [48]. Thus, this method cannot be directly used for MFT design, but it can serve as a guideline and an upper limit of design feasibility.

## 2.2 MFT Design Optimization Problem

As already mentioned in the introduction, the fundamental operating principle of a transformer is grounded on the electromagnetic induction phenomenon (creation of electromotive force across a conductor in a changing magnetic field), which is employed for power transfer purposes. In the process, losses are created due to inevitable material resistances, which introduces the thermal aspect of the problem. Lastly, transformer parts on different potentials need to be isolated from each other which brings in the dielectric domain and considerations. Finally, a transformer design implies a coherent interaction of the four relevant domains.

Additionally, as a part of the power conversion process, magnetics are often the heaviest and bulkiest components. Thus, they have a significant effect on the overall efficiency and performance of the power converter system. As a designer, one must weigh out all the available technologies, materials, and their limiting constraints, against the requirements and desired performance numbers, considering also the cost effectiveness. Thereby, interdomain interactions need to be carefully considered.

The analysis of the scaling law, provided in Section 2.1.3, already discussed several dependencies between design parameters. Depending on the application for which the transformer is designed, the goal can be set to achieve minimal weight, volume, or cost, maximal efficiency, and so on. The various goals are considered to be performance indicators, once a certain design is selected. If volume and weight are of importance, the reduction can be achieved by increasing the operating frequency, but at the cost of reduced efficiency. If the frequency is limited, power density increase can be achieved with more efficient materials, yet, at an increased cost. Furthermore, the selection of the core material has an impact on the weight and efficiency, as well as the cost, since there are significant cost differences between silicon-steel material families and amorphous or nanocrystalline materials. Therefore, the design trade-offs need to be well understood, with clearly defined optimization goals, as well as mutual effects that the design parameters have on each other. Due to existing interdependencies, it is impossible to optimize all the performance indicators in a single transformer design.

**Fig. 2.3** illustrates what are the implications on several design parameters of a reference MFT design (marked with a subscript 0) when the change of the volumetric power density and efficiency is considered. The change is seen through another MFT design, marked with an asterisk. The considered parameters are properties of the transformer geometry (volume  $V_T$ , core and conductor cross section  $A_{\text{core}}$ ,  $A_{\text{cond}}$ ), frequency ( $f_{\text{sw}}$ ), core and winding losses ( $P_c$ ,  $P_w$ ), flux density ( $B_m$ ) and current density magnitude ( $J_m$ ). Note that the two designs fulfill the same electrical requirements, in sense of nominal power, primary and secondary voltages, and currents. Thereby, the volumetric power density is given on the x-axis, efficiency on the y-axis, and the four quadrants (I-IV) show the four possibilities of change, regarding the reference MFT design ( $\rho_{T0}$ ,  $\eta_0$ ). It is assumed that the conductor type and core material are selected in a way that they are suitable for the nominal power and the range of the considered operating frequency, with increase and decrease included. The underlying principles of the illustrated interdependencies are described in the remainder of the chapter.

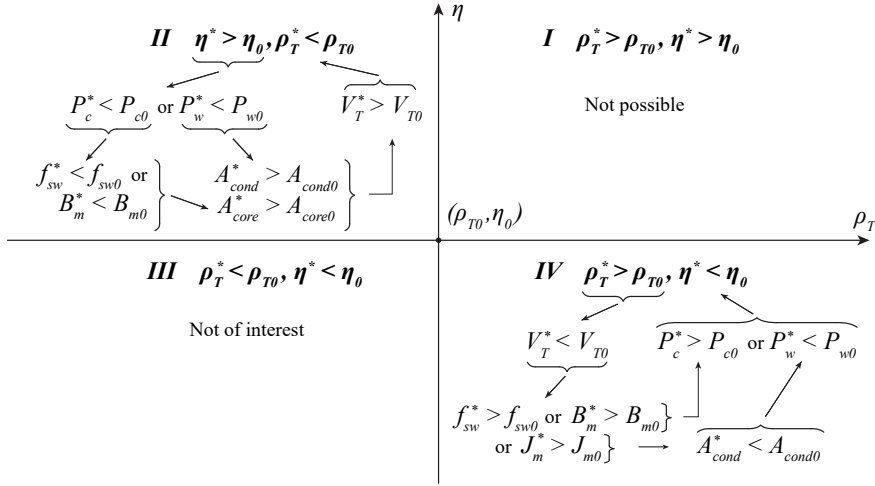


**Fig. 2.3** Efficiency ( $\eta$ ) versus volumetric power density ( $\rho_T$ ) design implications compared with an imaginary MFT design of power density  $\rho_{T0}$  and efficiency  $\eta_0$  and observed in four quadrants: (I) increase of power density and efficiency, (II) power density decrease, efficiency increase, (III) both quantities decrease, (IV) power density increase, efficiency decrease.

Before addressing the main design challenges, note that even though the design practice of MFTs goes many decades back, still today their design is highly non-standardized and application-specific. There are no unified voltage, current or frequency levels, nor required standardized insulation tests.

### 2.2.1 Design Challenges

The main design challenges are discussed in the following sections depending on the influence domain. Thereby, the underlying mechanisms are explained, and more detailed descriptions and the relevant models are provided later in the corresponding chapters.

#### 2.2.1.1 Eddy Current Effects

The advantages of operation at elevated frequencies come at a price of increasing conduction losses. This is exhibited through the skin and proximity effects, caused by arising eddy currents. For the first effect this current is induced by changing magnetic field coming from the conductor itself, whereas for the latter effect, it is caused by the alternating current passing through the adjacent conductors. This directly implies a non-uniform current density distribution across the conductor's cross section, as can be observed from **Fig. 2.4**, which results in increased AC resistance, thus, higher conduction losses. Consequently, the conductor's current carrying capacity is underutilized. Note that the total magnitude of the current remains the same, only the current density distribution changes. Besides increasing the conduction losses, eddy current effects influence the total leakage inductance. Owing to the fact that the induced eddy currents suppress the magnetic field inside of the conductors, as shown in **Fig. 2.4a**, the total magnetic energy decreases and it results in a lower leakage inductance value.

The limiting design factor related to windings and current conduction is known as the skin depth and

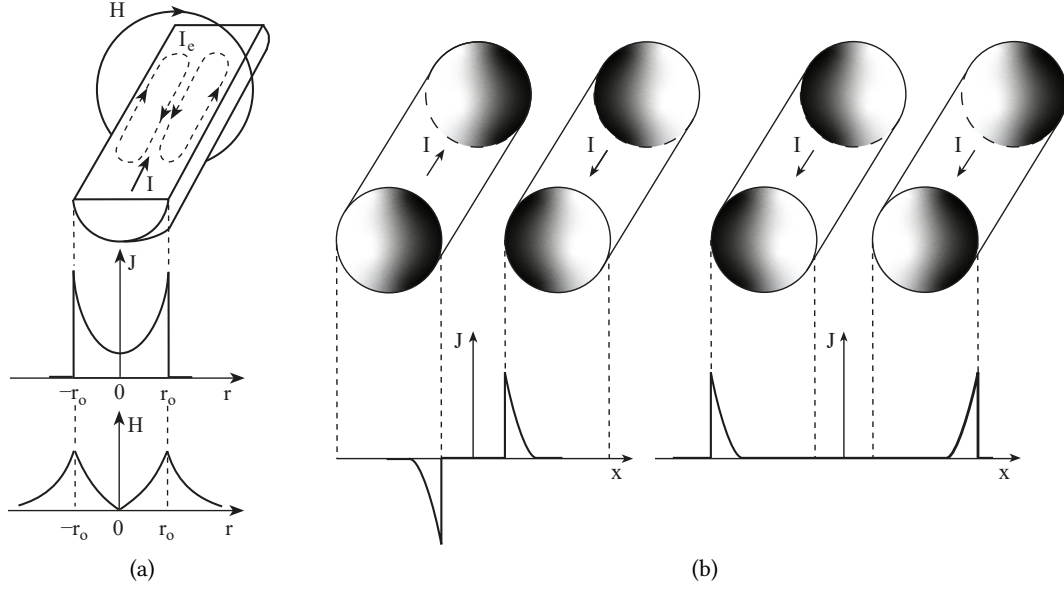


**Fig. 2.4** (a) Skin effect in a single round conductor with current density and magnetic field distributions; (b) Proximity effect illustrated on the example of two parallel round wires conducting high-frequency current (left) in the opposite and (right) in the same direction, with the corresponding current density distributions. Figures are adapted from [49].

it is defined by the following relation:

$$\delta = \frac{1}{\sqrt{\pi f_{sw} \sigma \mu}} = \sqrt{\frac{\rho_e}{\pi f_{sw} \mu_0 \mu_r}} \quad (2.16)$$

The parameter  $\rho_e$  [ $\Omega \text{ m}$ ] stands for the electrical resistivity of the material,  $\sigma$  [ $\text{S/m}$ ] is the respective conductivity, whereas  $\mu$  [ $\text{H/m}$ ] is the permeability of the material. In case the frequency-dependent skin depth (2.16) is in the range of the thickness of the wire, or in the range of the strand diameter in case of a Litz wire, then the utilization of the wire is optimal and the current flow in the windings is optimized. Therefore, for higher operating frequencies, very thin conductors are needed. Both effects can be minimized by proper conductor selection, which considers the characteristic skin depth at the operating frequency. Moreover, depending on the conductor material, Cu or Aluminum (Al), the lower conductivity of Al implies lower eddy current losses, which is beneficial. Nevertheless, for the same reason, the DC resistance of Al is higher compared to Cu.

### 2.2.1.2 Accurate Electrical Parameter Design

As previously mentioned, MFTs are designed as integral parts of DCTs, in charge of providing galvanic isolation and voltage adaptation between the power stages of the DC-DC converter. Depending on the converter topology, the most common being LLC-SRC and DAB, as introduced in the previous chapter, the MFT electrical parameters, such as magnetizing and leakage inductance, need to be carefully determined and designed. Note that the correct parameter values are necessary for proper converter operation.

In the case of LLC-SRCs, inductors from the resonant tank can be directly integrated into the transformer, in the form of leakage and magnetizing inductance. Thus, together with the resonant ca-

pacitors, their values govern the resonant frequencies of the converter. Additionally, this type of resonant converter shows load-independent gain characteristics when the switching frequency is in close proximity to the higher resonant frequency. This further enables open-loop operation, without externally provided power set point.

Regarding the influence of the characteristic MFT inductances on the DAB operation, the appropriate leakage inductance value can ensure robust power flow control with respect to phase shift variations. Moreover, the maximal value of transferred power between the power stages is limited by leakage inductance. Thus, this electric parameter requires accurate specification and modeling. In the case of a DAB converter, the magnetizing inductance is usually significantly larger than the leakage inductance, implying the magnetizing current can be neglected. However, its value affects the size of the ZVS region, as well as the power transfer capability of the overall converter [50].

### 2.2.1.3 Non-Sinusoidal Excitation

In contrast to grid-frequency operating LFTs, which experience sinusoidal excitation, the MFTs are operated within power electronic converters, and thus, deal with square voltage excitation. The currents are generally non-sinusoidal, depending on the converter topology. Consequently, non-sinusoidal excitation has an effect on the overall transformer losses. Additionally, the resulting high  $dV/dt$  ratios increase dielectric stress and negatively impact the insulation coordination of the transformer.

Regarding the core losses, the core manufacturers typically provide loss density curves of magnetic materials that are obtained with sinusoidal voltages. However, to accurately estimate the core losses, regardless of the excitation waveform shape, the information from the data sheets needs to be generalized to any arbitrary voltage waveform. As for the winding losses, the conduction losses are frequency dependent. Thus, the entire frequency spectrum of the current has to be considered to determine the total losses.

### 2.2.1.4 Insulation Coordination

To ensure proper and safe transformer operation, particularly when designing MV and MF transformers, operated within power electronics converters, the insulation material and the corresponding distances need to be selected carefully. In general, there are three main insulation types [52]:

- **Functional insulation:**  
Its purpose is to ensure the correct functioning of the component. However, it does not protect or isolate against electrical shock. For an MFT it includes turn-to-turn insulation, layer-to-layer insulation, interwinding insulation, and winding-to-core insulation.
- **Basic insulation:**  
Its task is to ensure protection against electrical shock. Furthermore, it needs to make sure that failure of the functional insulation does not endanger life as a consequence of the grounding of the exposed parts.
- **Protective separation:**  
It includes supplementary, double, and reinforced insulation. Supplementary insulation mitigates the risk of electrical shock in case of basic insulation failure. Double insulation is a redundant insulation layer, which doubles the basic insulation and increases the protective

separation. Lastly, the reinforced insulation increases the distance prescribed by the basic insulation requirement (additional air clearance or insulation thickness of solid or liquid basic insulation).

The presented insulation types are illustrated in **Fig. 2.5**. Thereby, the clearance provides the shortest air distance, whereas the creepage provides the shortest distance along an insulator surface between two conductive parts. The creepage distance is regarded as supplementary insulation. When it comes to the insulation design of traditional grid-frequency operated transformers, this is well studied and understood. However, operation at elevated frequencies and non-sinusoidal excitation bring various challenges. Thereby, several points need to be taken into consideration. Namely, the square voltage excitation that the MFTs experience has a much smaller rise time compared to the sinusoidal voltage, i.e. high time derivatives ( $dV/dt$ ). This in turn can lead to overvoltages between winding turns and turns-to-ground due to existing parasitics, coming from the capacitive coupling. The result is uneven voltage distribution across the windings and increased electrical stress [53]. This in turn leads to a higher probability of Partial Discharge (PD) occurrence which, if it is continuously repeated causes premature aging and insulation failure. Secondly, increased operating frequency implies increased core and winding losses, as well as dielectric losses, which altogether contribute to higher operating temperatures and higher thermal stress. As a result, many insulation materials experience a decrease in insulating capability, which eventually can lead to thermal breakdown.

#### 2.2.1.5 Thermal Coordination

During operation losses are generated and the main contributors for the MFT are the core and the winding losses. Depending on the construction type and geometry of the transformer, the generated heat has to be evacuated through the existing interfaces in the environment. However, as previously mentioned, the reduction in the transformer size reduces the available surfaces for heat extraction which further contributes to the increase in the operating temperature. Considering the maximum allowed material temperatures, this may call for necessary enhancements of the cooling efforts.

Moreover, the selection of core and winding materials plays a significant role in thermal coordination. This can be observed in the property of thermal anisotropy, which describes the directional dependence of the material's thermal conductivity. It has to be considered for laminated core materials, since they are composed of metallic tapes and insulation layers, with different thermal capabilities. Thus,

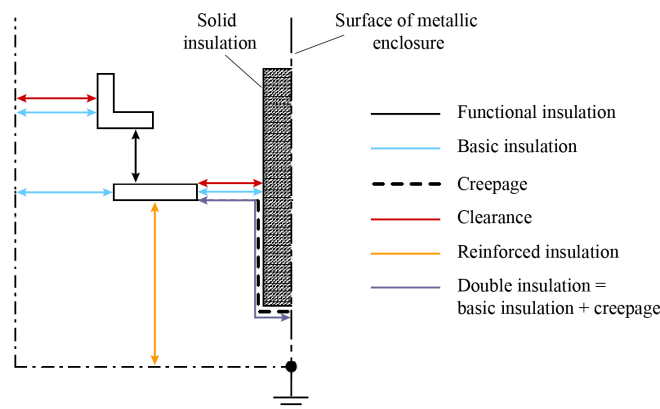


**Fig. 2.5** Illustration of different insulation types. The figure is adapted from [51].



depending on the axial or radial direction, the thermal conductivity assumes different values. The same effect needs to be considered when enameled, i.e. isolated wires are used as conductors.

An additional inter-domain challenge is the interaction between thermal and insulation coordination. An illustrative example is the solid type of insulation, where materials exhibit relatively low heat dissipation capabilities. Therefore, when dealing with high powers together with solid insulation, designs with more efficient cooling methods are required. On other hand, due to the coherent dielectric and thermal properties of a liquid insulation medium, such as oil, it presents both an efficient cooling and insulation method.

## 2.3 Available Technologies

In this section, the MFT design space is introduced in more detail. This involves specifications of commonly used magnetic materials for the core, typically employed conductor types for the windings, as well as existing cooling and insulating solutions. Many examples of the available technologies are given with the help of already realized MFT prototypes found in the literature.

### 2.3.1 Core Material

In general, magnetic cores have two constraints, which are saturation and core losses. At low frequencies, core saturation is the limit, whereas at high frequencies, e.g. 100 kHz, core losses become the limiting factor [56]. The border frequency depends on the employed core material and for particular winding arrangements, it can reduce to 7 kHz in the case of nanocrystalline material [57]. On the other hand, the right selection of the magnetic core material depends on numerous transformer parameters, such as the operating frequency, the desired flux density value, volume, and weight requirements. Typically, four core materials are mainly considered, namely, electrical steel, amorphous metal, nanocrystalline material, and ferrite. **Fig. 2.6a** provides a graphical comparison of the hysteresis loss density versus frequency. In **Tab. 2.2**, some of the main properties of the commonly used material representatives are summarized. Dimensionless parameters  $K$ ,  $\alpha$ , and  $\beta$  are

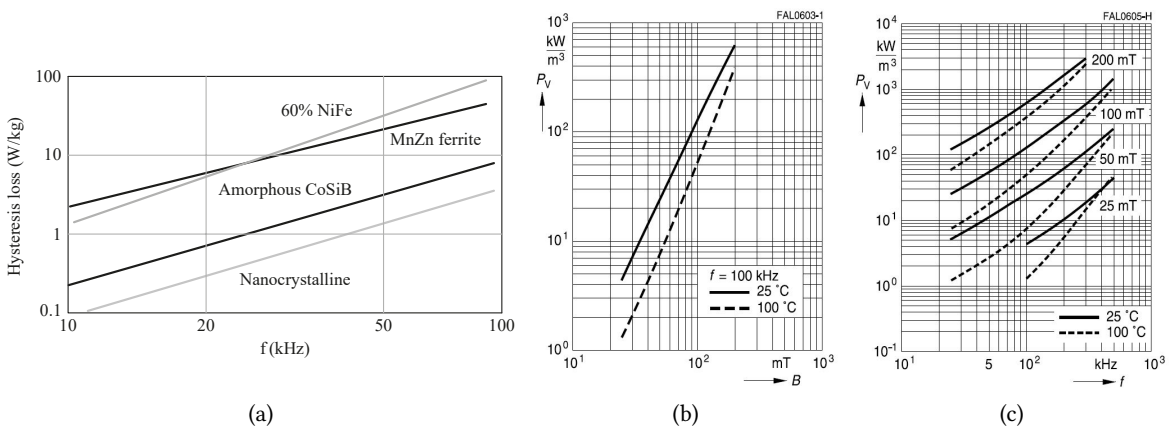


**Fig. 2.6** (a) Comparison of hysteresis power loss densities for typical core materials in regard to the operating frequency [54]. NiFe is a nickel-based iron alloy. Power loss density curves (b) versus magnetic flux density, and (c) versus frequency, measured at different temperatures with ferrite material N87 [55].

Magnetic material	$B_{\text{sat}}$	K	$\alpha$	$\beta$	Density	Stack. factor	Magn. permeability
GOES Powercore H	2.03 T	$9.76 \cdot 10^{-5}$	1.81	2.2	$7650 \text{ kg/m}^3$	0.95	2700
Amorphous Metglas 2605SA1	1.56 T	6.5	1.51	1.74	$7180 \text{ kg/m}^3$	0.84	5600
Nanocrystalline Finemet	1.23 T	2.7	1.36	2.27	$7300 \text{ kg/m}^3$	0.77	30000
Ferrite N87	0.39 T	$20 \cdot 10^{-4}$	1.43	2.13	$4850 \text{ kg/m}^3$	0.98	3200

**Tab. 2.2** Properties of the considered magnetic core materials.

the Steinmetz coefficients, extracted from the corresponding loss density curves. Examples of typical core loss density values measured with the ferrite material N87 are shown in **Fig. 2.6b** and **Fig. 2.6c**, corresponding to dependency on the flux density and operating frequency, respectively.

### 2.3.1.1 Silicon Steel

Silicon or electrical steel (SiFe) is an alloy of iron with a certain silicon percentage, in the range of 1% to 6.5%. In general, the material exhibits high saturation flux density, it is mechanically robust and resilient to high temperatures. Its low cost makes it a very good selection for high-power low-frequency applications. The exact percentage varies depending on the properties that need to be achieved. Namely, the controlled addition of silicon to the iron helps to increase the material's resistivity, permeability and reduce hysteresis loss. The most widely used SiFe material contains around 3%, whereas the version with 6.5% exhibits the most enhanced electric and magnetic properties, yet, at the price of being more brittle [58]. Moreover, an excess in silicon can also lead to a decrease in saturation flux density [43], [59]. Depending on the production process, there are non-oriented SiFe, which can be fully or semi-processed, and Grain Oriented Electrical Steel (GOES).

When employed as the magnetic core material, it is provided in the form of the axially stacked and isolated laminations sheets, in order to reduce the eddy current losses. The steel sheets are produced by mechanically punching out a desired shape by means of a specialized press, or with the help of laser cutting technology. This allows for various lamination shapes and provides additional design degrees of freedom. Compared to amorphous and nanocrystalline lamination tapes, SiFe sheets are mechanically more robust. Due to magnetostriction and change of shape during the magnetization process, acoustic noise is produced. The flux quantity in the core determines the amount of magnetostriction and hence, the noise level.

According to [60], this grain-oriented type with a lamination thickness of approximately  $180 \mu\text{m}$  is suitable for MFTs with an operating frequency of up to 4 kHz. The major advantages include reduced eddy current losses, i.e. improved core loss characteristics, great mechanical robustness, and the ability to withstand very high temperatures (up to  $400^\circ\text{C}$ ). Several representative examples of the MFT prototypes are given in **Fig. 2.7**. Thereby, **Fig. 2.7a** shows 16 single-phase MFTs and a choke inductor without the top tank cover.

### 2.3.1.2 Amorphous Material

In contrast to other magnetic materials, amorphous metals do not have a crystalline structure. The alloys are prepared by rapid cooling of the melted substance at about million degrees per second. Such fast cooling does not give the atoms enough time to rearrange into a stable crystalline form.

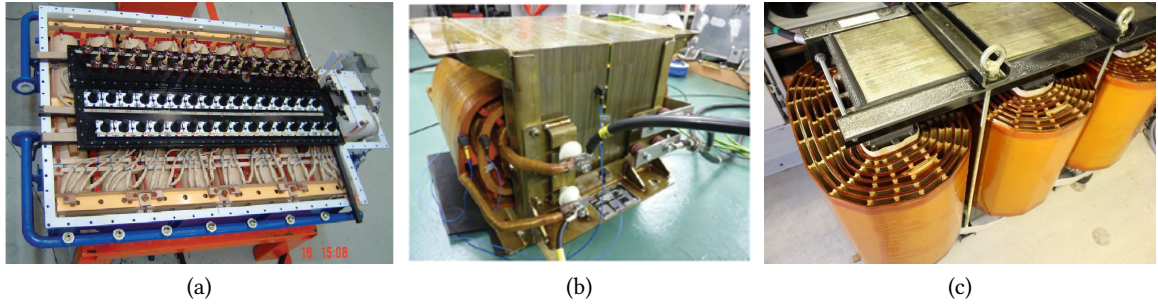


**Fig. 2.7** MFT prototypes made with SiFe core material, reported in the literature: (a) ABB, 2007 [61], 75 kV A at 400 Hz, oil cooling and insulation; (b) IKERLAN, 2012 [62], shell type, 400 kV A at 1 kHz, air cooling; (c) RWTH Schaffner, 2019 [63], 3-phase core type, 5 MW at 1 kHz, air cooling.

As a result, one gets a metastable amorphous structure. This further applies that its atoms are randomly arranged, giving it a higher resistivity value (about three times) than that for the crystalline counterpart. Because of such structure amorphous alloys are magnetically soft, meaning the material can be easily magnetized and demagnetized. Some of its properties are lower coercivity up to 1000 A/m, lower core loss, and higher permeability. High electric resistivity accounts for lower losses at higher frequencies and for this material, the losses are among the lowest of any known magnetic material. They are mechanically robust and exhibit high Curie temperatures.

Amorphous alloy is another type of laminated material, except the lamination is performed radially with wound strips or tapes, that can be very thin, approximately 20  $\mu\text{m}$ . In this way, the eddy current losses remain limited for frequencies up to 50 kHz. The cores are produced by winding thin tapes, which are isolated among each other and are eventually pressed together. However, since the tapes are difficult to form, only limited core shapes are available, and they are also relatively expensive. The saturation flux density is lower compared to SiFe, but it exhibits significantly lower losses. Lastly, amorphous materials exhibit anisotropic thermal conductivity, i.e., this property is directionally de-

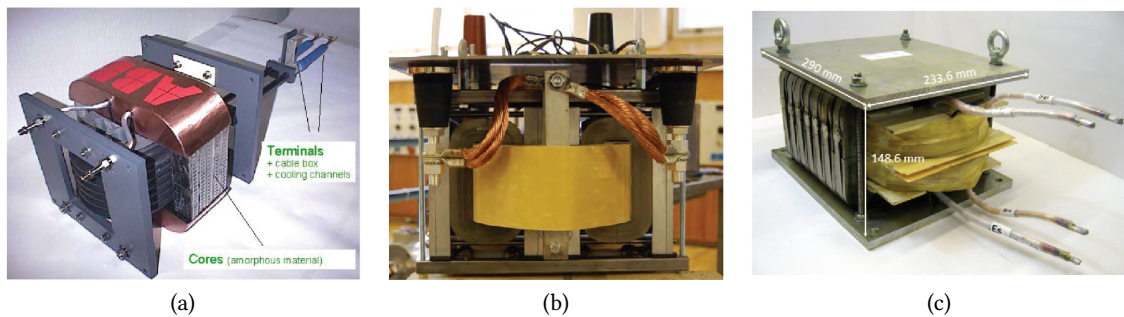


**Fig. 2.8** MFT prototypes made of amorphous material, found in the literature: (a) ABB, 2002 [64], shell type, 350 kW at 10 kHz, VAC Vitrovac 6030F, air cooling and deionized water cooling for the coaxial windings, air and solid insulation; (b) KTH, 2009 [65], shell type, 170 kV A at 4 kHz, Metglas 2605SA1, water-cooled plates for the core and oil cooling for the windings, Litz wire for the PW, foil for the SW, oil-impregnated paper insulation; (c) EPFL, 2010 [47], shell type, 25 kV A at 2 kHz, Metglas AMCC 367S material and Litz wire, air cooling, air and solid insulation with NOMEX and GPO-3 Glass polyester sheets.

pendent. The material presents a constant magnetic behavior with increasing temperatures. However, cores made of this material suffer from very high acoustic noise due to magnetostriction, similar to SiFe material. Prominent examples of MFT prototypes are shown in **Fig. 2.8**.

### 2.3.1.3 Nanocrystalline Material

This type of material is produced with the help of rapid solidification technology (invented in 1960) as a thin tape. Nanocrystalline material is initially in the amorphous state and from there, it is subsequently crystallized by heat treatment with temperatures of around 500 °C - 600 °C. As a result, the material has an extremely fine grained microstructure with grain sizes of 10 nm, hence the material's name. It is optimized to combine high magnetic permeability levels over a wide frequency range, combined with high saturation flux density, low core losses, and low coercive field strength. However, it has slightly lower saturation induction compared to the amorphous material.

Nanocrystalline alloys exhibit low magnetic anisotropy and low magnetostriction together with good thermal stability. They can be used for both line frequency and switching frequency applications. Similar to amorphous materials, they show a constant magnetic behavior with temperature. However, they are relatively expensive and are available only in limited core shapes. From the mechanical side, this type of material is fragile and quite brittle. From a thermal point of view, nanocrystalline material is complex. It is made of sheets with relatively high thermal conductivity which are glued together to make the core. Therefore, in the direction of the magnetic flux, the resulting thermal conductivity retains a similar value, whereas in the direction normal to the sheets due to dominating glue layers, the thermal conductivity reduces significantly.

Similar to amorphous materials, nanocrystalline material is radially laminated and due to the specific way of construction, predominantly C-cores and toroids are made. Nevertheless, both materials can be wound and cut into block cores which then can be used to assemble various kinds of core shapes. Metallic thin tape-wound cores (approximately 20  $\mu\text{m}$ ) made of nanocrystalline material have flat hysteresis loops without any notable remanence at a high saturation induction. Such cores have high electrical resistance (1.1  $\mu\Omega\text{m}$  - 1.2  $\mu\Omega\text{m}$ ), which ensures minimal eddy current losses. Generally, the losses of the amorphous material are significantly higher compared to nanocrystalline in the frequency range between 1 kHz and 50 kHz. Nevertheless, it tends to have a lower stacking factor

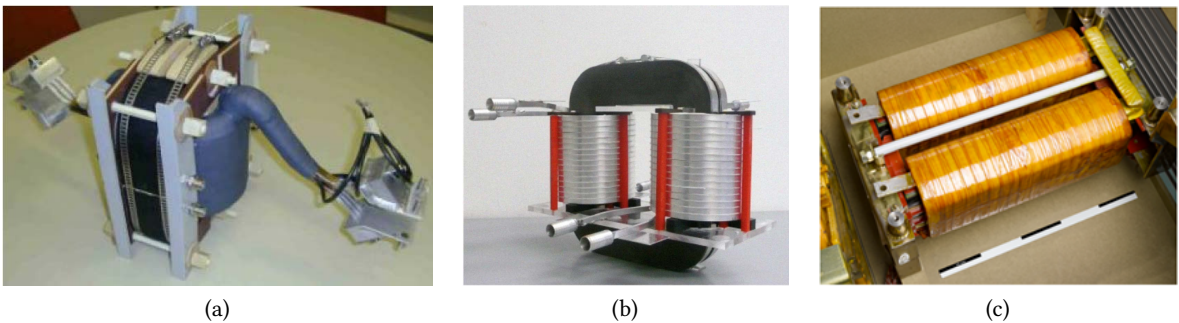


**Fig. 2.9** MFT prototypes made of nanocrystalline material, reported in the literature: (a) Bombardier, 2007 [66], shell type, 500 kV A at 8 kHz, Deionized (DI) water cooling with hollow Al conductors, solid insulation box; (b) FAU, 2011 [67], [68], core type, 450 kV A at 5.6 kHz, Vitroperm 500F, DI water cooling with hollow Al conductors, oil cooling and insulation; (c) IKERLAN, 2012 [62], core type, 400 kV A at 5 kHz, forced air cooling.

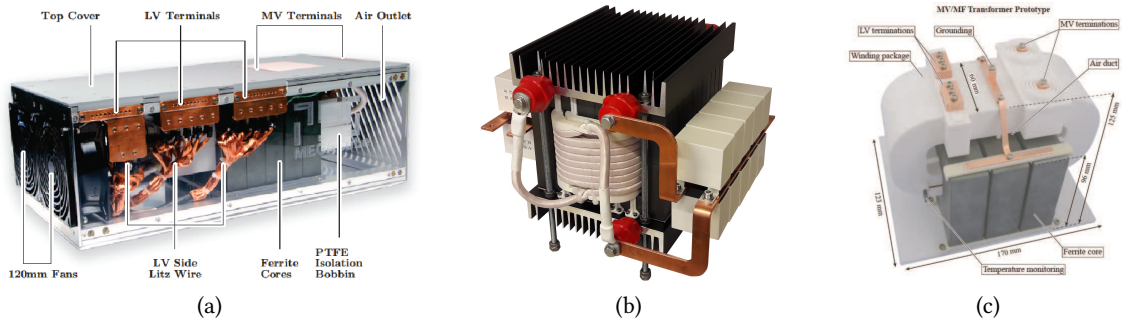


**Fig. 2.10** MFT prototypes made of ferrite core material, reported in the literature: (a) ETH, 2014 [69], [70], shell type, 166 kV A at 20 kHz, N87 material, Litz wire windings, forced air cooling, and solid insulation with PTFE bobbin; (b) EPFL, 2017 [71], [72], shell type, 100 kW at 10 kHz, N87 material, rectangular Litz wire windings, natural air cooling, and insulation; (c) ETH, 2018 [73], shell type, 25 kW at 48 kHz, BFM8 material, Litz wire windings, forced air cooling, insulation through silicone elastomer potting.

which will additionally affect the core volume. Several MFTs of similar power in the range of 500 kW and operating below 10 kHz are summarized in **Fig. 2.9**.

#### 2.3.1.4 Ferrite

Ferrites are ceramic materials that are electrically non-conductive, i.e., they are both insulators and ferrimagnetic, in contrast to the so far mentioned materials which are ferromagnetic. This material has lower saturation flux density, as well as comparably lower relative magnetic permeability compared to other core materials, and is isotropic. Due to its very low conductivity, it is considered that eddy current losses can be neglected, which is true only up to a certain temperature point. Moreover, ferrite cores produce low acoustic noise and have a relatively low cost. This type of material exhibits low-loss densities (both hysteresis and eddy current losses), which makes them suitable for high-frequency applications above 25 kHz. Here the lack of higher saturation levels can be compensated with increased operating frequency, instead of increasing the core cross-sectional area [59]. They are also available in many different core shapes, since they are powder based and can be easily moulded, but are mechanically fragile. Furthermore, ferrites display temperature-dependent behavior, i.e., their magnetic properties deteriorate with temperature increase. Examples of MFT prototypes made with ferrite are given in **Fig. 2.10**.

#### 2.3.2 Winding Technology

The choice of the appropriate winding technology depends, among other factors, on the frequency, since skin and proximity effects cause conduction losses and are also frequency dependent. For high-power and low-frequency applications mostly round and rectangular solid wires are used, which can be realized as solid or as a hollow, i.e. tube conductor. Foil conductors are mostly used for high power and moderately high-frequency applications, up to several kHz. They are relatively cheap and have good thermal properties. However, a typical problem encountered when dealing with foil conductors is proper termination of the winding, which may require soldering of terminating wires or other types of foil manipulations. An example MFT prototype from the literature is reported in [65] and shown in **Fig. 2.8b**.



Material	$\rho_e$ [ $\Omega$ m]	$\alpha_e$ [ $1/^\circ\text{C}$ ]	$\rho_{\text{Cu}}$ [ $\text{kg}/\text{m}^3$ ]	$\alpha_l$ [ $1/^\circ\text{C}$ ]	$\sigma$ [ $\text{S}/\text{m}$ ]	$k$ [ $\text{W}/\text{K m}$ ]
Cu	$1.68 \cdot 10^{-8}$	$3.862 \cdot 10^{-3}$	8940	$17 \cdot 10^{-6}$	$5.95 \cdot 10^7$	401
Al	$2.82 \cdot 10^{-8}$	$3.9 \cdot 10^{-3}$	2712	$23.1 \cdot 10^{-6}$	$3.77 \cdot 10^7$	237

**Tab. 2.3** Winding material properties measured at a temperature of  $20^\circ\text{C}$  [74], [75].

Regarding solid wires, the standard shapes of this conductor type are round and rectangular. Additionally, they can be realized as a solid or a hollow conductor, with various shapes of the conductor's cross section. Due to the skin effect, the solid type of conductor is commonly used in high power, but for lower frequency applications. Some of the examples from the literature can be found in [61] and in **Fig. 2.7a**. On the other hand, hollow conductors are an attractive option even for higher operating frequencies, since the conductor's inner channel can be used for active cooling, see **Figs. 2.9a** and **2.9b**. More details are provided in [66] and [67], [68], respectively.

For higher operating frequencies (above 5 kHz), Litz wire is commonly seen as the technology of choice. It is made by twisting a number of strands with each other in order to form a bundle. A certain number of bundles can be twisted again to form a higher-level bundle. The transposition of bundles and strands is performed both in the tangential and radial directions. If the twisting is performed correctly, then each strand should take each of the places in the bundle which helps reduce high-frequency effects between the strands. Due to the very small diameter of the isolated strands, eddy current effects are greatly reduced. This results in a reduction of AC resistance. However, the thermal conductivity of Litz wire winding is anisotropic and quite low compared to the solid wire winding in a direction across the strands. This type of wire can be found in many different shapes and sizes: flat, round, square, or with a cooling duct in the middle. In order to achieve a higher Cu fill factor, rectangular Litz wire can be used instead of the round Litz wire, as can be seen in [62], [72] and **Fig. 2.7b** and **Fig. 2.13b**, respectively. Examples of MFTs realized with Litz wires are numerous, independent of the core material, i.e. the operating frequency. It makes sense because the strand thickness presents a degree of freedom, which can be used to adapt this winding type to almost any operating frequency.

Lastly, a Continuously Transposed Conductor (CTC) is another winding type, commonly employed for high-power transformer windings at low-frequency applications. The conductor is usually made of an odd number of enameled solid rectangular wires, which together assume rectangular-shaped cable, which is eventually covered by a paper insulation layer. Thereby, the solid conductors inside the CTC are radially transposed and can, thus, reduce the eddy current effects compared to a single solid conductor of the same cross-section area. During the literature review, no MFT prototypes are found realized with CTCs, since they are not optimized for high frequencies.

Regarding the materials used for the MFT windings, the most common are Cu and Al. Cu has better electric conductivity and therefore lower DC resistance compared to Al, but for higher frequencies, Cu is more prone to additional losses due to eddy current effects. Since it has a significantly lower weight compared to Cu, Al is a good design alternative if high gravimetric power density is required and it is cheaper, but it is harder to manipulate mechanically. The selection of a certain conductor material effects significantly conduction losses and thermal management of the windings. Important material properties of the two conductors are given in Table 2.3. The parameters  $\rho_e$  [ $\Omega$  m] and  $\alpha_e$  [ $1/^\circ\text{C}$ ] present the electric resistivity and the respective temperature coefficient, whereas  $\rho_{\text{Cu}}$  [ $\text{kg}/\text{m}^3$ ] and  $\alpha_l$  [ $1/^\circ\text{C}$ ] are

the material density and the coefficient of the linear thermal expansion, respectively. The parameter  $\sigma$  [S/m] represents the electric conductivity of the material, whereas  $k$  [W/Km] stands for the thermal conductivity of the conductor. Both conducting materials have relative permeabilities  $\mu_r$  [1] very close to 1. The electrical resistance of both Cu and Al as a winding material is strongly temperature dependent, i.e. the resistance increases with temperature, as given in (2.17). As a consequence, the conduction losses increase as well, assuming constant current density is considered.

$$\rho_e(T) = \rho_{e0} \cdot (1 + \alpha_e(T - T_0)) \quad (2.17)$$

### 2.3.3 Cooling Technology

There are three main cooling methods or mediums for both core and windings, which are employed depending on the cooling effect that the designer wants to achieve. Those are namely, air, oil, and water. Natural convection with air, also known as the self-cooled and Air Natural (AN) method, is the simplest, cheapest solution, but not efficient for high powers. The cooling effect can be improved by adding fans, i.e. including force convection, known as the air blast or Air Forced (AF) method. However, this can additionally complicate the design. Another possibility is to use heat sinks for the core cooling, which can be placed on any of the core limbs' sides, as depicted in **Fig. 2.13b**. Examples of AN convection are given in **Figs. 2.7c** and **2.13b**, the one of AF in **Fig. 2.13a**.

As for oil, it is a well-known and utilized solution, both for thermal and insulation coordination, and it offers stronger convective cooling compared to air. However, this option comes with increased complexity and cost due to additional heat exchange apparatus (containers with oil, pumps to achieve force convection and heat exchangers). This increases the volume of the whole design, but it is commonly used for high-power distribution transformers. Examples given in **Figs. 2.8b** and **2.9b** are fully immersed in oil for cooling purposes, however, the MFTs are shown before the immersion step.

Lastly, forced convection with water is very efficient, either as a direct or an indirect cooling method. To use it for active cooling of the windings, the designs need to use either hollow conductors or have the conductors encompassed with cooling jackets. Considering that the cooling medium comes in contact with components at various voltage potentials, it is important that it has low electrical conductivity, which is achieved with DI water. For core cooling special ducts or panels can be inserted for the water to circulate, which represents an indirect method. Additionally, it also relates to using water for cooling the oil in heat exchangers, or Al coolers with water channels that can be placed on transformer surfaces. **Figs. 2.9a** and **2.9b** provide examples of MFT prototypes that use active DI water cooling with Al hollow conductors.

Regarding different cooling arrangements and combinations of cooling media, the following terminology is standardized for the oil-immersed transformers [76]:

- Oil Natural Air Natural (ONAN):  
The tank surface area of the fully-immersed transformer is used to dissipate the heat into the environment. Depending on the power rating, radiators can be added directly to the tank or in a form of a radiator bank, in order to increase the available heat exchange surface.
- Oil Natural Air Forced (ONAF):  
To increase the heat exchange between the radiator and the environment, fans can be added to blow air on the radiator surfaces. In this way, the Heat Transfer Coefficient (HTC) is significantly

improved. Moreover, it is possible to combine ONAF with the ONAN method, depending on the overall size, complexity, as well as noise level that the design needs to achieve.

- Oil Forced Air Natural (OFAN) or Oil Forced Air Forced (OFAF):  
In order to increase the heat carrying capacity of oil, its mass flow needs to be higher and this can be achieved by introducing an external pump. In this way, a forced convection heat exchange is achieved between the oil and the transformer parts. Depending on the absorbed heat, the oil can be cooled with natural or forced air convection. Oil Directed Air Forced (ODAF) is an advanced version of OFAF, where the oil is guided through specific channels in the core and around the windings.
- Oil Natural Water Forced (ONWF):  
Considering the fact that the HTC of water is higher than the one of air, the use of oil-to-water heat exchangers is common, and it represents a more efficient cooling method compared to ONAF. In this way, radiators of smaller sizes can be used.
- Oil Forced Water Forced (OFWF):  
Similar to OFAF, forced water convection can be combined to cool the pumped oil. Compared to the above listed cooling arrangements, it achieves the most efficient heat exchange.

Note that particularly in the design of MFTs, the component does not have to be fully oil-immersed and that designs are existing, where e.g. only the windings are oil-insulated.

#### 2.3.4 Insulation Technology

Depending on the blocking voltage and the target power density of the designed MFT, there are several ways transformer insulation can be achieved. The three main insulation types are already introduced in **Sec. 2.2.1.4**, and according to each type, the blocking voltage, and the selected insulation material, appropriate distances can be determined. Note that the term *oil* is used to describe all the insulation liquids, including esters as well, which are not oil substances. The suitable insulating material is usually selected based on its dielectric and mechanical strength, which are interdependent properties. The parameter that affects both properties is the temperature. When exposed to high temperatures above the allowed values for a long time, the insulation experiences aging and a decline in both insulating and material, i.e. mechanical properties.

Note that high insulation voltage levels, common for MV and High Voltage (HV) applications, require larger distances for the insertion of the insulation material, which implies a reduction of the transformer power density. This can be compensated and improved by selecting a material with enhanced dielectric properties. The main insulation concepts rely on air, solid, or oil as insulating medium and they are discussed in the following:

- Air:  
In general, it is considered to be a good electrical insulator with a breakdown voltage of  $\approx 3$  kV. However, considering the humidity percentage and polluting particles in the air, this value usually reduces to 1 kV. Both values are defined for 1 mm distances. Hence, in case air is the only insulating material employed, large clearance distances are needed, which reduces the power density. Nevertheless, an obvious advantage of this medium is its availability, no additional cost, and mass to the design. Additionally, it allows for combined insulation and cooling, with the help of natural or forced convection.



- Oil:

Dielectric fluids used for transformer insulation can be divided into mineral-based and vegetable-based oils, which are used to produce natural ester liquids. Mineral oils have been in use for a very long time, however, they suffer from low fire resistance (flammable by nature) and have a damaging effect on the environment. Therefore, ester oils were introduced to improve these aspects and they additionally exhibit higher breakdown voltages [77]. Regarding PD occurrence, oil, similar to air, possesses a self-healing ability, particularly when in motion, and it offers combined cooling and insulation capabilities. Nevertheless, oil degradation can occur after a long period of use. As mentioned in the previous section, the use of oil for insulation and cooling requires additional equipment, which adds weight and volume to the design. Moreover, there are considerable integration issues, since it is not a typical power electronics technology. Typical values for this type of insulation medium are 5 kV/mm - 47 kV/mm, regarding the dielectric strength, and 2 – 5 regarding the dielectric constant [78].

- Solid:

Designs that do not use any type of liquid insulation are known as dry-type designs. There are three main possibilities, namely, Vacuum-Pressure Impregnation (VPI), resin impregnated, and cast resin transformers, which differentiate from each other based on the insulation procedure and the temperature class. VPI transformers use insulating materials, such as Nomex, Glastic, Kapton, Glass tape, and similar for winding insulation. After application of the material, the windings are dried to remove moisture, impregnated with varnish under vacuum pressure and additionally baked to cure the varnish. In this way, the resulting windings are both electrically and mechanically well made. The second method includes the insulating material, which is pre-impregnated with resin or pulled through a resin bath during winding, after which the windings are baked to cure the resin. Lastly, the cast resin dry type was developed as an alternative to the resin impregnation method, and it includes encapsulation of the windings with epoxy resin in order to prevent moisture from reaching them. The windings are placed into moulds where the resin is introduced under vacuum, followed by baking for curing, cooling, and removing the moulds. Both casting methods are susceptible to cracking, due to the use of epoxy-based materials, and require replacement, in case the insulation gets damaged. Note that all three solid insulation designs are usually air-cooled with natural or forced convection.

One of the key differences between solid type and air and liquid insulation is the potential presence of air pockets or voids between the conductor and the insulating material. This can lead to the accumulation of high electric fields that can discharge into the insulation and make irreparable damage. On the other hand, the complete casting of the transformer windings yields cooling problems, due to the low thermal conductivity of cast resin. Furthermore, thermal stresses can cause delamination, i.e. material fracturing into layers, as well as internal PD. Nevertheless, cast resin windings improve the power density compared to air, due to an increase of breakdown voltage to around 45 kV [79] and reduced insulation distances. A list of frequently used insulating materials together with some dielectric properties is given in **Tab. 2.4**. Lastly, for insulation of large power and distribution transformers, the common practice includes solid insulation for the windings, in the form of paper and pressboards, and the whole component is immersed in the dielectric fluid, i.e. oil. As already emphasized before, the thermal and insulation coordination must be considered together since they impact each other significantly.

Safety standards exist for different types of transformers, depending on their electrical specifications,

Dielectric material	Dielectric strength [kV/mm]	Dielectric constant $\epsilon_r$ [1]
Air	1 – 3	1
Oil	5 – 47	2 – 5
Mica tape	60 – 230	5 – 9
NOMEX 410	18 – 27	1.6 – 3.7
PTFE	60 – 170	2.1
Mylar	80 – 600	3.1
Paper	16	3.85
PE, XLPE	35 – 50	2.3
KAPTON	118 – 236	3.9

**Tab. 2.4** Dielectric properties of insulating materials.

construction type, and similar, and they give minimal creepage and clearance distances that need to be obeyed by the manufacturer. The values are generally determined depending on the following criteria [51], [52]:

- Over-Voltage Protection Category (OVC), describes the electrical conditions the component is installed in;
- Pollution Degree (PoD), describes the level of dust deposit and humidity, which influences the conductivity of the particles present in the environment;
- Material group - Comparative Tracking Index (CTI), describes the ability of the insulating material to resist degradation;
- System voltage, depending on the specific standard, this value could be the maximal or RMS of the working voltage, impulse voltage, or temporary overvoltage.

Additional influencing factors are altitude, the shape of the insulating surface, time under voltage, and others. However, considering the increase of the operating frequency into the MF range, there are still no concrete standards dealing with the insulation coordination of MFTs. Consequently, MFT designers are obliged to follow different standards. In this work in order to determine the correct distances, IEC 61800-5-1 [80] and IEC 60076-3 [81] were considered. The first standard is defined for adjustable speed drives, but it can be also used as the basis for MV converter applications. It is a standard for systems up to 35 kV which is most commonly applied to power semiconductor-based power conversion and MV drive systems. The second standard applies to power transformers that are liquid-immersed or gas-filled.

There are standard insulation tests used to verify the insulation design performance in normal operating conditions and for occasional overvoltage pulse incidences. Namely, those are the PD test, Basic Lightning Impulse (BIL) test, and the dielectric withstand test, also known as the high voltage, i.e. Hi-pot test. The PD test is used to ensure that the solid insulation is PD-free in a certain voltage range, i.e. to test the level of gradual insulation material degradation due to repeated localized PDs. The impulse test is a type of safety test, which aims to simulate overvoltages of atmospheric origins

and the ones generated due to equipment switching. Lastly, the Hi-pot test verifies the ability of safe operation of the component during the rated electrical conditions, i.e. the effectiveness of the designed insulation. During the test, the nominal voltage is applied and the resulting leakage current is measured. For low enough values, the component has fulfilled the prescribed dielectric withstand requirements. All the tests should be set according to recommendations stated in the corresponding safety standards.

## 2.4 MFT Construction Types

For higher power components, the selection of core shapes and sizes is rather limited, mostly because of the required dimensions of the magnetic cores. Nevertheless, the shell and the core type structures have been adopted for most of the MFT prototypes found in literature, as can be seen from the selected designs shown in **Fig. 2.7** - **Fig. 2.10**. For the sake of completeness, the main characteristics of the most common existing MFT construction types are summarized in the following:

- **Shell type:**  
This type is usually assembled of two or more E-shaped magnetic cores, with the PW and SW placed concentrically around the middle core leg. To achieve the required cross-section area, several core sets can be stacked together. Needless to say, this applies to the ensuing construction types. As a result of the winding arrangement, the analytical calculation of the leakage inductance can be relatively easily performed, and in general, a low inductance value can be achieved. Compared to the core type, it offers a larger core surface available for convective cooling.
- **Core type:**  
It consists of two or more rectangular or C-shaped magnetic cores, with the windings concentrically arranged around each of the core legs. This represents a typical way to construct this type of transformer, nevertheless, by employing a proper winding technique (with split coil formers) non-cut cores can be used as well [83]. Thereby, improved winding insulation can be achieved, in case the windings are separately placed around the legs. However, such an arrangement requires a more complex analytical model of the leakage inductance, due to unknown magnetic field distribution outside of the windings. According to [20], this construction type is the most convenient for manufacturing and offers a more compact transformer design than the one realized with the shell transformer type. Compared to the shell type, the leakage inductance is lower by a factor of two due to effective doubling of the winding height.

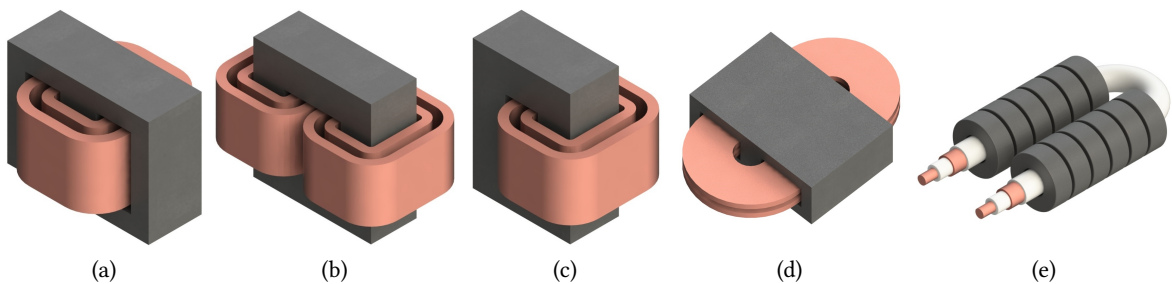


**Fig. 2.11** MFT types: (a) Shell; (b) Core; (c) C-type; (d) Planar; (e) Coaxial. Figures are adapted from [82].

- C-type:

This type is, by construction, a combination of the core and the shell type. The windings are arranged in the same way as for the shell type, except that C-shaped cores are used to assemble the core. Additionally, the core can be constructed from two U cores or a combination of U and I cores. In this way the core window area can be significantly reduced compared to the core type but at the cost of limited winding arrangement possibilities. Similar to the core type, this type allows relatively good access of the cooling media within the windings, however, it features a slightly larger free convection cooling surface of the core, similar to the shell type. MFT prototypes with C-type construction can be found in [22], [84].

- Planar type:

This particular construction type is employed when the target application requires transformers with a low flat profile and easy integration. Due to its characteristic construction, which features longer MLT of the windings, this type occupies a bigger volume and mass, for the same core and winding cross sections. The resulting benefits are larger cooling surfaces for the same volume, due to the flat shape, which offers more efficient convective cooling and shorter heat conduction paths. In combination with the disc or PCB winding construction, the cooling medium can easily access the windings and the inner core surfaces. However, this type is mostly restricted to lower power ranges. An MFT prototype of the planar construction type, made of amorphous material, can be found in [85].

- Coaxial type:

The main feature of this type is the use of the coaxial concept, where the PW and SW are implemented as the inner and the outer conductor of the coaxial cable. As a result, electromagnetic shielding is inherently provided. Regarding the construction, ring cores are typically used since the shape allows for a better fitting of windings inside of the core window and an improved fill factor. Owing to the symmetric field distribution, the leakage inductance value can be easily analytically calculated. Regarding the achievable turns ratio, 1:1 is the most typical. Nevertheless, for higher turns ratios, some advanced designs are necessary and more complex constructions are required [86]. Some MFT examples realized with this particular construction type are reported in [85], [87].

## 2.5 Modeling

To achieve the best design, it is of utmost importance to have reliable and accurate models. Secondly, considering that in the same design process, several different effects need to be considered, it is desirable that the models are additionally fast in execution. This further implies analytical models with closed forms are the ones to look at and hope for. Nevertheless, depending on the complexity of the modeled effect, sometimes it is not possible to reach a closed-form solution and numerical methods need to be employed in order to reach an optimal design. Lastly, very accurate MFT models can be obtained with the help of numerical field simulations, such as FEM. The following sections provide the state-of-the-art of some of the most important models necessary for the MFT design.

### 2.5.1 Electrical Parameters

Modeling of the MFT electrical parameters, which include magnetizing and leakage inductance, needs to be considered from two perspectives. Namely, from the converter side, depending on the

selected topology and based on its operating principles, control, and sizing rules, set requirements and constraints on the values of electrical parameters; and from the MFT side, where the transformer geometry plays a role in determining the parameter values.

### 2.5.1.1 Leakage Inductance

In the case of LLC-SRCs, the leakage ( $L_\sigma$ ) and magnetizing inductances ( $L_m$ ) of the MFT are a part of the resonant tank. Together with the resonant capacitors ( $C_r$ ), they govern the resonant frequencies ( $f_o$ ,  $f_p$ ), given by the following equations [43]:

$$f_p = \frac{1}{2\pi\sqrt{(L_\sigma + L_m)C_r}}, \quad f_o = \frac{1}{2\pi\sqrt{L_\sigma C_r}} \quad \Rightarrow \quad L_\sigma = \frac{1}{4\pi^2 f_o^2 C_r} \quad (2.18)$$

The  $f_o$  is the higher resonant frequency and the one of interest since the resonant converters exhibit stiff output voltage characteristics when switching in close proximity to it. Thus, the leakage inductance, necessary to serve the LLC-SRC design, requires accurate specification and modeling.

In the case of single-phase DAB controlled with phase shift modulation, the minimal required leakage inductance value [47] can be derived from the expression for the active output power as follows

$$P_o = \frac{V_{DC,1} V_{DC,2} \varphi (\pi - \varphi)}{2\pi^2 f_{sw} L_\sigma} \quad \Rightarrow \quad L_{\sigma,min} = \frac{V_{DC,1} V_{DC,2} \varphi_{min} (\pi - \varphi_{min})}{2\pi^2 f_{sw} P_o}. \quad (2.19)$$

Thereby, the power flow is controlled by the phase shift  $\varphi$  between the primary and secondary square-wave voltages. For both converter topologies, the precise mechanical realization of the windings is important, with as narrow tolerance band, regarding design, as possible.

From the transformer point of view, the leakage inductance can be estimated in several ways, firstly, with the help of numerical methods and FEM software, which are very accurate but time consuming and heavy on resources. Secondly, reluctance network models can be used, which are faster but not as accurate, and lastly, analytical methods. They are fast to compute, reliable and suitable for design optimization tools. Regarding the analytical modeling path, a standard approach is integration of the magnetic energy which results from the leakage magnetic field within the core window area. It can be determined from integration of the magnetic field or the product of the vector potential and the current density, which reduces the integration domain to the conductor surfaces. As already mentioned, the magnetic field distribution in the windings changes due to eddy current effects, and for accurate leakage inductance estimation at elevated frequencies, this needs to be taken into consideration. **Chap. 4** deals in depth with leakage inductance modeling.

### 2.5.1.2 Magnetizing Inductance

As for the magnetizing inductance, it usually takes a high value and is designed to limit the magnetizing current. For the LLC-SRC topology, when the switching frequency is slightly lower than the resonant one, the turn-off current of the switches is load-independent and its value is controlled by the magnetizing inductance. It is governed by the following relation

$$L_m = \frac{V_{DC,1}}{4f_{sw} I_m}, \quad (2.20)$$

and with a careful design, both the turn-off current and the corresponding losses can be kept low. Note that  $V_{DC,1}$  refers to the primary voltage applied during half of the switching period, and it is not the DC link voltage.

As already derived in (2.7) from the magnetic circuit of the transformer, by defining the core and air gap reluctances,  $\mathcal{R}_c$  and  $\mathcal{R}_g$ , the magnetizing inductance can be obtained as follows

$$\mathcal{R}_c = \frac{l_m}{\mu_0 \mu_r A_{core}}, \quad \mathcal{R}_g = \frac{l_g}{\mu_0 A_{core}} \quad \Rightarrow \quad L_m = \frac{\mu_0 A_{core} N_1^2}{\frac{l_m}{\mu_r} + l_g}. \quad (2.21)$$

Thereby,  $l_m$  [m] is the Magnetic Path Length (MPL) of the core,  $l_g$  [m] is the total air gap.

### 2.5.2 Core Losses

Magnetic core losses can be principally divided into three parts. Namely, frequency-independent hysteresis loss (due to hysteretic behavior of the material), frequency-dependent eddy current loss (due to the electrical conductivity of the material), and relaxation loss (due to other physical mechanisms) [88]. The three loss contributors can be modeled separately and in different ways. Regarding the modeling method, the core loss estimation can be performed [47]:

- Based on empirical observations expressed in Steinmetz-alike equations:  
Regarding modeling of core losses for the MFT design optimization tool, a closed analytical expression is the most convenient form. In the wide range of existing analytical models, the particular simplicity is related to the original Steinmetz equation [89] and its numerous improvements, which address different core materials and excitation waveforms. Thereby, the original equation, which is discussed in more detail later in this section, includes the direct impact of switching frequency and flux density weighted with the so called Steinmetz coefficients ( $K, \alpha, \beta$ ), which are characteristic for each magnetic material. Regarding derivations of the Steinmetz equations, some of the prominent ones are: Modified Steinmetz Equation (MSE) [90], where the operating frequency is replaced by an equivalent one, which is related to the magnetization rate, i.e. magnetic induction rate of change; Waveform Coefficient Steinmetz Equation (WCSE) [91] defines the flux waveform coefficient, which correlates the non-sinusoidal waveform with the sinusoidal thereby assuming equal flux density magnitude and can be added to the original Steinmetz equation; Improved Generalized Steinmetz Equation (IGSE) [92] is thoroughly discussed in **Chap. 6**.
- Based on the loss separation method:  
According to [93], the core losses are divided into hysteresis loss, eddy current loss, and anomalous or excess loss. All three proposed expressions resemble the Steinmetz equation, however, with different exponents for the frequency and flux density magnitude, as well as different proportional coefficients. They are based on physical interpretations of the losses in ferromagnetic materials and are valid in the case of sinusoidal excitation.
- Based on time domain expressions:  
This approach developed in [94] starts with the loss separation method, but it derives time-dependent expressions which can be applied to arbitrary excitation waveforms since the general expression depends on the time derivative of flux density. The model is able to estimate the

instantaneous value of core losses and is usually employed for the characterization of electric machines.

- Based on mathematical models of magnetic effects within the material that cause core losses: To model hysteresis losses, two main macroscopic models, which are based on actual physical assumptions, are common: the more complex Jiles-Atherton model [95], [96] and the Preisach model [97]. The first model considers the hysteresis effect as a consequence of frictional forces opposing the motion of the Bloch domain-wall [98], whereas the latter model is specific due to its phenomenological character. This implies that the model is able to reproduce the hysteresis curve and the corresponding magnetic field history with great accuracy and reliability without explaining the physical processes occurring during the magnetization of the material [47]. Moreover, both models are capable of accurate hysteresis modeling under different operating conditions, i.e. for various excitation voltages. Regarding modeling of relaxation losses, the work in [99] proposed a model which is based on the Preisach model and the permeance-capacitance analogy [100], for the purpose of magnetic components modeling for a circuit simulation environment. Thereby, the relaxation effect is considered by adding a parallel branch of series connected permeance and “magnetic” resistor to the hysteresis permeance block. The model was successfully verified for various excitation waveforms. Lastly, the eddy current loss can be accurately modeled by a magnetic circuit of permeance and resistor loops, which model a single laminated sheet in laminated core materials, where the eddy current losses are usually present [101]. A good overview of existing mathematical models for the three core loss types is given in [102]. However, most of these models require additional material characterization, which is not always possible to conduct and it requires a suitable measuring setup.

A more detailed summary of the existing core loss models can be found in [47]. Depending on the properties of the selected magnetic material, the operating frequency, and the excitation voltage shape, it can be assumed that certain loss type dominates the overall core losses, which simplifies modeling. An example is ferrite, where the eddy current losses can be neglected due to low conductivity [99]. Moreover, the relaxation losses are most pronounced for applications above 20 kHz and voltage waveforms which include zero phase voltages, or asymmetrical Pulse-Width Modulation (PWM) with duty cycles different than 50 % [103]. Therefore, it can be assumed that, within predefined limits, the hysteresis effect generally dominates the core losses. Nevertheless, note that above a certain operating temperature (100 °C), the electrical conductivity of the material increases, and the eddy current losses need to be included [104], [105]. Regarding modeling of core losses for the MFT design optimization tool, the most convenient modeling method is a closed analytical form. Therefore, this type is discussed more thoroughly in one of the following chapters.

### 2.5.3 Winding Losses

In order to estimate winding power losses, it is common to use the analytical Dowell model [106], developed in 1966. The original model is derived for ideal foil windings and it is based on the solution of two-dimensional Maxwell’s equations under two main assumptions:

- The foil conductors occupy the entire core window height, assuring thereby a one-dimensional field  $H_y(x)$  along the core window,
- The use of a magnetic core with infinite permeability, so that a magnetic field exists only within the core window area.

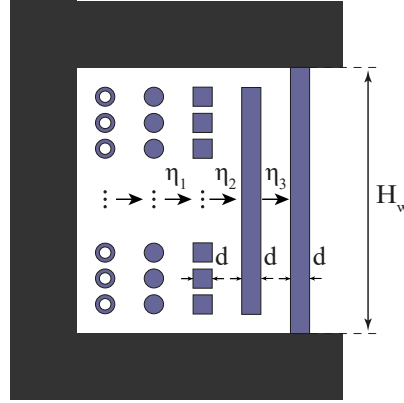


**Fig. 2.12** Adaptation of different winding structures to the equivalent foil winding, extending over the full window height of the size  $H_w$ , which is used as the basis of Dowell's model.  $\eta_1 - \eta_3$  are the respective porosity factors,  $d$  is the equivalent thickness of the foil conductor.

As a result, Dowell obtained closed-form expressions for the magnetic field distribution in and around the conductors, from where the corresponding current density distributions in the foils were derived, and eventually from there, conduction losses. Moreover, the model can identify loss contributions from skin and proximity effects, which are frequency-dependent effects. As a result, Dowell defined the resistance factor which represents the ratio between the total AC and DC resistance of the foil winding. In this way, the winding loss contribution of the whole current harmonic spectrum can be taken into account. However, note that the model is accurate as long as the assumptions stated above are fulfilled, which for practical reasons is almost never the case. Considering the necessary insulation distances between the windings and the core, or any other more complex winding arrangement implies a two-dimensional magnetic field and current density distributions, which make the accurate analytical solution too complex to obtain.

Nevertheless, to expand the model validity to round and rectangular conductor types, Dowell introduced the porosity factor. Its purpose is to ensure that an equal magnetic field is generated along an enclosed path for the two different winding types. In this way, an equivalence can be achieved between the ideal foil winding, for which the model was initially developed, and some other winding type, as illustrated in **Fig. 2.12**. Several works [107], [108] have subsequently inquired about the validity of this factor as a corrective measure. Moreover, some works [109], [110] suggested improvements of the developed resistance factor, in order to increase the model's accuracy for different winding types and penetration ratios (ratio between the conductor thickness and the respective skin depth) and provided comparisons between already published works. Many recent improvements [108], [110], [111] are based on the results of numerous FEM simulations, from where corrective factors and weighting parameters are deduced. A more detailed summary of the subsequent improvements of the original Dowell model can be found in [47].

Besides analytical modeling related to Dowell's model which is derived for foil windings, there are other models which describe skin and proximity effects for round conductors [112]–[114]. Closed analytical expressions are derived for single solid conductors, as well as for isolated Litz bundles, where skin and internal proximity effects are dominant, and round conductors within an external field, which gives rise to the external proximity effect. Loss modeling of Litz wires has been to date thoroughly covered in literature [47], [115], and is thus not further considered in this thesis.



Lastly, one of the most accurate ways to model winding losses of any conductor type is with help of numerical methods, such as FEM. Studies conducted in [116], [117] are able to consider higher harmonics of nonharmonic transformer currents and the core saturation influence on the winding losses. However, the cost of accuracy is paid with long computation time, which is not suitable for design optimization tools.

#### 2.5.4 Thermal Modeling

From the energy balance viewpoint, the heat generated predominantly by the core and windings is transferred to the available surfaces and then further to the ambient. The heat is dissipated through one of the three heat exchange mechanisms, namely, conduction, convection, or radiation. An equilibrium is reached when the thermal energy generated through losses is in balance with the heat which is transferred away. Note that only the conduction mechanism is linear, whereas the other two are generally both non-linear and temperature dependent. The power density of the MFT is limited by the maximal allowed operating temperatures, which get imposed by the ambient temperature and by transformer losses and thermal resistances, which are also partly determined by the involved materials. Furthermore, due to the complex structure of transformers, the heat paths from the hot spots to the surface are not necessarily well defined. Nevertheless, the thermal aspect is another important limiting factor for transformer design, therefore, it is crucial to accurately estimate the temperature distributions.

##### 2.5.4.1 Heat Transfer Mechanisms

In order to properly model the MFT thermally, the heat exchange mechanisms need to be closely defined and understood. They are typically characterized by HTC's,  $h$  [ $\text{W}/\text{m}^2 \text{K}$ ], which can be seen as a measure of the resistance of heat exchanging body to the heat flow [118]. The three heat transfer modes are illustrated in **Fig. 2.13** and described below:

- Conduction:

It is a process in which the heat is transferred from the high to the low-temperature part of the body, due to temperature differences and by means of free electrons. It is considered to be a slow, but linear process. The heat transfer rate  $q_{cd}$  [W] is governed by Fourier's law

$$q_{cd} = -kA \frac{\partial T}{\partial x} \quad \Rightarrow \quad q_{cd} \approx -kA \frac{T_1 - T_2}{x_1 - x_2} = kA \frac{T_2 - T_1}{d}, \quad (2.22)$$

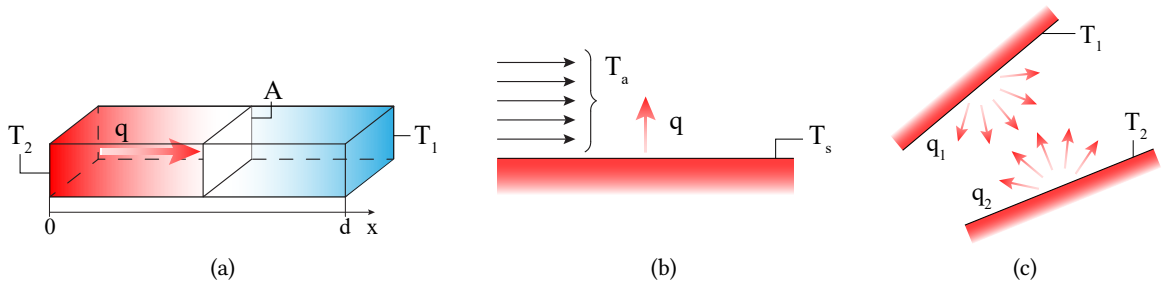


**Fig. 2.13** Heat transfer mechanisms: (a) Conduction; (b) Convection; (c) Radiation. Adaptation from [82].

with  $k$  [W/mK] as the thermal conductivity of the material,  $A$  [m<sup>2</sup>] as the area of the cross section, normal to the heat flow direction, and  $d$  [m] as the material length in the flow direction [44]. The negative sign signifies that the heat is transferred in the opposite direction of the temperature gradient. Regarding conduction in an MFT, it typically takes place inside the conductors and the core. The conduction HTC is defined by the equation below:

$$h_{cd} = \frac{k}{d} \quad (2.23)$$

- Convection:

It is a process that involves heat transfer from a solid surface to a fluid in motion. It is comprised of two mechanisms, namely, diffusion, which is energy transfer due to the random motion of molecules, and advection, which describes energy transport due to the bulk (aggregated) motion of the fluid. One of the two mechanisms prevails depending on the distance from the solid surface [82]. The convective heat transfer rate  $q_{cv}$  [W] can be described by Newton's law of cooling defined by

$$q_{cv} = h_c A (T_s - T_a), \quad (2.24)$$

with  $h_c$  [W/m<sup>2</sup>K] as the convection HTC of the material,  $A$  surface area that participates in the heat exchange, and  $T_s$  [°C],  $T_a$  as the surface and ambient temperatures, sufficiently far from the surface [44]. The particularity of this heat transfer mechanism lies in the respective HTC. Its value is reflected in the complexity of the convection process, and thus, it is dependent on the temperature, physical properties of the fluid and the fluid type, and the position and shape of the surface, which makes it very difficult to determine accurately. One of the common ways is to start with an approximation and adjust it with the help of measurements for a specific structure. Convection is one of the main heat exchange mechanisms relevant for MFT cooling, and it takes place for every available surface in contact with air or another cooling medium. The convection HTC is defined by the equation below

$$h_{cv} = Nu \frac{k}{L}, \quad (2.25)$$

with  $Nu$  as the Nusselt number, and  $L$  as the characteristic length, which predominantly depends on the surface geometry of the particular convective heat exchange. The  $Nu$  number is dimensionless and it is defined as the measure of heat transfer rate by convection, i.e. gives the ratio between the convective and conductive heat transfer at the fluid boundary [82]. It is typically empirically determined and it depends on the convection type (natural/forced), fluid properties (described by Prandtl number  $Pr$ ), surface geometry, and flow type (laminar/turbulent). In the case of natural convection, the  $Nu$  number is usually presented as a function of  $Pr$  and Rayleigh ( $Ra$ ) number, whereas for forced convection the  $Ra$  number is replaced by the Reynolds ( $Re$ ) number, as shortly summarized in the following:

$$Nu = f(Pr, Ra), \text{ natural convection} \quad (2.26)$$

$$Nu = f(Pr, Re), \text{ forced convection} \quad (2.27)$$

Lastly, the values of  $Ra$  and  $Re$  numbers describe the flow regime of the fluid, i.e. whether the laminar or turbulent type of flow is dominant. Thereby, the Rayleigh number indicates the

relation between buoyancy and viscosity forces combined with the Prandtl number, whereas the Reynolds number presents the ratio of inertial to viscous forces within a fluid [82]. The relevant dimensionless numbers are addressed in more detail in **App. A**. Temperature-dependent physical properties of the fluids relevant to the heat exchange in the MFT are provided in **App. B**.

- Radiation:

In contrast to the previous two mechanisms, this heat transfer is based on electromagnetic radiation and it occurs even without any medium. Moreover, it is considered a fast-speed process and it takes place for all objects with a temperature above 0 K, i.e. above absolute temperature. The heat transfer rate  $q_r$  [W] is described by the Stefan-Boltzmann law

$$q_r = \varepsilon \sigma A T^4, \quad \text{and} \quad q_r = \varepsilon \sigma A (T_1^4 - T_a^4), \quad (2.28)$$

with  $\varepsilon$  [1] as the emissivity of the radiating surface with the area  $A$ , which describes the factor between the power transferred from the observed surface and a black surface with  $\varepsilon = 1$ . Parameter  $\sigma = 5.67 \cdot 10^{-8} \text{ W/m}^2 \text{ K}^4$  is the Stefan-Boltzmann constant, and  $T$  [K] is the absolute surface temperature. The radiant energy exchanged between a hot body (of absolute temperature  $T_1$ ) and the surrounding environment ( $T_a$ ) can also be determined. Lastly, radiation plays an important role in MFT cooling, particularly for high-temperature differences between the surfaces, and materials with high emissivity. The HTC relevant for radiative heat transfer is defined by

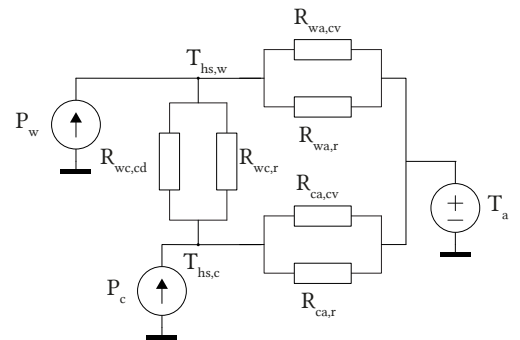
$$h_r = \frac{\varepsilon \sigma (T_1^4 - T_a^4)}{(T_1 - T_a)}, \quad (2.29)$$

which transforms (2.28) to  $q_r = h_r A (T_1 - T_a)$ .

#### 2.5.4.2 Thermal Networks

The standard way of thermal modeling of MFTs includes building networks of thermal elements. For this purpose, the electrical-thermal analogy is typically used as the model basis, provided in **Tab. 2.5**, which helps thermally describe the transformer through a network of thermal resistances, capacitances, and sources. A thermal model can be developed for steady-state operation, as well as to characterize transient thermal behaviour. While the first is important for a sound and optimal design, the latter provides insight in case of overloading or similar [119], [120]. The static thermal model

Electrical domain	Thermal domain
Voltage $v$ [V]	Temperature drop $\Delta T$ [°C]
Current $i$ [A]	Power loss $P_{\text{loss}}$ [W]
Resistance $R = \rho \frac{l}{A}$ [ $\Omega$ ]	Thermal resistance $R_\theta = \frac{1}{h_c A}$ [K/W]
Capacitance $C = \varepsilon \frac{A}{d}$ [F]	Thermal capacitance $C_\theta = \rho c_p V$ [J/K]
Ohm's law: $\frac{v}{R} = i$	$\frac{\Delta T}{R_\theta} = P_{\text{loss}}(q)$
Kirchhoff's current law: $\sum_k i_k = 0$	$\sum_k P_{\text{loss},k} = 0$



**Tab. 2.5** Analogy between electrical and thermal quantities. **Fig. 2.14** Simplified MFT thermal network.

estimates the arising hot-spot temperatures and the general temperature distribution in the steady state. The corresponding thermal network consists of thermal sources and resistances. On the other hand, the transient model is in charge of dynamic temperature distributions at different interfaces, which is completed by adding the corresponding thermal capacitances to the static model.

Until now numerous thermal models have been developed, depending on the transformer type and the employed cooling and insulation methods [121]–[126]. Another valid way to model is with the help of simulations and numerical methods, such as FEM, finite-volume, finite-difference methods and so on. Depending on the complexity of the transformer structure and the modeling aspect, this can be significantly more computationally intense, but also more accurate. For the same reasons, numerical simulations (particularly in the case of Computational Fluid Dynamics (CFD), which is strongly non-linear) are not suitable to use during the MFT design phase, but are employed for validation purposes. On the other hand, simulations of linear problems, such as heat exchange or electrostatics, for design optimization purposes may be affordable.

**Fig. 2.14** shows a simplified thermal resistance network, which describes the main heat exchange processes between the windings and core, and their interaction with the ambient, according to the analogy set in **Tab. 2.5**. The core and winding losses,  $P_c$  and  $P_w$ , are determined with the help of models, the thermal resistances by identifying the relevant exchange mechanisms and defining the corresponding HTC. Finally, the hot-spot temperatures of the core and windings,  $T_{hs,c}$  and  $T_{hs,w}$ , can be determined by applying the thermal equivalent of Kirchhoff's current law. A more elaborate thermal model is presented in **Chap. 6**.

### 2.5.5 Mechanical Withstand Considerations

In the winding design phase, it is important to consider the mechanical stresses that the transformer can be submitted to during abnormal conditions. Electromagnetic axial and radial forces are generally exerted on the windings in regular operation. However, in the case of inrush or short-circuit currents in different fault conditions, these forces reach substantial values which can deform or even destroy the windings. The forces increase due to high current values passing through the windings and the magnified leakage field owing to the core saturation. Regarding the effect, the radial components act to reduce the radius of the inner winding and increase the radius of the outer winding, which leads to buckling. In contrast, the axial forces compress the windings in the vertical direction, which can cause the winding structure to bend and reduce its height. Therefore, these destructive forces need to be predicted already in the design phase, so that clamping mechanisms can be designed to avoid breakdowns at a later stage.

For this purpose, analytical models [127], [128] exist, which are usually verified with time-stepping FEM simulations. Another way is to directly use FEM simulations [129], [130]. Both methods require the previous estimation of short-circuit and in-rush currents. Additionally, the leakage field can be reduced by interleaving the windings, which would decrease the magnitude of electromagnetic forces and, thus, the mechanical stress applied to the windings [129]. However, lower leakage inductance values lead to higher short-circuit currents which is again counterproductive.

### 2.5.6 Design Methods

Computer-aided design of power transformers was developed end of the 60s and the beginning of 70s of the last century and quickly became standard practice [131]. Having in mind the computation

capabilities of the computers at the time, the governing equations and models needed to be as simple as possible, yet, capable of accurately describing the relevant effects and design trends. Therefore, the relevant models were usually of analytical nature [48], [132].

One must admit, based on the relevant phenomena discussed in the previous sections, that the problem of the MFT design is highly complex, non-linear, non-convex and it is a multi-objective problem. To apply any optimization technique to this problem, we need to define objectives, specifications, variables, and constraints. Therefore, as the first step, it is necessary to define an objective function, also known as a cost function, which can reflect a single design criterion or make a combination of criteria with weighting factors. Finally, the selected optimization algorithm needs to find the (global) optimum, maximum, or minimum, of the defined cost function. Different optimization methods can be compared based on their execution time, accuracy, robustness, sensitivity to variations, and so on.

There are various optimization algorithms reported in the literature. Firstly, genetic algorithms rely on operators such as mutation, crossover, and selection, that are inspired by natural biological evolution in order to find optimal solutions. Secondly, design algorithms that use machine learning and neural networks have been reported. From given specifications and goals, a pretrained artificial neural network generates Pareto fronts and selects the optimal designs. A drawback here is that large data sets of good quality need to be available to train the network before use. Some numerical methods, such as Newton-Raphson, which is a gradient-based method can also be employed. Lastly, there are brute force or parametric sweep algorithms which look into all possible combinations of optimization variables. In case a large number of optimization variables is defined, this method can be very computationally intensive, but on the other hand, it is easy to implement. Deeper classification with prominent algorithms can be found in [133].

## 2.6 Summary

As can be seen from the previous sections, there is a plethora of technologies and options that can be combined for an optimal MFT design. Starting from the materials used for core and windings, as well as insulation and cooling, over the specific transformer construction type, to different methods that can be used to implement the design optimization algorithm.

Finally, a specific MFT design comes as a solution to a multi-parameter optimization problem, selected based on a certain criterium. This could be e.g. minimal transformer weight, minimal volume, minimal material and manufacturing cost, or even a combination of different parameters expressed in form of a cost function. The transformer design space is large and thereby, many different effects, which are often coupled, need to be taken into account, with the help of corresponding models.



# 3

## MFT Design Space

*In this chapter the MFT-specific requirements are introduced, deduced from the envisioned 1MW direct current transformer. Additionally, a set of materials and technologies relevant to the MFT design is selected from the plethora of existing options, which are presented in the previous chapter. Thereby, three winding arrangements are defined, which are further studied in the remainder of the thesis, in order to achieve an optimal MFT design. The optimization algorithm behind the design process is established and explained.*

### 3.1 Introduction

The MFT is envisioned as an integral part of a 1 MW DCT, i.e. galvanically isolated DC-DC converter, which is implemented based on the LLC-SRC topology. Owing to this selection, the voltage transfer ratio characteristic is considered stiff when the operating frequency is close to the resonant one. As a result, the DCT can be operated in open loop, without the need for an external power set-point. In this regard, the DCT resembles the conventional AC transformer.

The electrical circuit of the DCT is presented in **Fig. 3.1**. The two power stages, which are interconnected with the transformer and the resonant capacitors, are based on the 3-level NPC topology, with split capacitors used as the second leg. Both inverter and rectifier stage use RC-IGCTs as switching devices, due to their high current conducting capabilities and low conduction losses [134]. Combined with the soft-switching capabilities of the selected resonant topology, the power stages promise high efficiency.

As a design benchmark for the MVDC voltage domain, the primary side of the DCT is operated

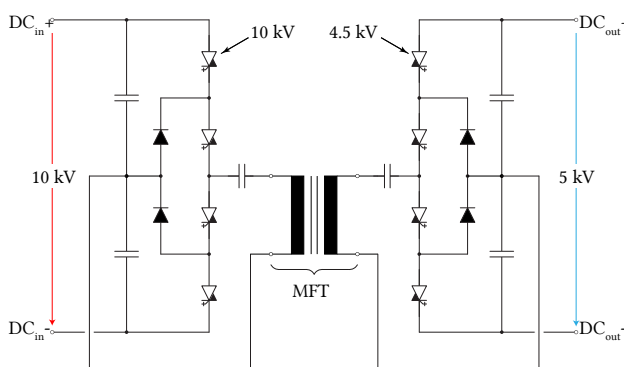


**Fig. 3.1** DCT realized as the LLC-SRC converter.

Characteristics	Unit	Value
Frequency	kHz	5
Nominal power	MW	1
Turns ratio	1	2:1
Primary voltage	kV	$\pm 5$
Secondary voltage	kV	$\pm 2.5$
Reference magnetizing inductance	mH	25 – 50
Reference leakage inductance	$\mu$ H	25 – 50

**Tab. 3.1** Required MFT electrical specifications.

from a 10 kV DC-link and is supported by 10 kV RC-IGCTs, acquired as engineering samples from Hitachi Energy Semiconductors. The secondary side operates with a 5 kV DC-link and 4.5 kV RC-IGCT devices, which are commercially available [134]. Note that even though the DCT is fully bidirectional, the 10 kV side is referred to as the primary, and the 5 kV one as the secondary side. Therefore, the rated primary and secondary voltages of the MFT under analysis are  $\pm 5$  kV and  $\pm 2.5$  kV, respectively, whereas the turns ratio is fixed to 2:1. Moreover, having a different than 1:1 turns ratio is introducing additional challenges, such as more complex analytical modeling of the windings, but it is also granting an additional degree of freedom regarding the possible winding arrangement.

The electrical requirements, derived from the DCT design specifications which govern the transformer design, are catalogued in **Tab. 3.1**. For flexibility reasons due to the mechanical realization of the windings, a target range is defined for both magnetizing and leakage inductance. A factor of 2 between the minimum and maximum acceptable value is selected to provide larger exploration of the MFT design space. Regarding the modeling aspect of the leakage inductance, the wide range of values is not there to imply a large modeling tolerance. The reference range of the magnetizing inductance corresponds to the turn-off (magnetizing) current of roughly 6 A–10 A at the primary side, which corresponds to a range of 12 A–20 A on the secondary side.

**Figs. 3.2** and **3.3** show the primary and secondary voltage and current waveforms, respectively, obtained through simulation of 1 MW DCT for several operating points, in case the ideal model of the transformer is used. Additionally, **Fig. 3.3a** shows a closer view of the turn-off event at 250  $\mu$ s, which confirms the turn-off current matches the magnetizing current, regardless of the amount of transferred power. The electrical simulations are performed with the simulation software tool PLECS. The simulation parameters are set according to **Tab. 3.1** with the transformer intrinsic inductances set to  $L_\sigma = 44.4 \mu\text{H}$ ,  $L_m = 42.8 \text{ mH}$ , and the primary and secondary side resonant capacitances to  $C_{r1} = 37 \mu\text{F}$ ,  $C_{r2} = 170 \mu\text{F}$ .

The voltage levels match the expected values, whereas the deviations from perfectly square waveforms are due to voltage drops on the resonant capacitors. The primary current at no load conditions gives the magnetizing triangular current of the transformer, depicted by a green curve labeled with 0%. Both PW and SW current waveforms have the typically expected (quasi-sinusoidal) shapes for the LLC-SRC converter. Considering that the switching frequency is selected below the resonant frequency, a half-cycle discontinuous conduction mode can be observed in **Fig. 3.3b**, which consequently allows the soft commutation of the rectifier diodes in the secondary power stage.

Considering the fact that thyristor-based switches, such as RC-IGCTs, are mainly employed for high-power applications operated at lower switching frequencies (up to 900 Hz), the operation at 5 kHz presents a record-high switching frequency for this semiconductor type [135]. At the same time, it sets an upper limit on the operating frequency for the MFT design.

Regarding the selected resonant topology, together with the resonant capacitors, the MFT is intrinsically part of the resonant tank with its leakage and magnetizing inductance. This further emphasizes the need for accurate modeling and design of the electrical parameters of the MFT.

The DCT design relies on actively cooled RC-IGCT stacks with DI water, available in the laboratory. The two power stages are shown in **Fig. 3.4a** and **Fig. 3.4b**, whereas the Water Cooling Unit (WCU) is presented in **Fig. 3.4c**. The availability of forced water cooling prompted the decision to have actively cooled transformer windings, which further led to a choice of Cu pipes as winding conductors.



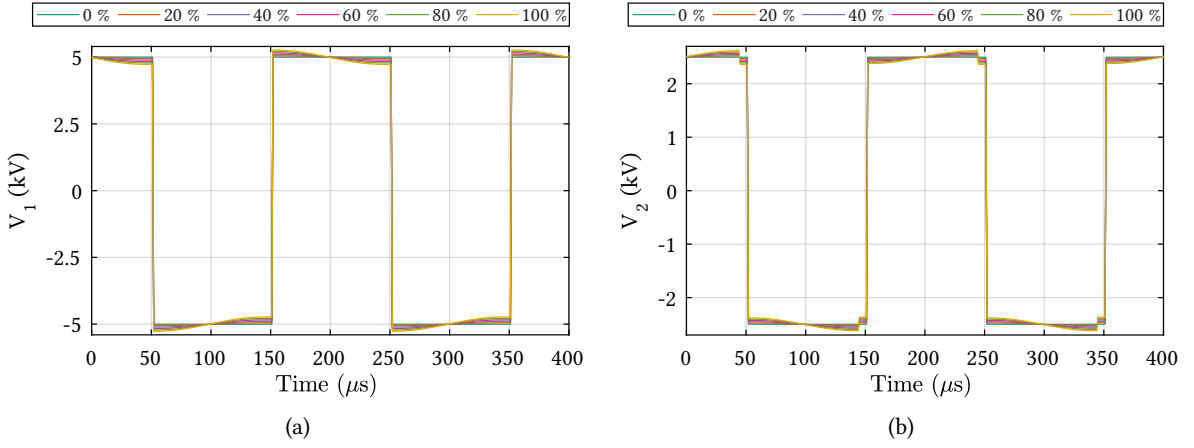


**Fig. 3.2** Simulated primary (a) and secondary (b) transformer voltage waveforms at various loading conditions.

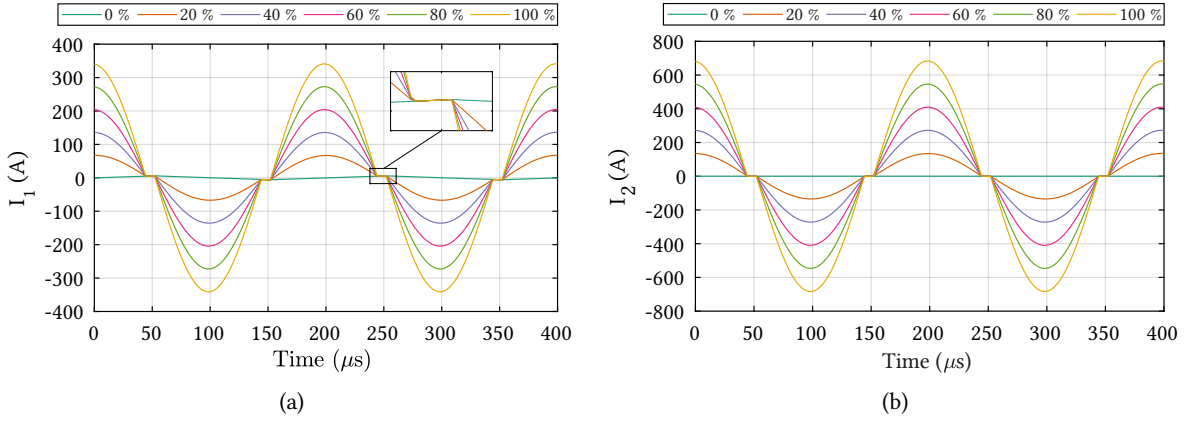


**Fig. 3.3** Simulated primary (a) and secondary (b) transformer current waveforms at various loading conditions.

## 3.2 Selected Technologies

In the previous chapter, a plethora of options are presented regarding MFT construction and winding types, as well as materials, cooling, and insulation technologies. Moreover, considering the electrical requirements outlined in **Tab. 3.1**, the following set of technologies is preselected for deeper scrutiny:

- MFT structure: Core type
- Magnetic materials for the core: SiFe, amorphous and nanocrystalline material
- Windings: Round hollow conductors made of Cu
- Core insulation: Air
- Winding insulation: Oil
- Core cooling: Natural air
- Winding cooling: Forced DI water.

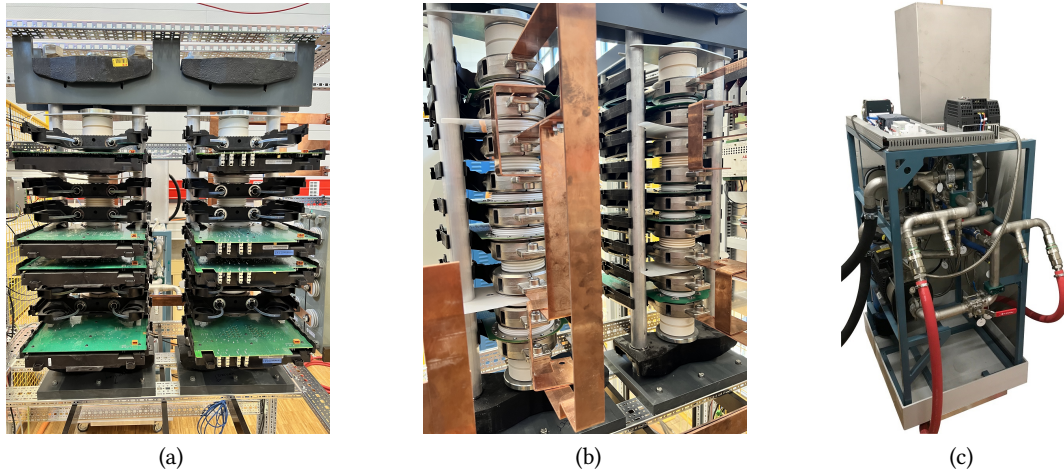


**Fig. 3.4** Figures (a) and (b) show 10 kV and 4.5 kV RC-IGCT stacks used for the two power stages of the 1 MW DCT demonstrator. Figure (c) displays the employed ACS 1000 WCU.

Needless to say, every design selection/decision has an impact on the modeling aspect of the MFT, as well as on the optimization algorithm behind the design process. The inspiration for the selection of the insulation and cooling methods is owed to LFT designs from traction applications.

A literature review on high-power MFT designs revealed that shell and core types are among the most commonly used construction types. This can be also observed from the limited number of illustrated MFT prototypes shown in **Chap. 2**. According to [136], in regard to power transformers, the core construction type is more widely used due to its simpler design and lower cost, compared to the shell type. Additionally, the existing competence in MFT design in the laboratory was so far focused on the design of shell-type transformers, which further motivated the decision to adopt the core construction type. The set operating frequency of 5 kHz still allows consideration of SiFe as the core material, whereas nanocrystalline and amorphous materials come as a natural choice. Nevertheless, the frequency is too low for efficient ferrite MFT prototype (due to low saturation flux density), thus, the first three materials are considered. With actively cooled windings, i.e. more effective cooling methods, the ratio between the core and winding losses can be shifted from 50:50% distribution, as usually claimed to be optimal and achieve the highest efficiency [45], to a more uneven one, which allows the core to be air-cooled. Lastly, oil insulation of the windings was motivated by reduced insulation distances and superior dielectric properties, needed in the MV range, which in turn helps to achieve smaller transformer designs.

### 3.3 Winding Arrangements

In order to achieve oil-immersed windings for insulation purposes and air-insulated core, the windings are placed in one or two oil vessels, depending on the analyzed winding disposition. The MFT requirement of a 2:1 voltage ratio implies that the PW has double the number of turns compared to the SW. Considering that this can be achieved and realized in more than one way provides a possibility to look into several winding arrangements, to find an optimal one. Note that the criterion of optimality can be defined in numerous ways, e.g. lowest losses, least amount of Cu needed, convenient mechanical

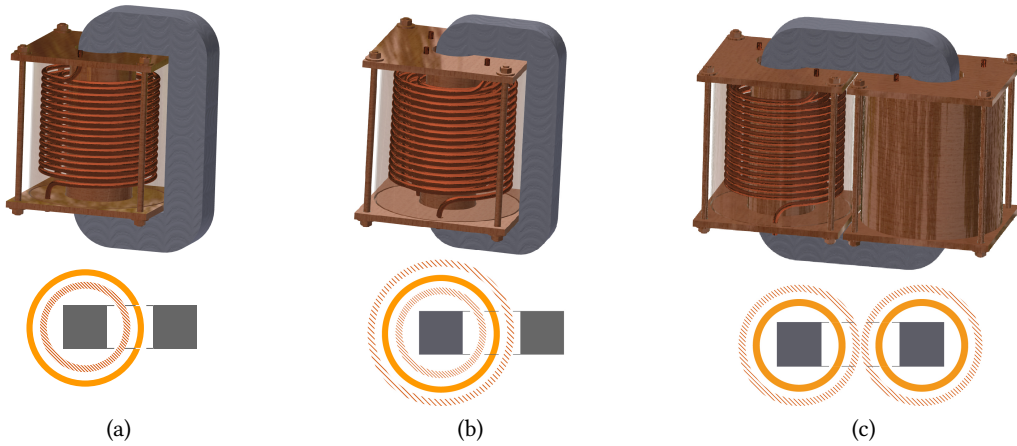


**Fig. 3.5** Illustrated design concept of (a) 1-layer, (b) 3-winding, and (c) 2-vessel MFT structures. The corresponding bottom figures show the top cross-section views of each structure. PWs are marked with striped patterns, and the SWs in orange.

realization, and so on. However, in this work the optimality is sought-after on the overall MFT level, hence, the optimal winding arrangement is determined based on the highest achievable efficiency of the MFT, keeping in mind the convenience/ease of manufacturing. In combination with the core type MFT structure, three different winding configurations are considered and described in the following sections together with their advantages and disadvantages, as illustrated in **Fig. 3.5**.

Regardless of the winding arrangement, by design, the cold DI water is set to enter each of the windings at the top and exit with a higher temperature at the bottom. In this way, a temperature gradient is formed in the vertical direction along the windings, from the top to the bottom, which contributes to natural convection and enhances oil circulation.

### 3.3.1 1-layer MFT Structure

The first considered winding disposition is the most simple one, and it includes a single layer of the PW and a single layer of the SW placed concentrically around each other. To optimally use the core window area and having in mind the required turns ratio, the first suggested winding disposition implies using different cross-section profiles for the PW and SW, however, fulfilling a constraint that the current densities of the two windings remain equal. Since the SW has twice the value of the PW current, it implies that the SW cross-section area of the conductor is two times the area of the PW conductor. Nevertheless, the inner diameters of both PW and SW conductors remain approximately in a similar range. In this way, the available core window height can be better used for both windings. Yet, the symmetry inside the oil vessel is generally disturbed.

The decision to have only one layer for each winding is explained by the increased complexity of mechanical realization in the case of multiple layers. Namely, the continuous winding of Cu pipes in order to form several layers for PW and SW, considering thereby different external radii for each layer, poses a mechanical challenge. Alternatively, the layers of the same winding could be subsequently electrically connected outside of the vessel. This would, however, require every winding layer to exit the vessel with properly sealed connectors, to avoid oil leaking. Besides increased complexity,

this alternative also implies increased winding resistance, which results in higher winding losses. Therefore, for simplicity reasons, the winding design in the case of 1-layer MFT considers having only one layer each for PW and SW. An alternative name, closer to the standard construction types, for this MFT structure could be *C-type, non-interleaved*.

The structure is shown in **Fig. 3.5a** together with the corresponding top cross-section view. In view of the fact that the PW has double the number of turns and to reduce its length and therewith losses, PW is placed closer to the core limb, i.e. closer to the inner wall of the oil vessel. Such an arrangement significantly contributes to the pressure drop decrease along the winding. The available pressure drop is one of the cooling constraints presented in **Sec. 3.4**. Nevertheless, having the core grounded requires sufficient air distance to be left between the PW terminal outside of the vessel and the core surface. Lastly, an advantage of the 1-layer MFT structure is simple mechanical realization regarding winding termination, compared to the other two suggested dispositions explained in the following.

Introducing a design constraint to use the same conductor cross section for both windings led to the arrangement of three windings in a single oil vessel, which is presented in the following section. To improve the use of space in the vessel, the PW is interleaved around the SW.

### 3.3.2 3-winding MFT Structure

The second considered winding disposition is shown in **Fig. 3.5b**. Thereby, the PW is concentrically interleaved around the SW inside of a vessel, which is placed around one of the core limbs. Compared to the first and the last suggestion (with four windings), the 3-winding MFT structure offers a compact compromise with the improved power density and a total of three windings. On the other hand, a drawback of this structure is that by using the same conductor type for both PW and SW, which is beneficial for optimal use of core window area, suggests the PW current density is two times smaller than the SW one. Bearing in mind that the same cooling conditions are applied to all the windings, the PW conductors are to a certain extent oversized compared to the SW conductors. The necessary turns ratio can be established either internally, inside of the oil vessel, or by an external connection. Lastly, additional attention needs to be paid to keeping the windings in a fixed position, relative to each other and to the vessel walls, which can be done with the help of a supporting system. This applies to all three MFT structures, however, the middle coil, i.e. SW winding, in the case of the 3-winding MFT requires more consideration since it is being surrounded by windings under voltage. Similar to the previous arrangement, the alternative naming for this structure could be *C-type, interleaved*.

### 3.3.3 2-vessel MFT Structure

For this winding arrangement and as the name implies, there are two windings sets (a layer of PW + a layer of SW per set), each placed in one of the two oil vessels, which are positioned around the core limbs, as shown in **Fig. 3.5c**. Thereby, the PW encircles a layer of SW, and both layers in a set have the same number of turns. Compared to the 1-layer MFT, the number of windings is doubled. Nevertheless, in this way, it is possible to use the same conductor type for both PW and SW and by appropriate electrical connection achieve the desired turns ratio. This is accomplished by externally connecting the PWs from the two vessels in series and the SWs in parallel. Moreover, equal current densities are achieved in all the windings, which compared to the previous winding disposition helps restore transformer symmetries, both thermal and electromagnetic, and makes modeling easier. The last presented MFT structure could be differently named as *core type, non-interleaved*.

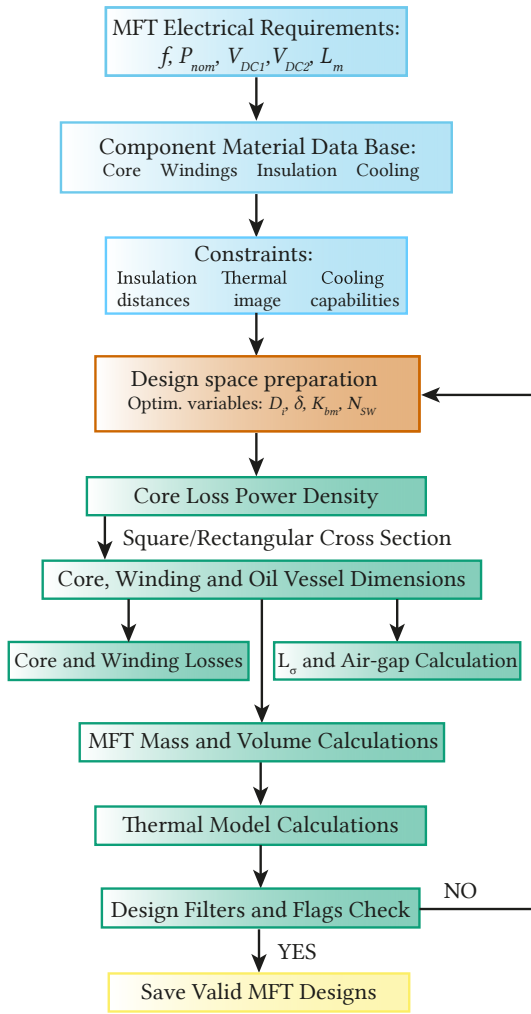
Note that with this winding disposition, a multi-winding transformer is created, with many different usable configurations (15 to be precise) depending on the need and application. They are summarized and provided in **App. C**. However, such a transformer also requires an additional winding termination panel for easier external connection and access to each of the winding conductors. Thus, the practical realization of the windings is significantly more complex compared to the first suggested arrangement, and it also requires more space, which negatively impacts the volumetric power density.

### 3.4 Design Optimization Algorithm

The algorithm employed for the design optimization of high-power MFTs is based on the exhaustive search concept, also known as the brute-force algorithm. As previously mentioned in **Sec. 2.5.6**, this method is relatively fast and simple to implement. A compact overview, i.e. the flowchart of the implemented design algorithm, is given in **Fig. 3.6**, which is an extension of work conducted in [137]. Before the algorithm is described in more detail, it is important to clarify the optimization criterion. When designing any type of magnetic component, a compromise needs to be made between the highest achievable efficiency and maximal power density. In addition, an industry design typically includes investment cost as one of the design optimization goals. However, in this thesis this was not prioritized. Considering the application the DCT is intended for, the MVDC PDNs, the optimization criterion is set on reaching the highest efficiency.

The design process starts by collecting user-defined inputs (denoted with blue), such as electrical requirements (outlined in **Tab. 3.1**), constraints regarding mechanics, insulation, and thermal coordination, as well as general properties of the employed materials. The most relevant constraints are summarized in **Tab. 3.2**. It is possible to imagine that any of the defined dielectric constants can be selected as an additional optimization variable, however, this would result in unnecessary complications in the design process. The current insulation distances are set as low as physically possible without jeopardizing insulation capabilities, and considering the imperfections of the winding process. The last refers to mechanical deformations of the hollow conductors, i.e. imperfectly circular turns, during the manipulation process. Moreover, considering high oil viscosity compared to e.g. water, this fluid requires minimal space to reach all the winding surfaces, and in this way avoids forming of air bubbles inside of the vessels, which according to industrial experience amounts to at least 2 – 3 mm. For the same reason, the turn-to-turn distance is fixed at 3 mm, which excluded this parameter from the set of design variables. Regarding the vertical insulation distance between the windings and the core, the minimum bending radius of the conductor has to be considered (due to necessary winding termination through the vessel lids), which depends on the size of the outer radius of the Cu pipe. Note that the cooling constraints regarding maximal pressure drop and maximal available flow are obtained from the existing WCU and the capacity needs to be shared between the MFT windings and the two RC-IGCT stacks of the power stages. Additionally, the inlet temperature and the volumetric flow of the coolant are set according to the worst cooling conditions, in order to rule out the designs which do not comply with thermal constraints and to have robust MFT designs. The worst conditions imply reaching the pressure drop limit of the DI water cooling unit (achieved with the high volumetric flow, long windings, and small conductor's inner diameter) and having maximal available inlet coolant temperature (30 °C).

In the next step of the design process, marked with orange in the flow chart of **Fig. 3.6**, the design space is formed, where each combination of optimization variables defines a unique MFT design.



Thermal constraints:

Const.	Value	Description
$T_{c, \max}$	150 °C	Max. core temp.
$T_{w, \max}$	130 °C	Max. winding temp.
$T_{o, \max}$	180 °C	Max. oil temp.
$T_{cf, \max}$	70 °C	Max. DI water temp.
$T_{cf, \min}$	10 °C	Min. DI water temp.

Dielectric constraints:

Const.	Value	Description
$d_{pw, sw}$	8 mm	PW to SW distance
$d_{hor}$	10 mm	Hor. distance betw. windings and walls
$d_{vert}$	41 mm	Vert. distance betw. windings and the core
$d_{vv}$	3 mm	Distance betw. vessels
$d_{tt}$	3 mm	Turn-to-turn distance

Cooling constraints:

Const.	Value	Description
$\Delta p_{cf, \max}$	350 kPa	Max. DI water pressure drop
$Q_{cf, \max}$	130 l/min	Max. DI water flow

Design variables:

Var.	Min/Max/Res	Description
$D_i$	4 mm/8 mm/20	Inner diameter
$\delta$	$0.9\delta_{Cu}/2.2\delta_{Cu}/14$	Wall thickness
$N_{SW}$	10/30/21	SW turns No.
$K_{bm}$	0.2/0.9/80	Flux dens. ratio

**Fig. 3.6** Flowchart of the design algorithm. **Tab. 3.2** User-defined thermal, dielectric, and cooling constraints relevant to all three winding configurations, and the selected variables for MFT design optimization with appropriate lower, upper boundaries, and respective resolutions.

The design optimization variables are provided at the bottom of **Tab. 3.2**, together with the lower and upper boundaries and the respective resolutions. The values are accordingly selected to fully explore the design space regarding possible winding geometries and the operating range of the core. The four key selected design variables are the internal hollow conductor diameter ( $D_i$ ) and the corresponding wall thickness ( $\delta$ ), the SW number of turns ( $N_{SW}$ ), and the ratio between the set flux density amplitude and the saturation density magnitude of the considered magnetic material ( $K_{bm}$ ). Thereby, the conductor's wall thickness is defined as the multiple of the frequency-dependent skin depth. One can notice that three out of the four selected design variables directly influence the winding design. Thus, it can be concluded that the winding design has a considerable role in defining the performance of the MFT.

The evaluation part of the optimization process is marked green in **Fig. 3.6**, where all the relevant models are applied to the formed designs. Firstly, in order to estimate core loss density the analytical IGSE [92] is employed, since it provides accurate loss projections for non-sinusoidal voltage excitation. For large cross-section areas of the core, the algorithm is able to consider the production limits of specific core materials, due to size limitations of the manufacturing machines, and branch out to MFT designs with rectangular cross sections. The default option is naturally a square core cross section, due to the optimal use of the inner hollow cylinder area of the oil vessel. Note that this applies to the tape-wound cores, made of amorphous or nanocrystalline materials, and it does not apply to SiFe, where the state-of-the-art manufacturing enables a stepwise approximation of a circular cross-section. Starting with the determined core cross-section size and known winding properties (number of turns and the geometry of conductor's cross section), the remaining core properties and oil vessel dimensions can be deduced. Once the MFT geometry is settled, the core and winding losses can be determined.

Due to the particular selection of the winding type, the well-known frequency-dependent Dowell model cannot be directly applied. Moreover, the analytical loss modeling of round pipe windings is not adequately researched in the literature. Nevertheless, a model is adopted as a combination of the standard Dowell model and a FEM-obtained factor [111], which is able to consider the frequency-dependent AC resistance of pipe conductors. The core and winding loss models are described in detail in **Chap. 6**. The corresponding leakage inductance is estimated based on the magnetic images method [138], and the analytical model is adapted to the number of windings (in the range of 2 – 4) depending on the selected winding disposition. **Chap. 4** deals with the exact implementation and verification. Nevertheless, the selected model is not able to capture the eddy current effect that decreases the value of the leakage inductance at higher frequencies. This is subsequently observed with the help of FEM simulations.

As already mentioned, the magnetizing inductance is determined by the transformer geometry and the core air gap, but also by the turn-off current of the switching devices, due to the resonant operating principle. In the next step, the gravimetric and volumetric power densities are determined. Lastly, each of the generated MFT designs needs to be assessed regarding its thermal perspective, i.e. whether the available surfaces and selected cooling methods are capable of dissipating the generated heat created by the losses. Owing to a particular selection of technologies (active DI water cooling and natural-convection based insulation), an analytical Thermal-Hydraulic Model (THM) is developed along with the static thermal model to aid the estimation of the overall transformer thermal image. The THM describes the thermal behavior of the insulation oil, depending on the winding losses and the cooling conditions. The two models are explained in more detail in **Chaps. 5** and **6**. The necessary models are developed or adapted from previous works found in the literature, verified, and presented in the following chapters. Eventually, designs that pass all the user-defined filters and constraint checks are marked as valid. The specific filters are discussed in **Chap. 7** in more detail. In the final step highlighted with yellow the valid designs are saved into a database.

As one of the novel design filters, the algorithm offers the possibility of influencing the core to winding loss ratio ( $R_{wc}$ ) during the design phase. In this way, due to the availability of aggressive DI water cooling, the majority of the losses can be forced to the windings, if it shows to be advantageous from the optimization perspective. To reduce design complexity, many parameters are set to constant values, such as the wall and lid thickness of the oil vessels. The two values, along with the vessel material, are determined together with the manufacturer (Elektro-Isola [139]), considering the weight

of the contained oil and windings and the highest temperatures that can be reached.

### 3.5 Summary

In this chapter, the electrical requirements for the design of 1 MW MFT are highlighted, based on the design of a DCT framework that the MFT is an integral part of. Moreover, the converter design further conditioned the use of forced convection with DI water as the winding cooling method. From the plethora of options presented in **Chap. 2**, a selection of materials and technologies for the MFT design is made, which is further studied and modeled together in the coming chapters of the thesis.

According to initial studies of the three presented winding arrangements, the 2-vessel, and the 3-winding MFT structures outperform the 1-layer option regarding the efficiency criterion. Furthermore, considering the previous discussion presented in **Sec. 3.3**, the 2-vessel MFT is selected to be the focus of the rest of the thesis work. Some of the main reasons include:

- Higher versatility of the 2-vessel option, which offers 15 different configurations depending on the external connection of the four available windings, while this is not the main objective of the work, it offers interesting prospects for the future research activities;
- Improved thermal and electromagnetic symmetry, considering all the windings have the same conductor's cross section. For the analysed 2:1 turns ratio configuration, this implies the same current densities of both windings, which additionally supports modeling;
- Less challenging manufacturing compared to the 3-winding MFT structure.

This further implies that the relevant models introduced in the coming chapters are developed predominantly for the 2-vessel structure.

Finally, based on the flowchart of the design optimization algorithm, the MFT design process is explained in more detail. All the relevant constraints and design variables are catalogued and accounted for. The missing models for a complete design optimization process are identified and explained in more detail in the following chapters.



# 4

## MFT Leakage Inductance Modeling

*As stated previously, achieving the appropriate leakage inductance value is important for the correct operation of the LLC-SRC converter. Therefore, accurate modeling is imperative. For this purpose, an analytical model based on the method of magnetic images is employed, which is however frequency-independent. The frequency effect is subsequently considered with the help of FEM simulations. In addition, the influence of the relative PW position to SW on the leakage inductance is experimentally investigated on the MFT prototype windings, and the results are presented.*

### 4.1 Introduction

The leakage inductance models and quantifies the amount of magnetic field that does not participate in the magnetic coupling of the windings. In the case of transformers, the leakage field leaves the core and closes the loop through the air. In this way, certain magnetic energy gets stored in and around the windings, which is represented and typically modeled by a series leakage inductance for each winding of the transformer. The values need to be determined and controlled, since for some applications high leakage inductance values can be damaging and lead to overvoltages. The leakage inductance value depends on the magnetic field distribution, the overall winding geometry, and frequency. The value can be reduced with various interleaving methods, which reduce the number of consecutive layers of the windings and in this way reduces the frequency effect caused by proximity.

For correct operation of the selected resonant converter topology, the windings' intrinsic parameters, such as leakage and magnetizing inductance, have to match the needs of the converter and fall in a certain range. This is important considering the fact that for the selected topology, the two characteristic inductances make a larger part of the resonant tank. In the previous chapter, the range is clearly defined in **Tab. 3.1** for both parameters. The leakage inductance value is determined by the windings' geometry, i.e. by the magnetic energy stored primarily in the interwinding space, whereas the magnetizing inductance is additionally influenced by the core geometry. Consequently, accurate and reliable models are necessary to model the relevant inductances.

As shortly mentioned in **Chap. 2**, there are several ways transformer leakage inductance can be estimated, such as numerical methods aided with FEM software [140]–[142], which are very accurate but time consuming and heavy on resources, and thus, not adequate for design optimization algorithms. Reluctance network modeling, also known as magnetic equivalent circuit [143], is a faster method suitable for iterative design procedures, but not as accurate as the first method. It is based on the analogy with electric circuits, as shown in **Tab. 2.1a**, and draws conclusions from the well-known circuit analysis. Lastly, the analytical methods are both fast to compute and suitable for design optimization tools. A thorough and detailed comparison of analytical and semi-analytical leakage inductance estimation methods can be found in [144], [145]. The models are compared to each other

based on the accuracy and computational effort, whether they are 1D or 2D, i.e. whether the fringing flux is considered, or whether they can take into account the frequency-dependence of the leakage inductance and some other properties.

Regardless, a standard method of obtaining an analytical expression for the leakage inductance is by integrating the magnetic energy resulting from the leakage magnetic field in and around the windings, under the assumption of zero magnetizing current. This is achieved in the case when the transformer is supplied with two currents of opposite directions whose ratio corresponds to the turns ratio, i.e. the total current in the core window area is zero and the magnetic energy is solely stored in the leakage inductance. Thereby, the magnetic energy can be determined from the integration of the magnetic field ( $H$  [A/m]) or by the product of the vector potential ( $A$  [Wb/m]) and the current density, which is given by the following:

$$W_m = \frac{1}{2} \iiint \mu \vec{H}^2 dV, \quad W_m = \frac{1}{2} \iiint \vec{A} \cdot \vec{J} dV \quad (4.1)$$

In the case of magnetic field integration, the integration domain extends infinitely, whereas, in the case of vector potential integration, it is limited to the cross section of the conductor with non-zero current density ( $J$  [A/m<sup>2</sup>]). The latter path bounds the integration domain to the conductor cross section, which in general simplifies the model derivation. Lastly, the total leakage inductance referred to the primary side is obtained from the following relation:

$$W_m = \frac{1}{2} L_\sigma I_1^2 \quad \Rightarrow \quad L_\sigma = \frac{2W_m}{I_1^2} \quad (4.2)$$

From the 1D models, Dowell's model [106] is the one that has been attracting a lot of attention since its introduction in 1966 for ideal foil windings and based on the solution of Maxwell equations in two dimensions. By acquiring closed analytical expressions for the magnetic field distribution within the core window, it is able to provide closed-form estimations of AC winding resistance and leakage inductance. To account for other winding types different than foil, a porosity factor is added. The wide use of this model is due to the fact that it is able to consider the frequency influence.

In the case of 2D models, the method of magnetic images from [146] is usually employed as a base. The idea is to replace the magnetic material with current sources located on the magnetic side, symmetrical to the winding currents in the core window area. The magnitude of the mirrored current is set to preserve the initial magnetic field around the windings. They are more accurate than 1D models, however, their main drawback is that they are frequency-independent. Noticeably, more complex 2D models are predominantly static or valid for low frequencies, where the eddy-current effect can be neglected, and the current density is uniform in the conductors. The following two sections present a 1D and a 2D model in more detail and provide a comparison.

Note that compared to analytical/theoretical modeling of winding losses, i.e. AC resistance of windings, the leakage inductance modeling has received less interest. As a result, Dowell's model is the only one able to consider the frequency effect. Otherwise, the value is generally estimated with FEM analysis.

## 4.2 1D Dowell's Model

As already mentioned in **Sec. 2.5.3** for the winding loss modeling, the original Dowell model was developed for ideal foil windings assuming the conductors occupy the full core window height, which

implies the magnetic field is one dimensional inside the window area, and an infinite permeability core material. For the leakage inductance estimation, the model provides a frequency-dependent expression that describes the magnetic energy portion within the windings, and frequency-independent expressions, which account for magnetic energy in the dielectric space between the windings and between the layers of each winding. The magnetic energy in the windings is frequency dependent, due to the skin and proximity effects and this is represented by Dowell's frequency-dependent factor ( $F_L$ ), which can quantify the influence of both eddy-current effects. A complete model derivation can be found in [47], [137].

All the used variables in the closed-form analytical expression for the leakage inductance are illustrated in the transformer example in **Fig. 4.1**. It is assumed that the MFT has a single primary and a single secondary winding. In the case of multi-winding transformers, the equations can be easily extended. The figure shows the required adaptation of the winding structure, from the original MFT winding, made of round hollow conductors, given on the left, to the equivalent foil conductors on the right, which represent the basis of Dowell's winding model. Below each of the transformer sections a corresponding magnetic field in  $x$  direction is given, assuring the same distribution is preserved. The parameter  $H_w$  gives the height of the core window area.

In order to obtain the  $L_\sigma$  expression, Dowell combined the theoretical expressions of the magnetic field inside of the core window with equations (4.1) and (4.2). The initial expression for ideal foil windings is adapted to round solid windings, by modifying the argument  $\Delta$  (to  $\Delta'$ , defined later in the text), and it is given below:

$$L_\sigma = \mu_0 N_{pw}^2 \frac{MLT}{H_w} \left[ \underbrace{\frac{d_{pw,eq} m_{pw}}{3} F_{L1} + \frac{d_{sw,eq} m_{sw}}{3} F_{L2}}_{\text{Frequency-dependent component due to the magnetic energy stored within the windings}} + \underbrace{d_{pw,sw}}_{\text{Component due to magnetic energy in the inter-winding dielectric space}} + \dots \right. \\ \left. \dots + \underbrace{d_{pw,i} \frac{(m_{pw} - 1)(2m_{pw} - 1)}{6m_{pw}}}_{\text{Component due to magnetic energy in the inter-layer dielectric of the PW}} + \underbrace{d_{sw,i} \frac{(m_{sw} - 1)(2m_{sw} - 1)}{6m_{sw}}}_{\text{Component due to magnetic energy in the inter-layer dielectric of the SW}} \right], \quad (4.3)$$

with Dowell's frequency factor  $F_L$  and the corresponding coefficients  $\varphi_1$  and  $\varphi_2$ :

$$F_L = \frac{1}{2m^2 \Delta} [(4m^2 - 1)\varphi_1 - 2(m^2 - 1)\varphi_2], \quad \varphi_1 = \frac{\sinh(2\Delta) - \sin(2\Delta)}{\cosh(2\Delta) - \cos(2\Delta)}, \quad \varphi_2 = \frac{\sinh(\Delta) - \sin(\Delta)}{\cosh(\Delta) - \cos(\Delta)} \quad (4.4)$$

Thereby,  $N_{pw}$  is the number of turns in the PW, MLT is the respective mean length turn of the windings, and the expression describes leakage inductance referred to the primary transformer side.

Equation (4.3) clearly differentiates between different parts contributing to the leakage inductance value. The frequency-independent components depend on the dielectric distances and the number of layers, as well as the conductor thickness of each winding. Regarding the frequency-dependent component which is determined by the factor  $F_L$  from (4.4), the argument of the coefficients is known as the penetration ratio

$$\Delta = \frac{d_{x,eq}}{\delta_{Cu}}, \quad (4.5)$$

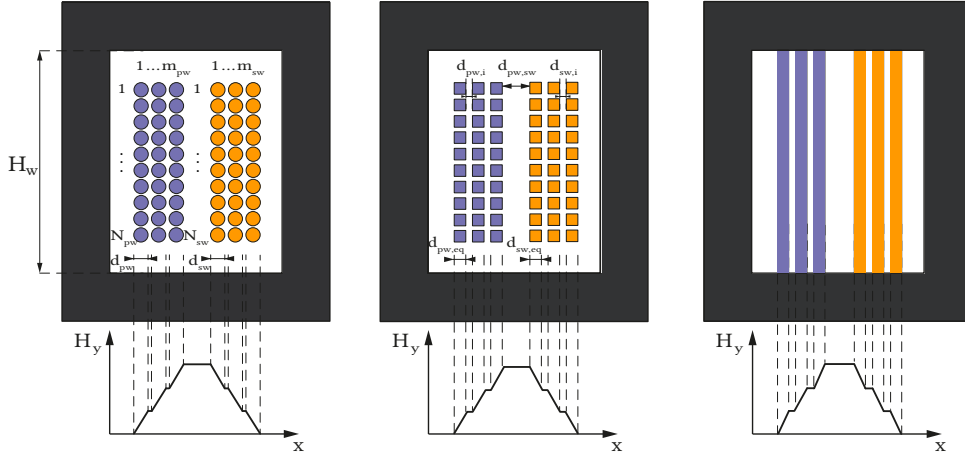


**Fig. 4.1** Winding equivalence with corresponding magnetic field distribution showing the necessary transformation from round solid wires in several layers per winding, over equivalent squared wires, to equivalent foil conductors covering the whole core window height. The field distributions correspond to low penetration ratio values ( $\leq 1$ ).

where  $d_{x,eq}$  is the equivalent foil winding width of the PW or SW, and the parameter  $\delta_{Cu}$  describes the Cu skin depth at the operating frequency.

To enable the application of Dowell's model to some other winding types, such as round solid conductors shown in **Fig. 4.1**, a porosity factor  $\eta$  was introduced. Its purpose is to ensure that an equal magnetic field is generated along an enclosed path for the two different winding types and that the correct DC conductor resistance is provided. Correspondingly, the winding porosity factor represents the ratio of the actual layer copper area to the effective foil conductor area, and it is determined by the following

$$\eta = \frac{N_x d_{x,eq}}{H_w} \quad \text{with} \quad d_{x,eq} = d_x \sqrt{\frac{\pi}{4}}, \quad \text{where } x \text{ can replace PW or SW.} \quad (4.6)$$

The parameter  $d_x$  gives the diameter of the round solid conductor of PW or SW, whereas  $d_{x,eq}$  stands for the equivalent diameter of the squared solid conductor, as well as the equivalent thickness of the foil winding. Lastly, the introduction of the porosity factor has an influence on the penetration ratio as well, which is expressed in the following relation

$$\Delta' = \Delta \sqrt{\eta}. \quad (4.7)$$

A review study on existing development and extension of Dowell's model from [47] showed that the above presented model holds a good accuracy for tightly packed windings (considered to be the case for  $\eta > 0.7$ ) and when the conductor's diameter is in the range of the skin depth ( $\Delta \approx 1$ ).

### 4.3 2D Margueron's Model

In contrast to the considered 1D magnetic field (only axial leakage field assumed) in the previous model, some models [138], [147]–[149] take into consideration flux fringing at the top and the bottom

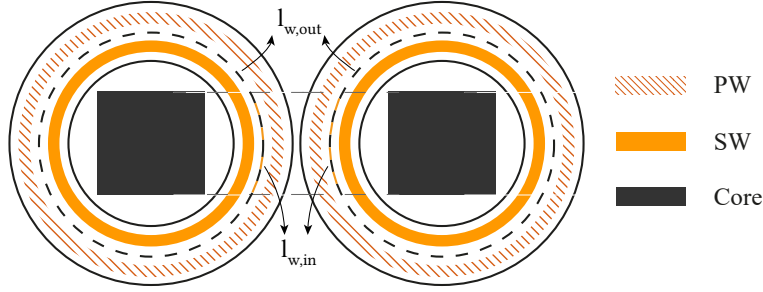


**Fig. 4.2** Illustration of partial winding MLT inside and outside of the core window area for 2-vessel MFT.

of the windings, that is the radial field component. Such models are characterized as 2D models and they provide higher accuracy.

Moreover, in recent publications [150]–[152], the so-called Double-2D modeling concept is adopted, which considers separate estimation of the per unit length leakage inductances in the inside core window and the outside core window area, marked with IW and OW, respectively. Based on the respective partial lengths of the windings,  $l_{w,in}$  for IW and  $l_{w,out}$  for OW, which are illustrated in **Fig. 4.2** on the example of 2-vessel MFT structure, the total leakage inductance is obtained with the following relation

$$L_{\sigma} = L'_{\sigma,IW} \cdot l_{w,in} + L'_{\sigma,OW} \cdot l_{w,out}. \quad (4.8)$$

Note that the sum of the partial lengths corresponds to the average MLT value of the PW and SW.

The 2D leakage inductance model presented in this section is of analytical nature and was developed by Margueron et al. [138], which utilizes the method of magnetic images from [146]. The idea is to replace the magnetic material of high permeability with current sources located on the magnetic side, symmetrical to the winding currents in the core window area. Thereby, the current magnitude is set to preserve the initial magnetic field in the air. In this way, the method is able to capture the effect of the transformer core on the leakage inductance. Transformer windings are modeled as rectangular blocks, regardless of the winding type. **Fig. 4.3** provides the illustration of the magnetic image method for both OW and IW winding parts, and for illustration purposes, the total number of windings is set to two. The similar illustration for the 2-vessel MFT from **Fig. 4.2** would have four windings inside of the core window area (IW). Thereby,  $m$  and  $n$  are indices of the mirrored windows in the  $x$  and  $y$  direction, relative to the original one ( $m = 0, n = 0$ ). The width and height of the core window are marked with  $B$  and  $C$ , the distances of the winding centers from the coordinate system origin (lower left corner of the IW) are marked with  $d_{xi}$  and  $d_{yi}$  for the winding  $i$ . Note that in the core window area, the mirroring effect can be applied indefinitely. However, in practice, it is sufficient to take into account a limited number of images, typically the 8 images from the first layer ( $m = \pm 1, n = \pm 1$ ) surrounding the core window [138]. The field of the mirrored currents for  $|m| > 1, |n| > 1$  significantly reduces, since they are located further from the original core window and can be neglected. Thereby, the corresponding current density of each winding is determined based on the number of turns and the winding cross-section area:

$$J_k = \frac{N_k I_k}{A_k} \quad (4.9)$$

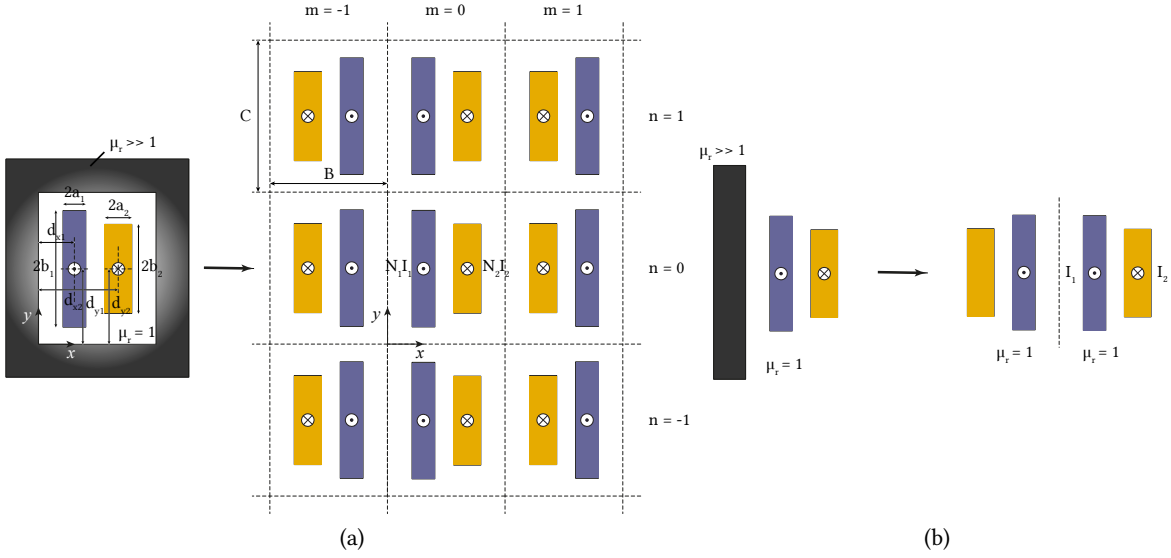


**Fig. 4.3** Magnetic image method applied to PW and SW conductors (a) inside and (b) outside of the core window area. The distances between the windings and the coordinate system origin are marked in (a), as well as the respective sizes of primary and secondary winding blocks.

Additionally, the presented model allows us to consider finite core permeability  $\mu_r$ , which has an effect on the mirrored current compared to the original current value. The effect is represented by a scaling factor, defined in the following:

$$I_{\text{image}} = \frac{\mu_r - 1}{\mu_r + 1} I_{\text{original}} \quad (4.10)$$

Explicit equations, which are derived for  $L'_{\sigma, \text{IW}}$  and  $L'_{\sigma, \text{OW}}$  based on the complete analytical static leakage inductance calculation from [138] and for the MFT shown in **Fig. 4.3**, are presented in the following. The total magnetic leakage energy per length is defined as:

$$W'_m = -\frac{\mu_0}{8\pi} \sum_{i,j=1}^2 J_i J_j M_{i,j}, \quad (4.11)$$

with  $M_{i,j}$  determined by the following expression

$$M_{i,j} = \sum_{k=0}^{15} (-1)^d \sum_{m,n=-1}^1 \left( \frac{\mu_r - 1}{\mu_r + 1} \right)^{|m|+|n|} G(X, Y). \quad (4.12)$$

The arguments,  $X$  and  $Y$ , of the function  $G$  are defined in the following:

$$X = d_{xj} - (mB + (-1)^m d_{xi}) - (-1)^{d_3} a_i - (-1)^{d_2} a_j, \quad Y = d_{yj} - (nC + (-1)^n d_{yi}) - (-1)^{d_1} b_j - (-1)^{d_0} b_i \quad (4.13)$$

The above equation applies to the IW part of the leakage inductance, whereas for the OW, the  $n, m$  parameters need to be adjusted, namely, to  $n = 0$  and  $m = -1, 0$ . Coefficients  $d_0 - d_3$  give the binary representation of  $k$ , with  $d_0$  as the least significant bit, and their sum corresponds to  $d$ , i.e.  $d = d_0 + d_1 + d_2 + d_3$ .

The function  $G(X, Y)$  is defined as below:

$$G(X, Y) = -\frac{1}{24} (X^4 - 6X^2Y^2 + Y^4) \ln(X^2 + Y^2) + \dots \\ \dots + \frac{XY}{3} \left[ X^2 \arctan\left(\frac{Y}{X}\right) + Y^2 \arctan\left(\frac{X}{Y}\right) \right] - \frac{7X^2Y^2}{24} \quad (4.14)$$

In the case of singularities ( $X = 0, Y = 0$ ), the  $\ln$ - and  $\arctan$ -terms are set to zero.

To summarize, the presented model combines estimation of the inside ( $L'_{\sigma, IW}$ ) and outside ( $L'_{\sigma, OW}$ ) leakage inductance values per unit length, based on the equations (4.2), (4.11) and (4.13), due to the fact that in the core type MFT certain winding portions lie outside of the core window area. The total leakage inductance is obtained by summing the two leakage inductances weighted with the correct length. Analytical expressions derived from [138] for the 2-vessel MFT structure are not provided explicitly. However, note that the applied model is able to determine only the static values of the inductance, i.e. it is valid for low frequencies where the eddy-current effect is negligible and it can be assumed that the current density is uniform in the conductor. Due to the current density and magnetic field redistribution inside and around the conductors at elevated frequencies, the stored magnetic energy reduces together with the resulting leakage inductance. This effect can be quantified by FEM simulations.

Lastly, some of the latest literature [151], [153] on leakage inductance estimation shows models which can separately consider and model curved winding sections, as well as transitioning regions between inside and outside of the core. They are indeed (slightly) more accurate but at the price of significantly increased complexity, as well as implementation.

#### 4.3.1 Model Validation

The model verification is performed with the help of FEM simulations performed with COMSOL, by utilizing the winding structure considered for the design of the 1 MW MFT prototype, which is presented in **Chap. 7**, and it is taken as an example. **Tab. 4.1** shows the per-length leakage inductance values from inside and outside of the core window area, as well as the total leakage inductance value at 0 Hz. It offers a comparison between the analytical results and 2D FEM results for the modeled and selected winding type, i.e. hollow conductors. FEM 2D foil simulation models the windings as rectangles, whereas FEM 2D pipe uses perfect helices, which match the reality better. Note that both 2D models are obtained as vertical cross sections of the corresponding 3D models, and are selected as a verification method in order to save computational time and effort compared to the 3D models.

	Analytical model	FEM 2D foil	FEM 2D pipe
$L'_{\sigma, IW}$ ( $\mu\text{H}/\text{m}$ )	43.12	42.59	44.53
$L'_{\sigma, OW}$ ( $\mu\text{H}/\text{m}$ )	41.15	40.97	42.81
$L_{\sigma, \text{tot}}$ ( $\mu\text{H}$ )	43.8	43.71	45.94

**Tab. 4.1** Comparison of the analytical leakage inductance values with FEM simulation results for 2-vessel MFT structure.

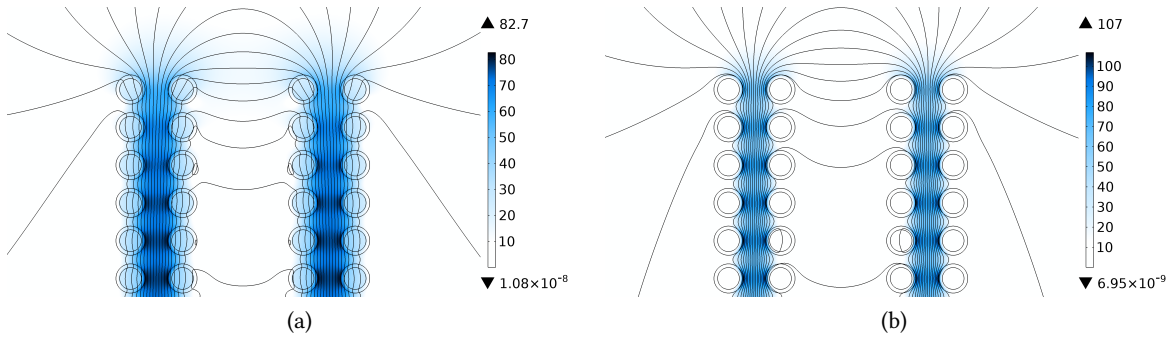


**Fig. 4.4** COMSOL simulation results of leakage magnetic field inside of the core window area with hollow conductors at (a) 0 Hz and (b) 5 kHz. The color legend shows the leakage field intensity inside the core window.

Overall, a good match can be observed between the theory and simulations. Yet, the analytical model slightly underestimates the leakage inductance when compared to the simulated pipe windings.

**Fig. 4.4** shows the distribution of the magnetic leakage field in the core window area of the 2-vessel MFT at 0 Hz and 5 kHz for pipe windings, presented with the color legend. The field is generated by currents of 1 A magnitude in all windings in the correct directions. The contour lines correspond to the magnetic vector potential  $A$  in  $z$  direction. By comparing the two figures, one can observe the effect of the magnetic field being suppressed from the conductors at the elevated operating frequency, thus resulting in a lower value of the leakage inductance. Lastly, simulation results at the operating frequency presented in **Tab. 8.4** show a leakage inductance value reduction of approximately 25 % compared to the value from **Tab. 4.1**, which is not negligible and should be adequately modeled.

#### 4.4 Sensitivity Analysis

Having in mind that for the valid operation of the LLC-SRC converter, the leakage inductance needs to be closely targeted, a study is conducted to examine the sensitivity of this intrinsic value to the position of PW and SW terminations relative to each other. Additionally, the effect of vertical disposition, bigger than the one resulting from an angle difference in PW and SW terminations, between the windings is observed. The analysis is performed with the core and a set of PW and SW, which are designed and manufactured to be a part of the final MFT prototype. Thereby, the PW is wound regarding the right chirality, whereas the SW is wound conversely, according to the left chirality, i.e. clockwise. According to the dot convection, the two windings are of inverse polarity. More details about the windings of the complete MFT prototype are provided in **Chap. 8**.

**Fig. 4.5a** shows the developed setup to measure the sensitivity of the leakage inductance at the PW side, in response to slight changes in the relative angular position of PW to SW. For this purpose, a single winding set is observed, made of one layer of PW and one layer of SW with the same number of turns and wound with the same Cu pipe. To observe the influence, the position of SW is fixed, whereas the PW can rotate around the SW in steps of  $5^\circ$ , reaching from  $0^\circ$  to  $245^\circ$ . The PW rotation ability is limited to  $245^\circ$  due to the horizontal top and bottom core parts that prevent the winding terminations to continue rotating. To enable its rotational movement, the PW is fixed to a plexiglass ring, which is able to rotate around one of the core limbs. The ring is calibrated with  $5^\circ$  markings and functions as a protractor. Thereby, parallel terminations of both windings correspond to the angle of



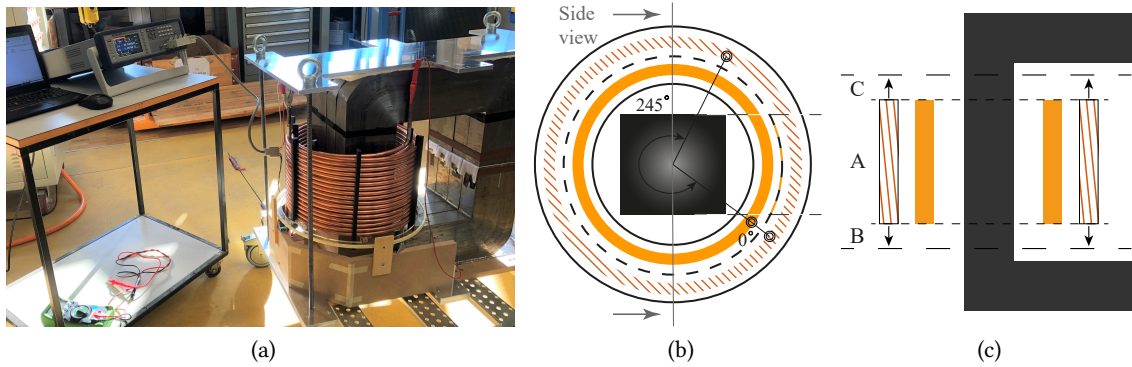


**Fig. 4.5** (a) Test setup used to study the sensitivity of the leakage inductance depending on the relative angular position of PW to SW. (b) A top cross-sectional view of the one-half of the considered 2-vessel MFT. Winding terminations are illustrated with round pipe cross sections. (c) Front side view of one-half of the MFT. A, B, and C mark the relative positions of PW to SW, corresponding to 0 cm, -1 cm, and +1 cm, respectively.

0°, whereas the upper limit angle corresponds to the terminations being at the opposite sides of the core, as illustrated in **Fig. 4.5b**.

Regarding the study of the vertical disposition of the windings, three different PW to SW arrangements are observed, which are illustrated in **Fig. 4.5c**, and those are namely:

- A) PW and SW are at the same height;
- B) PW is set 1 cm lower than SW;
- C) PW is 1 cm higher than SW.

To visualize the effect of the relative termination positions between the PW and SW, **Fig. 4.6** is introduced. There, three relative positions are illustrated, namely, 0°, 90°, and 180° in the clockwise direction, between the first two turns of both PW and SW and their upper terminations. As mentioned above, the SW winding remains fixed, whereas the PW is able to rotate around. For illustration purposes, the 0° alignment between the terminations is placed perpendicular to the frontal core side and corresponds to the side view, shown in **Fig. 4.5b**. However, note that this is only for illustration purposes since the 0° alignment between the windings is placed close to the core window area, as indicated in **Fig. 4.5b**. According to **Fig. 4.6**, as the angle between terminations increases, one can

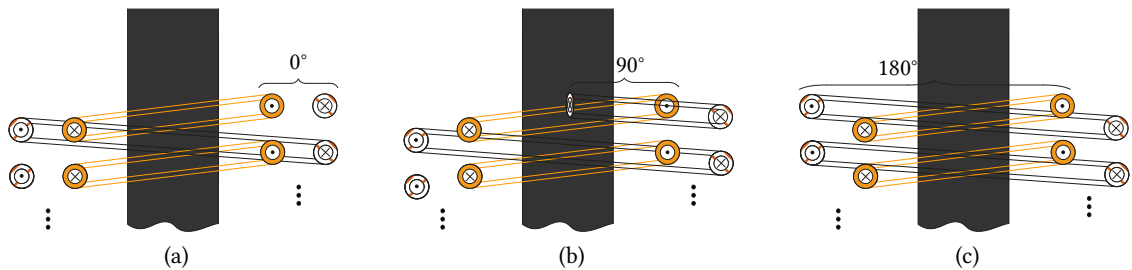


**Fig. 4.6** Illustration of differences in the relative position between the PW and SW considering an angle of (a) 0°, (b) 90°, and (c) 180°.

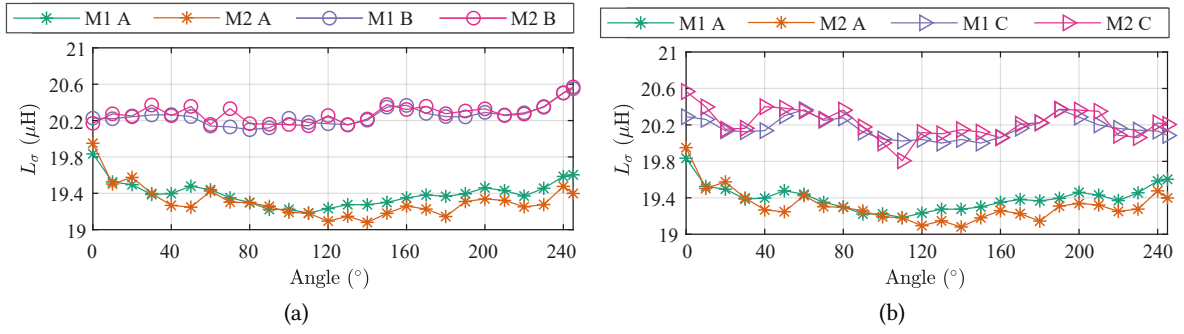


**Fig. 4.7** Influence of PW to SW relative position on the leakage inductance in the case when (a) PW is set 1 cm lower (case B) and (b) 1 cm higher than SW (case C). The orange and green show measurements when the PW and SW are at the same height, which corresponds to case A from **Fig. 4.5c**. They are repeated in both graphs for comparison purposes.

notice the change in relative position in the vertical direction between the turns of the two windings.

To perform the measurements, two different measuring devices are used, namely, an RLC meter (BK895), which measures impedances at fixed frequencies (marked as measuring method  $M_1$ ), and an impedance analyzer Bode 100 by Omicron Lab (marked as  $M_2$ ). The measuring frequency for both devices is set to 5 kHz. **Fig. 4.7** shows the measuring results for the three selected cases. Note that the values in the graphs do not correspond to the total leakage inductance of the final MFT prototype, since only a single set of PW and SW is observed. The first observation from **Fig. 4.7** is that the measurements performed with two different devices give matching results. Regarding the leakage inductance sensitivity to a change in angle, i.e. position between the PW and SW terminations, which contributes to slight vertical deviation in windings' heights, no significant dependency can be observed. Yet, slight ripples in the inductance value (below 1  $\mu\text{H}$ ) are detected as the angle increases, which can be ascribed to measurement errors. Lastly, the results of cases B and C exhibit very similar values, which is to be expected since the windings' surfaces overlap approximately to the same extent, regardless of whether PW is lifted higher or lower for the same amount.

It can be concluded that, in the case when the windings are at the same window height, the resulting leakage inductance value does not depend on the relative angular position of the PW to SW terminations, i.e. the overall effect is not relevant. This offers a degree of freedom when placing and orienting the windings inside of the vessel and in regards to the core. This is important since the windings need to be isolated from the core through the air, once they exit the oil vessel, and for this sufficient distance needs to be kept. The required insulation distances between the core and the windings are discussed in **Chap. 8**. Secondly, for higher values of vertical windings' disposition, higher leakage values are obtained, due to larger leakage field resulting from the misalignment of the windings. Similarly, the relative change in PW and SW terminations has no significant effect even for windings at different heights.

## 4.5 Summary

In this chapter, analytical modeling of leakage inductance is presented. In that respect, two models are presented, namely, 1D Dowell's model, which is capable of including the frequency-dependent effect,

and the 2D Margueron's model, which is valid for uniform current densities and low frequencies. The first model has very limited validity when applied to any other than foil windings, whereas Margueron's model can adjust and also offers higher accuracy, due to consideration of the radial magnetic field. This second model is based on the magnetic images method and can be adapted for any number of windings. It shows a good agreement with the values obtained through FEM simulations. Therefore, it is the one that is integrated into the MFT design optimization algorithm. However, it is not able to consider the reduction in leakage inductance value due to eddy current effects. In this regard, the model can be completed with additional FEM simulations at the desired operating frequency. The chapter ends with an experimental study of the relative position of the windings' terminations on the leakage inductance value. Additionally, the influence of a notable vertical disposition between the windings on the same electrical parameter is observed.



# 5

## Thermal-Hydraulic Model for Oil-Immersed Water-Cooled MFT Windings

*In this chapter, the details regarding the derivation and validation of the thermal-hydraulic model are presented. It is developed to estimate relevant characteristic oil temperatures, subject to the operating conditions of the MFT and the water-cooling unit, as well as to verify oil movement as a result of natural convection. The model is of analytical nature, derived based on energy and mass conservation, and pressure equilibrium in closed oil loops. To finalize the model, thermal oil measurements from a down-scaled vessel prototype are used to characterize and determine the missing model parameters.*

### 5.1 Introduction

As already emphasized throughout the thesis, thermal coordination, including constraints regarding operational temperatures, is an important limiting factor for transformer design. Therefore, it is crucial to be able to correctly estimate temperature distributions across the transformer, with a particular interest in the temperatures of the core and windings. The THM presented in this chapter helps determine the oil temperature distributions, useful for thermal modeling and coordination of the MFT designs with oil-immersed windings. Additionally, the model outputs average oil velocities, that form in steady state along different oil circulation paths in the vessel.

The way the windings are cooled has a strong impact on the thermal behavior of the whole MFT. To

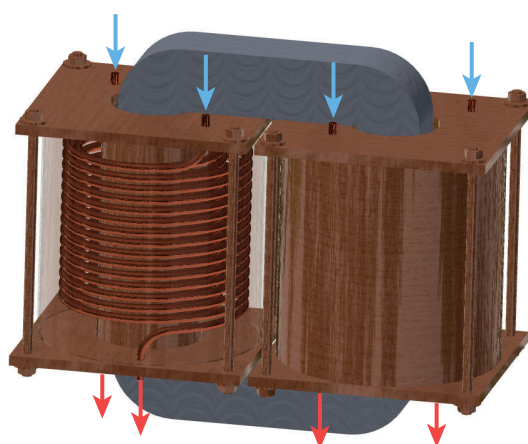


**Fig. 5.1** 2-vessel MFT with the indicated inlet of cold (blue) and outlet of warm (red) DI water.

optimize heat extraction during operation, the cold DI water from the WCU enters the windings at the top of each vessel (indicated with blue arrows in **Fig. 5.1**) and exits with an increased temperature at the bottom (indicated with red arrows). Due to existing winding losses and the way the WCU is connected to the inlets and outlets, a temperature gradient is formed vertically along the windings, with the conductors being colder at the top and hotter at the bottom. An important influence factor on the temperature gradient value is the cooling condition, which is described by the inlet temperature of the coolant, as well as its volumetric flow value and maximum allowed pressure drop. The last is defined by the WCU. Furthermore, owing to the vertical temperature gradient and acknowledging that a certain fraction of the winding losses will be exchanged with the surrounding oil, the natural circulation of oil can be achieved. The underlying heat exchange mechanism is natural convection. One should note that while DI water is selected as the main cooling method for the windings, the THM model describes the thermal problem inside the oil vessel and not inside the hollow conductors.

Regarding relevant literature, models similar to THM have been already developed for large distribution power transformers with different types of oil cooling (natural or forced) and predominantly disc transformer windings, as presented in [121]–[123]. Apart from fully oil-immersed large power transformers, the author has not found further relevant references to related models. One of the key differences compared to the existing models, however, is the fact that for large power transformers the oil is used not only for its insulation capabilities but also to provide adequate cooling. In this work, the oil is mainly selected to provide insulation and increase power density, but also due to its self-healing properties which are of crucial importance in case of partial discharges. Thus, the oil is not employed for cooling purposes of the windings.

The model is developed for the 2-vessel MFT structure, and it can be easily adjusted for the 1-layer MFT. However, in the case of 3-winding MFT, additional flow paths are present, which would increase the number of oil temperatures that are of interest, as well as relevant equations. Due to the symmetry of the 2-vessel MFT, it is sufficient to observe only one of the oil vessels.

## 5.2 Model Development

The presented model is analytical and it consists of two parts:

- Thermal part, which deals with heat exchange phenomenon following the principles of conservation of heat and mass;
- Hydraulic part, which is determined based on the pressure equilibrium established in identified closed loops in which oil circulates.

For both model parts laminar oil flow is assumed and only the steady-state operation is considered. To simplify model derivation, helical pipe windings are approximated with foil windings. **Fig. 5.2a** illustrates the 2D cross-sectional axis-symmetric front view of a single oil vessel containing the simplified winding representations, whereas **Fig. 5.2b** shows its top view cross section. Thereby, the axis of symmetry is presented by the red dashed line in the middle. The left and the right vessel side in **Fig. 5.2a** show many different parameters relevant to the THM derivation, nevertheless, the two sides are exactly symmetrical regarding their physical representation. The SW, with an average temperature  $T_{w2}$  [°C], is set closer to the inner wall of the vessel, which is usually occupied by the core limb (not explicitly shown in the figure) and the surrounding air. The PW is placed concentrically around the SW, closer to the outer vessel wall, and takes an average winding temperature  $T_{w1}$ . The

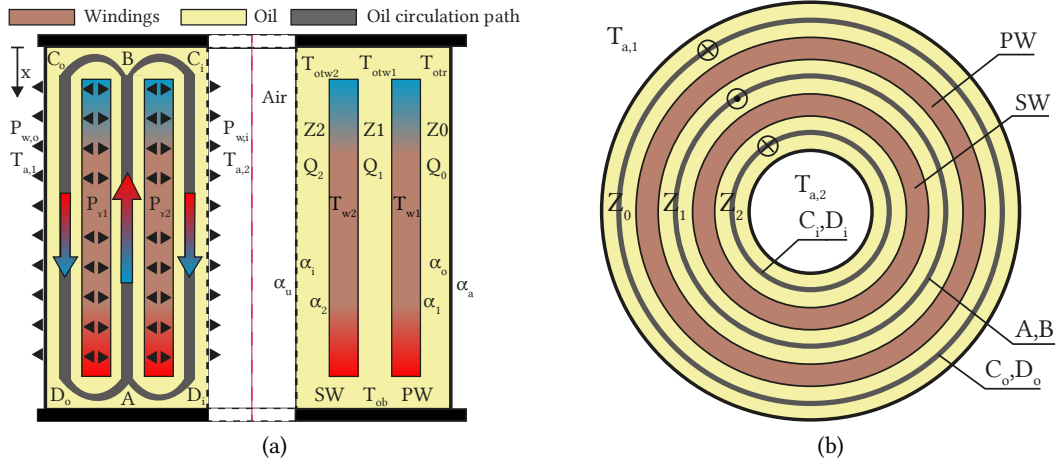


**Fig. 5.2** (a) 2D front and (b) 2D top view of an oil vessel with foil windings, used as a simplification of pipe windings. Blue and red colors in (a) indicate respectively lower or higher temperatures of copper or oil. The position of four characteristic oil temperatures ( $T_{otr}$ ,  $T_{otw1}$ ,  $T_{otw2}$ ,  $T_{ob}$ ) is given in (a).

two average temperatures are determined based on the Cu pipe temperatures measured or estimated at the top and bottom turn, once they exit the oil vessel.

In the steady state PW and SW release in the surrounding oil the losses  $P_{\gamma 1}$  [W] and  $P_{\gamma 2}$ , respectively, which represent a small portion of the total winding losses. The rest of the losses are being extracted by DI water, applied internally for the cooling of the conductors. The estimation is based on the DI water temperature data entering and exiting the winding, as well as the information about the injected losses. This point is explained in more detail later in the chapter. Moreover, the model considers two different ambient temperatures,  $T_{a,1}$  and  $T_{a,2}$ , which correspond to the air temperature outside the oil vessel and inside its inner wall. As illustrated in **Fig. 5.1** in the case of a functional MFT, the inner space of the vessel is occupied by a core limb, which is expected to have increased temperature due to core losses. Furthermore, the model is able to consider exact winding arrangements inside of the vessel, so that different insulation distances are included allowing to observe the geometry impact on the oil temperature and velocity distribution.

As previously mentioned, owing to the existing vertical temperature gradient along the windings, natural convection of oil is achieved. This is visualized with the blue and red color of foil windings in **Fig. 5.2a**, respectively. The increased temperature at the bottom causes the surrounding oil to warm up, leading to a decrease in mass density and oil expansion. As a result, two distinct oil paths can be observed:  $ABC_0D_0A$  and  $ABC_iD_iA$ . The points A, B,  $C_i$ ,  $C_0$ ,  $D_i$ , and  $D_0$  are selected as characteristic points in which the oil temperature is of interest. In fact, points A,  $D_i$ , and  $D_0$  belong to concentric circles (when observed in 3D) positioned vertically at the half distance between the bottom of the windings and the bottom vessel lid. In the horizontal direction (perpendicular to the figure plane) the concentric circles are placed between PW and SW (A) and the pairs of the outer vessel wall and PW ( $D_0$ ) and the inner vessel wall and SW ( $D_i$ ), respectively, as illustrated in **Fig. 5.2b**. To simplify the model derivation, it is assumed that the oil temperatures at the three concentric circles are identical and correspond to  $T_{ob}$ . The same logic is followed for the points B,  $C_i$ , and  $C_0$  at the top of the windings, however, it is assumed that the oil temperatures vary and they agree with  $T_{otw1}$ ,

$T_{otw2}$ , and  $T_{otr}$ , respectively. Herewith, the four characteristic oil temperatures ( $T_{otr}$ ,  $T_{otw1}$ ,  $T_{otw2}$ ,  $T_{ob}$ ), i.e. temperatures of interest to estimate, are defined. Three cylindrical zones of oil circulation  $Z_0$ ,  $Z_1$ , and  $Z_2$  are marked in **Fig. 5.2b** together with the direction of oil movement for each of the zones. Note that the color legend given in **Fig. 5.2a** applies to **Fig. 5.2b** as well.

In the following, the expected oil circulation paths in the steady state are explained. The oil in zone 1 ( $Z_1$ ), heated from the excess PW and SW losses ( $P_{\gamma1}$  and  $P_{\gamma2}$ ), experiences mass density decrease, i.e. volume expansion and rises from A to B (average volumetric flow  $Q_1$  [ $\text{m}^3/\text{s}$ ]) due to buoyancy forces. In **Fig. 5.2a**, this is indicated with a vertical colored arrow, illustrating the oil temperature change from blue/cold to red/hot. At the top, oil starts to cool down, becoming heavier, owing to lower winding temperatures compared to the bottom winding parts, which is achieved by the temperature gradient due to the existing DI water cooling. At this point, the oil splits into two paths  $C_0D_0$  (zone  $Z_0$ , flow  $Q_0$ ) and  $C_1D_1$  (zone  $Z_2$ , flow  $Q_2$ ), where it continues cooling at the outer and inner vessel wall through natural convection and returns down to point A, where the process of oil heating starts again. Thereby, the heat exchanged with the vertical vessel walls is denoted with  $P_{w,o}$  and  $P_{w,i}$  for the outer and the inner vessel wall, respectively. Moreover, horizontal heat exchange is considered as well, marked with  $P_{h,t}$  and  $P_{h,b}$ , corresponding to the top and bottom vessel lid. Note that the presented model is developed for the steady-state transformer operation, and it is not able to estimate oil temperatures and velocities during transient states. Nevertheless, this does not compromise the validity of the presented model, since steady-state temperatures are the ones observed for proper thermal coordination, owing to large time constants of thermal phenomena. Lastly, the complete model requires consideration of the hydraulic side of the problem as well, since moving oil causes pressure drops, which are directly connected to the oil velocity.

### 5.2.1 Thermal Part of THM

Energy balance equations established for each of the oil zones are given in (5.1)-(5.6), with  $w_0$  [ $\text{m/s}$ ],  $w_1$  and  $w_2$  as the respective average oil velocities, and  $A_0$  [ $\text{m}^2$ ],  $A_1$  and  $A_2$  as the horizontal cross sections for each of the zones. Their respective products yield average volumetric flows ( $Q_0$ ,  $Q_1$ , and  $Q_2$ ) for each of the defined zones.

Zone 0:

$$zP_{\gamma1} - P_{w,o} - P_{h,t}^{A_0} - P_{h,b}^{A_0} = \rho^o c_p^o Q_0 (T_{otr} - T_{ob}), \quad (5.1)$$

$$\text{with } Q_0 = A_0 w_0, \quad P_{h,t}^{A_0} = A_0 k_p^h (T_{otr} - T_{a,1}), \quad P_{h,b}^{A_0} = A_0 k_p^h (T_{ob} - T_{a,1}) \quad (5.2)$$

Zone 1:

$$(1 - z)P_{\gamma1} + (1 - y)P_{\gamma2} - P_{h,t}^{A_1} - P_{h,b}^{A_1} = \rho^o c_p^o Q_1 (T_{otw1} - T_{ob}), \quad (5.3)$$

$$\text{with } w_1 = \frac{1}{A_1} \underbrace{(Q_0 + Q_2)}_{= Q_1}, \quad P_{h,t}^{A_1} = A_1 k_p^h (T_{otw1} - T_{a,1}), \quad P_{h,b}^{A_1} = A_1 k_p^h (T_{ob} - T_{a,1}) \quad (5.4)$$

Zone 2:

$$yP_{\gamma2} - P_{w,i} - P_{h,t}^{A_2} - P_{h,b}^{A_2} = \rho^o c_p^o Q_2 (T_{otw2} - T_{ob}), \quad (5.5)$$

$$\text{with } Q_2 = A_2 w_2, \quad P_{h,t}^{A_2} = A_2 k_p^h (T_{otw2} - T_{a,1}), \quad P_{h,b}^{A_2} = A_2 k_p^h (T_{ob} - T_{a,1}) \quad (5.6)$$



Most of the variables from the above equations are defined in the preceding sections. The total HTC  $k_p^h$  [W/m<sup>2</sup>K] describes the heat exchange between oil and the surrounding air at the top and bottom horizontal surface of the vessel, whereas parameters  $\rho^o$  [kg/m<sup>3</sup>] and  $c_p^o$  [J/kgK] give the oil density and its specific heat capacity at oil temperature  $T_{ob}$ . Additionally, it is assumed that the excess PW and SW heat losses are distributed between the respective oil zones ( $Z_0$ - $Z_1$  and  $Z_1$ - $Z_2$ ) according to ratio parameters  $z$  [1] and  $y$ . The horizontal heat exchange ( $P_{h,b}^A$  at the bottom,  $P_{h,t}^A$  at the top) between oil and the surrounding air is distributed across the zones by the respective horizontal cross sections ( $A_{0,1,2}$ ). Finally, it is assumed that the air temperature at the top and bottom of the vessel takes the same values as  $T_{a,1}$ . The total excess winding losses ( $P_{tot} = P_{\gamma 1} + P_{\gamma 2}$ ) exchanged with the oil get evacuated both at the vertical and horizontal vessel walls. Nevertheless, the horizontal heat exchange, in regions  $AD_i$ ,  $AD_o$  and  $BC_i$ ,  $BC_o$  is significantly smaller compared to the heat exchanged vertically, i.e. between the windings, and the inner and outer vessel wall. Note that the average oil velocity  $w_1$  in zone  $Z_1$  is determined by the other two average oil velocities  $w_0$  and  $w_2$ , due to the assumption that the oil flowing through zone  $Z_1$  gets split into the flows of the zones  $Z_0$  and  $Z_1$ .

As already mentioned, the goal of the THM is to correctly estimate characteristic oil temperatures depending on the operating points of the MFT and the WCU, i.e. depending on the amount of winding losses and the characteristics of the DI water entering the windings, respectively. In the model, the WCU operating point is represented by the volumetric flow and the inlet temperature of the coolant. The outlet temperature depends on the amount of dissipated winding losses. The following equation determines the amount of losses absorbed by the flowing DI water

$$P_{DI,w} = \dot{m} c_p^w \Delta T_w, \quad (5.7)$$

Thereby, variable  $\dot{m}$  [kg/s] gives the volumetric flow of the DI water,  $c_p^w$  is its specific heat capacity and  $\Delta T_w$  stands for the water temperature increase from the bottom to the top due to winding loss absorption. Considering the total amount of winding loss and the previous equation, the excess PW and SW losses  $P_{\gamma 1}$  and  $P_{\gamma 2}$  can be estimated. The outlet water temperature is collected directly from experimental measurements of oil, DI water, and Cu temperatures. The experimental characterization of the model is given in **Sec. 5.3.2**.

The cooling powers along the vertical vessel walls are obtained by integration as given in the following

$$P_{w,o} = \int_0^H (T_{o,0}(x) - T_{a,1}) k_p^o O^o dx = \frac{A_o}{A_i + A_o} P_{diff}, \quad (5.8)$$

$$P_{w,i} = \int_0^H (T_{o,2}(x) - T_{a,2}) k_p^i O^i dx = \frac{A_i}{A_i + A_o} P_{diff}, \quad (5.9)$$

$$P_{diff} = P_{tot} - P_{h,b}^{A_0+A_1+A_2} - P_{h,t}^{A_0+A_1+A_2}, \quad (5.10)$$

where  $H$  is the vertical height of the oil in the vessel,  $A_o$ , and  $A_i$  are the vertical surfaces of the outer and inner vessel walls which are in contact with the oil, respectively. Further,  $T_{o,0}(x)$  and  $T_{o,2}(x)$  represent vertical oil temperature distributions for the outer and inner oil zones ( $Z_0$  and  $Z_2$ ),  $O^o$  [m] and  $O^i$  are the circumferences of the outer and inner vessel wall, respectively. As the last equation above implies, the excess winding losses which are exchanged with the ambient through vertical walls, marked as  $P_{diff}$ , are obtained by subtracting the horizontally exchanged losses from the total excess winding losses ( $P_{tot}$ ). At this point, it is assumed that the heat difference ( $P_{diff}$ ) is distributed across the vertical vessel walls based on the simple proportion of vessel wall surfaces that take part

in the heat exchange process. The coefficients  $k_p^o$  and  $k_p^i$  are the total HTC, relevant at the outer and inner vessel wall, respectively, and determined by the following equations

$$k_p^o = \frac{1}{\frac{1}{\alpha_o} + \frac{\delta_w}{\lambda_w} + \frac{1}{\alpha_a}}, \quad k_p^i = \frac{1}{\frac{1}{\alpha_u} + \frac{\delta_w}{\lambda_w} + \frac{1}{\alpha_i}}, \quad \text{with} \quad \alpha = \overline{\text{Nu}} \frac{\lambda_m}{L} \quad \text{in its general form.} \quad (5.11)$$

Parameter  $\alpha$  [ $\text{W/m}^2 \text{K}$ ] is the convection HTC between a certain surface and the passing fluid,  $\lambda_w$  [ $\text{W/mK}$ ],  $\delta_w$  [m] are the thermal conductivity and the thickness of the vertical vessel wall. Thereby,  $\alpha_u$ ,  $\alpha_a$  and  $\alpha_i$ ,  $\alpha_o$  in pairs give the HTCs for the convective heat transfer between the inner and the outer vessel wall in pair and the surrounding air and oil, respectively. The introduced convection HTCs, which eventually define the total HTC value, can be determined with the help of known average Nusselt correlations ( $\overline{\text{Nu}}$ ) obtained for natural convection in the laminar regime [82], [154], the medium's thermal conductivity  $\lambda_m$  and the characteristic length  $L$  [m] of the surface which participates in the convective heat transfer process. Each Nusselt correlation depends on the medium specifications and the geometrical arrangement through which the fluid is passing (e.g. tall vertical enclosure with uniform heat flux on the sidewalls, vertical cylinder with isothermal surfaces, and so on). Relations similar to (5.11) hold for the total HTC  $k_p^h$  which describes the convective heat exchange between the oil and the surrounding air at the top and bottom horizontal surface of the vessel. Nevertheless, due to the geometric specificity of the existing empirically determined Nusselt correlations, which do not exactly match the geometry of the considered oil vessel given in **Fig. 5.2a**, the total HTCs  $k_p^o$ ,  $k_p^i$ , and  $k_p^h$  and the convective HTCs  $\alpha_1$  and  $\alpha_2$  are determined for model purposes with the help of a genetic algorithm, explained in **Sec. 5.2.3**.

The vertical oil temperature distributions ( $T_{o,0}(x)$  and  $T_{o,2}(x)$ ) are calculated with the help of the following differential equations of energy balance

$$(k_p^i O^i(T_{o,2}(x) - T_{a,2}) + \alpha_2 O_2(T_{o,2}(x) - T_{w2})) dx = \rho^o c_p^o Q_2 dT_{o,2}(x), \quad (5.12)$$

$$(k_p^o O^o(T_{o,0}(x) - T_{a,1}) + \alpha_1 O_1(T_{o,0}(x) - T_{w1})) dx = \rho^o c_p^o Q_0 dT_{o,0}(x). \quad (5.13)$$

Thereby, parameters  $O_1$  and  $O_2$  provide the outer and inner circumference of the primary and the secondary winding, respectively. HTCs  $\alpha_1$  and  $\alpha_2$  characterize accordingly the heat transfer between the oil and PW and SW, as denoted in **Fig. 5.2a**. Once the solutions to oil temperature distributions in the  $x$  direction are derived, they are applied to equations (5.8)–(5.10).

Eventually, with the help of the statistical software package Maple and based on the equations (5.1)–(5.13), four analytical expressions for four distinct oil temperature points ( $T_{otr}$ ,  $T_{otw1}$ , and  $T_{otw2}$  selected at the top of zones  $Z_0$ ,  $Z_1$ , and  $Z_2$ , respectively, and  $T_{ob}$  as the homogeneous bottom oil temperature) are derived, which depend on the average oil velocities  $w_0$  and  $w_2$ , among other parameters. The obtained expressions are not explicitly provided in the thesis.

### 5.2.2 Hydraulic Part of THM

For the hydraulic part of the model, the following assumptions are made:

- Only a single oil phase exists;
- Oil passages have smooth walls;
- Flow is stabilized and in laminar regime;

- Oil takes part in forced convective heat transfer.

The last assumption stands in contradiction with obvious physics, but it is necessary, due to the fact that the expressions for hydraulic resistances are derived (exclusively) for the case of forced convection [155]. For this type of convective heat exchange, the dimensionless Reynolds number is important to consider.

### 5.2.2.1 Produced Pressure

As a consequence of oil density change, a thermal driving force, i.e. buoyancy force, is created which causes oil circulation and produces pressure [156], as illustrated on the left side of the oil vessel from **Fig. 5.3**. A general expression for the produced pressure is given in the first part of (5.14) and adjusted to the specific oil path geometry, shown in the same figure, in the second part of (5.14):

$$p_T = \rho^o g \beta \Delta T_o \Delta H \quad \Rightarrow \quad p_T = \rho^o g \beta \left( \frac{1}{2} T_{ot} - T_a + \frac{1}{2} T_{ob} - \Delta T_{o-a} \right) \quad (5.14)$$

Thereby, parameter  $\beta$  [ $1/^\circ\text{C}$ ] is the volume expansion coefficient,  $g$  [ $\text{m}^2/\text{s}$ ] is the gravity vector,  $\Delta T_o$  stands for the vertical temperature gradient ( $\Delta T_o = T_{ot} - T_{ob}$ ), whereas  $\Delta H$  is the corresponding height difference. Note that the temperature  $T_{ot}$  can assume any of the two top temperatures,  $T_{otr}$  or  $T_{otw2}$ , depending on the considered oil circulation path,  $ABC_o D_o A$  or  $ABC_i D_i A$ , respectively. Temperature  $\Delta T_{o-a}$  is known as the logarithmic mean temperature difference and it is defined by the following relation

$$\Delta T_{o-a} = \frac{T_{ot} - T_{ob}}{\ln(T_{ot} - T_a) - \ln(T_{ob} - T_a)}, \quad (5.15)$$

with  $T_a$  as one of the two ambient temperatures,  $T_{a,1}$  and  $T_{a,2}$ , depending again on the considered oil loop.

### 5.2.2.2 Pressure Drop

On the other hand, oil streaming causes dispersed and local pressure drops, as indicated on the right side of the oil vessel from **Fig. 5.3**. The local drops occur in elements where the oil changes the streaming direction, such as in cases of confluence and branching. Compared to the first type of pressure drops, it can be neglected, as marked with dotted lines in **Fig. 5.3** [155]. The first type, also known as the frictional pressure drop, is characteristic of flows through elements with constant cross sections and it is determined by a pressure drop coefficient  $\xi$  [1]. The value of the coefficient depends on the flow type and the geometry of oil passages, as well as the oil density and average velocity [155], as given by the following relations

$$\Delta p = \xi \frac{\rho^o w^2}{2} \quad \Rightarrow \quad \xi = \lambda \frac{l}{D_h}, \quad \text{with} \quad \lambda = k_{\text{non-c}} \frac{64}{\text{Re}} \quad \text{and} \quad \text{Re} = w \frac{D_h}{\nu}. \quad (5.16)$$

Parameter  $\lambda$  [1] gives the friction coefficient and it is determined by the smoothness of the oil passage walls and by the flow type,  $l$  [m] is the conduit length,  $D_h$  [m] is the hydraulic diameter,  $\nu$  [ $\text{m}^2/\text{s}$ ] is the kinematic oil viscosity, and  $\text{Re}$  [1] is the Reynolds number. For the assumption of laminar flow to be correct, the Reynolds number needs to have a value below 2000. The parameter  $k_{\text{non-c}}$  [1] is the correction factor for non-standard conduit shapes, since in the specific case illustrated in **Fig. 5.3** the

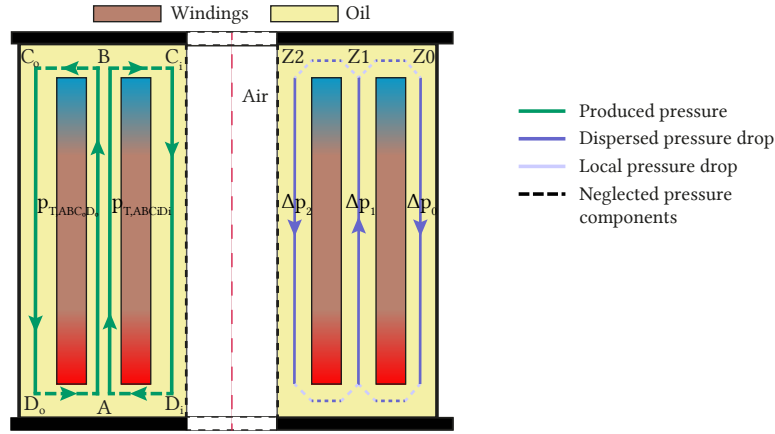


**Fig. 5.3** 2D front view of an oil vessel with indicated paths of generated and reduced pressures. Dotted lines of any color specify pressure components that are neglected in the hydraulic part of the THM.

oil flows through concentric annuluses of circular tubes. Depending on the inner ( $d$  [m]) and outer ( $D$ ) diameter values of the circular annulus, the correction factor is defined as follows [155]:

$$k_{\text{non-c}} = \frac{1 - \left(\frac{d}{D}\right)^2}{1 + \left(\frac{d}{D}\right)^2 + \frac{1 - \left(\frac{d}{D}\right)^2}{\ln\left(\frac{d}{D}\right)}} \quad (5.17)$$

Eventually, a steady state and stabilized oil flows are reached when the pressure equilibrium holds for each of the two oil loops, i.e. once the produced pressure matches the pressure drops caused due to oil movement. Both pressure components are illustrated in **Fig. 5.3**. The sought equilibrium is finally expressed by the following relations

$$p_{\text{eq,o}} : p_{T,ABC_oD_oA} = \Delta p_1 + \Delta p_0, \quad (5.18)$$

$$p_{\text{eq,i}} : p_{T,ABC_iD_iA} = \Delta p_1 + \Delta p_2, \quad (5.19)$$

with  $\Delta p_0$  [Pa],  $\Delta p_1$  and  $\Delta p_2$  describing the pressure drops in zones  $Z_0$ ,  $Z_1$  and  $Z_2$ , respectively, calculated based on (5.16). The left-hand side of the pressure balance equation is determined based on (5.14)-(5.15). Note that the pressures produced and lost in the horizontal parts of the two main oil paths ( $BC_o$ ,  $BC_i$ ,  $AD_o$ ,  $AD_i$ ) are not considered, as indicated with dotted lines in both side of oil vessel from **Fig. 5.3**. This second part of THM provides another two model-relevant equations which describe the pressure equilibrium of the two main oil loops, and they are coupled with the four characteristic oil temperatures and the two relevant average oil velocities.

### 5.2.3 THM Implementation

To summarize, the developed analytical model consists of four expressions for oil temperatures and two relations describing the pressure balance in the main oil loops. Due to the complexity of the considered heat transfer system, which includes both natural and forced convection, and existing uncertainty and difficulty regarding accurate analytical modeling of heat transfer phenomena inside of the oil vessel, a set  $x$  of 9 parameters, defined in **Tab. 5.1**, is considered optimizable within certain

boundaries. The set includes average oil velocity for each circulation path, all the relevant HTC's for vertical and horizontal heat exchange, and the split ratios of the PW and SW excess losses between the respective oil zones. The optimal values of the selected variables are determined based on the collected experimental thermal measurements, presented in more detail in **Sec. 5.3.2**, and with the help of multi-objective optimization. The main idea behind the THM implementation is that the selected optimization algorithm minimizes the difference between the measured and the analytically derived oil temperature values while respecting the pressure equilibrium in both loops and achieving this for a certain optimal set of parameters.

The optimization process can be described as following

$$\begin{aligned} & \underset{x}{\text{minimize}} && f(x), g(x) \\ & \text{subject to} && B_l \leq x \leq B_h \end{aligned} \quad (5.20)$$

with  $B_l$  and  $B_h$  as the lower and upper boundary sets of the optimization variables  $x$ . The respective objective functions, which are to be minimized, are defined as:

$$f(x) = \sum_{i=\text{otr,otw1,otw2,ob}} |T_i(x) - T_i^*|, \quad g(x) = |p_{\text{eq,o}}(x) + p_{\text{eq,i}}(x)| \quad (5.21)$$

The asterisk sign in  $T_i^*$  stands for the experimentally obtained oil temperatures, the expression  $T_i(x)$  stands for the four derived analytical expressions of the characteristic oil temperatures, whereas the variable  $x$  corresponds to the parameter set  $x = \{w_0, w_2, z, y, k_p^o, k_p^i, k_p^h, \alpha_1, \alpha_2\}$ . The two pressure balance equations,  $p_{\text{eq,o}}(x)$  and  $p_{\text{eq,i}}(x)$ , are defined by (5.18) and (5.19), respectively. The boundaries for the average oil velocities are determined based on computational fluid dynamics FEM simulations of similar geometries, whereas the total HTC values are estimated considering typically expected values of convective HTC's for forced convection of oil and air. Lastly, regarding split ratio variables, it is natural to select 0 and 1 as the respective lower and upper boundaries.

Parameter	Description	Lower boundary $B_l$	Upper boundary $B_h$
$w_0$	average oil velocity in $Z_0$	10 $\mu\text{m/s}$	10 $\text{mm/s}$
$w_2$	average oil velocity in $Z_2$	10 $\mu\text{m/s}$	10 $\text{mm/s}$
$k_p^o$	total HTC between air ( $T_{a1}$ ) and oil at the outer vessel wall	2 $\text{W/K m}^2$	25 $\text{W/K m}^2$
$k_p^i$	total HTC between air ( $T_{a2}$ ) and oil at the inner vessel wall	2 $\text{W/K m}^2$	25 $\text{W/K m}^2$
$k_p^h$	total HTC between air ( $T_{a1}$ ) and oil at the bottom and top lid	2 $\text{W/K m}^2$	25 $\text{W/K m}^2$
$\alpha_1$	convective HTC between the oil in $Z_0$ and PW	100 $\text{W/K m}^2$	15 000 $\text{W/K m}^2$
$\alpha_2$	convective HTC between the oil in $Z_2$ and SW	100 $\text{W/K m}^2$	15 000 $\text{W/K m}^2$
$z$	$P_{\gamma 1}$ ratio that heats the oil in $Z_0$	0	1
$y$	$P_{\gamma 2}$ ratio that heats the oil in $Z_2$	0	1

**Tab. 5.1** Set  $x$  of the selected optimizable variables and their corresponding lower and upper constraints.

Note that in the first objective function  $f(x)$ , none of the characteristic oil temperatures are weighted and prioritized over the others. The same applies to the pressure equilibria from the two oil circulation loops in the second optimization function. In order to maximize the probability of finding global minima, the implementation method is based on genetic algorithms [157]. A particular advantage of this method is that no initial conditions are required. The optimization part of the model is implemented with the help of the optimization toolbox from MATLAB and the function *gamultobj*, which uses a controlled elitist variant of the NSGA-II algorithm [158]. With appropriate selections of population size and number of iterations, it is ensured that the algorithm maximizes the diversity of the populations between each succeeding generation. The resulting Pareto fronts and the respective optimized sets of variables  $x$  are not explicitly provided for each operating point.

### 5.3 THM Characterization and Validation

To finalize the THM, thermal measurements of the insulating oil need to be collected. For that purpose, an adequate test setup is assembled, equipped with various sensors, and it is presented in more detail in the following sections.

#### 5.3.1 Experimental Setup

The experimental measurements necessary for the characterization of the THM are collected with the help of a down-scaled test setup shown in **Fig. 5.4**. The setup consists of a single oil vessel made of phenolic paper composite material, manufactured by Elektro-Isola [139]. It contains a set of PW and SW hollow conductors with fixed interwinding distances and is filled with synthetic ester dielectric oil (Midel 7131 [78]). The windings are made of standard 8 mm Outer Diameter (OD) Cu pipes, typically employed for plumbing purposes, and easily sourced for the test setup. **Tab. 5.2**

Property	Unit	Value
Inner conductor diameter $D_i$	mm	5.2
Conductor wall thickness $\delta$	mm	1.4
Turn-to-turn distance	mm	3
$N_{PW,SW}$	1	15
External PW diameter $D_{a,PW}$	mm	170
External SW diameter $D_{a,SW}$	mm	142
Electrical PW DC resistance	m $\Omega$	6.6/9.6
Electrical SW DC resistance	m $\Omega$	5.5/7.7
Interwinding distance	mm	10
Winding-to-wall horizontal distance	mm	15
Winding-to-wall vertical distance	mm	25

**Tab. 5.2** Catalogued electrical and physical properties of the windings and relevant insulation distances for the THM test setup. Calculated and measured values provided for the DC resistances of the windings.

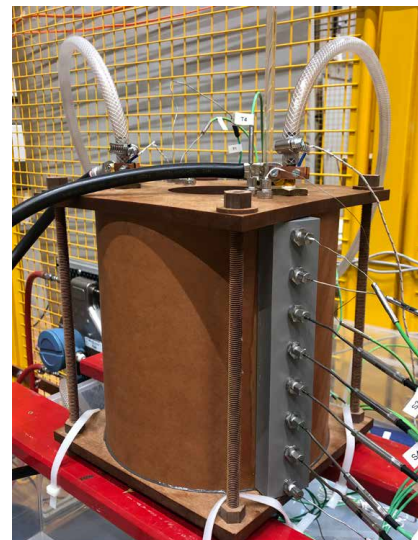


**Fig. 5.4** A vessel, made of phenolic paper material and instrumented with TCs, containing insulating oil and a pair of PW and SW connected in series to a DC power source and DI WCU.

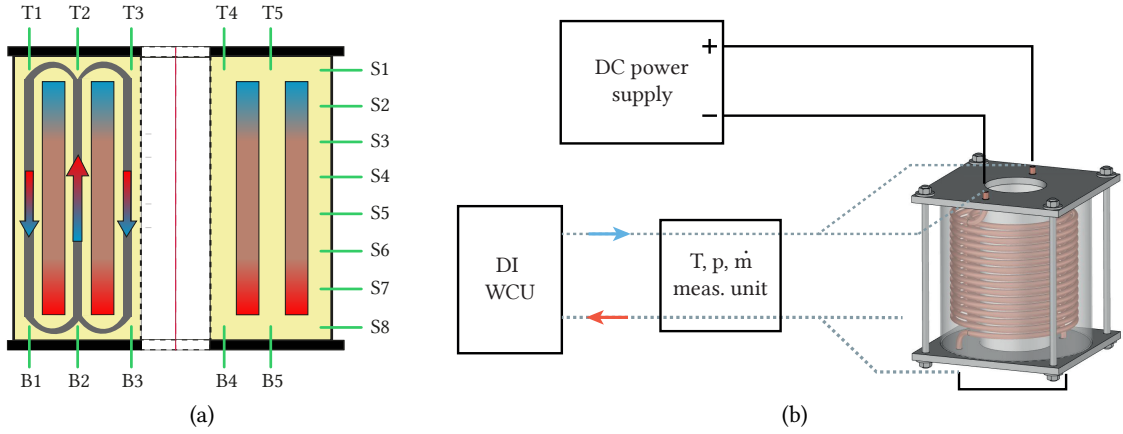


**Fig. 5.5** (a) Positions of 18 TCs inside of the oil vessel. (b) Schematics of electrical connections between PW and SW (in series) and a DC power supply, marked by black lines. DI water hoses distribute cold water to the top of the windings (in parallel) and collect the warm water from the bottom, marked with grey dashed lines.

provides a summary of the relevant winding properties and insulation distances. Two values are provided for the respective DC winding resistances, namely, the calculated and the measured values. In order to provide space for the oil to expand, a transparent glass tube is attached to the top lid. In this way, it is possible to observe the current oil level, and gather data regarding the thermal oil expansion, even though this is not relevant to the results presented in this chapter. Lastly, the vessel with oil and windings inside is placed over a large plastic tub, as a precautionary measure in case of oil leakage.

To measure oil temperatures, 18 Thermocouples (TCs) are placed in the same vertical plane which passes through the vessel center, as illustrated in the 2D front cross-section view in **Fig. 5.5a**. Thereby, five TCs are placed in the same horizontal line at the vessel top (marked with  $T_1 - T_5$ ) and five at the bottom (marked with  $B_1 - B_5$ ), measuring the temperatures at the center of each zone ( $Z_0$ ,  $Z_1$ , and  $Z_2$ ). Note that per TC group,  $T_1-T_3$ ,  $B_1-B_3$ ,  $T_4-S_1$ ,  $B_4-S_8$ , the TCs are placed equidistantly 20 mm apart. In the vertical direction, the TCs at the top and bottom are inserted 12.5 mm in the vessel, which corresponds to half of the vertical winding-to-wall insulation distance. The remaining eight TCs (denoted with  $S_1 - S_8$ ) are inserted equidistantly ( $\approx 30$  mm) on the vessel side exactly between the outer vessel wall and the PW in the horizontal direction, as shown in **Fig. 5.5a**. To observe the winding temperatures and determine the average values of  $T_{w1}$  and  $T_{w2}$ , another four TCs are attached to the top and bottom parts of the windings, directly outside of the oil vessel.

To imitate/induce winding losses present during transformer operation, a DC power supply (Magna-Power TS-Series) is used to provide controlled DC to PW and SW, which are connected in series. For cooling purposes, the windings are supplied with DI water from a WCU of controlled temperature and volumetric flow. **Fig. 5.5b** provides a schematic of the winding connections to the DC power source and the WCU. Additional setup (marked with T, p,  $\dot{m}$  meas. unit), shown in **Fig. 5.6**, is assembled to monitor temperature, pressure, and volumetric flow of the incoming and outgoing coolant. The employed sensing elements for the auxiliary measurement setup are summarized in **Tab. 5.3**. The flow sensor consists of two parts, namely, a Coriolis flow meter and a transmitter. The differential pressure sensor is added for the sake of confirmation of the obtained pressure differences measured between the incoming and outgoing coolant branches with absolute pressure sensors. For temperature sensing,

standard K-type TCs are used for both oil, DI water, and Cu temperature measurements with an accuracy of  $\pm 2.2^\circ\text{C}$ , which does not include possible deviation in the acquisition system.

Regarding the cooling arrangement, the employed WCU, presented in **Fig. 3.4c**, has cooling capabilities of 130 L/min and an allowed pressure drop of 350 kPa. The minimal outlet DI water temperature is limited to  $10^\circ\text{C}$ , however, an operating value of  $30^\circ\text{C}$  is closer to reality. The cooling capacity of the WCU is 90 kW. Thereby, the pump speed is controlled by a frequency converter in the range of 0 Hz to 50 Hz, and in this way, the volumetric flow of the DI water is regulated. To collect the necessary thermal measurements, the lower and upper-frequency limits are changed to 10 Hz and 45 Hz, respectively.

### 5.3.2 Measurements

The previous section describes the test setup, which is used to collect measurements for various operating points. This includes varying the induced winding losses, as well as cooling conditions. Thereby, the current of the DC source is varied in the range of 250 A – 450 A with a 20 A step, which corresponds to 11 measurements covering roughly 1 kW – 3 kW of total winding losses. Note that this range of losses relates to the available winding loss budget for a 1 MW MFT design. Thereby, the respective current density span for both windings is  $9.5\text{ A/mm}^2$  –  $17.5\text{ A/mm}^2$ .

The volumetric flow of the DI water is changed in the range of 10 mL/s – 35 mL/s. To be more precise, the 11 measurements with varied winding losses are repeated for four WCU operating points, which corresponds to 10 mL/s, 16 mL/s, 23 mL/s, and 36 mL/s of volumetric flow. Compared to the 130 L/min, i.e. 2.167 L/s available flow, the observed span seems very small. However, this can be traced back to the limiting WCU value of the pressure drop with the help of the Darcy-Weissbach equation [159]. It is of empirical nature and is able to estimate the pressure loss over the flow length considering the average velocity. Thereby, it assumes an incompressible and smooth fluid and it is defined by the following:

$$\frac{\Delta p}{L} = f_d \frac{\rho}{2} \frac{v_{\text{avg}}^2}{D}, \quad \text{with} \quad f_d = \frac{64}{Re} \quad \Rightarrow \quad \frac{\Delta p}{L} = 128 \mu \frac{Q}{D^4 \pi}. \quad (5.22)$$

The parameter  $f_d$  is known as the Darcy friction factor,  $\rho$  is the fluid density,  $v_{\text{avg}}$  is the mean flow

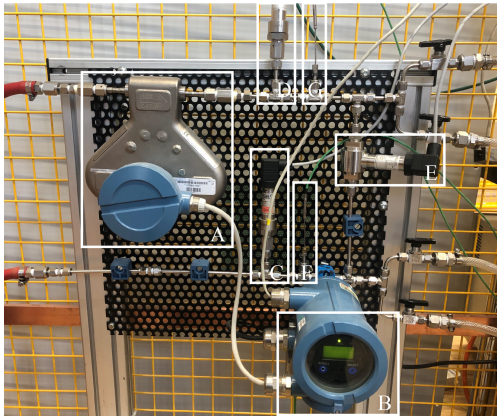


**Fig. 5.6** Auxiliary measurement setup equipped with thermal and pressure sensors for the incoming and outgoing DI water path and a Coriolis flow meter.

Component	Manufacturer
A Coriolis mass flow meter	Emerson CMF010M/L
B Transmitter	Emerson CMF010M/L
C Absolute pressure sensor	KELLER PAA-23/25
D Absolute pressure sensor	KELLER PAA-23/25
E Differential pressure sensor	KELLER PD-23
F Thermocouple	Thermocoax type K
G Thermocouple	Thermocoax type K

**Tab. 5.3** Main sensing components from the auxiliary measurement setup. The letters A – G correspond to the measuring units on the left figure.



velocity, measured as the volumetric flow rate  $Q$  per unit cross-sectional wetted area, with a diameter  $D$ . The complete test setup includes long connecting hoses between the WCU and the auxiliary measurement setup from **Fig. 5.6**, where the Inner Diameter (ID) of the stainless-steel pipes from **Fig. 5.6** is significantly reduced (to less than 4 mm) compared to the diameter of the connecting hoses (approximately 12 mm). According to (5.22), the pressure drop has a strong, power of four, pipe diameter dependency, and, thus, this part accounts for the highest pressure drop. In the last part of the cooling path, the windings are connected with the auxiliary setup by plastic hoses of 8 mm ID. From the pressure sensor measurements, which are not explicitly shown, it can be concluded that the pressure drop of the flow inside the windings, i.e. between the two measuring points of the absolute pressure does not surpass 80 kPa, i.e. 0.8 bar. This was confirmed analytically with the above-mentioned empirical equation. Nevertheless, the flow is sufficient to maintain reasonable oil and winding temperatures for relatively high losses, as well as for THM characterization.

**Fig. 5.7** provides examples of recorded oil temperature distributions for the operating point of 410 A, which corresponds to approximately 2.8 kW of total losses, for two volumetric flows. Namely, **Fig. 5.7a** is recorded for 23 mL/s and **Fig. 5.7b** for 36 mL/s WCU operating point. In the first place, one can notice a steady-state temperature drop for all TCs once the cooling conditions are improved, i.e. with higher

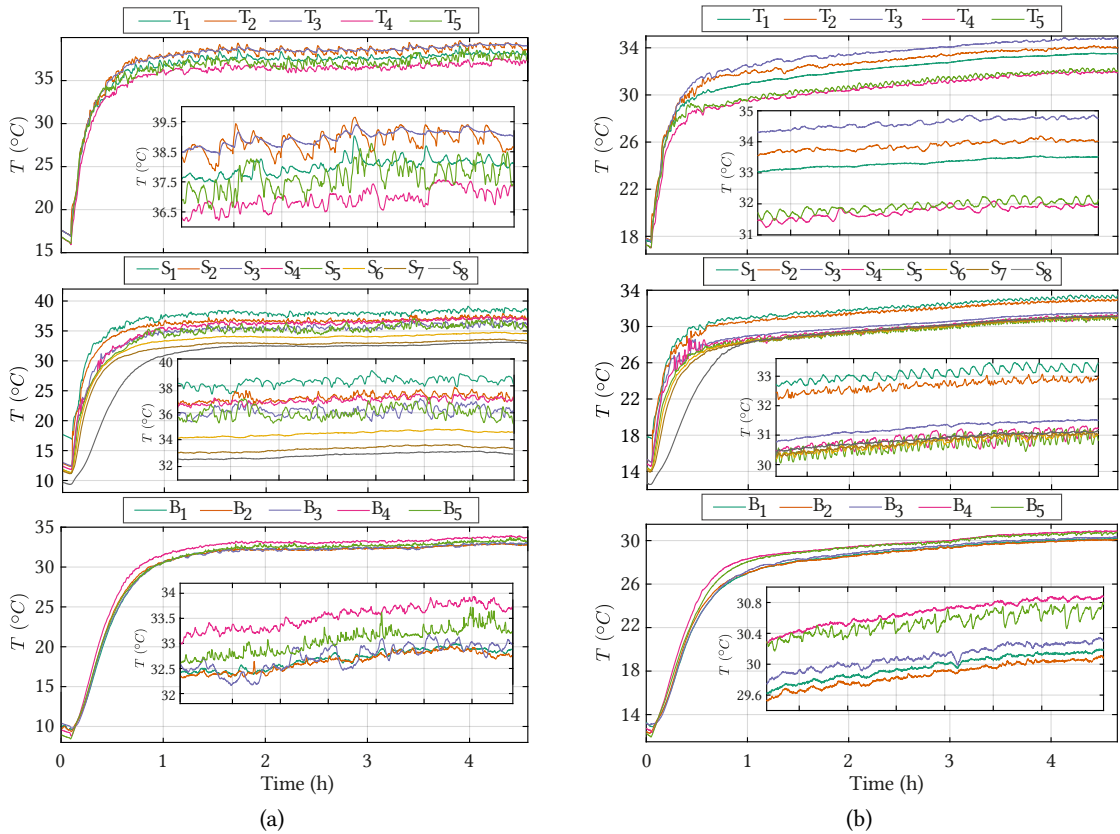


**Fig. 5.7** Oil temperature measurements taken at the top ( $T_1 - T_5$ ), on the side ( $S_1 - S_8$ ), and at the bottom ( $B_1 - B_5$ ) of the vessel for the operating point of 410 A for (a) 23 mL/s and (b) 36 mL/s WCU operating point. The magnified views provide the corresponding steady-state temperatures at the end of the recording time.

volumetric flow. By observing the obtained temperature forms for differently placed TCs and based on the magnified view of the steady-state temperatures, it is possible to make presumptions regarding the oil movement. In **Fig. 5.7a**, the temperature evolution recorded at the top of the vessel exhibits higher oscillations than the side or the bottom measurements, which corresponds to the fact that the oil is surging up towards the vessel top with elevated temperature and circulating back to the bottom while being cooled at the outer and inner vessel walls. Nevertheless, oscillations of the same extent are not observed in **Fig. 5.7b**. Additionally, the temperature span between  $T_1$  and  $T_5$  is bigger for the higher volumetric flow. This could be explained by the fact that the oil moves slower when subjected to a smaller winding temperature gradient and thus mixes less with the remaining oil, which results in less uniform temperature distribution at the top. Regarding the side temperature measurements, the trends between the figures are similar, however, the temperature evolutions from  $S_1$  to  $S_8$  are less equally distributed for higher cooling efforts. The possible explanation could be again connected to slower oil circulation. Lastly, the selection of a single characteristic bottom oil temperature compared to the three distinct top vessel temperatures confirms to be correct, considering the temperature span of the respective TC groups. This holds for both presented volumetric flows.

To obtain the four characteristic oil temperatures ( $T_{ob}^*$ ,  $T_{otr}^*$ ,  $T_{otw1}^*$ , and  $T_{otw2}^*$ ) from the collected measurements, which are necessary for the first objective function in (5.21), the averaging of steady-state temperatures is carried out as follows:

$$T_{ob}^* = \text{avg}(B_1, B_2, B_3, B_4, B_5, S_8), \quad T_{otr}^* = \text{avg}(T_1, S_1), \quad T_{otw1}^* = \text{avg}(T_2, T_5), \quad T_{otw2}^* = \text{avg}(T_3, T_4) \quad (5.23)$$

Finally, **Fig. 5.8** and **Fig. 5.9** compare the results obtained when the THM is used to estimate oil temperatures for various operating points with the recorded measurements. Thereby, both induced

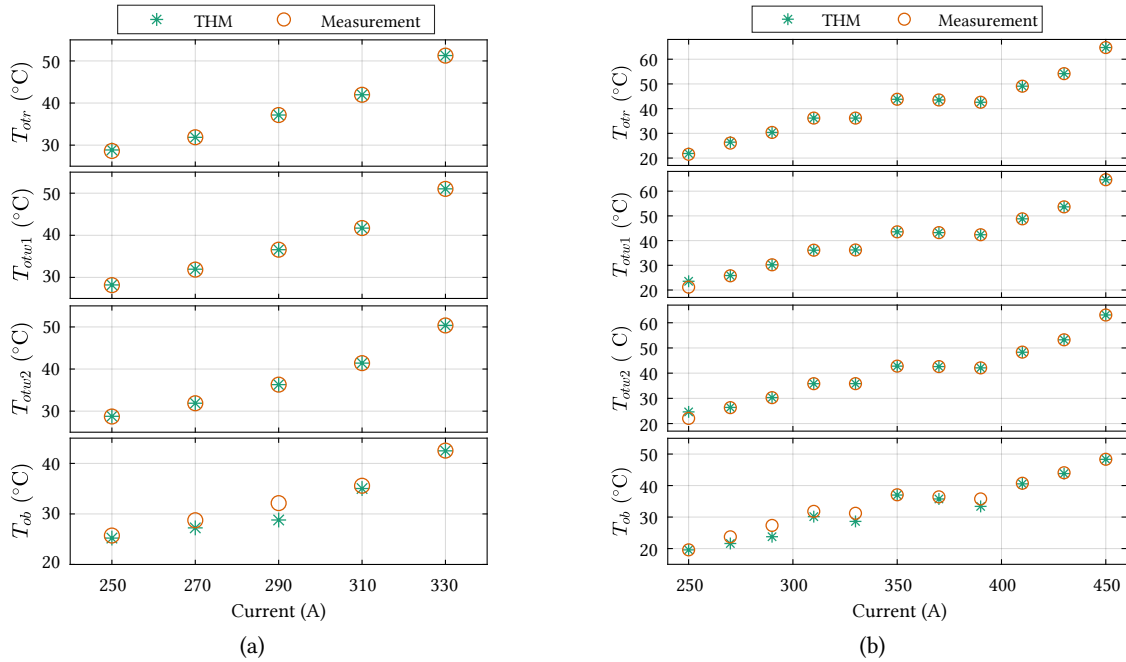


**Fig. 5.8** Comparison of experimentally obtained oil temperature measurements with the analytical THM results for various operating points measured at the volumetric flow of (a) 10 mL/s and (b) 16 mL/s.

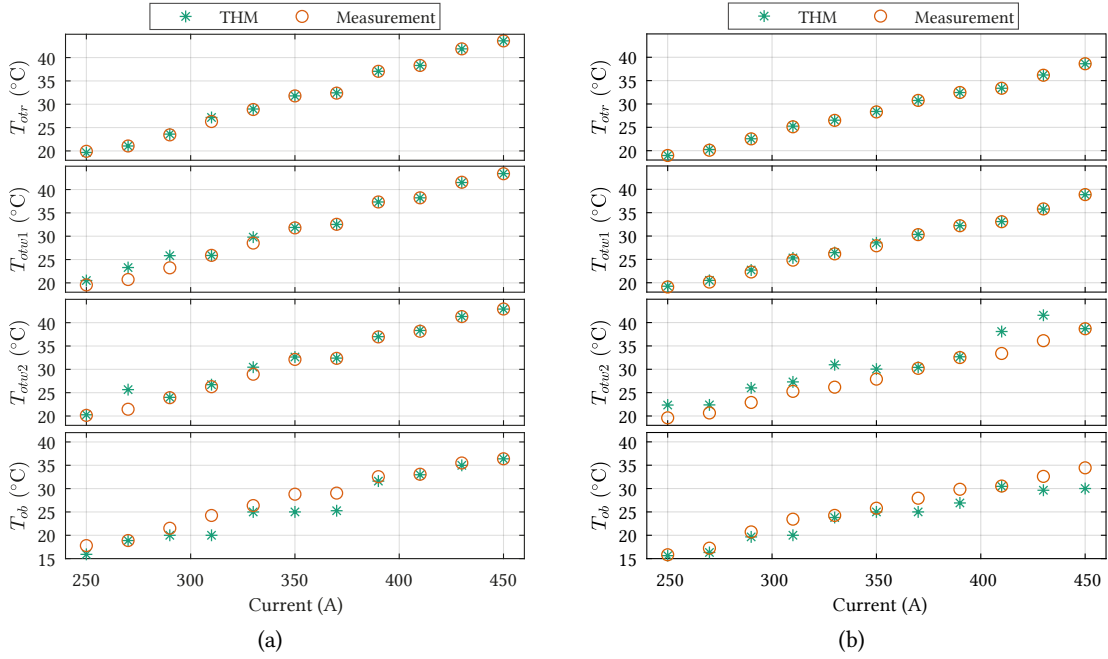


**Fig. 5.9** Comparison of experimentally obtained oil temperature measurements with the analytical THM results for various operating points measured at the volumetric flow of (a) 23 mL/s and (b) 36 mL/s.

winding losses and the cooling conditions are varied. In general, the two figures show an overall good agreement between the modeled and measured temperatures. In contrast to the other three cooling conditions, thermal measurements at 10 mL/s stop at 330 A, in order to avoid overexpansion and overheating of the oil. The highest deviations of the modeled from the measured values can be generally observed for estimation of the bottom oil temperature  $T_{ob}$ . Depending on the cooling conditions, they reach the following absolute values:

- 3.4 °C at 290 A DC and 10 mL/s WCU operating point;
- 3.6 °C at 290 A DC and 16 mL/s WCU operating point;
- 4.2 °C at 310 A DC and 23 mL/s WCU operating point;

Regarding the highest observed volumetric flow (36 mL/s), the largest difference (5.4 °C) is recorded for 430 A DC and top oil temperature  $T_{otw2}$ . As it can be concluded from the figures, the accuracy of the THM improves significantly with higher winding losses, where the deviation from the measured values for all four estimated temperatures, in case the same DC operating point is observed, remains very small. However, this is valid for faster oil movements, i.e. for lower volumetric flows, and worsens as the cooling conditions improve, as can be seen from **Fig. 5.9b**.

Considering that the average oil velocities are eventually determined by the genetic algorithm and due to the current inability to experimentally measure these values, as well as due to the complexity of such an experiment, the velocities obtained from the analytical model are not explicitly presented. Nevertheless, for all the considered operating points they remain in the range of several millimeters per second.

## 5.4 Summary

In this chapter an analytical model for characteristic oil temperature estimations is presented, especially relevant for MFTs with oil-immersed windings. Due to the fact that heating of the oil causes its movement, which further gives rise to pressure drops, both the thermal and hydraulic sides of the problem need to be considered for correct and accurate temperature estimation. Nevertheless, owing to the complexity of the analytical modeling of heat transfer phenomena combined with fluid dynamics, the introduced model had to be additionally characterized with the help of experimental temperature measurements and an optimization algorithm. Finally, a good agreement is achieved between the measured characteristic oil temperatures and the THM results for various operating points, including varied losses and cooling conditions.

The developed model is of importance for the thermal coordination of a design and it provides useful inputs to the overall steady-state thermal model of the MFT. However, due to the complexity of its current implementation, it cannot directly be included in the first layer of the MFT design process, where millions of potential designs need to be evaluated fast. To make the THM usable in optimization, the 9 model parameters need to be determined differently than with the help of optimization algorithm. The required HTC's can be expressed analytically with existing empirical relations, the two average oil velocities need to have their own analytical expressions and the two distribution ratio parameters can be considered implicitly. Nonetheless, it can serve well to aid the characterization of the overall thermal image of an MFT design with oil-immersed windings. The main drivers of the thermal imbalance during MFT operation are the inevitable losses. The following chapter explains in detail the modeling of the main loss contributors, i.e. core and winding losses, and finishes with the static thermal model of the MFT.

# 6

## MFT Losses and Static Thermal Modeling

*In order to accurately estimate the temperature distribution across the MFT, as well as to identify thermal hot spots, the heat sources within the MFT need to be correctly approximated beforehand. Therefore, this chapter starts with the introduction of employed models for core and winding losses. It is followed by a thermal network of resistances which is able to estimate and confirm the suspected hot-spot temperatures of the selected geometries for the core and windings. The thermal model is static by nature, i.e. thermal capacitances of the used materials are neglected.*

### 6.1 Introduction

To predict the efficiency of any magnetic component, one must first be able to accurately determine the losses resulting during operation. In the particular case of transformers, the core and the windings are the main loss contributors. Therefore, it is crucial to accurately model them in a reliable and appropriate way. Moreover, the generated losses need to be evacuated through the existing interfaces and materials to the surrounding ambient. The thermal behavior is determined by the amount of losses, the size of the component, and the materials and technologies used.

### 6.2 Core Loss Model

Different ways the core loss can be estimated have been summarized previously in **Sec. 2.5.2**. Considering the fact that the model is intended to be used in an MFT design optimization tool, it can be concluded that an accurate, reliable, yet simple and fast to execute model is needed. Therefore, an analytical model based on empirical observations expressed in the form of Steinmetz equation is selected as suitable for the task.

#### 6.2.1 Analytical Core Loss Model

As already mentioned, transformer core materials, operated within power electronics converters, are exposed to arbitrary square voltage waveforms, i.e. piece-wise linear flux waveforms. However, the material properties, such as loss density curves (as shown in **Figs. 2.6b** and **2.6c**), provided by core manufacturers are mostly acquired through standardized tests with sinusoidal waveforms and thus, they cannot be used directly for loss estimation in case of arbitrary excitation. The contained information needs to be generalized in some way.

Already in 1892 Steinmetz [89] introduced an expression for the loss density estimation of the core material. With time it evolved into a more general expression, which is commonly known as

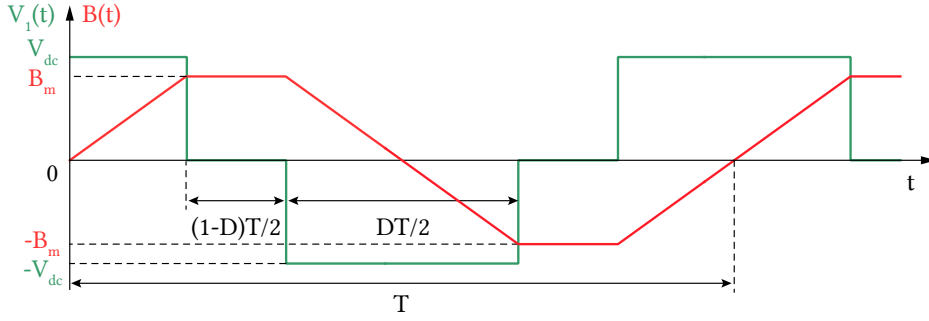


**Fig. 6.1** Square voltage excitation with zero-voltage periods and the corresponding flux density waveform.  $T$  is the time period,  $D$  the non-zero state duty cycle.

the original Steinmetz equation

$$P_c = K f_{sw}^\alpha B_m^\beta, \quad (6.1)$$

with  $K$ ,  $\alpha$ , and  $\beta$  as the Steinmetz loss coefficients. Their values can be determined based on the core loss density dependencies on the magnetic flux density  $B_m$  and the excitation frequency  $f_{sw}$ , usually provided in the magnetic material data sheets.

In order to extend the loss estimation to any non-sinusoidal excitation waveform, the IGSE is used. The equation builds on the original Steinmetz equation. According to [92], the IGSE is determined by the following expression in the integral form

$$P_c = \frac{1}{T} \int_0^T k_i \left| \frac{dB(t)}{dt} \right|^\alpha (\Delta B)^{\beta-\alpha} dt, \quad (6.2)$$

where  $T$  [s] represents the time period,  $\Delta B$  stands for the peak-to-peak induction ( $\Delta B = 2B_m$ ) and the coefficient  $k_i$  is defined as

$$k_i = \frac{K}{2^{\beta+1} \pi^{\alpha-1} \left( 0.2761 + \frac{1.7061}{\alpha+1.354} \right)}. \quad (6.3)$$

Ultimately, depending on the flux density waveform characteristic for each converter topology, a combination of (6.2) and (6.3) yields the final expression for the average power loss per unit of volume. Regarding the Steinmetz coefficients, **Tab. 2.2** from **Chap. 2** provides cataloged values for each of the three considered core magnetic materials. The values are obtained by fitting the available core loss density curves or by directly taking the coefficients from the literature.

Considering the particular converter the MFT is intended to be a part of, the LLC-SRC employed with the 3-level NPC topology for both power stages, the corresponding flux density waveform is provided in **Fig. 6.1** together with the voltage. The non-zero voltage is applied during the  $DT$  period, with  $D$  as the duty cycle, whereas the voltage is zero during the  $(1-D)T$  time. The flux density time derivative can be expressed as:

$$\left| \frac{dB(t)}{dt} \right| = \begin{cases} \frac{2\Delta B}{DT} & \text{during } DT, \\ 0 & \text{during } (1-D)T, \end{cases} \quad (6.4)$$

which simplifies derivation during the zero-voltage periods. Eventually, the core loss density from (6.2) can be calculated as:

$$P_c = 2^{\alpha+\beta} k_i f^\alpha B_m^\beta D^{1-\alpha} \quad (6.5)$$

Note that in order to obtain a two-level voltage waveform from the one presented in **Fig. 6.1**, the duty cycle needs to be set to 1. In this way, a 50 % rectangular voltage waveform is obtained and the corresponding flux density follows a triangular path. For a two-level voltage with an arbitrary duty cycle, the IGSE from (6.2) can be expressed as:

$$P_c = k_i f^\alpha (\Delta B)^\beta (D^{1-\alpha} + (1-D)^{1-\alpha}) \quad (6.6)$$

Magnetic materials are generally non-linear by nature and there is no orthogonality between the different harmonics [90]. Thus, it is not possible to observe the harmonic content of an arbitrary excitation waveform and apply the Steinmetz equation separately to each harmonic, in order to sum the calculated losses and in this way obtain the total core losses. For this reason, the best practice is to derive simpler analytical expressions from the original IGSE relation based on the characteristic voltage waveform.

## 6.3 Winding Loss Model

Unlike the core loss estimation, for the winding losses, it is possible to consider the full harmonic spectrum and sum the current contributions of different frequencies to the overall winding loss amount. However, for this purpose, the respective AC resistance of the windings needs to be correctly determined. One can recall that at increased frequencies the current density can be unevenly distributed across the conductor's cross section, due to skin and proximity effects, which in turn influences the conductor's resistance. Thus, it is important to be able to accurately model such effects.

### 6.3.1 1D Dowell's Model

As previously mentioned in **Chap. 2**, a standard and well-known approach of analytical nature for winding loss estimation relies on Dowell's model [106]. The model is derived by solving 2D Maxwell questions for ideal foil windings, under the assumptions of strictly 1D magnetic field inside of the core window area and the infinite permeability of the magnetic core. As a result, the model provides a frequency-dependent expression for the AC winding resistance by introducing a resistance factor  $F_r$ . In this way, the winding loss contribution of higher current harmonics can be taken into account. A detailed derivation of the model is provided in [47], [137]. Moreover, it is generally assumed that eddy current densities caused by the two eddy current effects inside a certain winding layer are orthogonal, which makes the calculation of winding losses easier. For the sake of completeness and the reader's comfort, **Fig. 6.2** is repeated from **Chap. 4**.

According to Dowell's model, the frequency-dependent AC resistance of an ideal foil winding is determined by

$$R_{ac} = F_r R_{dc}, \quad F_r = \Delta \left[ \zeta_1 + \frac{2}{3}(m^2 - 1)\zeta_2 \right], \quad \zeta_1 = \underbrace{\frac{\sinh(2\Delta) + \sin(2\Delta)}{\cosh(2\Delta) - \cos(2\Delta)}}_{\text{Skin effect factor}}, \quad \zeta_2 = \underbrace{\frac{\sinh(\Delta) - \sin(\Delta)}{\cosh(\Delta) + \cos(\Delta)}}_{\text{Proximity effect factor}}. \quad (6.7)$$

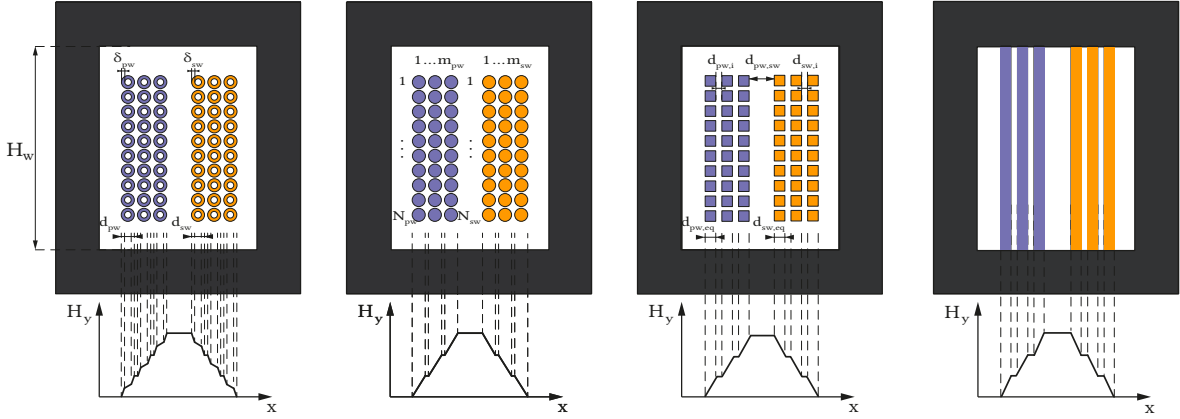


**Fig. 6.2** Winding equivalence with magnetic field distribution between hollow conductors and ideal foils as MFT windings, which cover the full core window height. The field distributions correspond to low penetration ratio values ( $\leq 1$ ).

The resistance factor  $F_r$  is able to consider both eddy current effects through the corresponding correction factors,  $\zeta_1$ , and  $\zeta_2$ . Their argument is the penetration ratio  $\Delta$  [1], which is defined by (4.5). Parameter  $m$  stands for the number of winding layers. **Fig. 6.3** shows the dependency of the skin and proximity effect factors on the penetration ratio. It can be noticed that for  $\Delta$  values higher than 3, in the case of  $\zeta_1$ , and 6, in the case of  $\zeta_2$ , the resistance factor  $F_r$  is determined solely by the penetration ratio itself and the number of layers. This observation is important for higher operating frequencies and larger conductor diameters.

The model from (6.7) can be as well applied to windings made of round solid wires, which is presented in the second figure on the left in **Fig. 6.2**. However, in that case, a porosity factor  $\eta$  needs to be introduced, to ensure equal effective conductivity of the two winding types, i.e. foil and solid round. The porosity factor is defined in (4.6), which affects the penetration ratio to change to (4.7). Pay attention to the winding current in the equivalence between the round and foil conductors. An  $N$ -turn winding of round conductors carrying the current  $I$  equates to a foil conductor with  $NI$  current. In other words, the AC resistance of another winding type of  $N$  turns needs to include a  $N^2$  multiplication factor compared to a single foil winding carrying the same current. A study conducted in [47] shows that high values of penetration ratio and a high number of layers in a winding rapidly increase the resistance factor  $F_r$ , i.e. the total winding resistance and consequently, the winding losses, as expected.

Finally, the total power loss experienced by a foil winding conducting the current  $NI$  is given by the following relation

$$P_{\text{loss},x} = \underbrace{\frac{\text{MLT}}{\eta \sigma m_x d_{x,\text{eq}} H_w}}_{R_{\text{dc}}} (NI_{\text{dc}})^2 + \sum_{n=1}^{\infty} R_{\text{ac},n} (NI_{\text{rms},n})^2. \quad (6.8)$$

The parameter  $n$  stands for the harmonic order of the winding current, MLT is the mean length turn,  $\sigma$  is the copper conductivity, and  $x$  replaces PW or SW. Note that the MLT value can be calculated for each winding layer to improve the  $R_{\text{dc}}$  estimation.

Similar to the leakage inductance estimation with the help of Dowell's model, the analytics behind cannot be directly applied to hollow conductors, e.g. by defining a suitable porosity factor. One can



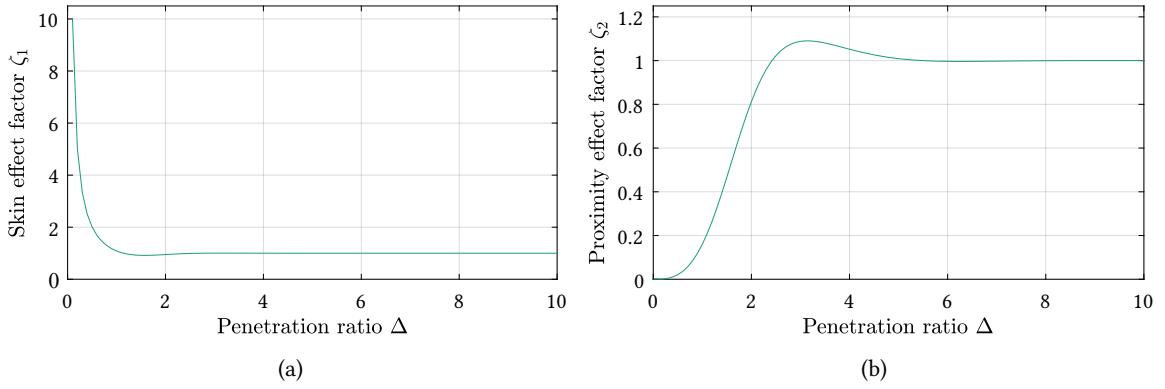


**Fig. 6.3** (a) Skin and (b) proximity effect factors from (6.7) presented as a function of the penetration ratio  $\Delta$ .

imagine that its value would be significantly smaller compared to a round solid winding of the same diameter, due to the presence of the hollow inner part, thus negatively impacting the validity of Dowell's model. Eventually, another solution for winding loss modeling in the case of pipe conductors needs to be found.

### 6.3.2 Model Extension for Hollow Conductors

Copper pipes as MFT windings are not as common as Litz or foil windings for MV high-power applications and are therefore insufficiently modeled and researched in the literature. Nevertheless, a literature review has revealed several works dealing with this topic in different ways. The authors in [112] first introduced the idea of dividing a hollow rectangular winding into parallel solid structures and derived an analytical expression for a single turn. The same idea is later used by many authors to derive loss analytical expressions for more complex winding structures, i.e. with multiple turns and multiple layers [160], [161] and including round hollow conductors as well. Note that the application here is not necessarily regarding MFT windings, but rather large capacity generators. The work from [162], [163] introduces the so-called A-model, which is based on the analytical solution of Laplace and Helmholtz equations in 2D for magnetic vector potential in the case of hollow round conductors, and it achieves the same accuracy as the finite element approach. Nevertheless, the AC loss model comes at a cost of high complexity expressions involving Bessel functions of first and second order. Lastly, the authors in [111] propose a semi-analytical solution to the problem by combining the analytical Dowell model and a numerically obtained resistance factor to determine the AC resistance of both round and rectangular hollow conductors. Having in mind that the winding loss model is vital for the MFT design optimization algorithm, the computationally least demanding model is selected from the above-mentioned ones, and that is the semi-analytical model from [111].

According to **Fig. 6.2**, to traverse the first step from the pipe to the solid round conductor, an additional resistance factor is characterized, termed as the hollow resistance factor  $F_h$  [1]. It gives the ratio between the AC resistance of a hollow and a solid round conductor. It is obtained with the help of numerous FEM simulations and determined particularly for both solid and square hollow conductors, defined by the following equation:

$$F_h = \frac{R_{ac,h}}{R_{ac,s}} \quad (6.9)$$

The round solid AC resistance  $R_{ac,s}$  is estimated with the help of (6.7). In order to characterize the necessary hollow resistance factor, two new parameters are introduced. Namely, the hollow permeability, also known as the hollow rate  $\chi$  [1] :

$$\chi = \frac{\delta_x}{d_x}, \quad (6.10)$$

which defines the ratio between the conductor's wall thickness ( $\delta_x$ ) and the external diameter ( $d_x$ ) for the respective winding  $x$ . Based on  $\chi$ , the hollow penetration ratio  $\Delta_h$  [1], is specified as

$$\Delta_h = \chi \Delta \Rightarrow \Delta_h = \frac{\delta_x}{\delta_{Cu}}. \quad (6.11)$$

The AC resistance correlation between the hollow and the solid conductor is determined with the help of numerous 2D simulations, looking into models with 1 – 3 winding layers, several ODs of the conductor (8 mm, 9 mm, and 10 mm), a wide range of  $\Delta_h$  from [0.6 – 2.5], i.e. various wall thicknesses, and a range of operating frequencies [2 kHz - 10 kHz]. In total, the AC resistance of a hollow conductor is obtained in the simulation of 1080 different models. The work explores both round and rectangular hollow conductors. A complete explanation and considered dependencies can be found in [111]. An important detail to keep in mind is that all the transformer models used in the FEM simulations had a high porosity factor, (0.6 – 0.8) in the case of round and (0.7 – 0.9) in the case of square conductors, which ensures that the AC resistance of the solid conductor is estimated accurately enough by the Dowell model. Nevertheless, note that the  $\eta$  factor is calculated with solid and not hollow conductors.

The analysis of the simulation data revealed that the  $F_h$  factor is not directly correlated with the OD or the number of layers in the winding, but it is related to the frequency and the hollow penetration ratio. The study from [111] concludes by providing several plots of hollow resistance factors at different frequencies and declaring the  $\Delta_h$  range [1.2 – 1.8] for both square and round conductors to be the one in which the winding losses are reduced and material utilization improved.

Considering the operating frequency of 5 kHz, the presented data in the plots is extracted and summarized in **Tab. 6.1** depending on the  $\Delta_h$  value. Having in mind the definition of the hollow penetration ratio, the study covers the conductor's wall thickness in the range of [0.5 mm – 2.3 mm].

The extracted values presented in **Tab. 6.1** are fitted with a polynomial function and implemented together with the analytical Dowell model. The fitted function is of sixth order and it is determined by the following equation

$$F_h = p_1 \Delta_h^6 + p_2 \Delta_h^5 + p_3 \Delta_h^4 + p_4 \Delta_h^3 + p_5 \Delta_h^2 + p_6 \Delta_h + p_7. \quad (6.12)$$

$\Delta_h$	0.6	0.7	0.8	0.9	1	1.1	1.2	1.3	1.4	1.5
$F_h$	1.63	1.443	1.303	1.198	1.126	1.069	1.02	0.99	0.969	0.956
$\Delta_h$	1.6	1.7	1.8	1.9	2	2.1	2.2	2.3	2.4	2.5
$F_h$	0.948	0.944	0.944	0.946	0.949	0.953	0.956	0.958	0.975	0.991

**Tab. 6.1** Extracted values of the hollow resistance factor  $F_h$  at 5 kHz and various values of the hollow penetration ratio  $\Delta_h$ .

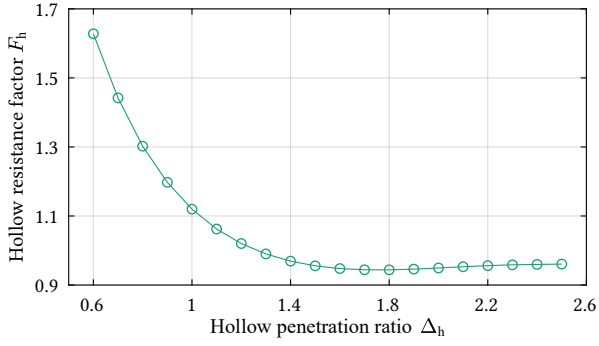


**Fig. 6.4** Graphical presentation of the hollow resistance factor  $F_h$  as a function of  $\Delta_h$ .

Coeff.	$p_1$	$p_2$	$p_3$	$p_4$	$p_5$	$p_6$	$p_7$
Value	0.07	-0.73	3.31	-8.19	12.04	-10.15	4.78

**Tab. 6.2** Coefficients of the fitted  $F_h$  at 5 kHz as a function of the hollow penetration ratio  $\Delta_h$ .

The scaling coefficients are provided in **Tab. 6.2**, whereas **Fig. 6.4** shows graphically the dependency between the hollow resistance factor and the penetration ratio. Eventually, the total winding losses are obtained by observing the full harmonic current content and applying the appropriate AC resistance, as stated in (6.8).

## 6.4 Static Thermal MFT Model

As already mentioned in **Sec. 2.5.4**, the selection of materials and technologies used for the MFT design has a key role in characterizing the component thermally. Because the windings are actively cooled, a temperature gradient is formed from the top to the bottom of the windings. Thus, one can observe that in the case of the 2-vessel MFT structure, only two plane symmetries exist, which are illustrated in **Fig. 6.5**. Partitioning the MFT in smaller symmetrical parts significantly simplifies the derivation of the analytical model, as well as reduces the computational and execution time of FEM simulations. Thus, in this particular case and according to **Fig. 6.5**, it is sufficient to model and simulate a quarter of the complete MFT. Nevertheless, for both core and winding parts only one-half of the component is analytically modeled. The oil vessels with windings are axially symmetric, therefore, as was the case in the previous chapter, it is sufficient to observe only one-half of the vessel.

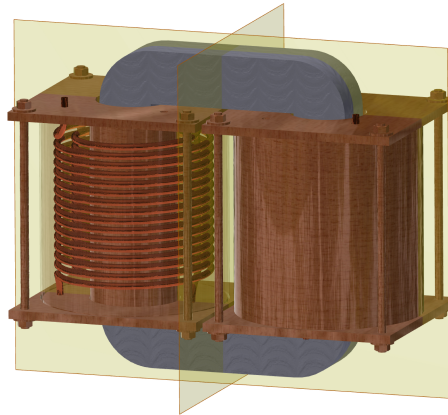


**Fig. 6.5** Partitioning of the 2-vessel MFT according to thermal and geometric symmetry planes.

The usual approach which can be found in the literature regarding thermal modeling is to assemble the thermal admittance matrix, based on the relevant temperature nodes and the injected power losses of the core and windings in the thermal network of the component. In this way, one can directly obtain the temperature differences between the suspected hot spots and the ambient temperature. However, in this case a uniform temperature of the ambient needs to be assumed, otherwise, setting up of admittance matrix with two or more ambient temperatures becomes very complex. An alternative approach would be to consider the worst case and assume all the different ambient temperatures take the highest expected value. Nevertheless, this approach could lead to overdimensioning of the MFT, since, in the considered case of the 2-vessel MFT structure, the lowest and the highest expected ambient temperatures can differ 2 – 3 times in value. This is explained in more detail in **Sec. 6.4.3**.

Moreover, a general tendency when developing a thermal model is to simplify and neglect certain heat exchange mechanisms, which is very often the case with radiation. However, before applying the simplification, one should first make sure that its effect on the hot-spot temperatures is indeed minor. To give an example, in the case of heat dissipation of the core, radiation plays an important role next to natural convection [44]. However, for actively cooled windings, radiation as a heat exchange mechanism can be overlooked, as it is shown in the example of the full and simplified thermal winding model. The static thermal model developed in this thesis combines two analytical parts, each corresponding to a major loss contributor, i.e. core and windings. The connection between the two is established with an interface ambient model since the two parts do not have direct physical contact. They can be, thus, modeled separately, which facilitates the derivation.

### 6.4.1 Thermal Core Model

For modeling purposes the considered core half is divided into three zones: a center, which corresponds to the core limb passing through the oil vessel, and two external core parts, top and bottom, as illustrated in **Fig. 6.6a**. The core half from the figure corresponds to a CAD model of the 2-vessel MFT and includes top and bottom Al plates, which are used for vertical clamping and stabilizing of the core, and additionally contribute to the heat exchange process between the core and the environment. The oil vessel from **Fig. 6.6a** is presented empty, without the windings, in order not to block the view of the core center leg. Accordingly, the core losses are shared in three parts, based on the respective volume of each part, namely,  $P_{ce}$ , for the two external core parts, and  $P_{cc}$ , for the core center. Due to a small expected air gap, the potentially higher core losses due to fringing effect have not been considered. The corresponding thermal model assumes a radially laminated core material, such as amorphous or nanocrystalline, and it is illustrated in **Fig. 6.6b**. This information is particularly important when modeling the conduction thermal resistances within the core.

To determine the thermal hot spot of the core, six various core temperatures are observed and estimated, namely, three center temperatures in each of the three core parts,  $T_{m,t}$ ,  $T_{m,b}$ , and  $T_{m,cc}$ , and three temperatures on the inner core surfaces,  $T_{ce,t}$ ,  $T_{ce,b}$ , and  $T_{cc}$ . The positions of the selected temperatures in the core are pointed out in **Fig. 6.6b** with red dots. The selection is supported by the fact that different ambient temperatures develop during transformer operation. Namely, the inner ambient temperature, marked with  $T_3$  in **Fig. 6.6a**, between the inner oil vessel wall and the inner surface of the core center leg, is higher than the outer temperature  $T_2$ , which is the air temperature between the same vessel wall and the outer surfaces of the core leg. Both of these temperatures reach higher values than the general air temperature  $T_1$ . Therefore, it makes sense to observe the inner core surface temperatures, rather than the outer ones. Lastly, one can conclude that the hottest

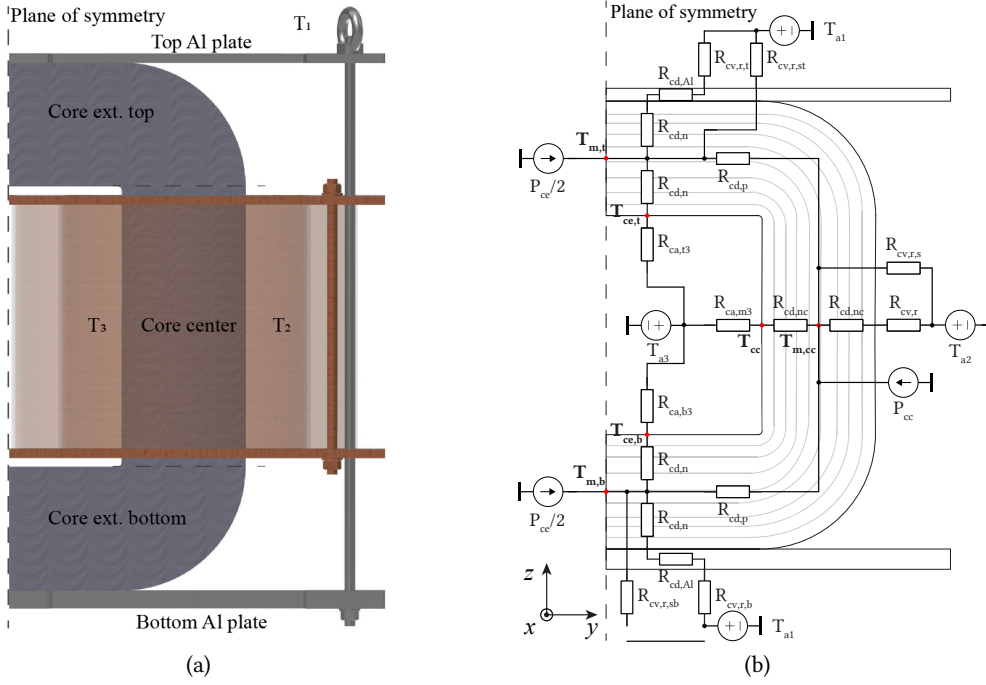


**Fig. 6.6** (a) Partitioned MFT half according to the symmetry planes shown in **Fig. 6.5**; (b) Detailed thermal network of the MFT core part, which considers three ambient temperatures that serve as interface between the winding and the core thermal model. Resistances with the subscript *cd* describe conductive heat exchange, whereas *cv* and *r* mark a parallel connection of corresponding convective and radiative resistances.

core point can be expected inside of the core for  $T_{m,cc}$ , due to heated ambient, in contrast to the two external core parts, which are surrounded by air temperature  $T_1$ . Additionally, black dots mark either a known temperature or a connection between the crossing of thermal lines. The three different air temperatures are additionally illustrated in **Fig. 6.11a**.

The governing equations of the thermal core model, which determine the six selected temperature points, are derived from the corresponding thermal network given in **Fig. 6.6b** and are given below:

$$T_{m,t} : \frac{P_{ce}}{2} + \frac{T_{ce,t} - T_{m,t}}{R_{cd,n}} + \frac{T_{a1} - T_{m,t}}{R_{ca,t}} + \frac{T_{m,cc} - T_{m,t}}{R_{cd,p}} = 0 \quad (6.13)$$

$$T_{m,b} : \frac{P_{ce}}{2} + \frac{T_{ce,b} - T_{m,b}}{R_{cd,n}} + \frac{T_{a1} - T_{m,b}}{R_{ca,b}} + \frac{T_{m,cc} - T_{m,b}}{R_{cd,p}} = 0 \quad (6.14)$$

$$T_{ce,t} : \frac{T_{m,t} - T_{ce,t}}{R_{cd,n}} + \frac{T_{a3} - T_{ce,t}}{R_{ca,t3}} = 0 \quad (6.15)$$

$$T_{ce,b} : \frac{T_{m,b} - T_{ce,b}}{R_{cd,n}} + \frac{T_{a3} - T_{ce,b}}{R_{ca,b3}} = 0 \quad (6.16)$$

$$T_{m,cc} : P_{cc} + \frac{T_{cc} - T_{m,cc}}{R_{cd,nc}} + \frac{T_{a2} - T_{m,cc}}{R_{ca,s}} + \frac{T_{m,t} - T_{m,cc}}{R_{cd,p}} + \frac{T_{m,b} - T_{m,cc}}{R_{cd,p}} = 0 \quad (6.17)$$

$$T_{cc} : \frac{T_{m,cc} - T_{cc}}{R_{cd,nc}} + \frac{T_{a3} - T_{cc}}{R_{ca,m3}} = 0 \quad (6.18)$$

The equations are acquired by applying the thermal equivalent of Kirchhof's laws to the established thermal circuit. Regardless of the 2D representation, the thermal network considers heat exchange in all three directions. To improve clarity, the resistances defined in the thermal core model in **Fig. 6.6b** are listed below:

- $R_{cd,n}, R_{cd,p}, R_{cd,nc}, R_{cd,Al}$ :

As already mentioned, the thermal conductivity of a laminated core material is an anisotropic quantity, therefore, three conduction resistances are defined within the core. The resistances  $R_{cd,n}$  and  $R_{cd,nc}$  describe conduction transfer following the heat flow in the direction normal to the core surfaces, i.e. in  $z$  and  $y$  direction, respectively. The difference between them is in the surface area that participates in the exchange. In the case of a laminated magnetic material, its thermal conductivity is worse in the direction normal to the lamination than along the lamination sheets. Therefore,  $R_{cd,p}$  describes the conductive exchange in the tangential direction. The resistance  $R_{cd,Al}$  introduces the conduction in Al plates in the  $z$  direction.

- $R_{cv,r,t/b}, R_{cv,r,st/sb}, R_{cv,r}, R_{cv,r,s}$ :

Thermal resistances with  $cv$  and  $r$  subscripts mark a parallel connection of the corresponding convective and radiative resistances, combined in a single component. The subscripts  $t$  and  $b$  stand for top and bottom since one can expect temperature differences between the two. To provide an example regarding convection, the Nusselt correlations differ for heat exchange from the upside and the downside of a horizontal plate, see **Tab. 6.3**. Moreover, the resistances marked with a subscript  $s$  account for the heat exchange in the out-of-plane, i.e.  $x$ , direction from the core to the surrounding ambient.

- $R_{ca,t}, R_{ca,b}, R_{ca,s}$ :

The three thermal resistances from (6.13), (6.14), and (6.17) characterize the heat exchange between the core middle points and the ambient. They combine all three heat exchange mechanisms in a single thermal resistance and in this way simplify the presented equations. In reality, they are compositions of several resistances, which are explained above and illustrated in **Fig. 6.6b**.

- $R_{ca,t3}, R_{ca,b3}, R_{ca,m3}$ :

The last three resistances describe similar to the ones defined above, heat exchange between the inner top, bottom, and the inner side core surface to the increased ambient temperature  $T_{a3}$ . For that reason, subscript 3 is added. They are presented as single components but include a parallel connection of convection and radiation thermal resistances.

As shortly explained in **Sec. 2.5.4.1**, thermal resistances are determined by the respective HTC and the contact surface. In the case of conduction HTC, one must know the flow direction and the respective thermal conductivity of the participating material. The convection HTC is heavily determined by the surface geometry and the medium properties. Convective heat transfer of the core includes loss dissipation on vertical sides of the core, as well as horizontals. Furthermore, the horizontal sides of the top and bottom Al plates aid in the cooling process. The relevant Nusselt correlations for these configurations are summarized in **Tab. 6.3**. Note that the corresponding reference for each of the stated correlations is given at the end of the row. Once the thermal resistances have been determined, based on the geometry and material properties as well as the relevant heat transfer mode, the equation system given in (6.13)-(6.18) is easily solved with the help of numeric computing software Maple. The obtained analytical expressions for the six selected core temperatures are used in the MFT design tool

to estimate the thermal core image, and they are not explicitly provided.

### 6.4.2 Thermal Winding Model

A typical electrical application of Cu hollow conductors is as stator windings of electrical machines, which exploit the direct liquid cooling option that this type of conductor offers. Being a more common application than the transformer windings, the relevant literature regarding thermal modeling in the context of direct cooling for electrical machines was researched. In this regard, the majority of modeling techniques rely on CFD simulations [164], [165], however, this is not suitable for implementation in a design optimization procedure, due to increased computational time. Some of the alternatives include setting up a thermal network made of lumped parameters combined with a fluid model, which determines the fluid distribution [166], or a thermal model of hollow cuboidal elements which is computationally more efficient than CFD [167].

#### 6.4.2.1 Full Model

As a first step, one should predict the location of the warmest winding point. Considering the active cooling of the windings, the conductor temperatures increase from the top to the bottom, therefore, it can be assumed that the thermal hot spot during operation will appear at the bottom of the two windings. This is further confirmed with the winding temperature measurements of the down-scaled experimental setup, shown later in **Sec. 6.4.2.3**. Similar to the THM, winding terminations, in and out from the vessel, are not explicitly considered in the derivation of the thermal model. Nevertheless, one can suspect that the Cu temperature keeps increasing with the rising temperature of the descending DI water coolant. In other words, the conductor is slightly warmer at the vessel bottom than at the end of the last turn, which is considered for modeling purposes. Secondly, the conductor pipe changes the medium once it leaves the vessel, from oil to air. The convective HTC of oil to Cu is significantly higher than the one between the air and Cu, due to improved thermal properties of the insulation oil, whereas the temperature difference between the two media close to the vessel bottom can go up to a factor of 1.5 in favor of the oil temperature, i.e. the oil temperature is higher than the one of air up to 1.5 times. Still, considering that the highest amount of winding losses gets exchanged with the DI water, the Cu temperature is strongly determined by the output DI water temperature and the forced convection heat exchange. Thus, one can expect that the actual Cu warmest point is at the very bottom of the winding outside of the oil vessel, at the contact with the hose, which electrically decouples the winding from the WCU and takes away the warmed DI water. Nevertheless, compared to the bottom of the last winding turn, which is considered to be the hot spot for modeling purposes, the physical hot spot temperature is only slightly lower, since the two points are spatially close.

In order to estimate the relevant winding temperatures, the windings are horizontally divided into top and bottom parts, and the corresponding winding losses,  $P_{\text{loss,pw}}$ , and  $P_{\text{loss,sw}}$ , are divided into two accordingly. The thermal network developed for this part of the static thermal model is given in **Fig. 6.7a**. **Fig. 6.7b** introduces the nomenclature used for describing the windings, namely, helical radiuses of the PW and SW,  $R_{a,\text{PW}}$ , and  $R_{a,\text{SW}}$ , and the ID and OD of the pipe cross section,  $D_i$  and  $D_u$ , respectively. Note that in order to improve the estimation accuracy, the winding losses can be divided into a higher number of smaller parts which would be evenly distributed between the top and bottom winding parts. However, this would significantly complicate the model solution and have a negative effect on its execution time.

The equations which describe the thermal image of the windings inside of the oil vessel, derived from

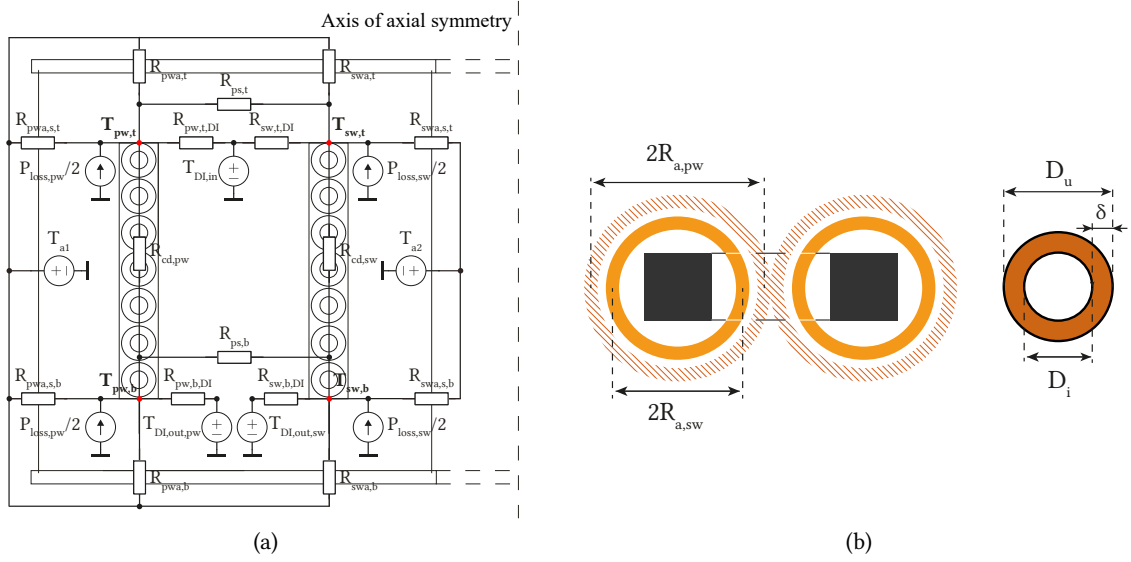


**Fig. 6.7** (a) Thermal model of the oil vessel with windings, due to axial symmetry only one-half is considered; (b) Size properties of pipe conductors used as PW and SW, shown on the examples of the 2-vessel MFT and pipe cross section.

the thermal network shown in **Fig. 6.7a**, are given in the following for each of the characteristic winding temperatures:

$$T_{pw,t} : \frac{P_{loss,pw}}{2} + \frac{T_{sw,t} - T_{pw,t}}{R_{ps,t}} + \frac{T_{a1} - T_{pw,t}}{R_{pwa,t}} + \frac{T_{a1} - T_{pw,t}}{R_{pwa,s,t}} + \frac{T_{pw,b} - T_{pw,t}}{R_{cd,pw}} + \frac{T_{DI,in} - T_{pw,t}}{R_{pw,DI,t}} = 0 \quad (6.19)$$

$$T_{pw,b} : \frac{P_{loss,pw}}{2} + \frac{T_{sw,b} - T_{pw,b}}{R_{ps,b}} + \frac{T_{a1} - T_{pw,b}}{R_{pwa,b}} + \dots \\ \dots + \frac{T_{a1} - T_{pw,b}}{R_{pwa,s,b}} + \frac{T_{pw,t} - T_{pw,b}}{R_{cd,pw}} + \frac{T_{DI,out,pw} - T_{pw,b}}{R_{pw,DI,b}} = 0 \quad (6.20)$$

$$T_{sw,t} : \frac{P_{loss,sw}}{2} + \frac{T_{pw,t} - T_{sw,t}}{R_{ps,t}} + \frac{T_{a1} - T_{sw,t}}{R_{swa,t}} + \frac{T_{a2} - T_{sw,t}}{R_{swa,s,t}} + \frac{T_{sw,b} - T_{sw,t}}{R_{cd,sw}} + \frac{T_{DI,in} - T_{sw,t}}{R_{sw,DI,t}} = 0 \quad (6.21)$$

$$T_{sw,b} : \frac{P_{loss,sw}}{2} + \frac{T_{pw,b} - T_{sw,b}}{R_{ps,b}} + \frac{T_{a1} - T_{sw,b}}{R_{swa,b}} + \dots \\ \dots + \frac{T_{a2} - T_{sw,b}}{R_{swa,s,b}} + \frac{T_{sw,t} - T_{sw,b}}{R_{cd,sw}} + \frac{T_{DI,out,sw} - T_{sw,b}}{R_{sw,DI,b}} = 0 \quad (6.22)$$

Regarding the pipe conductor, the conductive thermal resistance can be correctly determined by observing the ways of the heat flow. Namely, the heat is flowing tangentially between the top and bottom part, as well as radially, between the pipe and two liquid media (DI water and oil). The two thermal resistances [82] are defined as

$$R_{cd,tan} = \frac{L_x}{k_{Cu} A_{Cu}}, \quad \text{with } A_{Cu} = (D_u^2 - D_i^2) \frac{\pi}{4}, \quad \text{and } R_{cd,rad} = \frac{\ln(D_u/D_i)}{2\pi k_{Cu} L_x}, \quad (6.23)$$

thereby,  $x$  stands for PW or SW. Parameter  $L_x$  gives the winding's length,  $A_{Cu}$  is the pipe cross-section area and  $k_{Cu}$  is the thermal conductivity of Cu.



The thermal resistances defined in the thermal winding model are listed below with explanations:

- $R_{cd,x}$ :  
The conductive heat transfer between the top and bottom of the two windings, i.e. tangential to the winding direction, is described by the thermal resistance  $R_{cd,x}$ .
- $R_{xa,t/b}$ ,  $R_{xa,s,t/b}$ :  
According to the thermal network presented in **Fig. 6.7a** and the relative position of the thermal resistances in regard to the illustration of one-half of the oil vessel, 8 thermal resistances describe the heat exchange between the windings and the ambient air. Thereby, each of them represents an aggregation of all three heat exchange mechanisms. The letters  $t$  and  $b$  in the subscript denote top and bottom winding parts, whereas  $s$  stands for the side heat exchange, either on the outer or the inner vessel wall. To provide an example,  $R_{pwa,s,t}$  combines a series composition of a parallel connection (convection and radiation) to describe top PW to outer vessel wall exchange, conduction through the wall, and another parallel connection for the outer oil vessel wall to ambient air exchange.
- $R_{ps,t/b}$ :  
The heat exchange between the PW and SW is described by convection and the Nusselt correlation empirically obtained for vertical coaxial cylinders, with oil as the participating medium. Considering that the top and bottom conductors are of significantly different temperatures, two separate thermal resistances are defined.
- $R_{xt/b,DI}$ :  
To describe the heat transfer between each of the windings and the incoming and outgoing DI water, the corresponding thermal resistance is defined as a series connection of radial conduction through Cu and forced convection resistances.

Unlike the thermal model of the core, the winding model involves delicate/problematic to describe convective heat transfers. A good example is the natural convection of oil between the two windings inside of the vessel or between the windings and the outer and inner vessel walls. Such configurations are addressed/solved by introducing a simplification, i.e. windings are assumed to be made of foil conductors with the same thickness as the OD of the pipe. In this way, it is possible to approximate the heat exchange to the one in a vertical coaxial cylinder. Similarly, the convection inside the inner vessel wall and outside the outer wall is described by Nusselt correlations empirically obtained for the internal and external exchange of a vertical cylinder, respectively.

Moreover, forced convection inside vertical helical pipes is more complicated than in straight pipes, due to forming of secondary flows in the cross section, and it is, thus, more difficult to characterize. Luckily, helical pipes are used in many industries as part of heat exchangers, and as a result, it is possible to find numerous Nusselt correlations. They are usually defined in a certain range of dimensionless parameters and developed based on experimental data. Moreover, the resulting HTC has a geometric aspect as well and is strongly dependent on the curvature factor (ratio between the conductor's ID and helical diameter of the winding) and turn-to-turn distances. Therefore, the number of different geometries of helical pipes covered in literature is limited. Lastly, considering that the pipes are employed as MFT windings, the Nusselt correlations used to determine the respective HTC need to be particularly developed for constant heat flux Boundary Conditions (BCs). It is one of the two common BCs, the other one being constant wall temperature. Having in mind that convective HTCs are temperature dependent, it is differentiated between the top and bottom thermal resistances

describing the exchange between each of the windings and DI water, reflected in  $R_{x,DI,t}$  and  $R_{x,DI,b}$ , respectively. All the relevant Nusselt correlations used in the model and their respective ranges of validity are cataloged at the end of this chapter in **Tab. 6.3**, due to space reasons. In case the geometrical and thermal conditions between the vertical vessel walls and windings do not match the conditions of the Nusselt correlations employed for vertical coaxial cylinders, i.e. vertical circular annuli, as a replacement, the geometry is approximated with a rectangular enclosure. Taking into consideration that the convective and radiate HTC's are strongly temperature-dependent, the thermal model is implemented iteratively, so that all the applicable HTC's are determined at the correct medium and surface temperatures. In contrast to the thermal core part, this model considers only two ambient temperatures,  $T_{a1}$  and  $T_{a2}$ , since the latter temperature has significantly larger contact with the inner oil vessel wall, see **Fig. 6.6a**, compared to  $T_{a3}$ .

Furthermore, the inlet DI water temperature ( $T_{DI,in}$ ) is one of the design constraints, as stated in **Tab. 3.2**, however, the corresponding outlet temperature for each winding is not known. Its value depends on the amount of dissipated winding losses, the volumetric flow of the passing fluid, and other factors, and it can be estimated by the following relation

$$T_{DI,out,x} = T_{DI,in} + \frac{P_{loss,x}}{c_{p,DI}\dot{m}}. \quad (6.24)$$

Thereby,  $P_{loss,x}$  is the conduction loss of the winding  $x$  modeled in **Sec. 6.3**,  $c_{p,DI}$  is the specific heat capacity of DI water and  $\dot{m}$  is the mass flow passing through the observed winding.

Finally, once all the thermal resistances have been determined, the closed expressions for the four winding temperatures are obtained by solving the system (6.19) - (6.22) with the help of Maple. Explicit expressions are not provided. Nevertheless, considering the fact that an MFT design optimization algorithm requires accurate but fast to execute models, a simplified version of the thermal winding model is considered, which is presented in the following. After introducing the simplified version of the model, both the full and simplified model are compared with the experimentally obtained winding temperatures from the THM test setup.

#### 6.4.2.2 Simplified Model

The idea for a less complicated thermal winding model comes from the understanding that active cooling, i.e. forced convection, is the dominant heat exchange mechanism, which when considered alone can to a great extent predict the winding temperatures. This is to say that any other heat transfer from the surface is not considered in this simplified version. The top and bottom Cu temperatures are determined based on the input DI water temperature and the number of dissipated losses, as well as the HTC based on the Nusselt correlation for a helical pipe. The simplified analytical expressions for the top and bottom temperatures of the winding  $x$  are marked with  $\sim$  and given below:

$$\tilde{T}_{x,t} = T_{DI,in} + \frac{P_{loss,x}}{A_{in,x}h_{cv,x,t}} \quad (6.25)$$

$$\tilde{T}_{x,b} = T_{DI,out,x} + \frac{P_{loss,x}}{A_{in,x}h_{cv,x,b}} \quad (6.26)$$

Thereby,  $A_{in,x}$  is the contact surface area between the cooling medium and the Cu conductor, expressed by the following equation:

$$A_{in,x} = D_i\pi L_x \quad (6.27)$$

Similar to the model from the previous section, the simplified model also considers the temperature effect on the convective HTC, reflected in top and bottom values,  $h_{cv,x,t}$  and  $h_{cv,x,b}$ . In a like manner, both HTC are determined iteratively. The output temperature of the DI water ( $T_{DI,out,x}$ ) is estimated with the help of (6.24).

### 6.4.2.3 Model Verification

The thermal winding model is verified with the help of thermal measurements acquired for characterization of the THM, presented in the previous chapter, in **Sec. 5.3**. **Figs. 6.8 to 6.10** show the

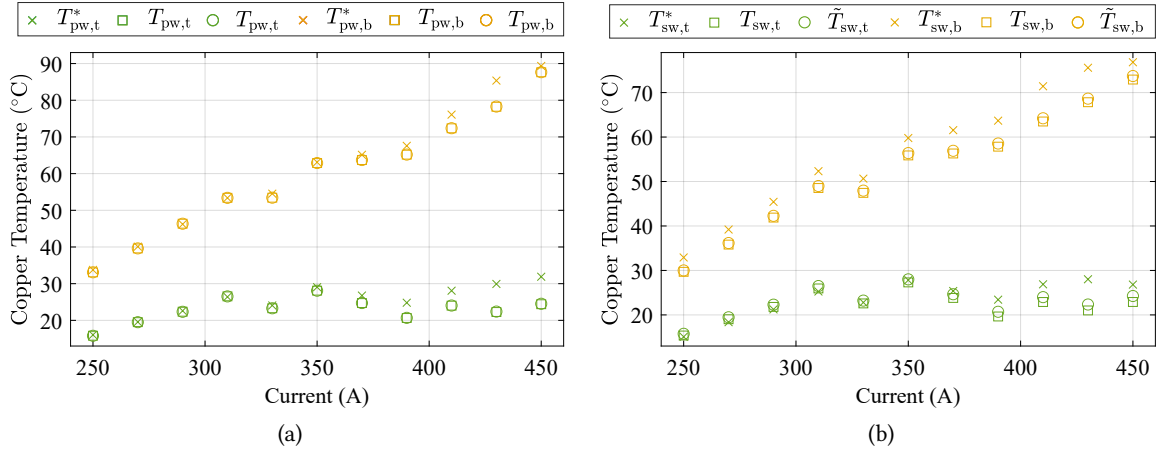


**Fig. 6.8** Comparison of measured and modeled (a) PW and (b) SW top and bottom conductor temperatures for various operating points at the volumetric flow of 16 ml/s. Measured winding temperatures ( $T_{x,t/b}^*$ ) are marked with  $\times$  in the graphs, the full model temperature estimations ( $T_{x,t/b}$ ) are denoted with  $\square$ , and the simplified model estimations ( $\tilde{T}_{x,t/b}$ ) with  $\circ$ .

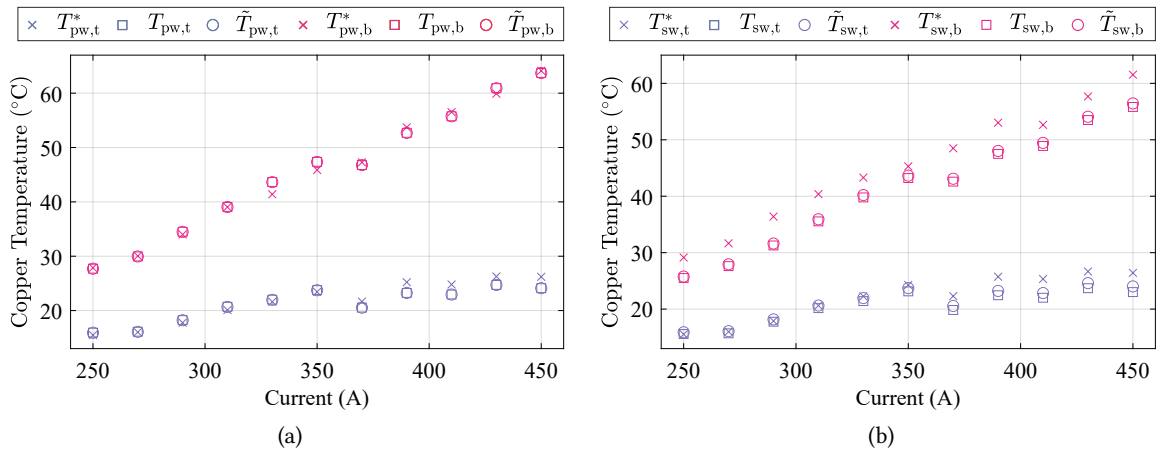


**Fig. 6.9** Comparison of measured and modeled (a) PW and (b) SW top and bottom conductor temperatures for various operating points at the volumetric flow of 23 ml/s. Measured winding temperatures ( $T_{x,t/b}^*$ ) are marked with  $\times$  in the graphs, the full model temperature estimations ( $T_{x,t/b}$ ) are denoted with  $\square$ , and the simplified model estimations ( $\tilde{T}_{x,t/b}$ ) with  $\circ$ .

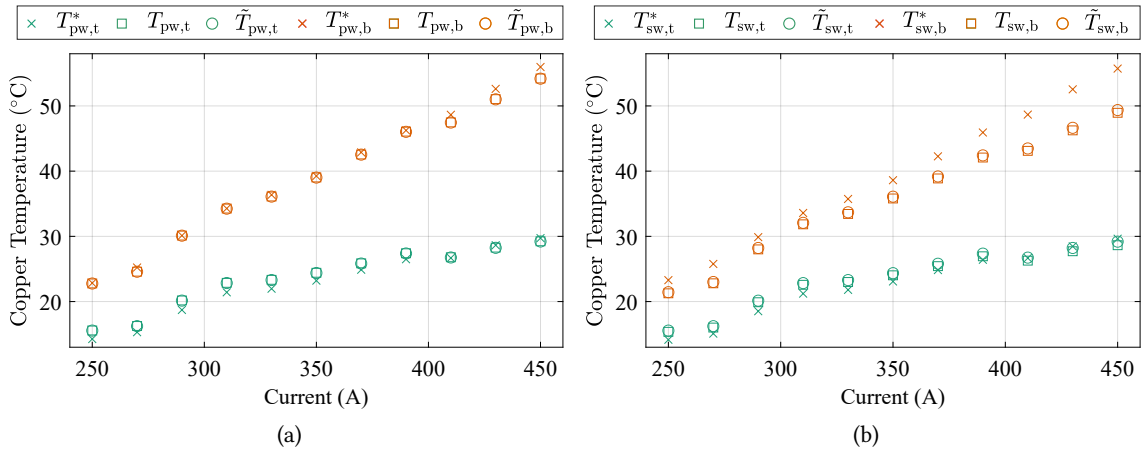


**Fig. 6.10** Comparison of measured and modeled (a) PW and (b) SW top and bottom conductor temperatures for various operating points at the volumetric flow of 36 mL/s. Measured winding temperatures ( $T_{x,t/b}^*$ ) are marked with × in the graphs, the full model temperature estimations ( $T_{x,t/b}$ ) are denoted with □, and the simplified model estimations ( $\tilde{T}_{x,t/b}$ ) with ○.

comparison between the measured and modeled top and bottom winding temperatures for various volumetric flow values, namely, 16 mL/s, 23 mL/s, and 36 mL/s, respectively, and for various induced winding losses. Thereby, both full and simplified thermal winding models are presented. Depending on the operating point and the cooling conditions, the alignment between the values varies. Some of the observations that can be made from **Figs. 6.8** to **6.10** are the following:

- For most of the observed experimental measurements, both model estimations match well with the measured temperatures.
- Estimation of the SW temperatures regardless of the cooling conditions is worse compared to PW temperatures. Moreover, it could be said that top conductor temperatures are generally modeled more accurately than the temperatures at the bottom. The reasons for such trends are at this point unclear.
- Regarding the comparison between the full and simplified model, the latter predicts slightly higher SW temperatures and very similar values of the PW temperatures for all the considered operating points compared to the full model.
- The discrepancy between the modeled and the measured temperatures generally increases for higher conduction losses, which can be nicely observed in **Fig. 6.10b**. Additionally, the deviation is growing for both top and bottom Cu temperatures for less efficient cooling conditions, as opposed to having a higher value of DI water volumetric flow. This can be observed by comparing **Figs. 6.8a** and **6.8b** with **Figs. 6.10a** and **6.10b**, respectively.
- The highest relative underestimation disparity between the measured value and the full model estimation is reaching 25% for the bottom PW and SW temperature estimations in **Fig. 6.8a** at 430 A operating point. The highest relative difference for the simplified model is recorded around the same value and operating point at the bottom PW temperature. In the case of SW, the relative discrepancy reduces to 20%. The stated percentages show the relative temperature

difference expressed in °C between the measurements and the models.

- In conclusion, the model which considers solely the forced convection between the windings and the DI water has almost the same accuracy as the detailed model and is even slightly better at estimating the measured temperatures in the case of SW when compared in the context of available thermal measurements from the THM experimental setup.

Regarding the discrepancy between the modeled and measured values, its cause can lie in the measuring uncertainties of the temperatures, but also in the selection of the relevant Nusselt correlations and their respective ranges of validity. Lastly, the simplified version of the thermal winding model is selected to be a part of the MFT design optimization algorithm.

### 6.4.3 Ambient Interface Model

As already mentioned, the two separately thermally modeled MFT segments, core and windings, are connected by a thermal interface model. Thereby, the model provides two ambient temperatures,  $T_{a2}$  and  $T_{a3}$ , which are essentially influenced by the dissipated core and winding losses, as well as the selected cooling conditions. According to **Fig. 6.11a**, the temperature  $T_{a2}$  is affected by the temperatures of the inner vessel wall, the outer surfaces of the core center leg, and the general ambient temperature  $T_{a1}$ , whereas  $T_{a3}$  is the temperature of the air inclosed between the inner oil vessel wall and the top, bottom, and side core surfaces. To determine the interface thermal conditions for the nominal operating point of the MFT, two simple static thermal networks are developed, presented in **Fig. 6.11b** and **Fig. 6.11c**, based on the core and oil vessel arrangement illustrated in **Fig. 6.11a**. Having in mind the fact that the diameter of the inner vessel wall is selected to be as small as needed in order to accommodate the designed cross section of the core leg, it can be assumed that the two resulting ambient temperatures are effectively separated from each other.

According to **Fig. 6.11b** and **Fig. 6.11c**, the following governing equations can be derived for each of the interface temperatures:

$$T_{a2} : \frac{T_{vw,in} - T_{a2}}{R_{vwa2}} + \frac{T_{a1} - T_{a2}}{R_{a,ch}} + \frac{T_{cc,s} - T_{a2}}{R_{ca,s2}} = 0 \quad (6.28)$$

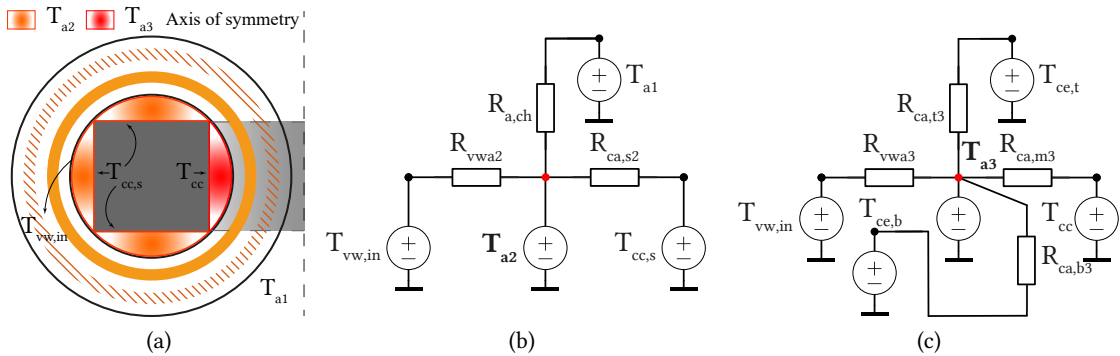


**Fig. 6.11** (a) Cross-section view of one-half of the 2-vessel MFT with indicated relevant temperatures for the ambient thermal models; Static thermal networks developed to estimate (b)  $T_{a2}$  and (c)  $T_{a3}$  ambient temperatures, located inside the inner oil vessel cylinders as marked in (a).

$$\mathbf{T}_{a3} : \frac{T_{vw,in} - T_{a3}}{R_{vwa3}} + \frac{T_{ce,t} - T_{a3}}{R_{ca,t3}} + \frac{T_{ce,b} - T_{a3}}{R_{ca,b3}} + \frac{T_{cc} - T_{a3}}{R_{ca,m3}} = 0 \quad (6.29)$$

The temperature  $T_{vw,in}$  is the average surface temperature of the inner vessel wall. For modeling purposes, it is assumed that it takes the average oil temperature. Regarding the core surfaces, all three non-inner core leg temperatures assume the value  $T_{cc,s}$ , which can be derived from the thermal core model from **Sec. 6.4.1**. The inner core surface temperature is  $T_{cc}$ , which together with the top and bottom temperatures of the external core parts,  $T_{ce,t}$ , and  $T_{ce,b}$ , respectively, is resulting from the same thermal core model.

The thermal resistances required for the two thermal ambient models are listed below:

- $R_{vwa2/3}$ :  
The two thermal resistances each describe a parallel composition of the convective and radiative heat exchange between the inner vessel wall surface and the interface temperatures  $T_{a2}$  and  $T_{a3}$ .
- $R_{a,ch}$ :  
The heat transfer to the top and bottom open areas, with assumed temperature  $T_{a1}$ , is modeled simply as convection in vertical channels with symmetric isothermal plates.
- $R_{ca,t3/b3}$ :  
The ambient temperature  $T_{a3}$  is affected by the presence of the external top and bottom core parts, which is characterized by the convective and radiative heat exchange between the core and the ambient.
- $R_{ca,s2}, R_{ca,m3}$ :  
The heat exchange between the surfaces of the core leg and the two defined interface temperatures are described by the two resistances. They both combine convection and radiation.

To determine the inner vessel wall temperature  $T_{vw,in}$ , it is necessary to determine the oil temperature inside the vessel. For this purpose, it is assumed that the oil takes a uniform temperature in each vessel and exchanges heat with the windings and the outside ambient through the vessel walls. Considering that the heat transfer is worse at horizontal than vertical surfaces and assuming that the vertical walls of the vessel have a higher surface area than the top and bottom lids, only vertical heat exchange is considered. The simple thermal network used to determine the oil temperature is provided in **Fig. 6.12a** and it is determined by the following equation:

$$\mathbf{T}_{oil} : \frac{T_w - T_{oil}}{R_{ow}} + \frac{T_{a1} - T_{oil}}{R_{oa1}} + \frac{T_{a2} - T_{oil}}{R_{oa2}} = 0 \quad (6.30)$$

The thermal resistance  $R_{ow}$  aggregates the heat exchange between both windings at the average winding temperature of  $T_w$  and the oil. Thereby, vertical surfaces of the windings, modeled as foil conductors, are considered. Similarly, the exchange with the ambient is modeled by  $R_{oa1}$  and  $R_{oa2}$ , which combines all three heat transfer mechanisms at the outer and inner vertical vessel walls, respectively.

At this point, all three parts of the static thermal model are presented and **Fig. 6.12b** illustrates their interactions and the participating temperatures from each model. In the simplified thermal winding model, the top and bottom winding temperatures are not directly affected by the ambient, but their values determine, among other things, the average oil temperature developed inside of the vessel. In

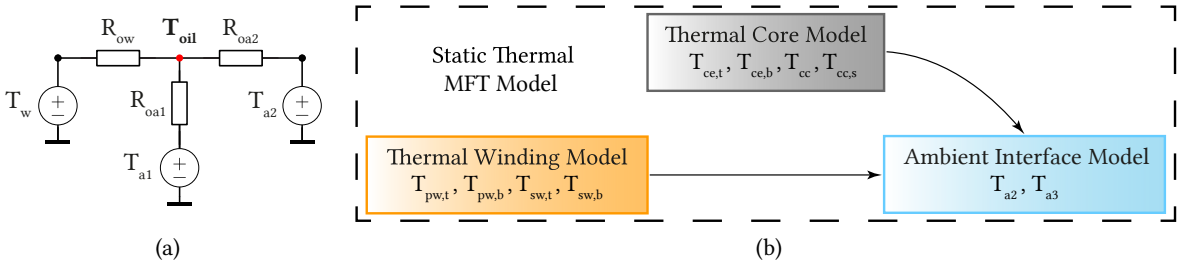


**Fig. 6.12** (a) Simple thermal model that provides the average uniform oil temperatures. (b) Complete static thermal model, where the three introduced thermal parts need to coexist together.

turn, this temperature helps determine the two defined ambient interface temperatures, which are also conditioned by the core surface temperatures.

## 6.5 Summary

This chapter introduced the critical loss models of the design optimization algorithm presented in **Chap. 3**, which are needed for the thermal evaluation of each MFT design. Two main heat sources, core and winding losses, are modeled with the help of well-known analytical models, namely, IGSE and an extension of Dowell's model. The respective estimations are further fed into the static thermal model, which is split into two main parts that process separately the core and winding loss contributions. The split is allowed due to the physical arrangements of the selected MFT structure.

In contrast to the thermal model of the core, two models describing the windings thermally are presented, a detailed and a simplified one. The first takes into account all three heat transfer mechanisms and models the full exchange link between the Cu and the ambient, whereas the latter focuses solely on the forced convective heat exchange between the coolant and the Cu windings. A model verification of the two versions with the winding temperatures, experimentally obtained with the down-scaled test setup used for THM characterization, indicates that the simplified version can be used as a reliable thermal model of the windings. In addition, it is computationally less intensive than the more detailed model.

The connection between the core and winding thermal models is achieved with a simple ambient interface model, considering the fact that the core and the oil vessels with windings are not in direct contact, but share the same environment. At this point, all the missing models of the design algorithm are introduced and adapted to the studied MFT structure. In the next chapter, the results of the design process are revealed and one of the designs is selected for prototyping.

Arrangement	Correlation	Range of validity	Remark
Vertical wall	$Nu = 0.68 + \frac{0.67 Ra_L^{1/4}}{\left(1 + \left(\frac{0.492k}{v_p}\right)^{9/16}\right)^{4/9}}$  $Nu = 0.825 + \left(\frac{0.387 Ra_L^{1/6}}{\left(1 + \left(\frac{0.492k}{v_p}\right)^{9/16}\right)^{8/27}}\right)^2$	$Ra_L \leq 10^9$  $Ra_L > 10^9$	Natural convection, $L = \text{Height}$ [82]  The same as above applies
Vert. cylinder ext.	$Nu = \frac{4}{3} \left( \frac{7Gr_L Pr^2}{5(20+21Pr)} \right)^{0.25} + \frac{4(272+315Pr)L}{35(64+63Pr)D}$	$Gr_L = \frac{g\beta L^3(T_s - T_\infty)}{\nu^2}, \frac{D}{L} < \frac{35}{Gr_L^{0.25}}, Pr < 0.72 \text{ or } Pr > 1$	Nat. convection, $L = \text{Height}, D = \text{Cyl. diameter}$ [154]
Vert. cylinder int.	$Nu = 0.042 Pr^{0.012} \frac{L^{0.3}}{H} Ra_L^{0.25}$	$10^4 \leq Ra_L \leq 10^7, 1 \leq Pr \leq 2 \cdot 10^4, 1 \leq \frac{H}{L_d} \leq 40$	Nat. convection, $H = \text{Height}, L = \text{Cyl. diameter}$ [168]
Vertical coaxial cylinder	$Nu = 0.595 Ra_{\text{av}}^{0.101} Pr^{0.024} \left(\frac{H}{r_{\text{av}}}\right)^{-0.052} \left(\frac{r_2}{r_1}\right)^{0.505}$ $Nu = 0.202 Ra_{\text{av}}^{0.294} Pr^{0.097} \left(\frac{H}{r_{\text{av}}}\right)^{-0.246} \left(\frac{r_2}{r_1}\right)^{0.423}$ $Nu = 0.286 Ra_{\text{av}} Pr^{0.006} \left(\frac{H}{r_{\text{av}}}\right)^{-0.238} \left(\frac{r_2}{r_1}\right)^{0.442}$	$Ra_{\text{av}} \frac{r_{\text{av}}}{H} < 400$ $Ra_{\text{av}} \frac{r_{\text{av}}}{H} = 400 - 3 \cdot 10^3$ $Ra_{\text{av}} \frac{r_{\text{av}}}{H} > 3 \cdot 10^3$	Natural convection, $Ra_{\text{av}} < 2 \cdot 10^5$ $Pr = 0.5 - 10^4, \frac{H}{r_{\text{av}}} = 1 - 33$ $\frac{r_2}{r_1} = 1 - 33, r_{\text{av}} = \frac{r_1 + r_2}{2}$ [168]
Rectangular enclosure	$Nu = 0.042 Pr^{0.012} \left(\frac{B}{H}\right)^{0.3} Ra_B^{0.25}$ $Nu = 0.046 Ra_B^{1/3}$	$\frac{H}{B} = 1 - 40, Pr = 1 - 2 \cdot 10^4, Ra_B = 10^4 - 10^7$ $\frac{H}{B} = 1 - 40, Pr = 1 - 20, Ra_B = 10^6 - 10^9$	Natural convection, $H = \text{Height}$ $B = \text{Width}$ [168]
Horizontal plate upside	$Nu = 0.54 Ra_L^{1/4}$ $Nu = 0.15 Ra_L^{1/3}$ $Nu = 0.27 Ra_L^{1/4}$	$10^4 \leq Ra_L \leq 10^7, T_s > T_\infty$ $10^7 < Ra_L \leq 10^{11}, T_s > T_\infty$ $10^5 < Ra_L \leq 10^{10}, T_s \leq T_\infty$	Natural convection, $T_s - \text{plate temp.}$ $T_\infty - \text{fluid temp. far from the}$ $\text{plate, } L = \text{Area/Perimeter}$ [82], [154]
Horizontal plate downside	$Nu = 0.54 Ra_L^{1/4}$ $Nu = 0.15 Ra_L^{1/3}$ $Nu = 0.27 Ra_L^{1/4}$	$10^4 \leq Ra_L \leq 10^7, T_s \leq T_\infty$ $10^7 < Ra_L \leq 10^{11}, T_s \leq T_\infty$ $10^5 < Ra_L \leq 10^{10}, T_s > T_\infty$	The same applies as for the upside
Straight pipe	$Nu = \frac{(f/8)(Re_D - 1000)Pr}{1 + 12.7\sqrt{f/8}(Pr^{2/3} - 1)}, h = \frac{Nu_p k}{D_h}$ $f = (0.79 \ln Re_D - 1.64)^{-2}$	$2300 < Re_D < 5 \cdot 10^6$ $0.5 \leq Pr \leq 2000, L/D \geq 10$	Forced convection [82], [118], $f = \text{Friction factor}$ $L = \text{Length}, D = \text{Inner diameter}$
Helical pipe, laminar flow	$Nu = (2.153 + 0.318 Dn)^{0.643} Pr^{0.177}$ $Nu = 0.0456 Re_D^{0.8} Pr^{0.4} \delta_R^{0.16}$ $Nu = 0.0254 f Re_D^{1.197} Pr^{0.159}$ $f = \frac{64}{Re (1.56 + \log_{10} Dn)^{5/3}}$	$20 < Dn < 2000, 0.7 < Pr < 175, 0.027 < \delta_R < 0.08$ $1700 < Re_D < 14000, 3 < Pr < 6, 0.015 < \delta_R < 0.076$ $200 < Re_D < 8000, 3 < Pr < 175, 0.015 < \delta_R < 0.077$ $2 < Dn < 5000, 0.0005 < \delta_R < 0.143$	Forced convection, constant heat flux [169] $\delta_R = \frac{r_0}{R} - \text{Curvature ratio}$ [170] $r_0 = \text{pipe inner radius}, R = \text{Helical radius}$ [171] $f = \text{Friction factor}$ [172]
Helical pipe, turbulent flow	$Nu = 0.0062 Re_D^{0.92} Pr^{0.4} (1 + 3.455 \delta_R)$ $Nu = 0.0013 Re_D^{0.93} Pr^{0.4} \delta_R^{0.177}$	$5 \cdot 10^3 < Re_D < 10^5, 0.7 < Pr < 5, 0.027 < \delta_R < 0.08$ $9.7 \cdot 10^3 < Re_D < 1.4 \cdot 10^5, 0.7 < Pr < 6, 0.012 < \delta_R < 0.177$	$Dn = Re_D^{1/2} - \text{Dean number}$ [169] [171]
Vertical channel	$Nu_S = \frac{1}{24} Ra_S \left(\frac{S}{L}\right) \left(1 - \exp\left(-\frac{35}{Ra_S(S/L)}\right)\right)^{3/4}$	$10^{-1} \leq \frac{S}{L} Ra_S \leq 10^5$	$L = \text{Channel height}, S = \text{Width}$ [82]

**Tab. 6.3** Nusselt number correlations for various geometrical arrangements.



# 1 MW MFT Design Optimization

*From the considered core materials, nanocrystalline material yielded the lowest losses for the set operating frequency and is selected as the core material for the final MFT prototype. The 2-vessel MFT proved to have the highest efficiency and to be the most versatile, compared to the other two configurations. This chapter looks into the Pareto front of the MFT designs generated by the design optimization tool, identifies and discusses the optimal design, and provides details about the design selected for prototyping.*

## 7.1 Introduction

In **Sec. 3.4**, the layout and procedure of the employed design optimization algorithm are presented. The design method relies on the brute-force search and thereby, four key design variables are selected which determine the core and winding geometry, cataloged in **Tab. 7.1**. Those are the ID of the pipe conductor, and the respective wall thickness, the SW number of turns, and the flux density magnitude. A combination of the four variables describes a unique MFT design. The chapters following after the design algorithm is introduced, up to this one, give insight into the models necessary to accurately describe the selected 2-vessel MFT structure. By integrating all the presented models in the design algorithm, a functional tool for finding an optimal MFT design within the created design space is obtained. For better readability, the electrical design requirements for the MFT are repeated in **Tab. 7.1**. In this chapter, the results of the introduced optimization algorithm applied to the defined MFT design problem are laid out.

One should recall that the main design criterion is to achieve maximal efficiency. This comes at the cost of increased weight and volume, i.e. lower gravimetric and volumetric power densities. To clarify, the high-efficiency requirement corresponds to the fact that the discussed MFT is intended for use in the MVDC power distribution networks, where the necessary weight or space is usually not severely restricted in any way.

Variable	Min.	Max.	Res.	Description
$D_i$	4 mm	8 mm	20	Inner diameter
$\delta$	$0.9\delta_{Cu}$	$2.2\delta_{Cu}$	14	Wall thickness
$N_{SW}$	8	30	23	SW turns No.
$K_{bm}$	0.2	0.9	80	Flux dens. ratio

**Tab. 7.1** Main design optimization variables.

Characteristics	Unit	Value
Frequency	kHz	5
Nominal power	MW	1
PW/SW voltage	kV	$\pm 5 / \pm 2.5$
Reference magnetizing inductance	mH	25 – 50
Reference leakage inductance	$\mu H$	25 – 50

**Tab. 7.2** MFT electrical specifications.

For the set operating frequency of 5 kHz, three different core materials are considered, namely, GOES, amorphous, and nanocrystalline materials. Their main properties are provided in **Tab. 2.2**. The initially conducted studies show that of the three magnetic materials, nanocrystalline material exhibits the lowest losses for the set electrical parameters which yields the highest operating efficiency of the MFT. Thus, this material is selected for further design considerations.

## 7.2 1 MW 2-vessel MFT Optimal Design

The outcomes of the design optimization algorithm applied on the 1 MW MFT are presented in the form of efficiency plots versus characteristic power densities that include all the generated designs. **Fig. 7.1a** shows the efficiency related to the gravimetric and **Fig. 7.1b** on the volumetric power density. Thereby, the color code of each plot can be set to any of the MFT parameters to help designers observe the existing trends. In the rest of the chapter, several efficiency plots are shown and each one of them has a different MFT parameter assigned to the color bar, which casts light on parameter effects in relation to efficiency and power density.

From **Fig. 7.1a** one can observe increased core temperatures for high gravimetric densities since this implies reduced core size and fewer surfaces to exchange the generated heat with the environment. Similarly, for the generated designs, higher bottom winding temperatures are expected at lower efficiencies, where the losses are higher, as can be seen in **Fig. 7.1b**. The maximum PW hot-spot temperature observed in the graph reaches only 46 °C, which can seem low. However, the nominal PW and SW losses are shared between two winding sets and cooled with a flow of 5.4 l/min. The selected value of the volumetric flow is explained later in the text.

The lower boundary lines provide information about the designs' thermal limits. According to **Fig. 7.1**, an increase in the power density of a design at the thermal limit (which suggests moving along the limit line in the direction of increased power density) implies size reduction, that in turn compromises

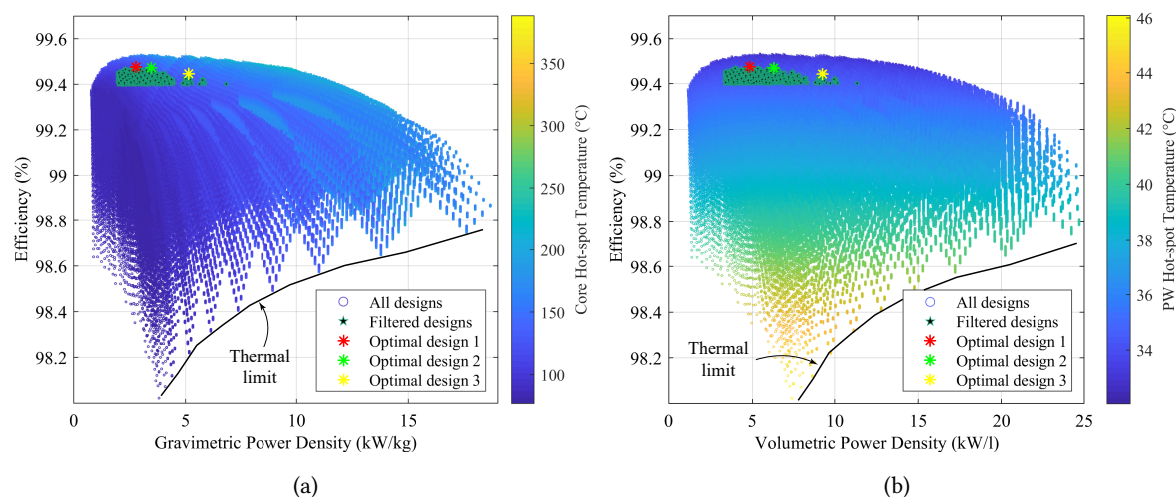


**Fig. 7.1** Plots of generated 2-vessel MFT designs with nanocrystalline at 5 kHz: (a) Efficiency vs. gravimetric power density vs. core hot-spot; (b) Efficiency vs. volumetric power density vs. PW hot-spot temperature, with indicated thermal limitation. The minimal efficiency of the filtered designs is 99.4 %.

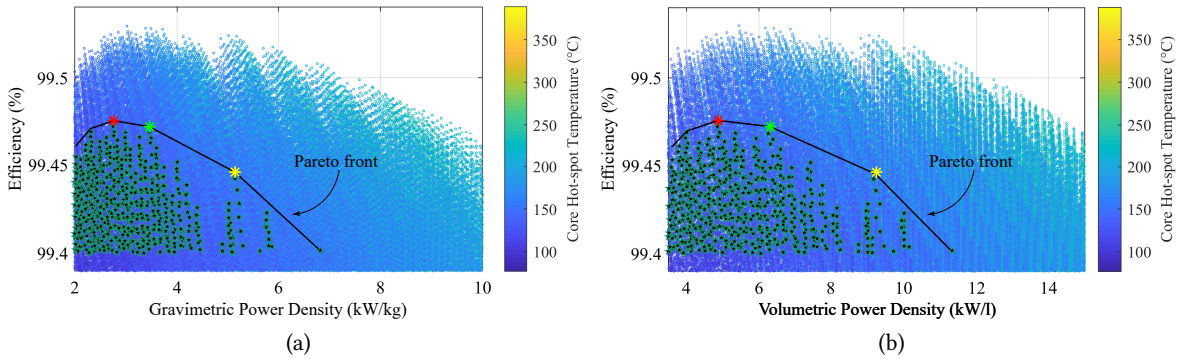


**Fig. 7.2** Zoomed version of **Fig. 7.1** to better appreciate the core temperature, provided as color information: (a) Efficiency vs. gravimetric power density; (b) Efficiency vs. volumetric power density, with indicated Pareto fronts. The same legend pertains as in **Fig. 7.1**. The minimal efficiency of the filtered designs is 99.4 %.

the cooling capabilities of the component. Thus, such a design is thermally feasible only if the losses are reduced. The increase of the power density is limited by the thermal constraints of the employed materials. Lastly, the limit on the left side of the generated designs comes from the lower limit of SW turns number to 8.

The designs which respect all the constraints regarding allowed temperatures and available cooling conditions are marked as valid. In **Fig. 7.1**, the filtered designs marked with green stars represent valid MFT designs in this work, which in addition comply with current densities above  $6 \text{ A/mm}^2$ , the core to winding loss ratio below 33 %, and a minimal gravimetric power density of  $2 \text{ kW/kg}$ . The core-to-winding loss ratio  $R_{wc}$  indicates the percentage of the overall MFT losses attributed to the core. This value is intentionally pushed to lower values, due to available and efficient DI water cooling of the windings. Additionally, the filtered designs have a lower efficiency limit of 99.4 %.

**Fig. 7.2** shows a zoomed frame of **Fig. 7.1** and illustrates that for power densities higher than the ones of the *Optimal designs* 1-3 the designs at the edge disrespect the maximal core temperature constraint. The color code of the presented designs, corresponding to the core hot-spot temperature, can be distinguished better in **Fig. 7.2**. The same legend applies as in **Fig. 7.1**. The upper boundary lines of the filtered groups are known as the Pareto fronts of valid designs, which represent a trade-off between maximum achievable efficiency and respective power densities. They are marked accordingly in both plots of **Fig. 7.2**. The descending trend shows that efficiency must be sacrificed for an increase in power density. Note that the specified efficiencies give theoretical values, calculated based on the estimated core and winding losses. The hot spot temperatures of the windings are determined by the generated conduction losses and the cooling conditions.

Before presenting some of the MFT designs, the cooling conditions fixed during the optimization are shortly introduced. The capacity of the WCU is  $130 \text{ l/min}$  at the nominal power, however, it is shared between two Integrated Gate-Commutated Thyristor (IGCT) stacks and four windings of the MFT, which are all hydraulically connected in parallel. This results in one-third of the flow being available for the cooling of the windings, i.e. one-twelfth for each of the four windings, which makes it approximately  $180 \text{ ml/s}$ . A large margin is considered in case the WCU is not operated at the nominal power and for designing purposes the DI water volumetric flow is set to  $90 \text{ ml/s}$ . An inevitable consequence of forced flow is pressure drop which is limited from the WCU side to  $350 \text{ kPa}$ . It is

primarily determined by the pipe geometry (the length and the inner diameter of the cross section) and the flow properties (the average volumetric rate and the flow type). A larger diameter of the pipe cross section provides for lower pressure drop, in case of a constant flow velocity. Roughly, 75 % is assigned to the pressure drop in the windings due to shorter cooling paths going through the IGCT stacks, compared to the MFT windings. Note that in the thesis, the MFT windings design is to a certain extent limited by the cooling capabilities of the available WCU, which is usually not the case, i.e. after the component design is finalized, the cooling system is selected so that it can match the design's needs.

Eventually, three optimal designs are selected from the prefiltered group for comparison, based on the highest achievable efficiency, and their specifications are given in **Tabs. 7.3 to 7.5**. All three designs have conductors with the same cross-section dimensions (ID and wall thickness) but with different numbers of PW and SW turns. The increased number of turns implies higher winding losses, higher pressure drops along the windings, and in general larger Cu pipe lengths for manufacturing. Moreover, the turns number combined with the core cross-section area determines the flux density magnitude, which is expressed in the form of the ratio  $K_{bm}$ . By comparing the development trends from **Tabs. 7.3 to 7.5**, one can notice that as the cross-section area decreases, the losses decrease as well, even though the flux density magnitude grows larger. Its growth is controlled by the increasing number of turns, which implies higher winding losses and slightly lower efficiencies. Nevertheless, the gain in both volumetric and gravimetric power densities between the first and the third selected optimal designs are doubled. Regarding thermal constraints, it is obvious that the core reaches its

$D_i$	$\delta$	$N_{PW}$	$N_{SW}$	$K_{bm}$	$P_{loss,PW}$	$P_{loss,SW}$	$P_{core}$	$A_{core}$	$T_{cc}$	$R_{wc}$
7.6 mm	1.3 mm	20	10	0.386	2.05 kW	1.84 kW	1.39 kW	$\approx 336 \text{ cm}^2$	147 °C	0.26
$J_{PW,SW}$	$T_{PW,b}$	$T_{SW,b}$	$\Delta p_{PW}$	$\Delta p_{SW}$	$L_{PW}$	$L_{SW}$	$L_{\sigma,DC}$	kW/kg	kW/l	$\eta$
$6.1 \text{ A mm}^{-2}$	33.5 °C	33.2 °C	119 kPa	107 kPa	22.7 m	20.4 m	25.6 $\mu\text{H}$	2.76	4.87	99.48 %

**Tab. 7.3** Specifications of the 2-vessel MFT design marked as *Optimal design 1* in **Fig. 7.1**.

$D_i$	$\delta$	$N_{PW}$	$N_{SW}$	$K_{bm}$	$P_{loss,PW}$	$P_{loss,SW}$	$P_{core}$	$A_{core}$	$T_{cc}$	$R_{wc}$
7.6 mm	1.3 mm	24	12	0.404	2.18 kW	1.94 kW	1.19 kW	$\approx 266 \text{ cm}^2$	147.7 °C	0.23
$J_{PW,SW}$	$T_{PW,b}$	$T_{SW,b}$	$\Delta p_{PW}$	$\Delta p_{SW}$	$L_{PW}$	$L_{SW}$	$L_{\sigma,DC}$	kW/kg	kW/l	$\eta$
$6.1 \text{ A mm}^{-2}$	33.7 °C	33.3 °C	126 kPa	112 kPa	24.1 m	21.3 m	27.8 $\mu\text{H}$	3.47	6.31	99.47 %

**Tab. 7.4** Specifications of the 2-vessel MFT design marked as *Optimal design 2* in **Fig. 7.1**.

$D_i$	$\delta$	$N_{PW}$	$N_{SW}$	$K_{bm}$	$P_{loss,PW}$	$P_{loss,SW}$	$P_{core}$	$A_{core}$	$T_{cc}$	$R_{wc}$
7.6 mm	1.3 mm	32	16	0.457	2.45 kW	2.12 kW	0.99 kW	$\approx 169 \text{ cm}^2$	147.8 °C	0.18
$J_{PW,SW}$	$T_{PW,b}$	$T_{SW,b}$	$\Delta p_{PW}$	$\Delta p_{SW}$	$L_{PW}$	$L_{SW}$	$L_{\sigma,DC}$	kW/kg	kW/l	$\eta$
$6.1 \text{ A mm}^{-2}$	34.1 °C	33.6 °C	141 kPa	122 kPa	26.8 m	23.2 m	32.1 $\mu\text{H}$	5.14	9.24	99.44 %

**Tab. 7.5** Specifications of the 2-vessel MFT design marked as *Optimal design 3* in **Fig. 7.1**.

thermal limit before the windings. The hottest point is located in the center of the vertical core leg and for all three designs the value is very close to the set limit of 150 °C.

Additionally, **Fig. 7.3** provides a visual comparison between the winding and core geometries of the three selected designs. Thereby, the figure perspectives are kept the same so that the sizes of the three designs can be directly compared. Noticeably, as the core cross-section area reduces from **Fig. 7.3a** to **Fig. 7.3c**, the external helical diameters of PW and SW decrease, and the turns number rises which corresponds to higher core window height and taller MFT structures.

As already mentioned in **Chap. 3**, the algorithm is able to differentiate between square and rectangular core cross sections, depending on the required area. The first choice, if possible, is to have a square cross section since it requires a smaller inner vessel diameter, considering its circular shape. However, one must decide on a rectangular cross section in case of e.g. manufacturing limitations. The radial core dimension, i.e. normal to the direction in which the tapes are wound, is limited by the number of tape layers that can be wound and the maximum is set to 140 mm. The value comes from a discussion with the core manufacturer and it is determined by the limit of the winding machine. In the case of the considered MFT designs, the first two designs have rectangular shapes, whereas the *Optimal design 3* has a square core cross section.

Regarding the leakage inductance, its value is predominantly determined by the interwinding distance and the number of winding turns. The employed analytical model is capable of estimating only the static value and a certain decrease needs to be considered at elevated operating frequencies. Thus, while selecting/looking for the optimal design a recommended reduction margin of at least 25 % should be kept in mind, otherwise, the interwinding distance can be increased or another design with a higher number of turns selected. Moreover, the designer can define and add an upper and lower limit for the leakage inductance as an additional filter, if necessary. As an illustration, **Fig. 7.4a** shows all the pre-filtered designs that exhibit leakage inductance values higher than 33  $\mu\text{H}$ . The value selected provides enough margin to fall within the required range from **Tab. 7.2** at 5 kHz operating frequency. Note that the calculated value corresponds to the total leakage inductance of the windings referred to the primary side.

The color bar of **Fig. 7.4a** provides insight into the distribution of leakage inductance values across

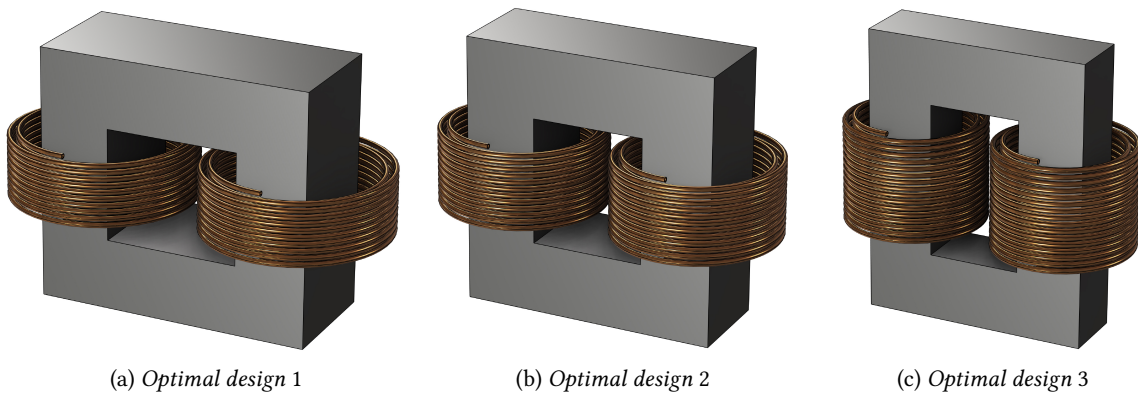


**Fig. 7.3** Simple 3D CAD models of the three selected optimal MFT designs presented in **Tabs. 7.3** to **7.5** illustrated to compare the dimensions of the core and windings.

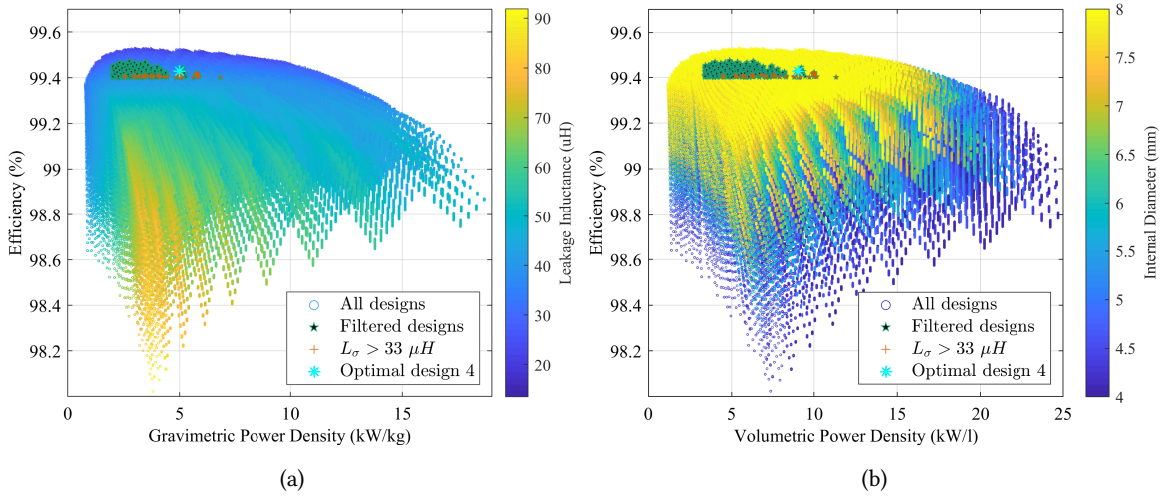


**Fig. 7.4** Repeated plots from **Fig. 7.1** with additional leakage inductance filter applied to the pre-filtered designs: (a) Efficiency vs. gravimetric power density vs. leakage inductance; (b) Efficiency vs. volumetric power density vs. ID. The minimal efficiency of the filtered designs is 99.4 %.

different efficiencies and power densities. Due to fixed interwinding distance, by design choice, high values are expected for high turns number and high core cross-section areas, i.e. for low gravimetric power densities. **Fig. 7.4b** shows the same filtered group of designs from **Fig. 7.4a** but as a function of the volumetric power density. Thereby, the color parameter is set to the ID of the pipe conductor. As expected, for low values of ID, the cross-section area of the conductor is low which corresponds to high resistance and thus increased winding losses. This also explains why all the selected designs from **Tabs. 7.3** to **7.6** have high values of ID.

The specifications of the design with the highest efficiency from the new group of filtered designs are given in **Tab. 7.6**. Compared to the previous three presented designs, it has the highest number of turns but approximately the same core cross-section area as the *Optimal design 3*. **Fig. 7.5a** shows the corresponding 3D CAD model of the MFT *Optimal design 4*. The magnetizing inductance of the presented designs is not explicitly given, since its value is not affected in the same way as the leakage inductance is. The desired reference value can be achieved by setting the correct air gap size and, thereby, taking account of the core geometry and the number of turns, as well as core material properties at the selected operating frequency.

From the presented and discussed optimal designs, it can be concluded that the *Optimal design 4* fulfills

$D_i$	$\delta$	$N_{PW}$	$N_{SW}$	$K_{bm}$	$P_{loss,PW}$	$P_{loss,SW}$	$P_{core}$	$A_{core}$	$T_{cc}$	$R_{wc}$
7.6 mm	1.3 mm	34	17	0.43	2.61 kW	2.26 kW	0.88 kW	$\approx 169 \text{ cm}^2$	138.7 °C	0.15
$J_{PW,SW}$	$T_{PW,b}$	$T_{SW,b}$	$\Delta p_{PW}$	$\Delta p_{SW}$	$L_{PW}$	$L_{SW}$	$L_{\sigma,DC}$	kW/kg	kW/l	$\eta$
6.1 A mm <sup>-2</sup>	34.4 °C	33.8 °C	150 kPa	129.8 kPa	28.5 m	25.7 m	33.4 μH	5.01	9.02	99.43 %

**Tab. 7.6** Specifications of the 2-vessel MFT design marked as *Optimal design 4* in **Fig. 7.4**.



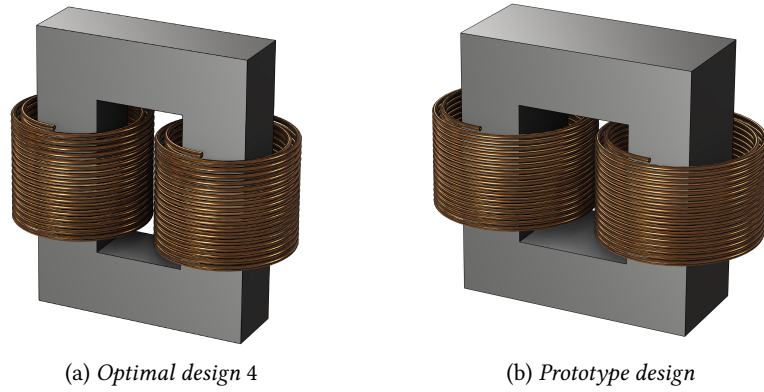


**Fig. 7.5** Simple 3D CAD models of the *Optimal design 4* and the MFT prototype design.

all the design requirements and is, thus, a good candidate for prototyping. Compared to the first presented design (*Optimal design 1*), the theoretical efficiency has reduced insignificantly by 0.05 %, yet, both power densities have increased by more than 80 %, which positively impacts the amount of material needed for manufacturing. This is a very significant comparison result, which confirms that a thorough inspection of the generated valid designs is required and necessary before continuing with the manufacturing phase. The following section presents the specifications of the MFT design selected for prototyping. Its 3D CAD model including solely the core and the windings is shown in **Fig. 7.5b**, for visual comparison purposes with the winner of the optimal design considerations presented in this section.

### 7.3 1 MW 2-vessel MFT Prototype Design

Unfortunately, due to an undetected scaling factor mistake in the design algorithm at an early stage, the MFT design selected for prototyping is not the optimal one for the set operating frequency and the voltage levels. A missing factor of 2 in the flux density equation resulted in a design with half of the desired flux density magnitude and double the area of the core cross section, larger than actually necessary for the set requirements. **Fig. 7.6** shows the position of the prototype design in the efficiency plots compared to the pre-filtered designs and the four selected optimal designs, which achieve slightly higher efficiency. The efficiency plots are repeated from the previous section in order to avoid information clutter. The optimal designs 1 – 4 are marked with the same color as in **Figs. 7.1** and **7.4**, thus, their legend is omitted. Due to the selection of the  $K_{bm}$  ratio resolution, the design selected for prototyping is not one of the generated designs but it is added for comparison purposes.

Another selection of different MFT parameters of the color bar in **Fig. 7.6** provides additional insight into the prevailing design trends. High values of current density in **Fig. 7.6a** correspond to the reduced cross-section area of the conductor which leads to increased winding losses, due to increased resistance, and results in reduced efficiency. On the other hand, a higher  $K_{bm}$  factor, observed in **Fig. 7.6b**, positively affects the mass and volume of the MFT and promotes their reduction, since for higher flux densities, the cross section decreases, but it causes an increase in the core losses, which influences the efficiency.

The characteristics of the prototype MFT design are summarized in **Tab. 7.7**. Compared to the first

$D_i$	$\delta$	$N_{PW}$	$N_{SW}$	$K_{bm}$	$P_{loss,PW}$	$P_{loss,SW}$	$P_{core}$	$A_{core}$	$T_{cc}$	$R_{wc}$
7.6 mm	1.3 mm	34	17	0.237	2.96 kW	2.45 kW	0.52 kW	$\approx 325 \text{ cm}^2$	101.6 °C	0.09
$J_{PW,SW}$	$T_{PW,b}$	$T_{SW,b}$	$\Delta p_{PW}$	$\Delta p_{SW}$	$L_{PW}$	$L_{SW}$	$L_{\sigma,DC}$	kW/kg	kW/l	$\eta$
$6.1 \text{ A mm}^{-2}$	44.7 °C	42.2 °C	36.5 kPa	32.8 kPa	37.8 m	33.9 m	43.8 $\mu\text{H}$	2.4	4.33	99.4 %

**Tab. 7.7** Specifications of the 2-vessel MFT design selected for prototyping.

three selected designs, the turns number is higher, as well as the core cross-section area, which results in a lower value of  $K_{bm}$ , i.e. flux density magnitude. It has a positive effect on the core losses, however, the achieved power densities are the lowest compared to the first three designs. Regarding the last presented design from **Tab. 7.6**, the turns number is the same, but the cross-section area of the core is almost half of the one in the prototype design and the same applies to the  $K_{bm}$  ratio. This is graphically visible in **Fig. 7.5**. In order to reduce the pressure drop and to get higher bottom winding temperatures (for better visualization of the MFT prototype thermal image), the volumetric flow has been reduced to 30 mL/s.

A consolation benefit of the selected MFT design compared to the ones selected as optimal is the fact that it can be operated at significantly lower frequencies than 5 kHz without the risk of core material saturation. This adds to the versatility of the prototype, presented in the following chapter, however, it was not done on purpose. **Fig. 7.7** shows the PW voltage excitation and the corresponding waveforms of the flux density at the design operating frequency of 5 kHz and two lower ones, 3 kHz and 1.5 kHz. Note that a single period of each voltage waveform is shown, whereas the flux densities are periodically continued. **Tab. 7.8** provides the values of the variables from **Fig. 7.7**. Applied to the same transformer (fixed geometry and the number of turns), the increased voltage-second area allows the flux density amplitude to rise. The lowest operating frequency of the selected MFT prototype

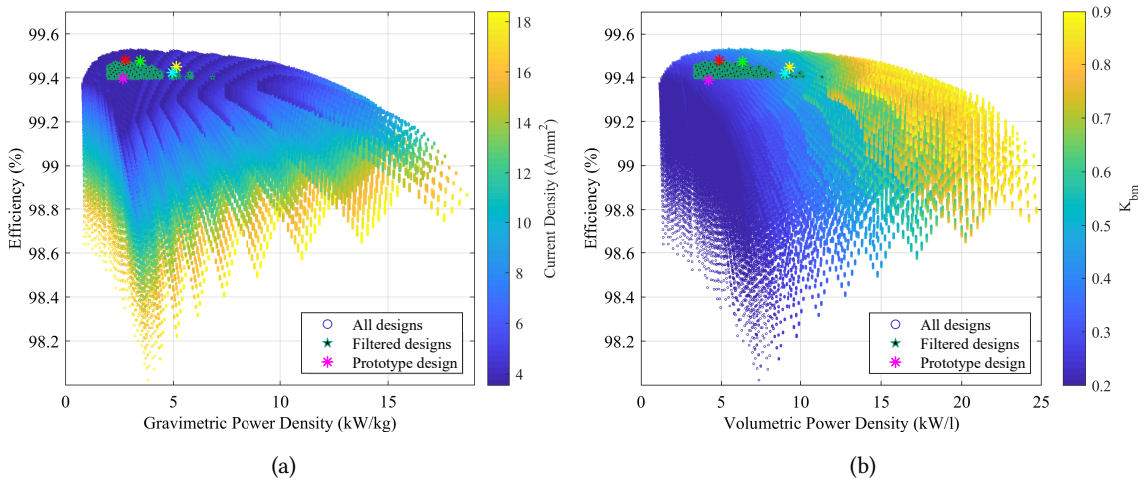


**Fig. 7.6** Repeated plots combining all the observed designs, *Optimal* 1 – 4 and the prototype design: (a) Efficiency vs. gravimetric power density vs. current density; (b) Efficiency vs. volumetric power density vs. flux density ratio. The minimal efficiency of the filtered designs is 99.4 %.



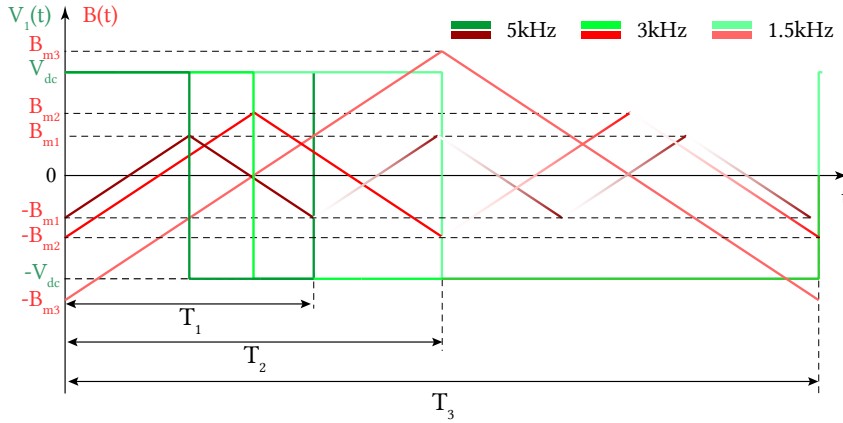


**Fig. 7.7** Square voltage PW excitation and the corresponding flux density waveforms at three different time periods.

Variable	Value
$V_{dc}$	5 kV
$T_1$	200 $\mu$ s
$T_2$	333 $\mu$ s
$T_3$	666 $\mu$ s
$B_{m1}$	0.3 T
$B_{m2}$	0.49 T
$B_{m3}$	0.98 T

**Tab. 7.8** Parameter values from **Fig. 7.7**.

design rests around 1.35 kHz with a 10 % safety margin from the saturation flux density value.

**Tab. 7.9** provides a comparison between analytically modeled and simulated AC resistance values of the PW and SW, in the case of solid and hollow conductors. Both conductor types are mentioned because the analytical model for the hollow type builds upon Dowell's model for solid conductors. A remark regarding the model implementation in the optimization algorithm is that due to the necessary vertical distance between the windings and the top and bottom core parts as well as the required turn-to-turn distances, the porosity factor from (4.6) will have lower values than needed for good accuracy of Dowell's model. Therefore, the actual height of the core window area is adjusted to match the winding height. In this way, the porosity factor value is increased and improved resistance estimations are obtained. An overall good match can be observed in **Tab. 7.9**, which provides fidelity in the modeled winding losses of the generated MFT designs. Regarding the resistance values simulated in FEM, they correspond to windings approximated with rings instead of helices and this contributes to the discrepancy observable between the modeled and simulated values.

**Fig. 7.8** provides temperature distributions of the simulated 3D MFT model in COMSOL. Thereby, the windings are modeled as foils and the top and bottom temperatures correspond to the values obtained from the analytical thermal model. In this way, the complexity of the model is reduced and the simulation converges faster. The induced core losses match the ones from **Tab. 7.7**. **Tab. 7.10** compares the characteristic core and ambient temperatures from the analytical models and the ones

Winding type	Analytical Model	3D FEM
Round solid, PW	29.6 m $\Omega$	26.7 m $\Omega$
Round hollow, PW	28.3 m $\Omega$	25.6 m $\Omega$
Round solid, SW	24.5 m $\Omega$	25.2 m $\Omega$
Round hollow, SW	23.4 m $\Omega$	24.2 m $\Omega$

**Tab. 7.9** Comparison of modeled and simulated AC resistance values at 5 kHz for round hollow and solid PW and SW of the MFT prototype design.

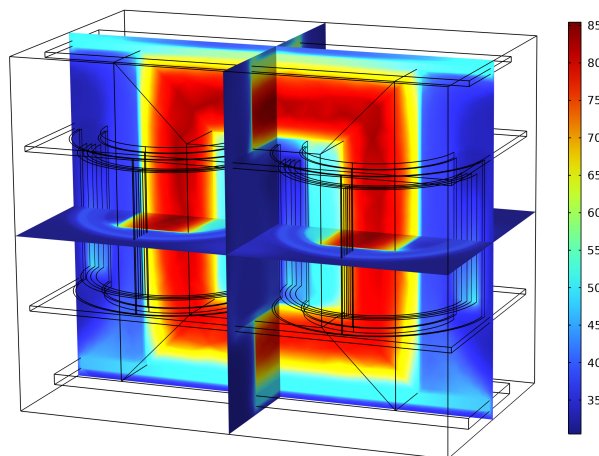


**Fig. 7.8** Results of thermal FEM simulation of the MFT prototype design in COMSOL.

Temperature	An. Model	3D FEM
$T_{ce,t}$	67.4 °C	68 °C
$T_{ce,b}$	66.1 °C	64.8 °C
$T_{cc}$	82.9 °C	70.2 °C
$T_{m,t}$	73.4 °C	79.6 °C
$T_{m,b}$	74.1 °C	74.3 °C
$T_{m,cc}$	93 °C	83.3 °C
$T_{a2}$	53 °C	35.3 °C
$T_{a3}$	62 °C	51.5 °C

**Tab. 7.10** Analytical model vs. FEM-simulated temperatures.

obtained in the simulation. The top and bottom surface and center core temperatures match to a good extent between the model and the simulation. The exact locations of the temperatures can be recalled in **Figs. 6.6** and **6.11**. However, there is a discrepancy between the temperatures of the center leg, where the values predicted by the developed analytical model are higher. The same applies to the two ambient interface temperatures of the air. A potential explanation lies in the inaccurate setting of the FEM simulation and modeling of the nanocrystalline core since it is not presented as laminated material. Nevertheless, its thermal anisotropy is included.

Before moving to the next and final chapter, where the construction of the MFT prototype is explained in detail, **Fig. 7.9** shows three CAD models of the transformer assembly steps. In **Fig. 7.9a**, the lower half of the core is placed on an Al plate and constrained from the left and right side with white plastic support pieces, which are attached between two E-shaped parts made of the same material. The two parts act as a base for the vessels with oil and windings to rest on, as shown in **Fig. 7.9b**. Four threaded poles are added in each corner of the bottom Al plate passing through the lids of the vessels and finally connecting to the top Al plate, which is not explicitly shown. In **Fig. 7.9c** the upper half of the core is placed on top of the lower part inside of the inner vessel walls and the side supports

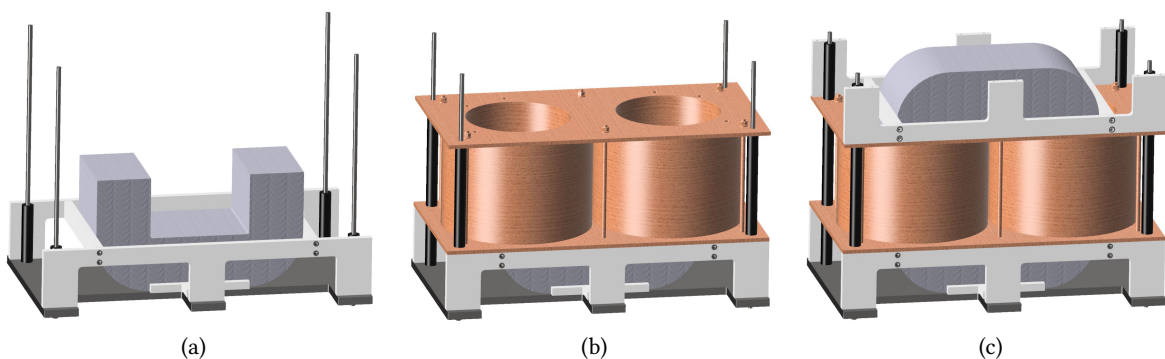


**Fig. 7.9** CAD models representing various steps in the MFT assembly.

are added. Another two E-shaped parts are added, similar to the bottom ones but mounted in the opposite way. Their purpose is to hold the top Al plate that covers the core and to exert pressure on the common lid of the two vessels. The final CAD model of the fully-assembled MFT prototype is provided in the next chapter.

## 7.4 Summary

This chapter elaborates on the results of the design optimization algorithm applied to the design problem of 1 MW 2-vessel MFT structure and a set of electrical parameters provided in **Chap. 3**. The results are given in the form of Pareto fronts that combine theoretical design efficiency versus gravimetric and volumetric power density. Out of numerous generated designs, a smaller group is determined based on several design filters, regarding minimal current density, minimal power density, defined range of leakage inductance, and similar. From the pre-filtered set, several optimal MFT designs are selected based on the highest achieved efficiencies for comparison. The differences between the designs are indicated and eventually, one of them is marked as the optimal design.

However, another design is selected for prototyping, due to a missing factor in the equation determining the flux density for each design. To clarify, the miscalculation was corrected and all the presented designs in this chapter are valid. The prototype design is compared to the optimal design and its characteristics are presented. Moreover, verification of the winding AC resistances and the static thermal image of the prototype design is achieved with the help of FEM simulations. The following chapter provides details about the construction of the prototype, determines the required insulation coordination and shows the experimental test results.



# 8

## 1 MW MFT Prototype

*In this chapter, the details regarding the assembly and construction of the 1MW 2-vessel MFT prototype are shared. Particular attention is dedicated to the use of round copper pipes as windings, and directions regarding their mechanical implementation are included. Furthermore, details concerning the necessary creepage and clearance distances for proper insulation are provided. Lastly, the chapter introduces the results of electrical and insulation tests conducted with the assembled MFT prototype.*

### 8.1 Introduction

In the previous chapter, the main characteristics (regarding core and winding geometries) of the selected 2-vessel MFT design are introduced. The following step is the construction of a prototype based on that design, which is discussed and presented in this chapter. Some of the properties of the selected transformer design relevant to the assembly are given in **Tab. 8.1**. It includes characteristic pipe winding properties and the main losses at the nominal operating point. Note that the values for loss and length of the PW and SW include summed values of both winding parts from the two vessels. However, the indicated winding lengths do not take into account the necessary terminations, i.e. they provide the required pipe lengths to form the full number of turns according to the corresponding external helical radius. The characteristic core sizes are provided separately in the next section.

The 3D-rendered models of the MFT with additional parts intended for support and fixation are shown in **Fig. 8.1**, with and without the termination panel. The addition of the panel simplifies the connection of the prototype to the power stages of the DCT. Thereby, each winding has its own top and bottom bushing, which allows access to the windings from the front side of the panel. In this way, configuring the MFT to have the desired turns ratio is made simpler. The mounting parts that fixate the panel to the top and bottom Al plates are made as sliders so that the distance between the panel and the rest of the transformer can be adjusted according to the needs. Nevertheless, note that the addition of the termination panel affects the power density and more strongly the volumetric than the gravimetric density. The external dimensions of the MFT with and without the termination

$D_{i,PW,SW}$	$\delta_{PW,SW}$	$N_{PW}$	$N_{SW}$	$R_{a,PW}$	$R_{a,SW}$	$J_{PW,SW}$
7.6 mm	1.3 mm	34	17	17.5 cm	15.5 cm	6.1 A mm <sup>-2</sup>
$L_{PW}$	$L_{SW}$	$P_{loss,PW}$	$P_{loss,SW}$	$P_{core}$	$K_{bm}$	$B_m$
37.8 m	33.9 m	2.96 kW	2.45 kW	0.52 kW	0.237	0.3 T

**Tab. 8.1** Design characteristics of the 2-vessel MFT structure selected for prototyping.

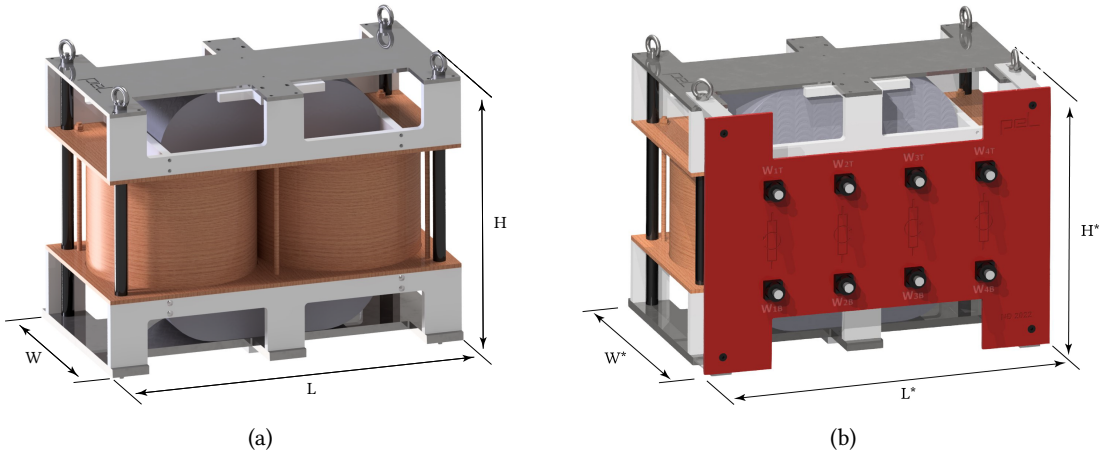


**Fig. 8.1** 3D CAD render of the 2-vessel core-type MFT design (a) without and (b) with the termination panel.

MFT	W	L	H	$V_{MFT}$	kW/l	$M_{MFT}$	kW/kg
without the panel	494 mm	851 mm	685 mm	$\approx 288$ L	3.47	$\approx 443$ kg	2.26
with the panel	600 mm	851 mm	685 mm	$\approx 350$ L	2.86	$\approx 450$ kg	2.22

**Tab. 8.2** External dimensions and volume of the selected MFT prototype design with and without the termination panel. The width and height remain the same, whereas the depth changes.

panel are provided in **Tab. 8.2**, together with the estimated weight and volume and their respective power densities. Moreover, the top and bottom Al plates are intended to act as a clamp, providing stability to the structure in the vertical direction. The two lower white plastic E-shaped supports help distribute the weight of the vessels and together with the upper supports compress and keep the vessel structure in place. Thereby, the core does not carry the weight of the vessels as they are not in direct contact in any way. CAD models of the MFT and its relevant parts have been very useful in the prototyping and construction phase of the transformer.

## 8.2 Mechanical Construction

The construction of the MFT can be broken down into simpler assembly units, such as the core with the clamping and stabilizing systems, Cu pipe windings immersed in oil within the two vessels, and auxiliary parts, such as the termination panel, DI water distributors, and so on. This section also includes considerations regarding insulation coordination, which provide the necessary distances between the grounded and under-voltage components.

### 8.2.1 Core

As previously discussed, the optimal cross-section shape for the considered core material is a square since it takes up the biggest surface inside of a circular cylinder, which is formed by the inner oil vessel walls. Nevertheless, due to the necessary cross-section size of the selected design and the manufacturing limits, the core cross-section area is of rectangular shape. The used nanocrystalline

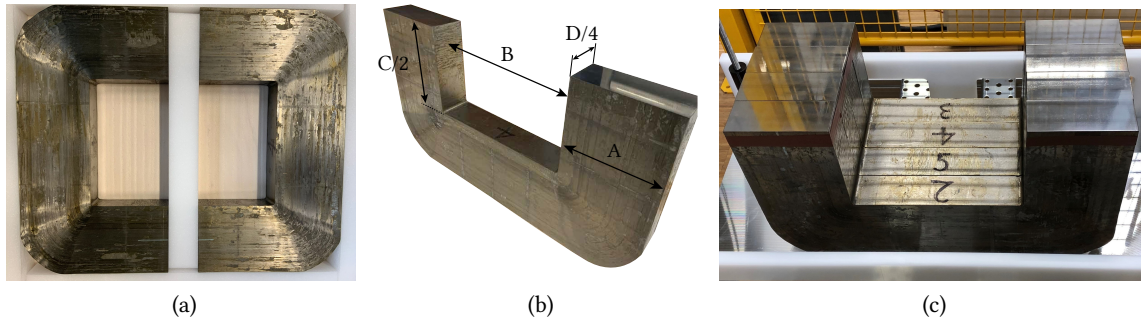


**Fig. 8.2** MFT magnetic core made of nanocrystalline material: (a) Set of two C-cut cores weighing  $\approx 92$  kg per pair; (b) Single C-cut core with indicated sizes; (c) Lower half of the core made of four C-cut cores stacked together and placed on the bottom Al plate.

A	B	C	D	$M_{\text{core}}$
140 mm	256 mm	318 mm	232 mm	$\approx 370$ kg

**Tab. 8.3** Properties of the fully assembled MFT core. Dimensions  $A$  to  $D$  are illustrated in **Fig. 8.2b**.

material is FINEMET FT-3 (with MgO coating), produced in the form of 58 mm wide tapes of  $18 \mu\text{m}$  thickness, which are isolated from each other by epoxy resin and produced by Hitachi Metals [173]. As reported by the manufacturers, the relative (effective) permeability of the nanocrystalline cut core is 30 000 at 5 kHz and 0.1 T. However, its value increases proportionally with the increase of  $B_m$  and at the same frequency and 0.6 T, an approximate increase of 50% can be expected. From there, the interpolated value of the relative permeability at the flux density magnitude of 0.3 T and 5 kHz is roughly 36 000. The magnetostriction of the nanocrystalline FINEMET is less than 1 ppm.

The transformer core is put together with four sets, each containing two C-cut cores per set, as displayed in **Fig. 8.2a**. **Fig. 8.2b** introduces a single cut core with indicated core sizes, whereas **Fig. 8.2c** shows the lower half of the full core. Finally, the dimensions of the assembled core are provided in **Tab. 8.3**, along with the weight of the fully assembled core. The two C-cut cores are held in a set with the help of stainless steel bands. Additionally, the core as a whole is kept in place by inserting supporting structures in all three directions.

### 8.2.2 Windings

For the implementation of transformer windings as described in **Tab. 8.1**, pipes made of soft temper Cu are used, produced by Luvata [174]. Per design, the wall thickness of the pipe is selected higher than the skin depth at the 5 kHz frequency and it corresponds to a hollow penetration ratio of  $\Delta_h \approx 1.4$ . Such a decision can be traced back to the hollow resistance factor, which is for this frequency and wall thickness slightly lower than 1. Depending on the desired OD of the conductor's cross section, there are manufacturing and mechanical constraints regarding the conductor's wall thickness and the allowed bending radius for the winding termination.

Furthermore, the process of bending the pipes into winding structures with a fixed external (helical) diameter and turn-to-turn distance turned out to be a challenging task, even though the soft type of



copper is used. According to [175] and depending on the bend radius, there are three fundamental approaches to pipe bending. Namely, compression, draw (mandrel), and roll bending. Compression bending applies to the use of manual pipe bending tools or manual bending for small diameters. In the case of mandrel bending, which is used for stiffer materials and pipes of larger diameters, the use of a winding machine is essential. There, the tube is pulled or drawn around the former tool, i.e. mandrel. Lastly, roll bending is used when a large radius of curvature is desired and it is usually achieved with three rollers. As for the size of the bending radius, a standard recommended by [175] is 2 OD, i.e. twice the size of the OD of the pipe, measured to the center line. An additional remark is given regarding the draw bending radius which can be as low as 1/2 OD. The value depends on the shape, size, and cost of the tool. On the other hand, pipe manufacturer Luvata [174] recommends respecting at least 3 OD for the bend radius. As for the direction of pipe winding, this can be performed counterclockwise, i.e. regarding the left chirality, or in the clockwise direction, regarding the right chirality. The direction itself does not have an influence on the difficulty/complexity of the winding process.

To manufacture MFT windings, **Fig. 8.3a** shows the method that is used for winding Cu pipes into the desired shape. The method belongs to the mandrel bending approach, and the description of the procedure is summarized in the following. A wooden mandrel of appropriate cross-section diameter is attached to a rotating shaft with an additional structure (framed in white) mounted in its vicinity to guide the Cu pipe onto the mandrel. Additionally, a similar fixing structure (framed in black) is added directly on the mandrel to keep the pipe in place during the rotation. Nevertheless, due to the high mechanical strength of even soft temper Cu, at the moment the winding, i.e. the coiled pipe, is released from the mandrel it loosens and increases its initially intended external radius. This practical challenge is resolved by trial and error method, i.e. by readjusting the outer diameter of the mandrel until the correct external winding radius is achieved.

**Fig. 8.3b** and **Fig. 8.3c** show the two oil vessels made of phenolic paper composite material, manufactured by Elektro-Isola [139], with windings and insulation fluid inside. As can be noticed, an air pocket of sufficient size is left at the top of each vessel, which allows the fluid to expand from an ambient temperature to 80 °C. In addition, the bottom vessel lid is glued to the cylinder walls, whereas the top part can be removed. For the excess air during the expansion, two additional outlets are added at the top of each vessel, which are connected to two air breathers [176] filled with silica gel. Their

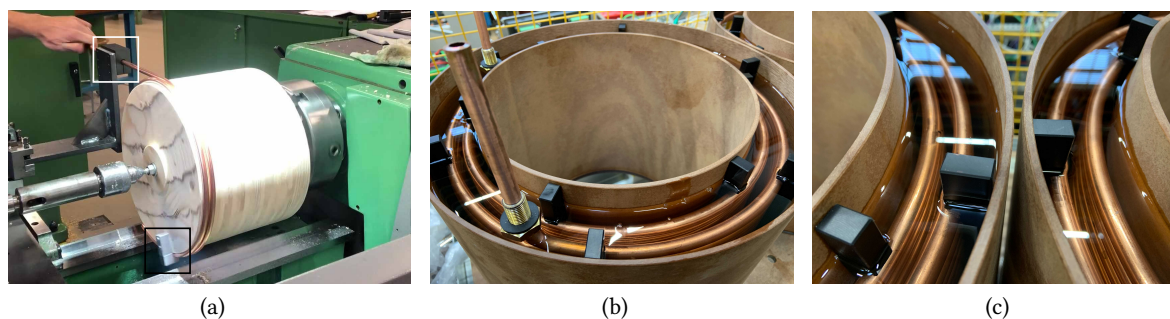


**Fig. 8.3** (a) Method used to make transformer windings of the correct external radius using Cu pipes; (b) One of the two MFT oil vessels, made of phenolic paper composite material Etronit I and B66; (c) Both vessels contain the insulation liquid and a set of PW and SW with spacers that provide desired turn-to-turn and interwinding distance.



task is to act as purifying and drying agents, thus keeping the moisture and particles away from the oil. They can be seen on the back side of the MFT assembly, attached to the E-shaped support, in **Fig. 8.7a** shown later in this chapter.

For the considered MFT prototype, both PWs are wound regarding the right chirality, that is in the mathematical or the counterclockwise direction looking from the top, whereas the SWs are wound reversely, according to the left chirality. Following the dot convention, the PW and SW in each of the vessels are of inverse polarity. Once the windings are brought to the correct shape, the next challenge is to keep the structure compact and in a fixed position regarding the required distance between the windings and the vessel walls. There are many ways how this can be done with more or less material, using more or less complex solutions. The goal was to minimize the size and volume of the supporting system, further referred to as the spacer, but maintain the functionality, since it represents an obstacle to the moving insulation fluid. Moreover, a suitable material needed to be selected considering the medium the windings are placed in, i.e. material's compatibility with oil, and considering high temperatures that both windings and oil can reach during operation. As a viable solution, six comb-like structures are added to both PW and SW, made of thermoplastic material POM which complies well with the described requirements. **Fig. 8.4a** gives the top cross-sectional view of one of the oil vessels, with the core limb in the inner tube, and describes the position of the 12 spacers. Note that for the PW the spacers are placed from the outside in order to keep a fixed distance to the vessel's outer wall. Accordingly, for the SW they are attached from the inner side. In this way, the spacers ensure concentricity of the windings, since both outer and inner vessel walls can be considered perfectly circular. **Fig. 8.4b** shows the SW with the mounted spacers. Apart from providing compactness and correct distancing to the vessel walls, the supporting structure keeps a fixed turn-to-turn distance, which is essential for correct insulation. A closer view of the fixed spacer is given in **Fig. 8.4c**.

Furthermore, additional attention needs to be paid to the terminations of each winding, since it is necessary to separate the cooling, i.e. DI water from the electrical connection. There are many ways to achieve an electrical connection, such as soldering or brazing a contact directly at the pipe's end or adding a removable Cu connector to interface the pipe and the rest of the system. On the other hand, the cooling medium is usually conveyed with the help of a plastic pipe of appropriate OD, by an overlap joint, or through an adequate connector to make a direct connection between two pipes.

Due to the presence of oil, it is required to make a leak-proof, i.e. sealed exit of both windings at

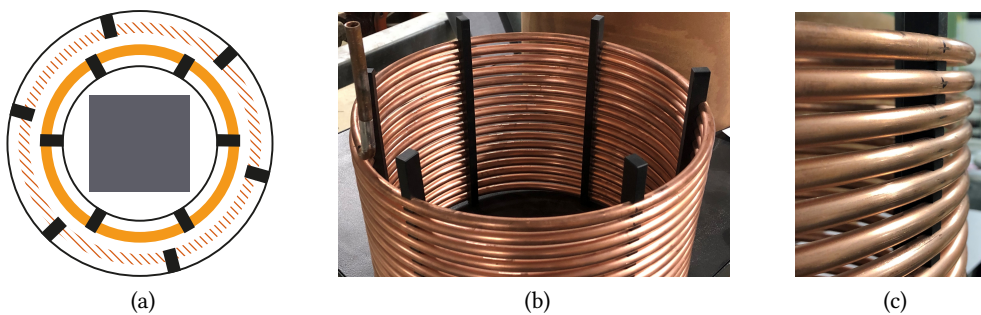


**Fig. 8.4** (a) Arrangement of spacers for PW and SW; (b) Comb-alike spacers mounted at every 60° on the SW from the inside; (c) A close view of a spacer mounted from the inner side of the SW.



**Fig. 8.5** (a) Brass pipe fitting used to ensure a sealed exit of the winding through the vessel lid; (b) Implementation of electrical and cooling connections between a pipe winding end and the rest of the system.

the top and bottom of each vessel. For this purpose, a brass pipe fitting of the appropriate ID, with a fixed jam nut and a seal rubber, is brazed at the top and bottom of each winding termination, as shown in **Fig. 8.5a**. After the vessel is closed, by adding another jam nut from the outer side a sealed connection can be made. A fully sealed connection is shown in **Fig. 8.5b**. Additionally, a plastic hose is attached to the pipe, secured with a clamp, to establish a cooling connection with the WCU. The electrical connection between the pipes, i.e. MFT windings and the surrounding power stages is made by clamp-alike Cu connectors, with appropriate cable lug endings to accommodate cable connection to the power stages, as shown in **Fig. 8.5b**.

### 8.2.3 Insulation Coordination

For insulation purposes, the biodegradable synthetic ester transformer fluid Midel 7131 is selected [78]. It provides superior dielectric and thermal properties (increased fire safety, high dielectric breakdown above 75 kV according to IEC 61099 [177]) compared to standard mineral oils used for transformer insulation. Furthermore, it exhibits superior dielectric properties with values of 47 kV of breakdown voltage at a 1 mm gap. Regarding the internal insulation of the MFT, the turn-to-turn and interwinding distances have been predetermined for the design optimization process and included in the list of dielectric constraints **Tab. 3.2**. During normal operation, any of the four windings, with 17 turns each in the case of the selected MFT design, experiences 2.5 kV voltage, which requires blocking of approximately 150 V between the two consecutive turns, and an existing electric field of 450 V/mm. Secondly, the interwinding voltage at any time during regular operation amounts to 2.5 kV, i.e.  $\approx 310$  V/mm, which is in both cases low compared to the insulation capabilities of the selected oil (47 kV/mm). Note that even in the case of a fault, when the applied voltages reach much higher values, the selected insulation distances are over-dimensioned on purpose and sufficient to provide insulation.

The standard which is followed for determining the correct clearance and creepage distances for the basic insulation is IEC 61800-5-1 [80]. The two characteristic distances are introduced in **Sec. 2.3.4** and their values are derived from the Root Mean Square (RMS) working voltages between winding terminals, and terminals to ground. The selected standard is defined for adjustable speed drives but it is also used for MV converter applications. It concerns systems of up to 35 kV and it is most commonly applied to power semiconductor-based power conversion and MV drives. Based on the DC-link voltages of the DCT power stages on the primary and the secondary side of the MFT, two

different system voltages are considered. Namely, 10 kV for the primary and 5 kV for the secondary side. In the next step, the suitable OVC and PoD are decided. Taking into account that the MFT is not exposed to transient over-voltages during regular operation and is placed indoors, it is sufficient to select category 1 for both OVC and PoD. Nevertheless, to ensure higher robustness of the MFT design, OVC 2 and PoD 2 are selected. For correct creepage value, another important parameter is the CTI, which describes the ability of the insulation to resist material degradation [52]. Based on the selected system voltages, it is possible to determine the impulse voltages and temporary overvoltages from the standard guidelines, which further help decide the necessary clearance and creepage values. For the PW terminal to ground the minimum clearance value is set to 55 mm and for the SW terminal to 30 mm. Both values are obtained through interpolation. The materials used for the oil vessel are of paper-phenolic origin which belongs to the IIIb material group, with a CTI of 100 V. Since this material group requires the highest creepage distances, it will be assumed that all the other solid insulators, encountered on the creepage path, belongs to the same group. Under the assumption the working voltage corresponds to the system voltage, the creepage value of 100 mm is selected for the PW terminal to ground, whereas for the SW 50 mm is set. During the design and construction of the prototype, it was ensured that the required distances are respected.

Regarding the necessary insulation distances between the winding terminals, the clearance is set to 50 mm, and the creepage value to 100 mm. Nevertheless, in the final prototype, both values have been increased to 200 mm. According to [80], the provided distances are valid for frequencies lower than 30 kHz and up to 2000 m altitude and they consider an inhomogeneous electric field distribution across the clearance path, which is normally the case in practice. Lastly, the same insulation distances are considered when placing the bushings for each winding terminal on the termination panel. Due to the available panel surface, the bushings are spaced out in greater amounts than actually necessary.

#### 8.2.4 Full Prototype

Finally, **Fig. 8.6** shows the assembled 1 MW MFT prototype. **Fig. 8.6a** presents the MFT without the

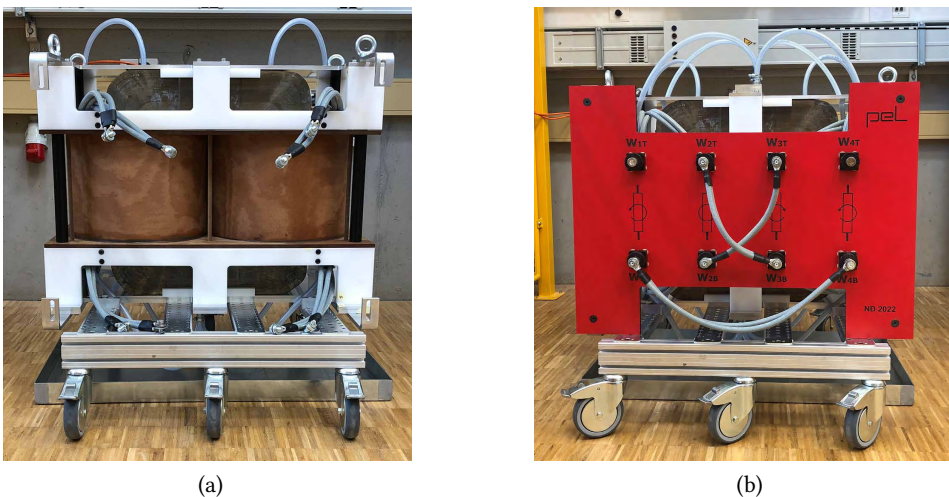


**Fig. 8.6** 1 MW prototype of the 2-vessel MFT (a) without and (b) with the winding termination panel and the top and bottom DI water distribution unit.

DI water distributor at the top and the winding termination panel, which are included in **Fig. 8.6b**. The addition of the panel further simplifies connection of the prototype to the power stages and forming of the necessary turns ratio. The Cu pipes are connected to the panel with the help of MV-isolated cables, as shown in **Fig. 8.6a**. The required turns ratio is accomplished by externally connecting the PWs from the two vessels in series, and the SWs in parallel, as can be seen in **Fig. 8.6b**. **App. C** shows the other possible configurations achieved by external connection of the four available windings.

To guide the DI water to and from the MFT, two water distributors have been added to the top and bottom. The top distributor receives the cold DI water directly from the WCU and shares it out to the four pipe windings. The connection between the distributors and the pipes is achieved with PVC hoses of appropriate ID. Conversely, the bottom distributor collects the warmed water at four inlets and returns it to the WCU. Depending on whether the transformer is placed on a cart, which allows it to move, or it is installed in the DCT cabinet which is shown later in the chapter, the top and bottom DI water distributions are placed differently. In the first case, the distribution blocks are mounted directly at the top and bottom Al plates, whereas in the cabinet, they are mounted separately on a rail in the cabinet wall.

### 8.3 Experimental Testing

Once the MFT construction has been finalized, and before the integration within the DCT, some initial tests have been conducted. Namely, the electrical parameters achieved by construction are identified and the insulation capabilities of the MFT are tested by conducting the PD test. After installation in the DCT, the MFT is tested in no-load conditions, as full power tests were not possible to perform during the writing of the thesis. Thereby, the arising core losses and temperature distributions across the transformer are observed and measured.

#### 8.3.1 Electrical Parameters

The first conducted measurements with the assembled MFT prototype deal with the verification of the required electrical parameters, namely, the leakage and magnetizing inductance. For this purpose, two measurement devices are employed, an RLC meter (BK895), which measures impedances at fixed predefined frequencies, and the Omicron Lab Bode 100, which works as an impedance analyzer over a certain frequency range. Depending on the winding side, primary or secondary, where the measurements are performed, different values can be expected. Note that the requirements made in **Tab. 3.1** are referred to the primary side. All the measurements are subsequently compensated for the inductances of the short-circuit cables, as well as the connecting cables of the used measuring instruments.

The measured leakage inductance values at the primary side are compared with the FEM-simulated value, as shown in the top part of **Tab. 8.4**. As for FEM simulations conducted in Comsol, the windings are modeled as perfect helixes in 3D, together with the core. However, to reduce the

$L_\sigma$ [ $\mu$ H]	FEM 2D pipe	RLC	Bode 100	$L_m$ [mH]	Ref. value	RLC	Bode 100
at 5 kHz	34	38.2	37.9	at 5 kHz	35.77	36.66	36.74

**Tab. 8.4** Comparison of the measured and modeled (left) leakage and (right) magnetizing MFT inductances.

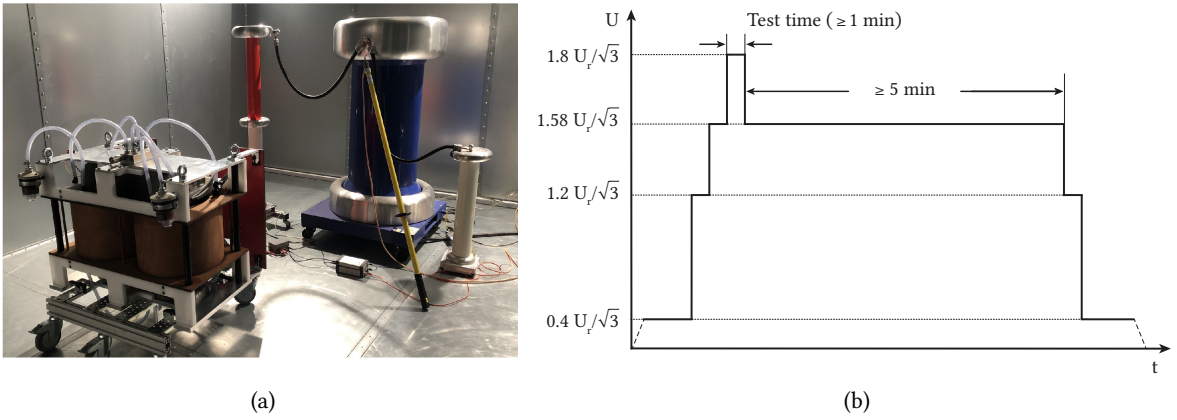


**Fig. 8.7** (a) PD measurement setup inside of the Faraday cage; (b) Test voltage sequence applied to the MFT to test its insulation capabilities.

computational time and burden, the leakage inductance calculations are performed in 2D, obtained from a vertical cross section of the 3D model. These simplifications explain the slight deviations from the measured values. Nevertheless, an overall agreement between the simulated and measured values at the operating frequency prevails.

While the leakage inductance is predominantly determined by the geometry of the windings, the magnetizing inductance can be controlled by adjusting the air gap between the core sets. Furthermore, its value is determined by the MFT magnetizing current, which is for the selected resonant converter topology also the turn-off current. Regarding the measurements of the magnetizing inductance, the air gap is set to around 1 mm, which, according to analytical calculations, corresponds to the peak magnetizing current of  $\approx 7$  A resulting from a 5 kV square voltage applied to the primary side with 0.5 duty cycle at 5 kHz operating frequency. According to **Tab. 8.4**, the reference value closely matches the measured ones. It can be concluded that the values of both electrical parameters lie in the required range stated in **Tab. 3.1**. Moreover, **App. C** provides measurements of electrical parameters of some of the other possible MFT configurations which can be achieved with the assembled prototype.

### 8.3.2 Partial Discharge Test

To verify the insulation capabilities of the assembled prototype, PD tests are performed. A PD stands for an electric discharge that only partly bridges the insulation under voltage. For this purpose, the high-voltage test setup, presented in **Fig. 8.7a** with the connected MFT, is used [178]. It is placed inside the Faraday cage and equipped with a PD measuring system MPD 600 by Omicron. The setup can be used for PD and AC dielectric withstand tests. It consists of a Low Frequency (LF) AC generator/source, which is in reality a step-up transformer able to reach 100 kV output voltage, connected to a current limiting resistor and a coupling capacitor, to which the device under test is connected in parallel. The applied voltage is controlled from the outside of the cage. Note that the test environment used to measure the PD is limited to operation with LFTs, and thus, the tests are conducted at a 50 Hz frequency, which does not match the MFT operating frequency. The standards dedicated to testing of high-power transformers operating at significantly higher than line frequency are still not available.



Typically, dry-type MFTs are tested with a voltage profile with included pre-stressing and testing period from a safety standard like IEC 60664 – 1. However, in this particular case, the transformer windings are oil-immersed and therefore, the test voltage sequence from IEC 60076 – 3 [81] standard is selected and followed. Thereby, the MFT is connected to the measurement setup over the termination panel. The insulation capabilities of the MFT were tested by applying the following voltages:

- A) Between the PW and SW connected in the required 2:1 turns ratio configuration;
- B) In both vessels, between the PW and SW;
- C) Between the windings and the conductive parts of the transformer (top and bottom Al plates);

In cases A and B, the PW is set on potential whereas the SW is grounded. Regarding the last case, both windings are set on potential and the remaining conductive parts are grounded. The tests are performed with applied and not induced voltage. The test voltage sequence is presented in **Fig. 8.7b** according to the recommendation from the selected safety standard.  $U_r$  gives the rated voltage of the windings, which corresponds to the line voltage of a 3-phase transformer. For the testing of the MFT, the voltage  $U_r/\sqrt{3}$  has been set to 5 kV, unless stated differently. The enhancement voltage and the PD measurement voltages are set to  $1.8U_r/\sqrt{3}$  and  $1.58U_r/\sqrt{3}$ , respectively. The standard prescribes running the measurement periods for longer times, in the hours' range, however, this was not blindly followed and the minimum required duration for each of the voltage levels was considered, or time periods long enough until a stable PD measurement was acquired. The test is considered successful if, among other conditions, the PD levels recorded during the measurement voltage time are below 250 pC, and subsequently, at the voltage level  $1.2U_r/\sqrt{3}$ , the measured PD is below 100 pC. More details about the test acceptance criteria can be found in [81].

The measured PD patterns for the recommended voltage profile for each of the considered test cases are shown in **Figs. 8.8 to 8.10**. Besides color-coded PD density, the applied voltage waveform can also be seen. The 250 pC PD limit is crossed during the test A at  $U_r/\sqrt{3} = 5$  kV, however, it is considered as passed at a lower voltage of 4.5 kV, as illustrated in the measured PD patterns, in **Fig. 8.8a** and **Fig. 8.8b**, respectively. The insulation was tested for each set of windings (PW against SW) in the two vessels and the corresponding measurements are shown in **Fig. 8.9** and **Fig. 8.10a**. Thereby, after passing the test at  $U_r/\sqrt{3} = 5$  kV, the windings in the left vessel were tested at an increased voltage of

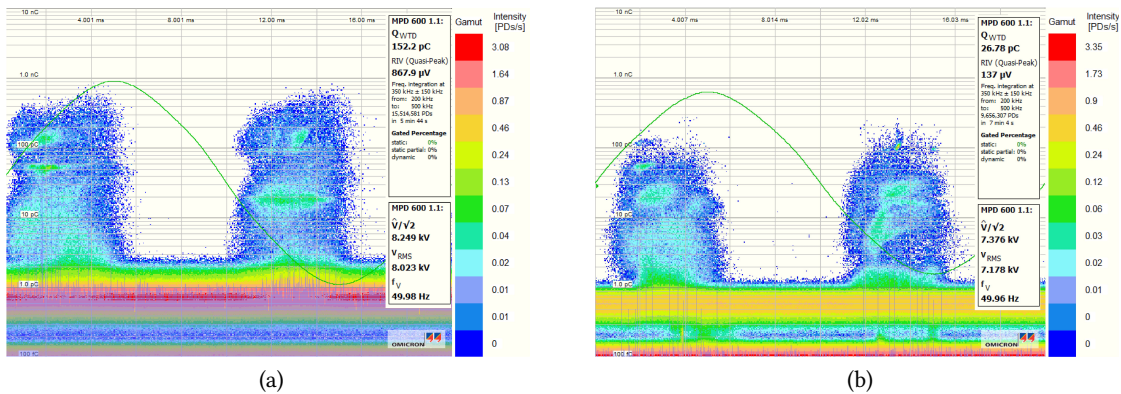


**Fig. 8.8** Measured PD between PW and SW in 2:1 configuration for: (a)  $U_r/\sqrt{3} = 5$  kV, (b)  $U_r/\sqrt{3} = 4.5$  kV.

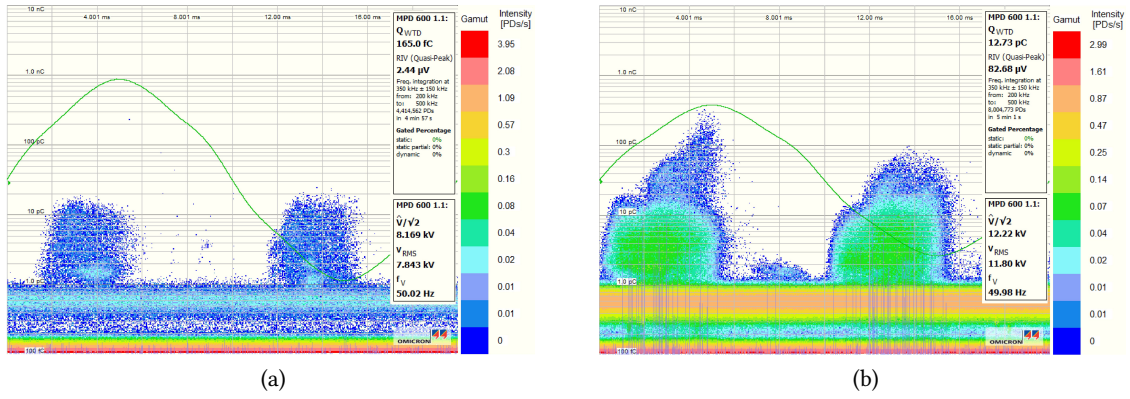


**Fig. 8.9** Measured PD between the PW and SW in the left vessel at (a)  $U_r/\sqrt{3} = 5$  kV and (b)  $U_r/\sqrt{3} = 7$  kV.

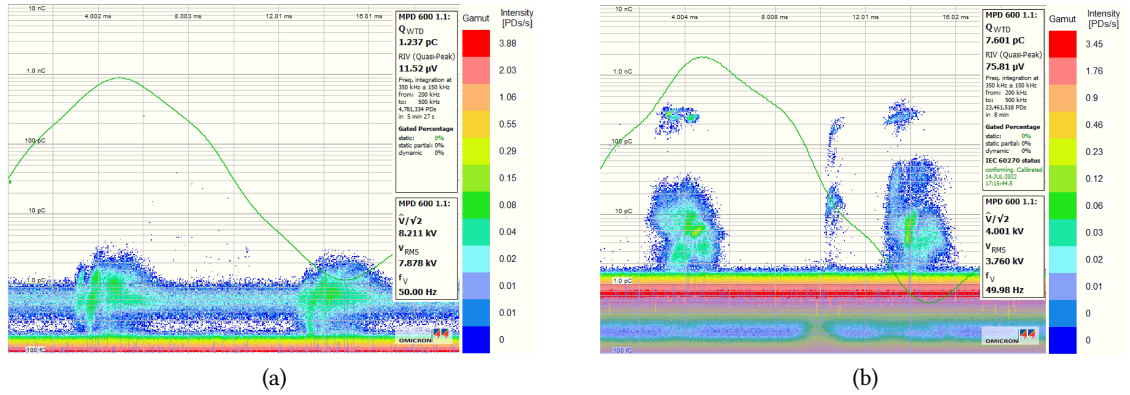


**Fig. 8.10** Measured PD patterns (a) between the PW and SW in the right vessel and (b) all the windings set on the same potential and other conductive parts of the MFT at  $U_r/\sqrt{3} = 2.5$  kV.

7 kV, which was the limit, as shown in **Fig. 8.9a** and **Fig. 8.9b**, respectively. Lastly, in the case of the test C, the characteristic voltage is reduced to 2.5 kV, due to the SW, and the allowed maximal PD limit for a positive test was crossed. The source of the slight voltage distortion was not identified. The specific shapes of the occurring PD patterns during different measurements were not further studied. However, the author suspects that occurring high PD values happen predominantly in the air and not inside the vessels.

### 8.3.3 MFT Operation in DCT Test Setup

To perform power tests and energize the transformer during no-load operation, the assembled MFT is installed in the DCT cabinet, as shown in **Fig. 8.11a**. In case of oil or DI water leakage, a tray of adequate size is attached to the bottom of the MFT. The connection with the two power stages, which are located above the transformer, is made by connections with MV cables over the termination panel. A preview of the fully-assembled 1 MW DCT demonstrator is presented in **Fig. 8.11b**. The employed WCU which is supplying the components with DI water is installed behind the cabinet.

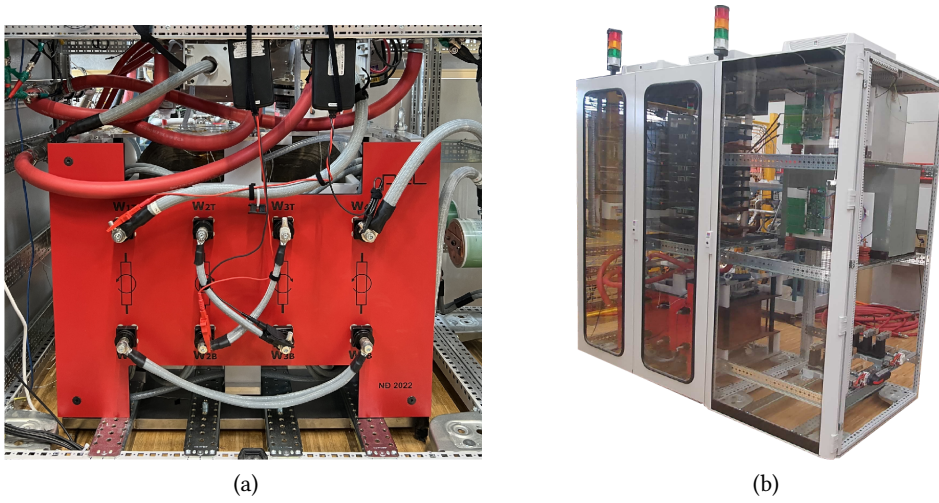


**Fig. 8.11** (a) The assembled MFT prototype with a 2:1 turns ratio, integrated inside of the (b) 1 MW DCT demonstrator cabinet.

### 8.3.3.1 No-Load Operation

During no-load operation, the MFT is energized from the SW side, but no power is transferred since the primary transformer side is left open. In that case, the only current flowing in the DCT is the magnetizing current. **Fig. 8.12** shows the PW and SW voltages and the magnetizing current on the secondary side in the 2:1 MFT configuration. The amplitude of the magnetizing current on the secondary side is lower than expected and announced in **Sec. 8.3.1** ( $\approx 14$  A, corresponds to the double of the PW magnetizing current). It is measured to reach  $\approx 11.6$  A which implies a slightly higher value of the magnetizing inductance, 42.8 mH to be precise, than first measured. This can be ascribed to the tightening of the stainless steel bands that hold the core halves in a set or of the vertical clamp with

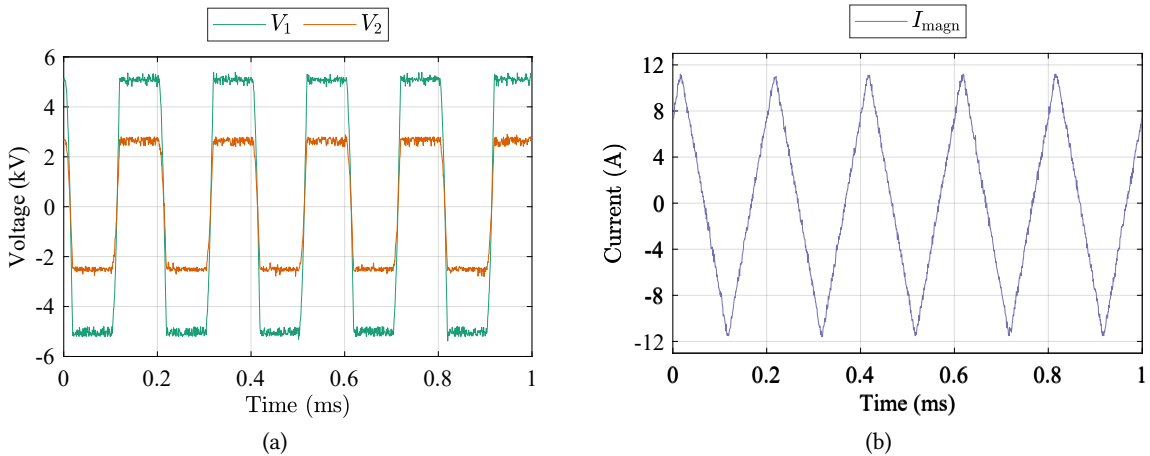


**Fig. 8.12** Measured voltage and current waveforms during no-load DCT operation: (a) PW and SW voltage, (b) magnetizing current recorded on the secondary side. The MFT windings are connected in a 2:1 configuration.



top and bottom Al plates which caused a slight reduction of the air gap from  $\approx 1$  mm to  $\approx 0.8$  mm.

By consulting the loss density measurements provided by the core manufacturer [173] performed on the delivered core sets for various operating points (varied frequency and flux density), the estimation of the core losses can be inspected. According to the obtained test report, the measured core loss density for 5 kHz sinusoidal excitation and 0.302 T amounts to 1.377 W/kg. Considering the core weight given in **Tab. 8.3**, the core losses calculate to 510 W. The losses are additionally estimated from the voltage and current readings of the DC power supply on the secondary side and the calculation of the semiconductor losses at the defined operating point. The injected power during no-load operation is measured to be 1.2 kW. With assumed ZVS, the conduction and turn-off losses of the semiconductors are estimated to 623 W. Thereby, a large part of the losses is attributed to the turn-off losses of the RC-IGCTs. The respective turn-off energy at ultra-low turn off currents is characterized for the employed switching devices in [179]. The other relevant parameters are obtained from the datasheet. The losses of the resonant capacitor and the DC-link on the secondary side are not considered. Finally, the core losses calculate to 577 W. Recalling the estimation of the losses obtained with the analytical IGSE from **Tab. 8.1**, which is  $\approx 520$  W, one can establish an overall agreement between the values. The slight deviation can be explained by measurement uncertainties, inaccuracy of the loss allocation in the setup or of the estimation of the Steinmetz coefficients.

### 8.3.3.2 Resonant Operation

Unfortunately, due to technical issues, no power tests were conducted at this point. Nevertheless, the following principles would be followed in order to achieve power transfer through the MFT. Due to the tardy commissioning of the 10 kV MV power stage, the DCT had to be reconfigured to a 1:1 configuration, in order to perform power tests on the MFT. For this purpose, the primary side DC-link is reduced to 5 kV and the 10 kV RC-IGCTs are replaced with 4.5 kV devices. The selected topologies of the two power stages have remained the same. Accordingly, the MFT prototype was reconfigured to provide a 1:1 turns ratio by connecting the PWs from the two oil vessels in parallel, in contrast to the series connection, which was necessary for the 2:1 configuration. The SWs remain connected in parallel. In this way, the magnetic flux density in the core remains preserved, corresponding to the original design. The according electrical parameters of the rewired MFT prototype are stated in **Tab. C.1** in **App. C**. To maintain the operating frequency at 5 kHz, the total value of the resonant capacitor was adjusted to 61  $\mu$ F, which is realized by two capacitors of 122  $\mu$ F symmetrically distributed on both sides of the MFT. This resulted in a new resonant tank frequency of 6.14 kHz. In this way, the sub-resonant converter operation is realized, which provides ZVS conditions to the primary side switches and ZCS operation for the diodes of the power stage on the secondary side, owing to the half-cycle discontinuous conduction mode.

To achieve resonant operation and power transfer through the MFT, the DCT is supplied by two DC sources. The corresponding electric scheme is shown in **Fig. 8.13**. Thereby, the primary side is actively switched and supplied by a controlled DC voltage source (Technix) operated at 5 kV, whereas the secondary side power stage is employed as a passive rectifier. The positive ends of the DC-links of the two DCT sides are connected directly, whereas the negative ends are linked through a controlled DC source (Magna TSA20-2250), which provides the load current. In this way, a back-to-back connection is established, which allows energy transfer from the secondary back to the primary side. Nevertheless, the maximal amount of power that can be circulated in the setup is limited by the maximal voltage provided by the Magna power supply. At the moment of the final

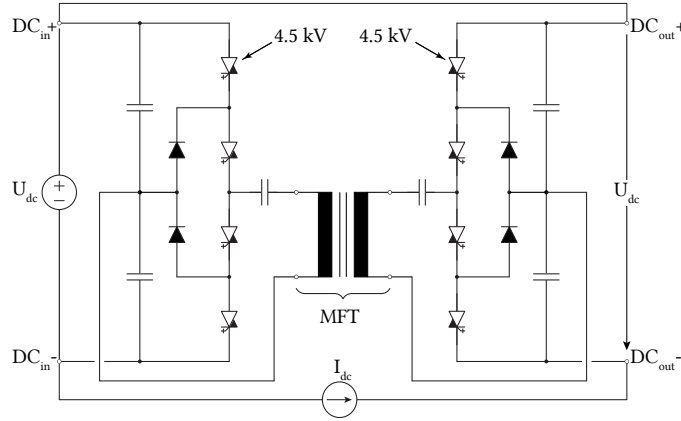


**Fig. 8.13** Electrical circuit schematic describing the testing principle to achieve power circulation. The switching devices of both power stages are 4.5 kV RC-IGCTs.

thesis submission, the experimental setup to collect the back-to-back results is not fully finalized, thus, the results including power tests of the MFT are not available.

### 8.3.4 Thermal Measurements

To observe the temperature development across the MFT during no-load operation, numerous TCs are added to accessible locations within the core, windings, and oil vessels. The oil temperature was not measured directly, in order to avoid the risk of leaking or irreparably damaging the vessel walls. **Fig. 8.14** shows recorded temperatures during 12 h no-load DCT operation for various air and core temperatures. The locations of the TCs measuring the air temperatures in the inner vessel cylinder are indicated in the top left corner of **Fig. 8.14a**. Temperature  $T_{out}$  shows the ambient temperature inside the closed DCT cabinet. As expected, the two air temperatures within the enclosed space between the vessel's inner walls and the core leg, top and bottom parts,  $T_{ac,Lin}$  and  $T_{ac,Rin}$ , are the

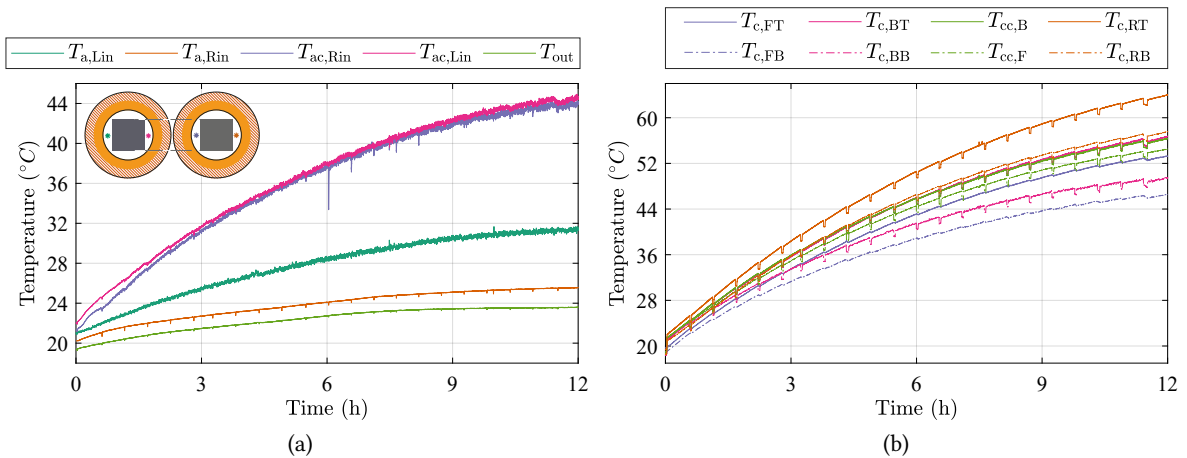


**Fig. 8.14** Measured temperatures of (a) the air around and between the inner vessel walls and the core and (b) at the core surface and inside of the core.

highest, whereas the other two temperatures,  $T_{a, \text{Lin}}$  and  $T_{a, \text{Rin}}$ , outside of the core, are notably lower. The discrepancy in values between the latter two temperatures is presumably due to the measurement uncertainty of the employed K-type TCs.

Various core temperatures are presented in **Fig. 8.14b**. Thereby, the letters in the subscript mark the location of the TC. It can be differentiated between  $F/B/R$ , front, back, and right, and  $T/B$ , which stands for top and bottom. In pairs, the following temperatures were observed with the help of attached TCs:

- $T_{c, \text{FT}}, T_{c, \text{FB}}$ : temperatures at the top and bottom of the frontal vertical core surface (the one facing the termination panel);
- $T_{c, \text{BT}}, T_{c, \text{BB}}$ : temperatures at the top and bottom of the back vertical core surface;
- $T_{c, \text{cF}}, T_{c, \text{cB}}$ : front and back core surface temperatures measured close to the air gap;
- $T_{c, \text{RT}}, T_{c, \text{RB}}$ : temperatures measured 3 cm inside of the core (between two sets) at the top and bottom on the right core side;

It can be observed that the temperatures measured at the top tend to be higher than the ones measured at the bottom. This trend can be nicely followed for three location pairs, namely, at the front and back surfaces, as well as inside the core. As anticipated, the temperatures are higher within the core than on the surface, due to worse cooling conditions. The notches that are visible in most of the core temperature measurements are due to seize operation in half an hour intervals. This was done with the idea to observe the difference in measurements owing to the presence of a magnetic field during operation, which, depending on the location of the TCs can introduce errors due to induced voltages. All the attached TCs were placed in a way to get minimal field effect, however, this was not fully achieved.

One can notice that during operation of 12 h no steady-state temperatures of the core were achieved, which implies a large thermal time constant. The thermal capacitance of the core can be easily estimated with the help of specific heat capacity ( $0.46 \text{ J/kg K}$ ) of the core material and the respective weight. The epoxy resin used for insulation of the nanocrystalline tapes has significantly higher heat capacity ( $1110 \text{ J/kg K}$ ) and takes 4% of the total core weight. Due to large differences in the heat capacity values, the presence of epoxy resin needs to be considered in order to accurately estimate the thermal core capacitance. Eventually, the value amounts to approximately  $16.6 \text{ kJ/K}$ .

## 8.4 Summary

A 1 MW, 5 kHz 2-vessel core-type MFT prototype with oil-immersed windings, which are actively-cooled with DI water, and an air-cooled nanocrystalline core has been realized. As explained in the previous chapter, the assembled prototype is not an optimal solution for the set electrical requirements, but it is fully functional. Considering that pipes as windings are not as common as Litz wires, their use and construction for the purpose of the task are explained in detail. This includes directions regarding coiling mechanisms, recommended bending radii and supporting structures to achieve the desired interwinding and turn-to-turn distances, and termination possibilities. Mechanical withstand capabilities of the windings and the MFT were not explicitly considered.

Furthermore, details regarding the insulation coordination of the MFT are presented, which includes

determining the necessary clearance and creepage distances for the functional and basic insulation. The prototype was partly tested, which meant undergoing electric parameter identification, and PD insulation tests. The achieved leakage and magnetizing inductances fall within the required range. To test the insulation, a different standard was used than the one commonly employed for this purpose. Regarding power testing, the no-load test was performed. The recorded voltage and current waveforms were used to estimate the respective core losses. Lastly, thermal measurements of the core and the ambient during the 12 h run are collected. Lamentably, no power tests were performed, thus, the overall achieved efficiency of the assembled MFT remains unknown.

## Conclusion and Future Work

*The final chapter concludes the thesis by providing a summary of all the contributions made in modeling and designing of core-type medium frequency transformers with actively cooled oil-immersed pipe windings. Additionally, ideas related to future research work which originate from the work presented in the thesis are listed and motivated.*

### 9.1 Summary and Contributions

Nowadays, the trend of increased deployment of renewable energy sources in modern power systems is undeniable and inevitably leads to the decentralization of traditional (predominantly AC) power systems. Moreover, it leads to an increased presence of DC-based technologies and systems, primarily through PV modules, consumer electronics and data centers in the LVDC domain, and bulk power transmission systems in HVDC. However, at this point, the MVDC range remains not fully exploited and capitalized. Its potential can be used for tasks of collection and distribution, namely, collection of e.g. off-shore wind and tidal power and transfer to the shore, and distribution, i.e. connection of various types of loads to renewable energy sources and storage facilities. The latter is known as the MVDC power distribution network (PDN). In this regard, SSTs, more precisely DCTs as a subset, are considered to be the key enabling technology, serving isolated DC-DC power conversion with the intention of providing an interface between DC grids at different voltage levels. The input-output voltage adaption and the galvanic isolation are achieved by MFT, which is one of the central components of the DCT. Conventionally, high conversion efficiency, reliability, and low cost are desired and while the progress in the semiconductor industry keeps delivering on these aspects and pushing the limits of voltage and current capabilities, the magnetic components in general seem to lag. Consequently, they become the bottleneck of power converters and curb the overall efficiency and power density. Therefore, investing effort into the research of design topics of magnetics and their modeling is very important.

This thesis focused on modeling and design optimization of high-power MFTs operated in the MV range with the purpose of enabling DCTs for future MVDC PDNs, which in itself represents a complex non-linear multi-objective problem. After the introduction chapter, where the background and importance of the thesis topic are explained in more detail than the above mentioned, the thesis commences with the state-of-the-art regarding modeling, challenges, and existing technologies regarding the MFT design in **Chap. 2**. Compared to a design of an LFT, which has been mastered for many years now, operation at elevated frequencies brings advantages and many additional challenges that need to be addressed and adequately modeled in the design process. On a good note, increased operating frequency leads to size and volume reduction of the component which is a lucrative benefit. To be able to fully exploit its potential, one must understand what are the limitations. The challenges

include eddy-current effects within the windings and non-sinusoidal voltage and current excitations, which hold higher-order harmonics and lead to increased losses. Furthermore, high  $dV/dt$  derivatives cause additional stress on the insulation. The MFT size reduction implies a reduced amount of surfaces available for heat dissipation, which leads to higher gradients of hot-spot temperatures. Moreover, depending on the converter topology, the intrinsic parameters of the MFT take part in enabling converter operation, which in turn has an effect on their geometry. Therefore, accurate modeling and design of leakage and magnetizing inductances are important. Depending on the employed technologies, the thermal and insulation coordination need to be considered together since they can have an undermining effect on each other. Lastly, in contrast to the traditional LFT, the MFT designs are still highly non-standardized and can have various specifications, take different shapes, and combine different technologies depending on the converter topology and the application, in general.

In **Chap. 3**, the resonant topology (LLC-SRC) employed for the DCT and converter specifications are introduced, which provide necessary information for the MFT design. From there, electrical requirements are derived. Thereby, a particular set of technologies is selected, namely, the windings are actively cooled with DI water and are therefore realized with round Cu hollow conductors. This selection is motivated by the fact that the IGCT stacks of the two power stages are water-cooled. To achieve the required insulation in the MV range, the windings are immersed in oil. The core is kept dry and its cooling and insulation from the windings are achieved through air. Initially, a core-type MFT with three different winding arrangements was analyzed. Based on the versatility and efficiency criterion, the 2-vessel MFT is selected to be studied in the rest of the thesis. The design algorithm is based on the exhaustive search concept and four key optimization variables are defined, together with the respective boundary range and resolution. After the design playground has been introduced, the following chapters focus on modeling various aspects of the MFT.

The first to be discussed is the analytical modeling of leakage inductance in **Chap. 4**. At elevated frequencies, due to eddy current effects, the leakage inductance value reduces and this needs to be quantified. For this purpose, two models are considered. The simple 1D Dowell model is frequency-dependent, which is convenient, however, its accuracy is limited for other than foil windings and outside of the conditions it was derived under. Moreover, it cannot be directly applied to hollow conductors. On the other hand, the 2D Margueron's model, which relies on the method of magnetic images, is more accurate since it additionally considers the radial component of the leakage magnetic field, but it is valid only at low frequencies. It assumes the windings take the shape of rectangular blocks, i.e. foils, and is able to accurately model the static leakage inductance of hollow conductors. Therefore, the model is employed to be a part of the MFT design optimization algorithm. However, the exact value of the leakage inductance at the set operating frequency is determined with the help of FEM simulations. Otherwise, during the design process, a minimal reduction of 25% is accounted for on top of the static value. Lastly, the experimental study conducted at the end of the chapter showed that there is no significant effect of the relative angular positions of the windings' terminations on the leakage inductance, regardless of the vertical displacement between the windings.

The particular technology selection of oil-immersed windings motivated the derivation of THM, which is presented in **Chap. 5**. The model is of analytical nature and able to estimate characteristic oil temperature within the vessels. It incorporates both thermal and hydraulic parts because oil expands when heated, which compels it to move. Owing to the choice to direct cold DI water to the top of the windings, instead of the bottom, a temperature gradient forms, going from colder at the top, to

warmer at the bottom of the windings, which helps oil move in two loops. Because of the intricate nature of the analytical modeling of heat transfer and fluid dynamics, the THM required further characterization using experimental measurements of oil temperatures and a genetic algorithm. As a result, a high level of agreement was achieved between the measurements and the model's output for different operating scenarios. Nevertheless, the current THM implementation is too complex for implementation in the MFT design procedure. Despite this, it can still be used to help characterize the overall thermal profile of an MFT design.

The last modeling chapter, **Chap. 6**, deals with loss and thermal evaluation of an MFT design. The core losses are estimated with IGSE, due to its accuracy, simplicity, and fast execution times, whereas for the pipe winding losses a combination of FEM-characterized hollow resistance factor and Dowell's model is employed. In addition, the static thermal model relies on the inputs of the two loss models to estimate the temperature distribution in the MFT. The model is developed for the characteristic geometry of the 2-vessel MFT, which allows a model division into two parts that independently handle the contributions of core and winding losses. Moreover, due to existing symmetries in the MFT geometry, the thermal modeling of the core is reduced to one core half, whereas for the windings, due to axial symmetry, the modeling reduces to half of a single vessel. Exploiting thermal symmetries of the component together with the splitting approach contribute to a large extent to the reduction of the computational effort. To connect the two thermal models, a straightforward ambient interface model is used, which considers that the core and windings, inside of the oil vessels, are in thermal contact through the same environment. Based on the fact that forced convection is a dominant mechanism in the windings-to-environment heat exchange process, a simplified version of the thermal windings model is developed, focusing solely on the exchange between DI water and Cu windings. For verification purposes, the model is compared with a more detailed one and against experimental measurements gathered during the THM characterization. The comparison revealed that the simplified version is reliable and can be included in the design algorithm.

Once all the essential models are presented and incorporated in the design optimization tool, the algorithm is applied to the design problem of a 1 MW core-type 2-vessel MFT structure and a set of electrical parameters provided in **Chap. 3**. The design outcomes are presented in the form of efficiency versus power density plots which are discussed in detail in **Chap. 7**. From a large number of created designs, a smaller set is identified using various design filters, which guide the designer to the optimal design solution. Among the pre-filtered group, four optimal MFT designs are chosen for further comparison following the highest efficiency criterion. The discrepancies between the designs are highlighted, and ultimately, one of them is designated as optimal. However, due to a scaling factor mistake in the flux density equation at an early stage of the design process, another MFT design is chosen for manufacturing with twice the core cross-section area than optimally set. As a result, significantly more material needs to be invested in its construction, however, it can be operated at three times lower frequencies without running into saturation. Before the construction phase, the winding loss and static thermal profile of the prototype design are verified with FEM simulations.

Finally, **Chap. 8** shows the assembly steps of a 1 MW, 5 kHz 2-vessel MFT prototype with actively cooled windings immersed in oil and air-cooled nanocrystalline core. Given that the utilization of pipes as windings is less typical compared to e.g. Litz wires, a thorough explanation is provided regarding their use and construction for this specific task. Additionally, the chapter includes good practices and recommendations when dealing with round hollow conductors. An important feature of the assembled prototype is the fact that besides the required 2:1 turns ratio, the MFT can be easily

connected into another 14 functional configurations, by rewiring the external connections between the MFT windings. Once completed, the prototype, as a single unit, underwent testing, including the identification of electric parameters and PD tests. As expected, the resulting leakage and magnetizing inductances were within the desired range. For insulation testing, a non-conventional standard was followed instead of the commonly employed one, due to a specific selection of technologies. Even though the prototype design does not correspond to the one marked as optimal by the design algorithm, the assembled MFT is fully operational and it is installed within the DCT for further evaluation. In terms of power testing, the no-load test was conducted, and the recorded voltage and current waveforms were analyzed to estimate the core losses. However, during a 12 h-thermal run the MFT prototype did not manage to reach a steady state for comparison with the FEM-simulated thermal image. Unfortunately, no power tests were carried out, resulting in the overall efficiency of the assembled prototype remaining unknown.

## 9.2 Final Conclusions

From the presented work, it can be concluded that technologies such as DCT, and SST in a broader sense, have what it takes to enable the future DC power distribution in the MV range but still, several challenges need to be answered. Aside from business-related matters, such as high converter cost, it is necessary to establish standards related to allowed voltage, current, and operating frequency levels of the converter and MFT, as well as introduce standardized insulation tests which match the operating conditions. In the meantime, research on topics similar to the one presented in this thesis should continue, i.e. exploration of feasibility and efficiency of different combinations of technologies, assisted by appropriate models and design methodologies. After all, a large body of knowledge on the topic of MFT design optimization already exists, which should be used and built upon.

Regarding the use of hollow conductors as MFT windings, their great advantage over the standard solution with Litz wires is the possibility of active cooling. This allows the weight of the total losses to be shifted to the windings' side, since with an adequate volumetric flow of the cooling fluid, the resulting temperature rise is kept under control. However, they have limitations in the operating frequency. From the available pipe manufacturers' information, MFT designs up to 10 kHz can be realized with Cu pipes having wall thicknesses up to 0.6 mm. Of course, the option of custom pipe manufacturing with even thinner walls is not excluded, however, one must count with impaired robustness and, thus, reduced reliability. Secondly, large number of turns with a small ID implies high pressure drop, which needs to be opposed and served with adequate pressure capacity of the WCU. The deficit on the efficiency side is visible from the modeling aspect, where the AC resistance of the hollow conductor is determined based on the one of the solid conductor. The hollow part of the pipe acts positively by reducing the resistance, however, this is limited and remains below 10%.

The oil insulation is very effective and has a positive influence on power density increase compared to a simpler isolation option such as air, though this was not explicitly shown in the thesis. However, it does require additional considerations regarding modeling, as well as implementation. Compared to air, the reliability of the insulation concept is generally reduced due to the possibility of leaking.

Regarding the EMPOWER project and the envisioned 1 MW DCT operation, it is unfortunate that at the end of the author's PhD time, the full-scale converter is not fully commissioned. Thus, the set goals of open-loop operation and improved efficiency due to resonant LLC-SRC topology selection cannot be fully appreciated. Moreover, at this point, no power loading of the MFT is performed,



MFT Design	$N_{PW}$	$N_{SW}$	$A_{core}$	$W$	$L$	$H$	$V_{MFT}$	kW/l	$M_{MFT}$	kW/kg
Optimal 4	34	17	$\approx 169 \text{ cm}^2$	310 mm	692 mm	577 mm	$\approx 111 \text{ L}$	9	200 kg	5
Prototype	34	17	$\approx 325 \text{ cm}^2$	488 mm	792 mm	598 mm	$\approx 232 \text{ L}$	4.3	$\approx 443 \text{ kg}$	2.26

**Tab. 9.1** Main MFT characteristics of the optimal design and the one selected for prototyping.

hence, the final estimation of its performance is missing.

Lastly, in light of the selected MFT design for prototyping which does not correspond to the optimal one, an important conclusion and remark arise. Namely, before any prototyping is started a thorough review and sanity check of the selected design needs to be performed. The design should be inspected from different angles so that any potential source of error can be detected early enough. **Tab. 9.1** summarizes the key design characteristics of the design, which is marked as optimal for the set requirements and the observed design space, and the design which was used to make the prototype. In this way, the main similarities and differences between the two designs can be easily observed. The provided dimensions do not consider the termination panel or any additional support. Thereby, the sizes  $W$ ,  $L$ , and  $H$  give depth, width, and height, respectively.

### 9.3 Future Work

The topics handled in the thesis cover the majority of relevant domains and aspects of the MFT design. However, several points have not been addressed or could be extended. Namely, estimations of the mechanical withstand capabilities of the windings in the case of short-circuit or in-rush currents, which are usually included in industrial designs, should be performed. Moreover, based on the estimated resulting electromagnetic forces adequate clamping systems for the windings could be determined, which guarantee the stability of the windings in case of high currents.

Similar to other magnetic components, MFTs can conduct and radiate electromagnetic energy, depending on the generated electromagnetic field, the transformer geometry, voltage and current excitation, and other factors. If not properly quantified and controlled through mitigation techniques, it can lead to electromagnetic interference issues and disturbance of the surrounding equipment. Thus, it is another point worth addressing.

Regarding the developed THM, as a next step in the research, the 9 selected optimization parameters could be determined differently, corresponding to a more physical approach and based on analytical equations. Once, this is achieved, the model could be generalized for any operating conditions (winding losses and WCU) and geometry. In this way, experimental characterization of the model could be avoided, which would make the THM much simpler to use and a part of the design algorithm. Secondly, advanced thermal-hydraulic networks for modeling of insulation/cooling liquids are more commonly used in the case of power distribution transformers, where the whole component is oil-immersed and disc windings are utilized, different from the ones typically employed for MF operation. Therefore, in this regard, more general models can be developed which are easily adapted to different winding types, and at the same time, can be used for design optimization algorithms.

To date, the literature review shows that modeling of different aspects and general use of hollow conductors, regardless of the shape of the cross section, for the task of MFT windings has not been

sufficiently researched, compared to the number of available works on the topic of Litz wires. The use of the magnetic images method for static leakage inductance modeling proved to be sufficiently accurate, however, it remains a frequency-independent model. Regarding the winding loss modeling, a combined analytical-FEM approach was used in this thesis. The weak spot of the selected model is its reduced accuracy for lower porosity factors, which is inevitable due to the required insulation of the windings from the core at zero potential. This becomes even more pronounced at MV levels. Only recently, works related to analytical loss modeling of hollow conductors started emerging. Thus, there is plenty of space to improve the existing models of hollow conductors to help close the modeling gap.

The design algorithm methodology at the current stage is based on the brute-force concept. Comparison based on performance and output with another design methodology, such as genetic algorithms or based on machine learning, would help in providing clarity on whether the increased implementation effort with more advanced optimization methods is justified and worthwhile.

# Appendices



# A

## Dimensionless Numbers

In fluid mechanics, dimensionless numbers are the ones that provide information and characterize the flow behavior of fluids. Due to the presence of active cooling in MFT windings, dimensionless numbers related to fluid dynamics are particularly important. The following sections define some of the commonly used numbers.

### A.1 Prandtl Number

The Prandtl number is an intrinsic property of the fluid, which describes the relation between momentum and heat transport capacity. It is defined as the ratio of the kinematic viscosity ( $\nu$  [ $\text{m}^2/\text{s}$ ]) and thermal diffusivity ( $\alpha$  [ $\text{m}^2/\text{s}$ ]), given by the following relation

$$Pr = \frac{\nu}{\alpha} = \frac{\mu}{\rho} \cdot \frac{\rho c_p}{k} = \frac{\mu c_p}{k}. \quad (\text{A.1})$$

Thereby,  $\nu$  can be expressed as a proportion of the dynamic viscosity ( $\mu$  [ $\text{Pa s}$ ]) and the fluid mass density ( $\rho$ ), whereas  $\alpha$  is a function of  $c_p$  [ $\text{J/kg K}$ ] as the specific heat capacity of the fluid, its thermal conductivity  $k$  and mass density.

### A.2 Rayleigh Number

In the case of free or natural convection, the Rayleigh number ( $Ra$ ) is employed to determine the transition between the laminar (low  $Ra$  numbers) and turbulent flow regime (high values). The transition depends on the ratio between buoyancy and viscous forces in the fluid. The  $Ra$  number is defined as the product of the Grashof and Prandtl numbers as follows:

$$Ra_L = Gr \cdot Pr = \frac{g\beta|T_s - T_\infty|L^3}{\nu^2} \cdot \frac{\rho c_p}{k} = \frac{g\beta\rho^2 c_p|T_s - T_\infty|L^3}{k\mu} \quad (\text{A.2})$$

The critical  $Ra$  value for which the fluid changes its flow pattern depends on the geometry of the surfaces participating in the heat exchange. Note that a Rayleigh number smaller than  $10^3$  implies conduction dominates over the convection mechanism.

### A.3 Reynolds Number

The Reynolds number is a dimensionless quantity that gives the ratio of inertial forces to viscous forces within a fluid, which is experiencing internal movements as a result of different fluid velocities.

Similar to  $Ra$  number, it is used to predict the transition from laminar to turbulent flow, but in the case of forced convection. The viscosity of the fluid tends to inhibit turbulence. The Reynolds number is defined by

$$Re = \frac{\rho u L}{\mu} = \frac{u L}{\nu}. \quad (\text{A.3})$$

Thereby,  $u$  [m/s] is the velocity and  $L$  [m] is the characteristic length of the flow. The other parameters have been previously defined. In the case of pipes, the internal diameter is the characteristic dimension.

The laminar flow is characterized by dominant viscous forces and a smooth, constant fluid motion, whereas for a turbulent flow, the inertial forces prevail, which tend to produce chaotic behavior and flow instabilities. The critical Reynolds number at which the flow becomes turbulent varies with the geometric configuration.

## A.4 Nusselt Number

The Nusselt number expresses the ratio of the convective to conductive heat transfer across the fluid boundary. It is a measure of the rate of the convection heat transfer and it is given by the following

$$Nu = \frac{\text{Convective heat transfer}}{\text{Conductive heat transfer}} = \frac{h d}{\lambda}. \quad (\text{A.4})$$

As already stated in (2.26) - (2.27), it is a function of fluid properties ( $Pr$  number) and  $Ra$  or  $Re$  number. A large value of  $Nu$  signifies very efficient convection. It is usually empirically determined for a prescribed geometry and certain fluid properties and is the main factor in establishing the convective HTC.

In general, the range of possible values for natural and forced convection HTCs is very wide. To provide an insight for the reader, a typical range in the case of natural convection involving a liquid medium is:  $h_{cv} \approx 50 - 1000 \text{ W/m}^2 \text{ K}$ , whereas for forced convection, this range is even wider:  $h_{cv} \approx 50 - 20\,000 \text{ W/m}^2 \text{ K}$ . As mentioned already, these values are strongly temperature dependent.

All the Nusselt correlations relevant to the thermal modeling of the MFT are summarized in **Tab. 6.3**. In case the geometrical and thermal conditions between the vertical vessel walls and windings do not match the conditions of the Nusselt correlations employed for vertical coaxial cylinders, i.e. vertical circular annuli, as a replacement, the geometry is approximated with a rectangular enclosure.

## Thermal Properties of Fluids

**Tab. B.1** provides some of the physical properties ( $\beta$  thermal expansion coefficient,  $c_p$  specific heat capacity,  $\lambda$  thermal conductivity,  $\nu$  kinematic viscosity,  $\rho$  mass density) of the employed liquid media (air, oil, and DI water) in the MFT design. The properties are expressed as functions of temperature, marked with  $T$ , and are obtained by fitting the temperature-dependent data.

Fluid	Property	Expression	Unit
Air	$\beta$	$-1.05 \cdot 10^{-10} T^3 + 4.63 \cdot 10^{-8} T^2 - 1.36 \cdot 10^{-5} T + 3.69 \cdot 10^{-3}$	[1/K]
	$c_p$	$40.36 \cdot 10^{-5} T^2 + 16.55 \cdot 10^{-3} T + 1006$	[J/kg°C]
	$\lambda$	$74.46 \cdot 10^{-5} T + 23.63 \cdot 10^{-3}$	[W/mK]
	$\nu$	$95.02 \cdot 10^{-12} T^2 + 87.91 \cdot 10^{-9} T + 13.32 \cdot 10^{-6}$	[m <sup>2</sup> /s]
	$\rho$	$93.98 \cdot 10^{-7} T^2 - 43.65 \cdot 10^{-4} T + 1.29$	[kg/m <sup>3</sup> ]
Oil	$\beta$	$7.7 \cdot 10^{-4}$	[1/K]
	$c_p$	$12.35 \cdot 10^{-7} T^4 - 36.21 \cdot 10^{-5} T^3 + 39 \cdot 10^{-3} T^2 + 79.84 \cdot 10^{-2} T + 1870$	[J/kg°C]
	$\lambda$	$32.38 \cdot 10^{-9} T^3 - 13.28 \cdot 10^{-7} T^2 - 28.82 \cdot 10^{-7} T + 0.15$	[W/mK]
	$\nu$	$3.36 \cdot 10^{-12} T^4 - 11.35 \cdot 10^{-10} T^3 + 14.28 \cdot 10^{-8} T^2 - 81.32 \cdot 10^{-7} T + 18.87 \cdot 10^{-5}$	[m <sup>2</sup> /s]
	$\rho$	$-72.17 \cdot 10^{-2} T + 982.2$	[kg/m <sup>3</sup> ]
DI water	$\beta$	$59.35 \cdot 10^{-11} T^3 - 13.79 \cdot 10^{-8} T^2 + 15.64 \cdot 10^{-6} T - 56.39 \cdot 10^{-6}$	[1/K]
	$c_p$	$11.95 \cdot 10^{-7} T^4 - 34.53 \cdot 10^{-5} T^3 + 43.95 \cdot 10^{-3} T^2 - 2.1 T + 4212$	[J/kg°C]
	$\lambda$	$3.21 \cdot 10^{-8} T^3 - 14.21 \cdot 10^{-6} T^2 + 2.3 \cdot 10^{-3} T + 55.72 \cdot 10^{-2}$	[W/mK]
	$\nu$	$14.44 \cdot 10^{-15} T^4 - 50.33 \cdot 10^{-13} T^3 + 68.16 \cdot 10^{-11} T^2 - 46.39 \cdot 10^{-9} T + 1.7 \cdot 10^{-6}$	[m <sup>2</sup> /s]
	$\rho$	$-72.34 \cdot 10^{-9} T^4 + 28.68 \cdot 10^{-6} T^3 - 65.6 \cdot 10^{-4} T^2 + 24.1 \cdot 10^{-3} T + 1000$	[kg/m <sup>3</sup> ]

**Tab. B.1** Temperature-dependent physical properties of the employed liquid media.





## Multi-Winding MFT Configurations

**Fig. C.1** provides a review of all the functional MFT configurations. Depending on the external connections of the windings and attributions of PWs and SWs in the two vessels, the prototype can be used for eight 2-winding configurations, presented in subfigures (a) and (b) of **Fig. C.1**. The two groups differ from each other based on the windings forming the PW and SW. Namely, in the first group, in each vessel one of the windings is attributed to the PW group and the other to the SW, whereas in the (b) case, the two windings in the same vessel are connected either in series or in parallel and make the primary/secondary side.

Additionally, six 3-winding options are identified, shown in (c). Thereby, the color code in **Fig. C.1** assumes there is one PW and two SW, which can also be interchanged. Lastly, a single 4-winding MFT option exists, as illustrated in subfigure (d) of **Fig. C.1**.

The four 2-winding MFT configurations from subfigure (a) are characterized regarding their leakage and magnetizing inductances at the frequency of 5 kHz, referenced to both the primary and secondary sides. The measured values are provided in **Tab. C.1**. Thereby, two measurement devices are used, an

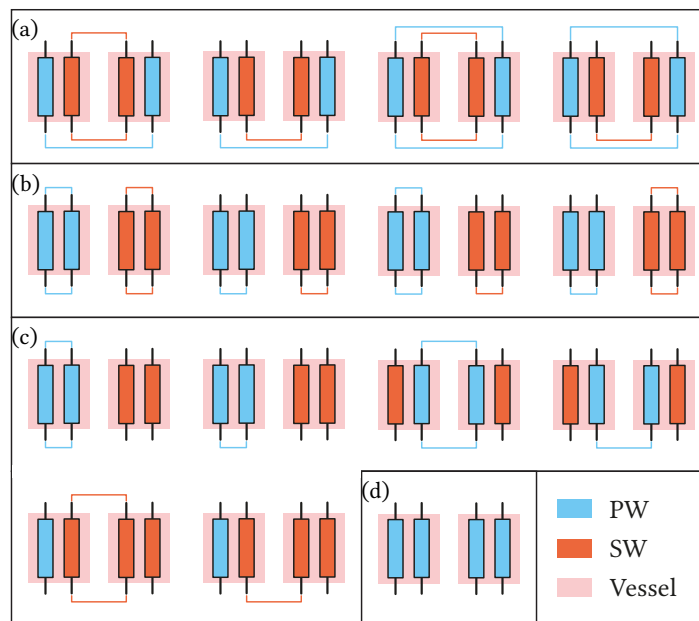


**Fig. C.1** Usable prototype configurations of the assembled 2-vessel MFT: (a) Four 2-winding configurations with a pair of PW and SW in each vessel; (b) Four more 2-winding configurations with PWs and SWs placed in separate vessels; (c) Eight 3-winding MFTs; (d) A single 4-winding MFT configuration.

<b>PWs series, SWs parallel</b>	<b><math>L_\sigma</math> [<math>\mu</math>H]</b>	<b><math>L_m</math> [mH]</b>
PW side	42.55 / 42.86	36.66 / 36.74
SW side	10.65 / 10.66	9.16 / 9.17
<b>PWs parallel, SWs parallel</b>	<b><math>L_\sigma</math> [<math>\mu</math>H]</b>	<b><math>L_m</math> [mH]</b>
PW side	11.53 / 11.09	10.09 / 10.1
SW side	11.56 / 11.3	10.08 / 10.09

<b>PWs series, SWs series</b>	<b><math>L_\sigma</math> [<math>\mu</math>H]</b>	<b><math>L_m</math> [mH]</b>
PW side	41.6 / 41.35	40.8 / 40.86
SW side	41.58 / 41.57	40.76 / 40.81
<b>PWs parallel, SWs series</b>	<b><math>L_\sigma</math> [<math>\mu</math>H]</b>	<b><math>L_m</math> [mH]</b>
PW side	10.68 / 10.45	10.08 / 10.09
SW side	43.57 / 43.2	40.25 / 40.37

**Tab. C.1** Measured leakage and magnetizing inductances of the four 2-winding MFT configurations from (a). For each measurement point two inductance values are provided, the first one is acquired with an RLC meter, and the second one with a Bode 100 impedance analyzer.

RLC meter (BK895), and the impedance analyzer Omicron Lab Bode 100. The measurements from both devices are indicated in the table. The slight deviations between the values can be ascribed to measurement uncertainties.

# Bibliography

- [1] IEA, *World Energy Model*, <https://www.iea.org/reports/world-energy-model>, [Online.] Accessed 2022.07.26, 2021.
- [2] IEA, *Renewables 2021*, <https://www.iea.org/reports/renewables-2021>, [Online.] Accessed 2022.07.26, 2021.
- [3] W. the free encyclopedia, *List of HVDC Projects*, [https://en.wikipedia.org/wiki/List\\_of\\_HVDC\\_projects](https://en.wikipedia.org/wiki/List_of_HVDC_projects), [Online.] Accessed 2022.08.18, 2022.
- [4] A. Nishioka, F. Alvarez, and T. Omori, "Global rise of hvdc and its background," *Hitachi ABB HVDC Technologies, Ltd., Tech. Rep.*, 2020.
- [5] H. Energy, *The Gotland HVDC link*, <https://www.hitachienergy.com/case-studies/the-gotland-hvdc-link>, [Online.] Accessed 2022.07.26, 2020.
- [6] D. Van Hertem, O. Gomis-Bellmunt, and J. Liang, *HVDC grids: for offshore and supergrid of the future*. John Wiley & Sons, 2016.
- [7] A. Kalair, N. Abas, and N. Khan, "Comparative study of hvac and hvdc transmission systems," *Renewable and Sustainable Energy Reviews*, vol. 59, pp. 1653–1675, 2016.
- [8] I. I. Hussein, S. Essallah, and A. Khedher, "Comparative study of hvdc and hvac systems in presence of large scale renewable energy sources," in *2020 20th International Conference on Sciences and Techniques of Automatic Control and Computer Engineering (STA)*, 2020, pp. 225–230.
- [9] D. Fregosi, S. Ravula, D. Brhlik, J. Saussele, S. Frank, E. Bonnema, J. Scheib, and E. Wilson, "A comparative study of dc and ac microgrids in commercial buildings across different climates and operating profiles," in *2015 IEEE First International Conference on DC Microgrids (ICDCM)*, 2015, pp. 159–164.
- [10] J. Brenguier, M. Vallet, and F. VAILLANT, "Efficiency gap between ac and dc electrical power distribution system," in *2016 IEEE/IAS 52nd Industrial and Commercial Power Systems Technical Conference (ICPS)*, IEEE, 2016, pp. 1–6.
- [11] S. Lundberg, "Wind farm configuration and energy efficiency studies-series dc versus ac layouts," Ph.D. dissertation, Chalmers University of Technology, 2006.
- [12] K. A. N. Al-Deen and H. A. Hussain, "Review of dc offshore wind farm topologies," in *2021 IEEE Energy Conversion Congress and Exposition (ECCE)*, IEEE, 2021, pp. 53–60.
- [13] M. A. Bezerra, J. L. Oliveira, P. P. Praça, D. S. Oliveira, L. H. S. Barreto, and B. R. de Almeida, "Isolated ac-dc interleaved converter for mvdc collection grid in hvdc offshore wind farm," in *2019 IEEE Applied Power Electronics Conference and Exposition (APEC)*, IEEE, 2019, pp. 1926–1933.
- [14] B. Li, J. Liu, Z. Wang, S. Zhang, and D. Xu, "Modular high-power dc-dc converter for mvdc renewable energy collection systems," *IEEE Transactions on Industrial Electronics*, vol. 68, no. 7, pp. 5875–5886, 2020.
- [15] U. Javaid, D. Dujic, and W. van der Merwe, "Mvdc marine electrical distribution: Are we ready?" In *IECON 2015 - 41st Annual Conference of the IEEE Industrial Electronics Society*, 2015, pp. 000 823–000 828.
- [16] U. Javaid, F. D. Freijedo, D. Dujic, and W. van der Merwe, "Mvdc supply technologies for marine electrical distribution systems," *CPSS Transactions on Power Electronics and Applications*, vol. 3, no. 1, pp. 65–76, 2018.
- [17] U. Javaid, F. D. Freijedo, W. van der Merwe, and D. Dujic, "Stability analysis of multi-port mvdc distribution networks for all-electric ships," *IEEE Journal of Emerging and Selected Topics in Power Electronics*, vol. 8, no. 2, pp. 1164–1177, 2019.
- [18] J. L. Brooks, "Solid state transformer concept development," Civil Engineering Lab (Navy) Port Hueneme CA, Tech. Rep., 1980.
- [19] L. Yang, T. Zhao, J. Wang, and A. Q. Huang, "Design and analysis of a 270kw five-level dc/dc converter for solid state transformer using 10kv sic power devices," in *2007 IEEE Power Electronics Specialists Conference*, IEEE, 2007, pp. 245–251.
- [20] X. She, A. Q. Huang, and R. Burgos, "Review of solid-state transformer technologies and their application in power distribution systems," *IEEE journal of emerging and selected topics in power electronics*, vol. 1, no. 3, pp. 186–198, 2013.
- [21] D. Dujic, C. Zhao, A. Mester, J. K. Steinke, M. Weiss, S. Lewdeni-Schmid, T. Chaudhuri, and P. Stefanutti, "Power electronic traction transformer-low voltage prototype," *IEEE Trans. Power Electron.*, vol. 28, no. 12, pp. 5522–5534, 2013.
- [22] C. Zhao, D. Dujic, A. Mester, J. K. Steinke, M. Weiss, S. Lewdeni-Schmid, T. Chaudhuri, and P. Stefanutti, "Power electronic traction transformer-medium voltage prototype," *IEEE Transactions on Industrial Electronics*, vol. 61, no. 7, pp. 3257–3268, 2014.
- [23] E. R. Ronan, S. D. Sudhoff, S. F. Glover, and D. L. Galloway, "A power electronic-based distribution transformer," *IEEE Transactions on Power Delivery*, vol. 17, no. 2, pp. 537–543, 2002.

- [24] D. Dujic, F. Kieferndorf, F. Canales, and U. Drofenik, "Power electronic traction transformer technology," in *Proceedings of The 7th International Power Electronics and Motion Control Conference*, IEEE, vol. 1, 2012, pp. 636–642.
- [25] X. She, R. Burgos, G. Wang, F. Wang, and A. Q. Huang, "Review of solid state transformer in the distribution system: From components to field application," in *2012 IEEE Energy Conversion Congress and Exposition (ECCE)*, IEEE, 2012, pp. 4077–4084.
- [26] U. of Nottingham, *UNIFLEX Project*, <http://www.eee.nott.ac.uk/uniflex>, [Online.] Accessed 2019.06.16, 2018.
- [27] M. L. Kiel University, *The Highly Efficient and Reliable smart Transformer (Heart)*, <http://www.heart.tf.uni-kiel.de/en/home>, [Online.] Accessed 2020.02.16, 2020.
- [28] A. Austrian Institute of Technology GmbH, *HYPERRIDE Project*, <https://hyperride.eu/>, [Online.] Accessed 2022.08.11, 2022.
- [29] E. Power Electronics Laboratory, *EMPOWER Project*, <https://www.epfl.ch/labs/pel/empower/>, [Online.] Accessed 2023.03.21, 2023.
- [30] Y. K. Tran and D. Dujic, "A multiport isolated dc-dc converter," in *2016 IEEE Applied Power Electronics Conference and Exposition (APEC)*, Mar. 2016, pp. 156–162.
- [31] Y.-K. Tran and D. Dujic, "A multiport medium voltage isolated dc-dc converter," in *Industrial Electronics Society, IECON 2016-42nd Annual Conference of the IEEE*, IEEE, 2016, pp. 6983–6988.
- [32] A. J. Bottion and I. Barbi, "Input-series and output-series connected modular output capacitor full-bridge pwm dc-dc converter," *IEEE Transactions on Industrial Electronics*, vol. 62, no. 10, pp. 6213–6221, 2015.
- [33] X. She, X. Yu, F. Wang, and A. Q. Huang, "Design and demonstration of a 3.6-kv-120-v/10-kva solid-state transformer for smart grid application," *IEEE Transactions on Power Electronics*, vol. 29, no. 8, pp. 3982–3996, 2014.
- [34] Z. Yu, R. Bai, Y. Zhang, and Y. Zhu, "Review of dc circuit breaker technology development," in *2022 7th Asia Conference on Power and Electrical Engineering (ACPEE)*, 2022, pp. 621–626.
- [35] S. Kim, J. Kucka, G. Ulissi, S.-N. Kim, and D. Dujic, "Solid-state technologies for flexible and efficient marine dc microgrids," *IEEE Transactions on Smart Grid*, vol. 12, no. 4, pp. 2860–2868, 2021.
- [36] R. Rodrigues, Y. Du, A. Antoniazzi, and P. Cairoli, "A review of solid-state circuit breakers," *IEEE Transactions on Power Electronics*, vol. 36, no. 1, pp. 364–377, 2020.
- [37] R. L. Steigerwald, "High-frequency resonant transistor dc-dc converters," *IEEE Transactions on Industrial Electronics*, vol. IE-31, no. 2, pp. 181–191, 1984.
- [38] R. W. De Doncker, D. M. Divan, and M. H. Kheraluwala, "A three-phase soft-switched high-power-density dc/dc converter for high-power applications," *IEEE transactions on industry applications*, vol. 27, no. 1, pp. 63–73, 1991.
- [39] Q. Zhu, L. Wang, L. Zhang, and A. Q. Huang, "A 10 kv dc transformer (dcx) based on current fed src and 15 kv sic mosfets," in *2018 IEEE Applied Power Electronics Conference and Exposition (APEC)*, 2018, pp. 149–155.
- [40] D. Dujic, S. Lewdeni-Schmid, A. Mester, C. Zhao, M. Weiss, J. Steinke, M. Pellerin, and T. Chaudhuri, "Experimental characterization of llc resonant dc/dc converter for medium voltage applications," *Tech. Rep.*, 2011.
- [41] T. Guillod, D. Rothmund, and J. W. Kolar, "Active magnetizing current splitting zvs modulation of a 7 kv/400 v dc transformer," *IEEE Transactions on Power Electronics*, vol. 35, no. 2, pp. 1293–1305, 2020.
- [42] R. W. Erickson and D. Maksimovic, *Fundamentals of power electronics*. Springer Science & Business Media, 2007.
- [43] M. N. Undeland, W. P. Robbins, and N. Mohan, "Power electronics," *Converters, Applications, and Design*, 1995.
- [44] V. C. Valchev and A. Van den Bossche, *Inductors and transformers for power electronics*. CRC press, 2018.
- [45] C. W. T. McLyman, *Transformer and inductor design handbook*. CRC press, 2004.
- [46] W.-J. Gu and R. Liu, "A study of volume and weight vs. frequency for high-frequency transformers," in *Proceedings of IEEE Power Electronics Specialist Conference - PESC '93*, 1993, pp. 1123–1129.
- [47] I. Villar, "Multiphysical characterization of medium-frequency power electronic transformers," *PhD thesis*, 2010.
- [48] W. G. Hurley, W. H. Wolfle, and J. G. Breslin, "Optimized transformer design: Inclusive of high-frequency effects," *IEEE transactions on power electronics*, vol. 13, no. 4, pp. 651–659, 1998.
- [49] M. K. Kazimierczuk, *High-frequency magnetic components*. John Wiley & Sons, 2009.
- [50] S. Yin, S. Debnath, R. Wojda, P. Marthi, and M. Saeedifard, "Impact of the transformer magnetizing inductance on the performance of the dual-active bridge converter," in *2021 IEEE 22nd Workshop on Control and Modelling of Power Electronics (COMPEL)*, IEEE, 2021, pp. 1–7.
- [51] I. Colak, *Insulation coordination for power electronics equipment*, 2019.
- [52] S. Ozdemir, N. Altin, A. Nasiri, and R. Cuzner, "Review of standards on insulation coordination for medium voltage power converters," *IEEE Open Journal of Power Electronics*, vol. 2, pp. 236–249, 2021.
- [53] C. Zheng, Q. Wang, H. Wang, C. L. Bak, and Z. Shen, "Uneven inter-turn voltage distribution among windings of medium-voltage medium/high-frequency transformers," in *2020 IEEE International Conference on High Voltage Engineering and Application (ICHVE)*, 2020, pp. 1–4.
- [54] S. Tumanski, *Handbook of magnetic measurements*. CRC press, 2016.

- [55] E. TDK, *SIFFERIT Material N87*, 2017.
- [56] G. Slama, *Professional education seminar: Magnetic design fundamentals - what they didn't tell you*, Würth Electronics, APEC, 2019.
- [57] T. B. Gradinger and M. Mogorovic, "Foil-winding design for medium-frequency medium-voltage transformers," in *2021 23rd European Conference on Power Electronics and Applications (EPE'21 ECCE Europe)*, IEEE, 2021, pp. 1–10.
- [58] A. Goldman, *Handbook of modern ferromagnetic materials*. Springer Science & Business Media, 2012, vol. 505.
- [59] P. Shuai, "Optimal design of highly efficient, compact and silent medium frequency transformers for future solid state transformers," Ph.D. dissertation, ETH Zurich, 2017.
- [60] T. Belgrand and R. Lemaître, *Grain oriented electrical steel for solid-state transformers*, 2019.
- [61] N. Hugo, P. Stefanutti, M. Pellerin, and R. Sablières, "Power Electronics Traction Transformer Semiconductors Keywords Multilevel converter topology," *Power*, pp. 1–10,
- [62] I. Villar, L. Mir, I. Etxeberria-Otadui, J. Colmenero, X. Agirre, and T. Nieva, "Optimal design and experimental validation of a Medium-Frequency 400kVA power transformer for railway traction applications," *2012 IEEE Energy Conversion Congress and Exposition, ECCE 2012*, pp. 684–690, 2012.
- [63] E. E. R. A. University, *Novel 5 MW-DC Converter Put Into Operation*, Accessed 2022.10.26, 2020.
- [64] L. Heinemann, "An actively cooled high power, high frequency transformer with high insulation capability," in *APEC. Seventeenth Annual IEEE Applied Power Electronics Conference and Exposition (Cat. No.02CH37335)*, vol. 1, Mar. 2002, 352–357 vol.1.
- [65] T. Kjellqvist, S. Norrga, S. Östlund, and K. Ilves, "Thermal evaluation of a medium frequency transformer in a line side conversion system," *2009 13th European Conference on Power Electronics and Applications (EPE)*, 2009.
- [66] M. Steiner and H. Reinold, "Medium frequency topology in railway applications," *2007 European Conference on Power Electronics and Applications, EPE*, 2007.
- [67] H. Hoffmann and B. Piepenbreier, "Medium frequency transformer for rail application using new materials," *1st International Electric Drives Production Conference 2011, EDPC-2011 - Proceedings*, pp. 192–197, 2011.
- [68] H. Hoffmann and B. Piepenbreier, "Medium frequency transformer in resonant switching dc/dc-converters for railway applications," *Proceedings of the 2011 14th European Conference on Power Electronics and Applications*, pp. 1–8, 2011.
- [69] G. Ortiz, "High-power dc-dc converter technologies for smart grid and traction applications," Ph.D. dissertation, ETH Zurich, 2014.
- [70] G. Ortiz, M. Leibl, J. W. Kolar, and O. Apeldoorn, "Medium frequency transformers for solid-state-transformer applications — design and experimental verification," in *2013 IEEE 10th International Conference on Power Electronics and Drive Systems (PEDS)*, 2013, pp. 1285–1290.
- [71] M. Mogorovic and D. Dujic, "100 kw, 10 khz medium-frequency transformer design optimization and experimental verification," *IEEE Transactions on Power Electronics*, vol. 34, no. 2, pp. 1696–1708, 2018.
- [72] M. Mogorovic and D. Dujic, "Medium frequency transformer design and optimization," in *PCIM Europe 2017; International Exhibition and Conference for Power Electronics, Intelligent Motion, Renewable Energy and Energy Management*, VDE, 2017, pp. 1–8.
- [73] T. Guillod, "Modeling and design of medium-frequency transformers for future medium-voltage power electronics interfaces," Ph.D. dissertation, ETH Zurich, 2018.
- [74] *Table of basic conductor properties: Resistivity and temperature coefficients*, <http://230nsc1.phy-astr.gsu.edu/hbase/Tables/rstiv.html>, Accessed 2022.10.25.
- [75] *Table of metals and alloys densities: The engineering toolbox*, <https://www.engineeringtoolbox.com/>, Accessed 2022.10.25.
- [76] S. Khaparde and S. Kulkarni, *Transformer Engineering: Design and Practice*. Taylor & Francis Limited, 2004.
- [77] V. A. Thiviyanathan, P. J. Ker, Y. S. Leong, F. Abdullah, A. Ismail, and M. Zaini Jamaludin, "Power transformer insulation system: A review on the reactions, fault detection, challenges and future prospects," *Alexandria Engineering Journal*, vol. 61, no. 10, pp. 7697–7713, 2022.
- [78] *Midel 7131 Selection Guide*.
- [79] T. B. Gradinger, U. Drofenik, and S. Alvarez, "Novel insulation concept for an mv dry-cast medium-frequency transformer," in *2017 19th European Conference on Power Electronics and Applications (EPE'17 ECCE Europe)*, 2017, P.1–P.10.
- [80] IEC61800-5-1, *International Standard, Adjustable speed electrical power drive systems, Part 5-1: Safety requirements - Electrical, thermal and energy*, Switzerland, 2007.
- [81] I. 60076-3, *International Standard, Power transformers, Part 3: Insulation levels, dielectric tests and external clearances in air*, Switzerland, 2013.
- [82] F. P. Incropera, A. S. Lavine, T. L. Bergman, and D. P. DeWitt, *Fundamentals of heat and mass transfer*. Wiley, 2007.

- [83] H. Miki, *Soft magnetic materials for medium frequency transformer*, 2019.
- [84] D. Aggeler, J. Biela, S. Inoue, H. Akagi, and J. W. Kolar, "Bi-Directional Isolated DC-DC Converter for Next-Generation Power Distribution - Comparison of Converters using Si and SiC Devices," pp. 510–517, 2007.
- [85] N. Schibli, "Symmetrical multilevel converters with two quadrant dc-dc feeding," Ph.D. dissertation, EPFL, 2000.
- [86] S. S. Baek, S. Bhattacharya, B. Cougo, and G. Ortiz, "Accurate equivalent circuit modeling of a medium-voltage and high-frequency coaxial winding DC-link transformer for solid state transformer applications," *2012 IEEE Energy Conversion Congress and Exposition, ECCE 2012*, pp. 1439–1446, 2012.
- [87] L. Heinemann, "An actively cooled high power, high frequency transformer with high insulation capability," vol. 00, no. c, pp. 352–357, 2002.
- [88] J. B. Goodenough, "Summary of losses in magnetic materials," *IEEE Transactions on magnetics*, vol. 38, no. 5, pp. 3398–3408, 2002.
- [89] C. P. Steinmetz, "On the law of hysteresis," *Proceedings of the IEEE*, vol. 72, no. 2, pp. 197–221, 1984.
- [90] J. Reinert, A. Brockmeyer, and R. De Doncker, "Calculation of losses in ferro- and ferrimagnetic materials based on the modified steinmetz equation," *IEEE Transactions on Industry Applications*, vol. 37, no. 4, pp. 1055–1061, 2001.
- [91] W. Shen, "Design of high-density transformers for high-frequency high-power converters," Ph.D. dissertation, Virginia Polytechnic Institute and State University, 2006.
- [92] K. Venkatachalam, C. R. Sullivan, T. Abdallah, and H. Tacca, "Accurate prediction of ferrite core loss with nonsinusoidal waveforms using only steinmetz parameters," in *2002 IEEE Workshop on Computers in Power Electronics, 2002. Proceedings.*, IEEE, 2002.
- [93] G. Bertotti, "Some considerations on the physical interpretation of eddy current losses in ferromagnetic materials," *Journal of magnetism and magnetic materials*, vol. 54, pp. 1556–1560, 1986.
- [94] D. Lin, P. Zhou, W. Fu, Z. Badics, and Z. Cendes, "A dynamic core loss model for soft ferromagnetic and power ferrite materials in transient finite element analysis," *IEEE Transactions on Magnetics*, vol. 40, no. 2, pp. 1318–1321, 2004.
- [95] D. C. Jiles and D. L. Atherton, "Theory of ferromagnetic hysteresis," *Journal of magnetism and magnetic materials*, vol. 61, no. 1-2, pp. 48–60, 1986.
- [96] D. C. Jiles and J. Thoeleke, "Theory of ferromagnetic hysteresis: Determination of model parameters from experimental hysteresis loops," *IEEE Transactions on magnetics*, vol. 25, no. 5, pp. 3928–3930, 1989.
- [97] F. Preisach, "Über die magnetische Nachwirkung," *Zeitschrift für Physik*, vol. 94, no. 5-6, pp. 277–302, 1935.
- [98] A. Benabou, S. Clénet, and F. Piriou, "Comparison of preisach and jiles-atherton models to take into account hysteresis phenomenon for finite element analysis," *Journal of magnetism and magnetic materials*, vol. 261, no. 1-2, pp. 139–160, 2003.
- [99] M. Luo, D. Dujic, and J. Allmeling, "Modeling frequency-dependent core loss of ferrite materials using permeance-capacitance analogy for system-level circuit simulations," *IEEE Transactions on Power Electronics*, vol. 34, no. 4, pp. 3658–3676, 2018.
- [100] D. C. Hamill, "Lumped equivalent circuits of magnetic components: The gyrator-capacitor approach," *IEEE transactions on power electronics*, vol. 8, no. 2, pp. 97–103, 1993.
- [101] M. Luo, D. Dujic, and J. Allmeling, "Permeance based modeling of magnetic hysteresis with inclusion of eddy current effect," in *2018 IEEE Applied Power Electronics Conference and Exposition (APEC)*, IEEE, 2018, pp. 1764–1771.
- [102] M. Luo, "Dynamic modeling of magnetic components for circuit simulation of power electronic systems," PhD thesis, EPFL, 2018.
- [103] J. Muehlethaler, J. Biela, J. W. Kolar, and A. Ecklebe, "Improved core-loss calculation for magnetic components employed in power electronic systems," in *IEEE Transactions on Power Electronics*, vol. 27, 2012, pp. 964–973.
- [104] M. Yang, Y. Li, Q. Yang, Z. Lin, S. Yue, H. Wang, and C. Liu, "Magnetic properties measurement and analysis of high frequency core materials considering temperature effect," *IEEE Transactions on Applied Superconductivity*, vol. 30, no. 4, pp. 1–5, 2020.
- [105] N. Djekanovic, M. Luo, and D. Dujic, "Thermally-Compensated Magnetic Core Loss Model for Time-Domain Simulations of Electrical Circuits," *IEEE Transactions on Power Electronics*, vol. 36, no. 7, pp. 8193–8205, 2021.
- [106] P. Dowell, "Effects of eddy currents in transformer windings," *Proceedings of the Institution of Electrical Engineers*, vol. 113, no. 8, p. 1387, 1966.
- [107] J. A. Ferreira, "Improved analytical modeling of conductive losses in magnetic components," *IEEE transactions on Power Electronics*, vol. 9, no. 1, pp. 127–131, 1994.
- [108] X. Nan and C. R. Sullivan, "An improved calculation of proximity-effect loss in high-frequency windings of round conductors," in *IEEE 34th Annual Conference on Power Electronics Specialist, 2003. PESC'03.*, IEEE, vol. 2, 2003, pp. 853–860.

- [109] A. Reatti and M. K. Kazimierczuk, "Comparison of various methods for calculating the ac resistance of inductors," *IEEE Transactions on Magnetics*, vol. 38, no. 3, pp. 1512–1518, 2002.
- [110] G. Dimitrakakis, E. Tatakis, and E. Rikos, "A new model for the determination of copper losses in transformer windings with arbitrary conductor distribution under high frequency sinusoidal excitation," in *2007 European Conference on Power Electronics and Applications*, IEEE, 2007, pp. 1–10.
- [111] C. Lu, Y. Guo, Y. Wang, D. Yu, and P. Li, "Ac resistance calculation method for hollow conductor windings in high power medium frequency transformers," *CSEE*, vol. 36, no. 23, 2016.
- [112] J. Lammeraner and M. Štafl, *Eddy currents*. Iliffe books, 1966.
- [113] J. Biela, "Optimierung des elektromagnetisch integrierten serien-parallel resonanzkonverters mit eingepprägtem ausgangsstrom," Ph.D. dissertation, ETH Zurich, 2005.
- [114] J. Ferreira, "Analytical computation of ac resistance of round and rectangular litz wire windings," in *IEE Proceedings B (Electric Power Applications)*, IET, vol. 139, 1992, pp. 21–25.
- [115] J. Mühlethaler, "Modeling and multi-objective optimization of inductive power components," Ph.D. dissertation, ETH Zurich, 2012.
- [116] J. Smajic, G. Di Pino, C. Stemmler, W. Mönig, and M. Carlen, "Numerical study of the core saturation influence on the winding losses of traction transformers," *IEEE Transactions on Magnetics*, vol. 51, no. 3, pp. 1–4, 2015.
- [117] J. Smajic, J. Hughes, T. Steinmetz, D. Pusch, W. Monig, and M. Carlen, "Numerical computation of ohmic and eddy-current winding losses of converter transformers including higher harmonics of load current," *IEEE Transactions on Magnetics*, vol. 48, no. 2, pp. 827–830, 2012.
- [118] I. Lienhard and H. John, *A heat transfer textbook*. phlogiston press, 2005.
- [119] T. Kjellqvist, S. Ostlund, S. Norrga, and K. Ilves, "Thermal evaluation of a medium frequency transformer in a line side conversion system," in *2009 13th European Conference on Power Electronics and Applications*, IEEE, 2009, pp. 1–10.
- [120] I. Villar, U. Viscarret, I. Etxeberria-Otadui, and A. Rufer, "Transient thermal model of a medium frequency power transformer," in *2008 34th Annual Conference of IEEE Industrial Electronics*, IEEE, 2008, pp. 1033–1038.
- [121] A. Oliver, "Estimation of transformer winding temperatures and coolant flows using a general network method," in *IEE Proceedings C (Generation, Transmission and Distribution)*, IET, vol. 127, 1980, pp. 395–405.
- [122] J. Zhang and X. Li, "Oil cooling for disk-type transformer windings-part 1: Theory and model development," *IEEE Transactions on Power Delivery*, vol. 21, no. 3, pp. 1318–1325, 2006.
- [123] Z. R. Radakovic and M. S. Sorgic, "Basics of detailed thermal-hydraulic model for thermal design of oil power transformers," *IEEE Transactions on Power Delivery*, vol. 25, no. 2, pp. 790–802, 2010.
- [124] R. Petkov, "Optimum design of a high-power, high-frequency transformer," *IEEE Transactions on Power Electronics*, vol. 11, no. 1, pp. 33–42, 1996.
- [125] W. Hurley, W. Wolfle, and J. Breslin, "Optimized transformer design: Inclusive of high-frequency effects," *IEEE Transactions on Power Electronics*, vol. 13, no. 4, pp. 651–659, 1998.
- [126] M. Sippola and R. Sepponen, "Accurate prediction of high-frequency power-transformer losses and temperature rise," *IEEE Transactions on Power Electronics*, vol. 17, no. 5, pp. 835–847, 2002.
- [127] B. M. Ebrahimi, A. Fereidunian, S. Saffari, and J. Faiz, "Analytical estimation of short circuit axial and radial forces on power transformers windings," *IET Generation, Transmission & Distribution*, vol. 8, no. 2, pp. 250–260, 2014.
- [128] G. P. Peter, "Calculations for short circuit withstand capability of a distribution transformer," *Annals of the Faculty of Engineering Hunedoara*, vol. 9, no. 3, p. 243, 2011.
- [129] P. Huang, C. Mao, and D. Wang, "Analysis of electromagnetic force for medium frequency transformer with interleaved windings," *IET Generation, Transmission & Distribution*, vol. 11, no. 8, pp. 2023–2030, 2017.
- [130] H.-M. Ahn, J.-Y. Lee, J.-K. Kim, Y.-H. Oh, S.-Y. Jung, and S.-C. Hahn, "Finite-element analysis of short-circuit electromagnetic force in power transformer," *IEEE Transactions on Industry Applications*, vol. 47, no. 3, pp. 1267–1272, 2011.
- [131] F. Judd and D. Kressler, "Design optimization of small low-frequency power transformers," *IEEE Transactions on Magnetics*, vol. 13, no. 4, pp. 1058–1069, 1977.
- [132] S. Farhangi and A.-A. S. Akmal, "A simple and efficient optimization routine for design of high frequency power transformers," in *Proceeding of 9th EPE Conference*, Citeseer, 1999.
- [133] A. Garcia Bediaga, "Optimal design of medium frequency high power converters," PhD thesis, EPFL, 2014.
- [134] D. Stamenković, U. R. Vemulapati, T. Stiasny, M. Rahimo, and D. Dujic, "IGCT low-current switching— TCAD and experimental characterization," *IEEE Transactions on Industrial Electronics*, vol. 67, no. 8, pp. 6302–6311, 2019.
- [135] G. Ulissi, U. R. Vemulapati, T. Stiasny, and D. Dujic, "High-frequency operation of series-connected igcts for resonant converters," *IEEE Transactions on Power Electronics*, vol. 37, no. 5, pp. 5664–5674, 2022.

- [136] X. M. López-Fernández, H. B. Ertan, and J. Turowski, *Transformers: analysis, design, and measurement*. CRC press, 2012.
- [137] M. Mogorovic, “Modeling and design optimization of medium frequency transformers for medium-voltage high-power converters,” Ph.D. dissertation, EPFL, 2019.
- [138] X. Margueron, A. Besri, P.-O. Jeannin, J.-P. Keradec, and G. Parent, “Complete analytical calculation of static leakage parameters: A step toward hf transformer optimization,” *IEEE Transactions on Industry Applications*, vol. 46, no. 3, pp. 1055–1063, 2010.
- [139] *Elektro-Isola A/S, Denmark*.
- [140] N. Y. Abed and O. A. Mohammed, “Physics-based high-frequency transformer modeling by finite elements,” *IEEE Transactions on Magnetics*, vol. 46, no. 8, pp. 3249–3252, 2010.
- [141] P. Poulichet, F. Costa, and E. Laboure, “High-frequency modeling of a current transformer by finite-element simulation,” *IEEE Transactions on Magnetics*, vol. 39, no. 2, pp. 998–1007, 2003.
- [142] J. Hayes, N. O’Donovan, M. Egan, and T. O’Donnell, “Inductance characterization of high-leakage transformers,” in *Eighteenth Annual IEEE Applied Power Electronics Conference and Exposition, 2003. APEC ’03.*, vol. 2, 2003, 1150–1156 vol.2.
- [143] M. Jafari, Z. Malekjamshidi, and M. R. Islam, “Optimal design of a multiwinding high-frequency transformer using reluctance network modeling and particle swarm optimization techniques for the application of pv-linked grid-connected modular multilevel inverters,” *IEEE Journal of Emerging and Selected Topics in Power Electronics*, vol. 9, no. 4, pp. 5083–5096, 2021.
- [144] R. Schlesinger and J. Biela, “Comparison of analytical models of transformer leakage inductance: Accuracy versus computational effort,” *IEEE Transactions on Power Electronics*, vol. 36, no. 1, pp. 146–156, 2020.
- [145] A. Fouineau, M.-A. Raulet, B. Lefebvre, N. Burais, and F. Sixdenier, “Semi-analytical methods for calculation of leakage inductance and frequency-dependent resistance of windings in transformers,” *IEEE Transactions on magnetics*, vol. 54, no. 10, pp. 1–10, 2018.
- [146] P. Hammond, “Electric and magnetic images,” *Proc. IEE*, vol. 107, p. 306, 1960.
- [147] W. Rogowski, “Ueber das streufeld und den streuinduktionskoeffizienten eines transformators mit scheibenwicklung und geteilten endspulen: Die aenderung der umlaufzahl und des wirkungsgrades von schiffsschrauben mit der fahrgeschwindigkeit,” Ph.D. dissertation, Springer, 1909.
- [148] E. Roth, “Analytical study of the leakage field of transformers and of the mechanical forces exerted on the windings,” *Revue Generale de l’Electricite*, vol. 23, pp. 773–787, 1928.
- [149] A. Boyajian, “Leakage reactance of irregular distributions of transformer windings by the method of double fourier series [includes discussion],” *Transactions of the American Institute of Electrical Engineers. Part III: Power Apparatus and Systems*, vol. 73, no. 2, pp. 1078–1086, 1954.
- [150] R. Prieto, J. A. Cobos, O. García, P. Alou, and J. Uceda, “Study of 3-d magnetic components by means of” double 2-d” methodology,” *IEEE Transactions on Industrial Electronics*, vol. 50, no. 1, pp. 183–192, 2003.
- [151] A. Sharma and J. W. Kimball, “Evaluation of transformer leakage inductance using magnetic image method,” *IEEE Transactions on Magnetics*, vol. 57, no. 11, pp. 1–12, 2021.
- [152] M. Eslamian, M. Kharezy, and T. Thiringer, “An accurate analytical method for leakage inductance calculation of shell-type transformers with rectangular windings,” *IEEE Access*, vol. 9, pp. 72 647–72 660, 2021.
- [153] R. Schlesinger, T. Ewald, and J. Biela, “Analytical hybrid quasi-3d transformer leakage inductance model,” *IEEE Transactions on Power Electronics*, pp. 1–15, 2022.
- [154] A. Bejan, *Convection heat transfer*. John wiley & sons, 2013.
- [155] I. E. Idelchik, “Handbook of hydraulic resistance,” *Washington*, 1986.
- [156] K. Karsai, D. Kerényi, and L. Kiss, “Large power transformers,” 1987.
- [157] J. H. Holland, “Genetic algorithms and adaptation,” in *Adaptive Control of Ill-Defined Systems*, Springer, 1984, pp. 317–333.
- [158] K. Deb, *Multi-objective optimisation using evolutionary algorithms: an introduction*. Springer, 2011.
- [159] G. O. Brown, “The history of the darcy-weisbach equation for pipe flow resistance,” *Environmental and water resources history*, vol. 38, no. 7, pp. 34–43, 2002.
- [160] J. Zhang, X. Zhu, Z. Zhang, and Y. Xia, “Ac loss calculation and analysis of hollow conductor for doubly salient brushless dc generator,” *IEEE Transactions on Magnetics*, vol. 58, no. 8, pp. 1–5, 2022.
- [161] X. Guo, Z. Zheng, and C. Li, “The full-analytical model of ac loss for hollow copper winding in medium frequency transformer,” *IEEE Transactions on Power Electronics*, pp. 1–9, 2023.
- [162] T. Delaforge, H. Chazal, J.-L. Schanen, and R. J. Pasterczyk, “Increasing windings efficiency at high frequencies: Hollow conductors and clad metal conductors formal solution based on the magnetic potential,” in *2015 IEEE Energy Conversion Congress and Exposition (ECCE)*, IEEE, 2015, pp. 5689–5695.



- [163] T. Delaforge, H. Chazal, J.-L. Schanen, and R. J. Pasterczyk, "Copper losses evaluation in multi-strands conductors formal solution based on the magnetic potential," in *2015 IEEE Energy Conversion Congress and Exposition (ECCE)*, 2015, pp. 3057–3063.
- [164] Z. Huang, S. Nategh, V. Lassila, M. Alaküla, and J. Yuan, "Direct oil cooling of traction motors in hybrid drives," in *2012 IEEE International Electric Vehicle Conference*, 2012, pp. 1–8.
- [165] R. Camilleri, P. Beard, D. A. Howey, and M. D. McCulloch, "Prediction and measurement of the heat transfer coefficient in a direct oil-cooled electrical machine with segmented stator," *IEEE Transactions on Industrial Electronics*, vol. 65, no. 1, pp. 94–102, 2018.
- [166] R. Camilleri, D. A. Howey, and M. D. McCulloch, "Predicting the temperature and flow distribution in a direct oil-cooled electrical machine with segmented stator," *IEEE Transactions on Industrial Electronics*, vol. 63, no. 1, pp. 82–91, 2016.
- [167] X. Chen, J. Wang, A. Griffo, and A. Spagnolo, "Thermal modeling of hollow conductors for direct cooling of electrical machines," *IEEE Transactions on Industrial Electronics*, vol. 67, no. 2, pp. 895–905, 2020.
- [168] O. G. Martynenko and P. P. Khramtsov, *Free-convective heat transfer: with many photographs of flows and heat exchange*. Springer Science & Business Media, 2005.
- [169] R. Xin and M. Ebadian, "The effects of prandtl numbers on local and average convective heat transfer characteristics in helical pipes," 1997.
- [170] B. Hardik, P. Baburajan, and S. Prabhu, "Local heat transfer coefficient in helical coils with single phase flow," *International journal of heat and mass transfer*, vol. 89, pp. 522–538, 2015.
- [171] H. Zhao, X. Li, Y. Wu, and X. Wu, "Friction factor and nusselt number correlations for forced convection in helical tubes," *International Journal of Heat and Mass Transfer*, vol. 155, p. 119 759, 2020.
- [172] H. Ito, "Theoretical and experimental investigation concerning the flow through curved pipes," *Mem. Inst. High Speed Mech., Tohoku Univ.*, vol. 14, pp. 137–172, 1959.
- [173] Hitachi Metals Ltd. Japan, <https://www.hitachi-metals.co.jp/e/>.
- [174] Luvata Pori Oy, Finland, <https://www.luvata.com/>.
- [175] *Tube Bending Design Guide*. Lister Tube., 2021.
- [176] ABB, *Conventional breathers Data sheet*, 2020.
- [177] IEC61099, *Insulating Liquids-Specifications for Unused Synthetic Organic Esters for Electrical Purposes*, Switzerland, 2010.
- [178] H+H, *H+H High Voltage Technology*, <https://www.hundh-mk.com/produktbereiche/emv-technik/>, [Online] Accessed 2023.04.25.
- [179] G. Ulissi, "High frequency igct operation for dc transformer," EPFL, Tech. Rep., 2022.



# Nikolina Đekanović

*PhD candidate in Power Electronics*

✉ [nikolina.djekanovic@alumni.epfl.ch](mailto:nikolina.djekanovic@alumni.epfl.ch)  
July 2<sup>nd</sup> 1993  
Bosnia and Herzegovina / Serbia

## HIGHER EDUCATION

École Polytechnique Fédérale de Lausanne, Lausanne, Switzerland

2019-2023 PhD candidate, EDEE Electrical Engineering Doctoral School  
Design, Modeling and Optimization of High-Power Medium Frequency Transformers

KTH Royal Institute of Technology, Stockholm, Sweden

2017-2018 Erasmus Exchange Programme

TU Wien, Vienna, Austria

2016-2018 MSc - Energy Systems and Automation Technology

2011-2016 BSc - Electrical Engineering and Information Technology

## TEACHING / SUPERVISION EXPERIENCE

2020 Teaching assistant for the course *Power Electronics*  
Design and prototype of a 50 W DC-DC converter

2021 Teaching assistant for the course *Industrial Electronics I*  
Modeling and control of grid-connected power electronics converters

2021 Teaching assistant for the course *Industrial Electronics II*  
Modeling and control of power electronics converters and motor drives

2019 - 2022 Supervision of various BSc, MSc student projects and a MSc thesis

## PROFESSIONAL EXPERIENCE

2018	KTH Royal Institute of Technology, Stockholm, Sweden Research Engineer
2015 - 2016	ABB Semiconductors, Lenzburg, Switzerland Intern at Work Center Testing & Metrology
2014 - 2015	Automation and Control Institute, TU Wien, Vienna, Austria Project Assistant
2014 - 2015	TU Wien, Vienna, Austria Teaching Assistant
2012	Robert Bosch AG, Vienna, Austria Intern at Diesel Gasoline Systems Department

## LANGUAGES

English	Full working proficiency
German	Full working proficiency
French	Elementary proficiency
Spanish	Limited working proficiency
Serbian	Native

## COMPUTER TOOLS AND CODING

Simulation	Matlab Simulink, PLECS, COMSOL, LabView, Autodesk Inventor
PCB Design	Altium Designer
Coding	Matlab, Maple, C, Latex
OS	Windows, iOS

## REVIEW

Regular reviewer for IEEE Transactions on Power Electronics, IEEE Transactions on Industrial Electronics and IET Electric Power Applications, plus various conferences